Nanoscale Characterization of Dye Sensitized Solar Cells - Kelvin Probe Force Microscopy in Liquid

Inauguraldissertation

zur

Erlangung der Würde eines Doktors der Philosophie

vorgelegt der

Philosophisch-Naturwissenschaftlichen Fakultät

der Universität Basel

von

Gino Günzburger

aus Basel, BS

Basel, 2016

Genehmigt von der Philosophisch-Naturwissenschaftlichen Fakultät

auf Antrag von:

Prof. Dr. Ernst Meyer
Prof. Dr. Catherine Housecroft

Basel, den 17.02.2015

Prof. Dr. Jörg Schibler
Dekan

Abstract

Dye Sensitised Solar Cells (DSSCs) are a recent solar cell type based on the sensitisation of a nanostructured wide band gap semiconductor such as titania with a light absorbing dye molecule. The sensitisation is necessary in order to exploit the energy content of the visible light, which is not absorbed by the titania. The nanostructuring of the semiconductor is fundamental for a highly efficient DSSC, since it multiplies the surface area and thereby the amount of adsorbed dye and thus of absorbed light. Despite the dependence of DSSCs on the nanostructuring of their active layer, most science treating DSSCs is concerned with entire cells, and studies examining the nanoscale properties such as the work function on the single nanoparticles are rare.

To fill this gap we performed surface potential measurements on bare and sensitised nanoporous titania layers for DSSCs in different environments including electrolyte solutions. The only recently described Open Loop Kelvin Probe Force Microscopy (OL-KPFM) mode was employed, since it enables the measurement of the surface potential with nanoscale resolution without the necessity to apply a direct voltage (dc-voltage) and thus is not limited to measurements in air and non-polar solvents.

Both the fabrication of DSSCs and the surface potential measurement in a liquid environment had to be introduced to our workgroup as part of this work. Thus the relevant background information and the development of the necessary methods and expertise is the basis of this thesis. After the introduction of the general setup and working principle of DSSCs and a more detailed discussion of its key components and processes, the basics of surface potential measurement on the nanoscale are outlined. The necessary steps to fabricate reproducible DSSCs are treated in detail together with the identification of some dead-ends on the way there.

Surface potential measurements in air, water, sodium chloride solutions of different concentrations, and highly diluted electrolytes for DSSCs were performed on titania layers and a model sample. The measurements in air were compared to data recorded by

traditional Kelvin Probe Force Microscopy (KPFM) measurements based on the compensation of the electrostatic force by the application of a dc-voltage between sample and tip. The comparison yielded equal contrast and distribution of the measured surface potential. All KPFM measurements are based on the modelling of tip and sample as the two plates of a plate capacitor. An excellent agreement of the measured data with the applied model used for the calculations of the surface potential was found not only for the measurements in air, but also in water. In combination with an excellent agreement between the data recorded in air and in water, the proof of the applicability of the basic model enabled the expansion of the application range of KPFM to polar liquids. In all the experiments performed in electrolyte solutions a strong non-linearity of the capacitance of the tip-sample system was observed. Possible reasons for the non-linear behaviour were identified and discussed. Examples are the diffusion of ions, shielding of electrical fields by charged layers and onsets of chemical reactions. The non-linearity impedes the application of the basic model, and thus the calculation of quantitative parameters from the measurement. However qualitative interpretation shows, that variations of the surface potential can still be detected and thereby valuable information about examined surfaces can be gained. Applied to the titania layers for DSSCs our measurements indicate a similar distribution of the dipoles on the titania surface upon sensitisation as was determined in air, and thus it shows the possibility to transfer findings made in air to the complete solar cell system and its electrolyte surrounding.

Contents

Glossary

a.u.	Units for the comparison of measurements of calculations made under equal circumstances or of normalised data. Arbitrary units of different measurements might not be comparable to each other.
$A_{1\mathrm{st}}$	Oscillation amplitude at the first resonance frequency, in this work used as control signal for the topography measurement.
$A_{1\omega_{\mathrm{ac}}}$	Oscillation amplitude of the cantilever due to $F_{1\omega_{\mathrm{ac}}}$, thus at $f_{\mathrm{det}} = f_{\mathrm{ex}}$.
$A_{2\omega_{\mathrm{ac}}}$	Oscillation amplitude of the cantilever due to $F_{2\omega_{\mathrm{ac}}}$, thus at $f_{\mathrm{det}} = 2 \cdot f_{\mathrm{ex}}$.
ac-voltage	Alternating voltage.
AFM	Atomic Force Microscopy, a very high resolution scanning probe microscopy capable of resolutions below 1 nm, based on the scanning of the surface with a sharp tip on a cantilever and on the interaction of the tip with the surface due to different intermolecular forces.
AFM-SECM	Atomic Force Microscopy Scanning Electro Chemical Microscopy.
AM-AFM	Amplitude Modulation AFM, tapping mode AFM, AFM-mode in which the amplitude is the control signal for the tip-sample-distance controller.
Cantilever	Cantilever, a small beam fixed to a chip on one end carrying a sharp tip at the bottom of the other end, used as sensor in an AFM.

CB	Conduction Band, the lowest energy band of a solid which is not completely filled with electrons.
CIGS-solar cell	Copper Indium Gallium Selenide solar cell, highly efficient type of thin film solar cell.
CL-KPFM	Closed Loop - Kelvin Probe Force Microscopy, traditional KPFM measuring the CPD by the nullification of the electrostatic forces between cantilever and sample by the application of a dc-voltage.
CPD	Contact Potential Difference, the difference in the work function between two metals.
$\mathrm{CPD_{CL}}$	CPD determined in the CL-KPFM measurement, thus by compensating the $F_{1\omega_{\mathrm{ac}}}$ with an applied V_{dc}.
$\mathrm{CPD_{OL}}$	CPD calculated from the OL-KPFM measurement, thus from the measurement of $F_{1\omega_{\mathrm{ac}}}$ and $F_{2\omega_{\mathrm{ac}}}$ by means of $A_{1\omega_{\mathrm{ac}}}$ and $A_{2\omega_{\mathrm{ac}}}$.
dc-voltage	Direct voltage.
DEFM	Dynamic Electrostatic Force Microscopy.
DL-OL-KPFM	Dual-Frequency Open Loop Kelvin Probe Force Microscopy.
DSSC	Dye Sensitised Solar Cell, a solar cell based on the sensitisation of a wide bandgap semiconductor by a light absorbing dye.
EC-STM	Electrochemical-Scanning Tunnelling Microscopy.
ECFM	Electro Chemical Force Microscopy.
EDL	Electrostatic Double Layer, double layer of ions forming on a surface in an electrolyte, described by the Guoy-Chapman-Stern model (GCS).
E_{F}	Fermi energy level, the electrochemical potential of electrons in a solid.
EFM	Electrostatic Force Microscopy.
EIS	Electrochemical Impedance Spectroscopy.
EtOH	Ethanol.
E_{vac}	Vacuum energy level.

$F_{1\omega_{ac}}$-setting	Measurement setting of the lock-in amplifier to measure the $F_{1\omega_{ac}}$. The lock-in or PLL is tuned to the first harmonic, thus it is detecting at the same frequency as the excitation ($f_{det} = f_{ex}$).
$F_{1\omega_{ac}}$	Component of the electrostatic force between two capacitor plates on the first harmonic of an excitation signal, thus at the excitation frequency itself.
$F_{2\omega_{ac}}$-setting	Measurement setting of the lock-in amplifier to measure the $F_{2\omega_{ac}}$. The lock-in or PLL is tuned to the second harmonic, thus it is detecting at the twice the excitation frequency ($f_{det} = 2 \cdot f_{ex}$).
$F_{2\omega_{ac}}$	Component of the electrostatic force between two capacitor plates on the second harmonic of an excitation, thus the double of the excitation frequency.
F_{dc}	Dc component of the electrostatic force between two capacitor plates.
f_{det}	Frequency at which a signal is detected. Usually f_{det} lies either at the excitation frequency or at twice the excitation frequency.
F_{vdW}	Van der Waals Forces, forces between neutral particles without permanent dipole in close proximity, due to dipoles arising from charge-fluctuations on the particle surfaces.
F_{es}	Electrostatic Forces, forces due to electrostatic interactions.
f_{ex}	Excitation frequency.
FF	The fill factor is a quality factor used to describe solar cells. It compares the theoretical maximal power output an absolutely ideal (but of course physically impossible to achieve) solar cell would have, with the power output of the examined solar cell.
FM-AFM	Frequency Modulation AFM, non-contact AFM, an AFM-mode in which the frequency is the control signal for the tip-sample-distance controller.
F_{mag}	Magnetostatic Forces, force between particles based on magnetic interactions.

FTO	Fluorine doped Tin Oxide, a TCO commonly applied in DSSCs.
F_{ts}	Resulting force acting on a cantilever tip and a sample (in close proximity).
GaAs-solar cell	Galium Arsenid solar cell.
GCS	Guoy-Chapman-Stern model, model describing the surface of a sample in a ion containing liquid by means of an electronic double layer of ions forming on the sample surface.
HH-OL-KPFM	Half Harmonic excitation Open Loop Kelvin Probe Force Microscopy, OL-KPFM technique where $A_{1\omega_{\mathrm{ac}}}$ and $A_{2\omega_{\mathrm{ac}}}$ are detected at the same frequency, preferably a resonance frequency of the cantilever.
HOMO	Highest Occupied Molecular Orbital.
HOPG	Highly Ordered Pyrolytic Graphite.
HPLC	High Pressure Liquid Chromatography.
I_{sc}	Short circuit current, the current generated by a solar cell when no voltage is applied, thus through an electrical circuit without any resistances.
ITO	Indium doped Tin Oxide, a TCO commonly applied in DSSCs, but not in our cells, which are made with FTO.
IV-curve	Current-voltage characteristics, a recording of the current produced by a diode or solar-cell depending on a voltage applied over the cell.
KPFM	Kelvin Probe Force Microscopy, AFM based technique to measure the CPD of a sample with nanoscale resolution.
Lennard-Jones potential	Lennard-Jones-Potential, empirical description of the potential of particles in close proximity.
lock-in	Lock-in amplifier.

LSM	Laser Scanning Microscope, a microscope based on the scanning of a laser beam over the sample surface and determination of the sample topography by means of the reflection-intensity of the laser beam.
LUMO	Lowest Unoccupied Molecular Orbital.
N3	A standard ruthenium-complex dye used for Dye Sensitised Solar Cells with the chemical name "cis-Bis(isothiocyanato)bis(2,2'-bipyridyl-4,4'-dicarboxylato)ruthenium(II)".
N719	A standard ruthenium-complex dye commonly used for Dye Sensitised Solar Cells with the chemical name "Di-tetrabutylammonium cis-bis(isothiocyanato)bis (2,2'-bipyridyl-4,4'-dicarboxylato)ruthenium(II)". Its chemical structure is shown in Fig. 2.2. N719 is the salt of N3.
nc-AFM	Non contact AFM, see FM-AFM.
NP	Nanoparticle, particles with diameters in the nanometre range, generally below 100 nm. However for this work also particles with larger diameters up to ~200 nm (which are used for the scattering layers) will be denoted nanoparticles.
OL-EPM	Open Loop Electrostatic Potential Microscopy, different name for OL-KPFM.
OL-KPFM	Open Loop - Kelvin Probe Force Microscopy, KPFM technique not depending on the compensation of electrostatic forces by the application of a dc-voltage, but on the measurement of the forces and subsequent calculation of the CPD.
PLL	Phase Locked Loop.
PSD	Position Sensitive Detector, a detector (e.g. for light) which measures not only the intensity of an incident light-beam, but also its position.

RT	Room temperature, temperature in a non air-conditioned room, generally in the region of 22 to 25 °C.
SCM	Scanning Capacitance Microscopy.
SECM	Scanning Electro Chemical Microscopy.
SEM	Scanning Electron Microscopy, microscopy technique based on the scanning of the sample surface with an electron beam and determination of the sample-topography by means of scattered and reflected electrons. Only applicable for conducting samples, but capable of fast imaging, large resolution in the nanometre regime and of easy and fast changes in the magnification from a few 10× to a few 100 000×.
SF-OL-KPFM	Single-Frequency Open Loop Kelvin Probe Force Microscopy.
solar simulator	Device to generate simulated sun light, thus a lamp producing light with a spectrum very close to the one of the sun.
SPM	Scanning Probe Microscopy, collective term describing all microscopy techniques which are based on scanning the surface of the studied sample by means of a probe, such as a cantilever of a needle.
STM	Scanning Tunnelling Microscopy, a very high resolution scanning probe microscopy technique based on the scanning of a sample surface with a needle employing the tunnelling-current between tip and sample as interaction signal. Only applicable on conducting samples.
TAA	"Titanium diisopropoxide bis(acetylacetonate)".
TCO	Transparent Conductive Oxide, transparent and conducting materials often applied as electrode-material for electronic devices.
THF	Tetra Hydro Furan.

UHV	Ultra High Vacuum, vacuum in the pressure range below 1×10^{-9} mbar.
V_{ac}-spectroscopy	Excitation voltage spectroscopy, measurement of the cantilever oscillation upon sweeping of the excitation voltage (V_{ac}).
V_{CPD}	Voltage corresponding to the potential of the CPD ($V_{\mathrm{CPD}} = \frac{1}{\mathrm{e}} \cdot \mathrm{CPD}$) and which needs to be applied between tip and sample to compensate the force introduced by the CPD.
V_{oc}	Open circuit voltage, voltage generated by a solar cell in an electrical circuit with an infinite resistance.

1. Introduction

The global energy consumption is increasing steadily [1, 2] while the reserves of fossil fuels diminish and negative effects of the burning of fossil fuels and nuclear energy on our environment become more and more evident [2, 3]. Examples thereof are not only the increasing temperature and the melting of glaciers and polar ice caps, but also catastrophes such as the one in "Fukushima" in the year 2011, which bring the complex of problems to the public mind. Therefore renewable energy sources such as wind, hydropower, solar thermal systems and photovoltaic systems which have been studied for a long time (e.g. [4–6]) but led a more or less niche existence, now receive a general interest. Every year a total of 1.56×10^{18} kWh, thus 5.6×10^{24} J of energy reach the earth as radiation from the sun [7]. This corresponds to more than $10\,000 \times$ the global annual energy usage. Thus solar energy harvesting has the potential to play an important role in a future energy politics based on renewable energies. One capital advantage of solar cells over wind and water turbines are the absence of moving parts. This allows a noiseless operation, reduces the abrasion of the devices and thus the amount of service necessary during their lifetime, and increases the lifetime in general. As an example one of the first solar facilities which was installed in 1984 on the roof of the Georgetown University in Washington DC is still running today [8]. While solar cells attract an increasing amount of attention, the public does not discern between different types of solar cell. However a multitude of different types of solar cell have been developed and are studied nowadays. Examples are mono- and polycrystalline silicon cells, thin-film solar cells such as amorphous silicon, Copper Indium Gallium Selenide solar cells (CIGS-cells) [9, 10], Galium Arsenid solar cells (GaAs-cells) [11], perovskite solar cells [12], DSSCs [13] and other organic solar cells [14, 15]. They differ widely in important parameters such as the maximum measured efficiency [16], the energy payback time (thus the time they need to be running until the energy expended for their production has been regained by transforming sunlight to electricity) [17, 18], their (expected) lifetime [17], the price and many others.

DSSCs [13] are an alternative kind of solar cell based on the sensitisation of a nanostruc-

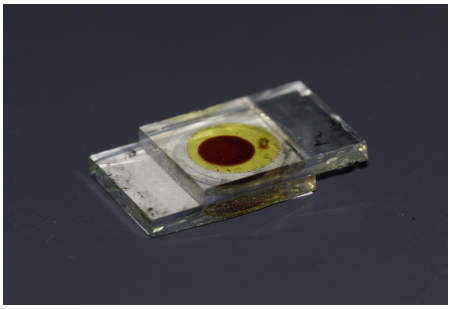

Figure 1.1.: *A DSSC sensitised with N719 fabricated in our lab.*

tured wide band gap semiconductor with a light-absorbing dye. An example of a DSSC made in our lab is shown in Fig. 1.1. The usual setup of a DSSC is a pair of transparent electrodes consisting of a Transparent Conductive Oxide (TCO) which is coated onto a glass-substrate. The photo-electrode is the substrate for the sensitised layer of titania nanoparticles (NPs), the counter-electrode is coated with a catalyst such as platinum. The two electrodes are connected by an electrolyte or a hole-conductor. Upon irradiation of light the dye molecules absorb photons and thereby are brought in an excited state. Thereof they inject an electron into the conduction band (CB) of the semiconductor. The dye-molecule is regenerated by a redox-molecule from the electrolyte and the electron travels through the external circuit and regenerates the redox-molecule at the counter electrode. Advantages of DSSCs compared to other types of solar cell, are high efficiency even at low light intensities or under diffuse light [13], which is presumably enabled by the nano- and microstructuring of the photo-active layer. Additionally the fabrication of DSSCs is less complicated and less expensive and requires less specialised and expensive gear and processes as compared to the fabrication of other types of solar cell, such as silicon solar cells. Also the necessary energy for the fabrication of DSSCs is lower and thus the energy payback time shorter [18].

The structure of a DSSC with its nanoporous anode and the inter-penetrating electrolyte connecting the electrodes reminds of a battery, which has a similar structure [19, 20]. This indicates presumable synergies for the study of the two systems. Also a combination of solar-cell and battery might be possible. The resulting combined energy-harvesting and storage device would be of great interest, since it would address two of the main bottle-necks in the global energy challenge.

Since their development by Michael Grätzel and Brian O'Regan in 1991 [13] DSSCs have been studied extensively (e.g. [21, 22]) and were continuously developed. Prominent improvements were the introduction of a scattering layer to improve the exploitation of

light [23], the introduction of solid state electrolytes [24] and many more (see e.g. the review of Hagfeldt and coworkers [21]).

Even though DSSCs are based on nanocrystalline or otherwise nanostructured layers, microscopic studies concerning DSSCs are rare. Most investigations take place on entire cells or entire layers. Examples are the measurement of current-voltage characteristics, impedance spectroscopy [25], current extraction measurements to examine the distribution of trap states in the semiconductor [26] and voltage decay measurement to determine the electron lifetime [27] and others as is summarised in chapters 10 and 12 of the book "Dye-sensitized Solar Cells" edited by Kalyanasundaram [22]. Examples for the more seldom investigation on the single dye-molecule or TiO_2-particle level are a study of single dye molecules on rutile-titania single crystals by Ikeda and coworkers [28], or of changes in the inorganic matrix of ZnO-DSSCs by Graaf and coworkers [29]. Such measurements might give additional insight into the cell and provide information about the homogeneity of the dye-adsorption, adsorption of co-adsorbents and "dirt", orientation and binding mechanisms of dye-molecules, conductivity of the NP-layers and many more.

Measurements in the nanoscale are a difficult task to accomplish. Effects being observed are necessarily small, and are often influenced and superimposed by larger effects occurring at larger scales, interactions between the measuring-device and the sample, noise or others. Examples are the examination of single molecules on surfaces. There are few measurement techniques which show a sufficiently high resolution to resolve a single molecule or even atom such as Atomic Force Microscopy (AFM) or Scanning Tunnelling Microscopy (STM). These measurements can only be accomplished on a sample surface which is atomically flat (thus has terraces on which all the atoms are exactly in one plane), since otherwise the examined molecules could not be distinguished from the atoms and molecules of the sample surface. Additionally the measurements have to be performed under Ultra High Vacuum (UHV) conditions, since else molecules from the air adsorb onto the surfaces and thus conceal the examined molecules. For molecules which do not bind strongly to the surface, the samples have to be cooled to very low temperatures in the range of 4 K, since else the movement of the molecules under examination due to their thermal energy makes their imaging impossible. One family of measurement techniques providing the necessary nanoscale resolution is Scanning Probe Microscopy (SPM). SPM techniques are based on the rasterised scanning of a measurement tip over the surface of the sample. Thereby its topography and other properties such as the work function are measured with nanoscale resolution. Furthermore SPM-

measurements have very small impacts on the surface, since the only interaction is between the small probe-tip and the surface where very small forces are acting. Examples for measurement techniques belonging to the SPM-family are the STM which uses the tunnelling of electrons between tip and sample as interaction signal in order to determine the tip-sample separation and thus for the topography measurement and to determine electrostatic properties of the surface [30]. A second example is the AFM [31], which uses a sharp tip on a Cantilever as probe for the measurement of different forces between the tip and the sample. Possible forces are short range repulsive- and chemical forces, and long ranged forces such as van der Waals forces (F_{vdW}), electrostatic forces (F_{es}), but also magnetostatic forces (F_{mag}). The AFM yields nanoscale resolution not only in UHV and air, but even in liquid environments [32, 33]. Additionally the AFM provides the possibility of nanoscale examination of other surface properties than the topography. An example is the measurement of electrostatical properties of the sample surface, such as its work function, which can be measured by separating the F_{es} from the other forces acting on the cantilever. In KPFM [34] the F_{es} are isolated by the application of an alternating voltage (ac-voltage) and subsequently the work function is determined by compensating the isolated F_{es} by means of a dc-voltage applied between tip and sample. The KPFM technique will be explained in more detail in section 2.2.2. Similarly general electrostatic properties are measured by separation of the F_{es} by Electrostatic Force Microscopy (EFM) where the force is not compensated but measured ([35] [36, chapter 6]), and of capacitative surface properties by the application of Scanning Capacitance Microscopy (SCM) wherein the capacitance between tip and sample is determined by measurement of the force at the second harmonic component of the applied ac-voltage (thus the response at twice the excitation frequency), which holds capacitative information about the sample surface as described by Matey and Blanc [37] and by Yoshitsugu Nakagawa in the book “Roadmap of Scanning Probe Microscopy” edited by Morita [36, chapter 5]. While EFM yields only qualitative information about the electrostatic properties of the sample surface, with KPFM a quantitative measurement of the work function is possible.

In a recent study [38] we compared bare TiO_2 layers, layers sensitised with a ruthenium based standard DSSC-dye (the bipyridyl-Ru-complex N719, chemical structure shown in Fig. 2.2) and a recently designed copper complex by means of KPFM [34]. The measurements revealed microscopic inhomogeneities of the work function of bare- as well as sensitised layers. Additionally the two dyes exhibit a surface-dipole of similar magnitude but opposite orientation. The inhomogeneities might hint to undesired ad-

sorption of water and solvent molecules to the surface, which would compete with the dye-binding and hinder the dye-TiO_2 interaction. The opposite dipole orientation of the two dyes might explain the far superior performance of N719 and deliver important clues about the reasons for the discrepancies in the performance of various dyes and thus might advance the general research and knowledge on DSSCs. We mainly attribute the measured open circuit voltage (V_{oc}) difference of the cells sensitised with the two dyes to their work function difference. Thus also the measured work function inhomogeneities are assumed to influence the V_{oc} of our cells. The studies we presented so far were all performed in a dry nitrogen environment. However, the cell environment consists of a highly concentrated electrolyte solution excluding oxygen and water. Thus the interface is very different, since effects of solvation and the presence of a large number of ions are bound to influence the behaviour of the dye-titania system. In order to get insights into this complex electrolyte-dye-TiO_2 interface measurements at the nanoscale and in electrolyte solution have to be performed.

Different techniques exist to study topography or electrochemical properties of surfaces and processes in electrolyte solutions. Examples are the Electrochemical-Scanning Tunnelling Microscopy (EC-STM) which was first reported by Yang and coworkers in 1986 [39] and is explained by Pobelov in the book "Encyclopedia of Nanotechnology" edited by Bhushan [40]. It consists of an STM which is run in an electrolyte solution using a modified setup with multiple electrodes, where tip and sample are two working electrodes. In order to minimise currents due to electrochemical reactions or flow of ions the entire tip except a very small part at the tip apex needs to be insulated and the relative potentials of tip and electrodes chosen accordingly. Insulating materials for the tip can be glass [41] as cited in [42], apiezon [43], and others. EC-STM enables the measurement of the topography down to atomic resolution [44], but also the monitoring of chemical reactions by the observation of surface changes, which enables conclusions about processes and mechanisms occurring on the sample surface and in the electrolyte, e.g. of the deposition of metals e.g. [45, 46].

A similar technique to examine surfaces in electrolytes is Scanning Electro Chemical Microscopy (SECM) which was introduced by Bard and coworkers [47] and reviewed e.g. by Mirkin [48]. As in EC-STM the setup consists of an insulated tip that is scanned over a sample in an electrolyte solution. Tip and sample can act as two working electrodes in the multi-electrode setup. Insulated tips in the range of nanometres to micrometers are employed. However in SECM-mode the measured signal is the Faraday-current generated by electrochemical processes at the surface of the sample, and not the tunnelling-current.

The SECM can be run in a multitude of different modes and thus perform a large variety of electrochemical measurements, which are explained in the review [48]. Examples are chemical reactions on the surface and thereby the reactivity and voltage dependence of the sample, in the nano or micro-scale depending on the tip-size. Also concentration gradients within a layer are accessible.

Both the EC-STM and the SECM measure the topography and the electrochemical properties by means of only one signal at a time. Since the signal depends on multiple factors (e.g. the topography and the reactivity of the sample, if this is the examined surface characteristic) a separation of the dependences is difficult to achieve. This introduces uncertainties in the recorded data. For an example imagine a measurement of a surface with unknown topography. The recorded signal is the current originating in a redox reaction where the redox molecule is oxidised at the tip and reduced at the sample surface. This setup is called Positive-feedback, since the approach of the tip towards the sample leads to an increase in the measured current. Upon scanning of the tip across the sample a decrease of the measured current could now originate either in a depression of the surface and thus a larger distance between tip and sample, or in a decreased reactivity of the sample which would decrease the rate of the redox-reaction.

This limitation is overcome by a technique combining the SECM with an AFM to Atomic Force Microscopy Scanning Electro Chemical Microscopy (AFM-SECM). Therein SECM measurements are performed, but the employed tip is a cantilever which provides nanoscale resolved topography information. A first approach to AFM-SECM was presented in 1996 by Macpherson et al. [49] and it was integrated by the same authors in 2000 [50] for contact mode (thus with the AFM-cantilever in contact with the sample surface during the measurement) and in 2001 for lift-mode (thus the surface is scanned two times, recording the topography in the first and scanning the tip again on a path equal to the measured topography, but having lifted the tip by a defined distance) [51].

The presented methods all reveal interesting electrochemical properties of the examined surfaces. However, they do not enable the measurement of the work function of the sample and of local variations thereof. This gap could be filled by KPFM measurements. KPFM has been implemented in air [34], vacuum [52], and non-polar liquids [53]. Since KPFM is based on the compensation of the F_{es} by the application of a dc-voltage it can not easily be applied in polar liquids or electrolyte solution, since in such an environment the application of a dc-voltage leads to a current due to the drift of ions and polarised molecules or even electrochemical reactions at the tip or sample surface.

Nevertheless a technique to measure the work function in liquid has been developed. It was presented by Kobayashi and coworkers and denominated Open Loop Electrostatic Potential Microscopy (OL-EPM) [54]. It is a two step process were first the electrostatic interaction is measured as in EFM, thus by excitation of the F_{es} by the application of an ac-voltage between cantilever-tip and sample, and measurement thereof by the oscillation of the cantilever. Secondly the capacitative interaction is measured by excitation of the electrostatic interaction and measurement of the capacitance at the second harmonic thereof, as in SCM. The work function of the sample is calculated from the two recorded signals and the magnitude of the V_{ac}, as is explained in more details in section 2.2.2 or in reference [54]. In contrast to the KPFM measurements based on the nullification of the electrostatic force which includes a control-loop and which is therefore also denoted Closed Loop Kelvin Probe Force Microscopy (CL-KPFM) the method presented by Kobayashi et al. does not include a control-loop, but relies on the measurement of the force. It is therefore denoted OL-EPM or (as in this work) Open Loop Kelvin Probe Force Microscopy (OL-KPFM). In the original publication Kobayashi et al. examine a film of adsorbed dodecylamine molecules on a Highly Ordered Pyrolytic Graphite (HOPG) sample in a 1 mM aqueous salt solution. The excitation for both signals is applied at the same frequency, namely $f_{\text{ex-}1\omega_{\mathrm{ac}}} = f_{\text{ex-}2\omega_{\mathrm{ac}}} = 30\,\mathrm{kHz}$. While the electrostatic signal is detected at the excitation frequency ($f_{\text{det-}1\omega_{\mathrm{ac}}} = 30\,\mathrm{kHz}$), the capacitative signal is detected at its second harmonic, thus at twice the excitation frequency, thus at $f_{\text{det-}2\omega_{\mathrm{ac}}} = 60\,\mathrm{kHz}$. The rather simple calculations assume equal sensitivity of the cantilever for the detection at the two different frequencies used to detect the electrostatic- and the capacitance signal. In a following publication the same authors expand their original model by including a transfer function which models the cantilever oscillation as a damped harmonic oscillator [55]. Thereby the increased sensitivity of the cantilever due to a resonance frequency lying close to the detection-frequencies can be determined and the measured signal can be corrected for it. Thereby quantitative measurements become possible, which the authors demonstrate by the measurement of latex beads with different sizes and charges in an 1 mM aqueous NaCl-solution at an excitation frequency of $f_{\text{ex-}1\omega_{\mathrm{ac}}} = 30\,\mathrm{kHz}$ and detection frequencies of $f_{\text{det-}1\omega_{\mathrm{ac}}} = 30\,\mathrm{kHz}$ and $f_{\text{det-}2\omega_{\mathrm{ac}}} = 60\,\mathrm{kHz}$ respectively. The measurements enable a clear distinction between both the size and charge of the beads. The measured Contact Potential Differences (CPDs) are proved to be quantitative by comparison of the measured surface potential of the examined beads with zeta-potential measurements of the same beads [55]. The low excitation frequency of 30 kHz limits the application of the described method to low concentration electrolyte [56]. The upper detection frequency of an AFM is limited by the experi-

mental setup, usually by the bandwidth of the detection-system. This upper limit for the detection also limits the excitation frequency, since the capacitance signal needs to be detected at twice the frequency of the excitation, and thus the excitation frequency has to be lower than half the upper limit of the detection-system. To overcome this limitation Kobayashi et al. further developed their OL-EPM technique [56]. By exciting with a signal consisting of two frequency components a dual-frequency-response of the cantilever is triggered. Thereof the work function is calculated. The two excitation and detection frequencies in this setup can be chosen arbitrarily and thus lie much closer together. Thereby the maximum excitation frequency can be brought close to the maximum of the detection system, enabling nearly twice as high detection frequencies. This so called dual-frequency OL-EPM not only enables work function measurements in liquids of higher concentration, but also increases the signal to noise ratio, as is shown by the measurement of latex bead of 25 nm diameter on HOPG in aqueous NaCl solutions with concentrations of 1 and 10 mM. Another variation of the technique was presented by Guo and coworkers [57] who performed work function measurements in half-harmonic mode. Therein an increased sensitivity is enabled, by detection of both the signals at the same mechanical resonance frequency of the cantilever. This is achieved by tuning of the excitation and detection frequency to a mechanical resonance for the measurement of the electrostatic signal, and by changing the excitation frequency for the measurement of the capacitance signal to half that frequency. Thereby also the detection frequency of the capacitance signal corresponds to the frequency of the mechanical resonance, and the resonance enhancement can be taken advantage of for both signal. Additionally in this measurement-mode the transfer-function correction introduced by Kobayashi et al. in 2011 in [55] is redundant, since both transfer-functions are equal. While Guo et al. use the half-harmonic mode only in air, it is applied in ultra pure water by Collins et al. who study graphene-layers on a copper substrate [58]. They measure surface potentials in water which are in good agreement with those measured in air.

In the present work starting from the techniques proposed by Kobayashi [54] and Guo [57] OL-KPFM in single-frequency half-harmonic excitation mode was used to investigate titania layers for DSSCs in different environments in order to gain deeper understandings of the relatively young measurement technique and the investigated interface. The applicability of the model of a plate capacitor, on which the calculations of the surface potential are based, was verified by means of spectroscopic measurements. Measurements on titania layers and a model-sample of gold and indium dots on an Si-wafer were performed in air, water, salt solutions of different concentrations (NaCl; 1 and 10 mM)

and in a simplified DSSC-electrolyte in two highly diluted concentrations (1/100 and 1/10 of the normal electrolyte concentration).

After having introduced the topic and the background of the present work and having given a very short overview over DSSCs, methods to perform nanoscale measurements in general and nanoscale measurements in liquid and electrolyte environments in particular in this chapter, in the following few paragraphs the structure of the present thesis will be shown, together with a short summary of each of the following chapters, wherein the introduced topics will be discussed in more detail.

In **chapter 2** theoretical background information necessary for the understanding of the present work is presented. The first part gives an overview over the working principle and the general setup of a DSSC before explaining the key components and the processes occurring within the cell in more detail. In the second part AFM and KPFM as techniques for the examination of the topography and electrostatical properties of surfaces with a nanoscale resolution are presented. Since they are both based on an AFM-equipment, AFM is introduced first. The working principle is explained and a special focus is put on the interactions between the measurement tip and the sample. The different operation-modes of an AFM are also mentioned. For the understanding of KPFM the contact potential difference is explained, together with a detailed discussion of the electrostatic force between tip and sample based on the modelling of the system as a capacitor. Two modes of KPFM are introduced which are based on the compensation of the electrostatic force using a control-loop or the measurement of the electrostatic and capacitative interactions between tip and sample.

In the first part of **chapter 3** the efforts which were necessary to implement the fabrication of reproducible DSSCs in a research group whose core competence are the study of surfaces in UHV are shown. Thereto the different steps of DSSC-fabrication are introduced. A main focus lies on the deposition and examination of the nanoporous titania layer. Additionally differences in the characterisation of DSSCs and silicon solar cells are pointed out. Afterwards methods for the production of DSSCs with highly sensitive dye-molecules are discussed. In the second part the instrumentation for the nanoscale analysis of the titania layers is explained.

In **chapter 4** the results of the nanoscale analysis of the titania layers by AFM and KPFM are presented, discussed and explained. A special focus is put on the deviation of the measured data upon measurement in electrolyte solutions from the expected data predicted by the models and the measurements in air and water, which is shown to be

due to the diffusion of the ions in the electrolyte and the formation of electronic double layers on the sample and the cantilever surface.

Chapter 5 presents a summary of the results and explanations of the work with the solar cells and of the KPFM-measurements presented in the previous chapter and a short outlook.

2. Theoretical and experimental basics

2.1. Dye Sensitised Solar Cells (DSSCs)

An interesting kind of solar cell is the Dye Sensitised Solar Cell (DSSC) (also called Grätzel-cell) which was first described in 1991 by Brian O'Regan and Michael Grätzel [13] and has been the subject of a large amount of research since (see e.g. the review of Hagfeldt and coworkers [21] and the book edited by Kalyanasundaram [22]). DSSCs are based on the sensitisation of a wide band gap semiconductor (e.g. TiO_2) with a light-absorbing molecule called dye. Excitation of the dye-molecules by incident light leads to the injection of electrons into the semiconductor and subsequent reduction of the oxidised dye. Thereby the charge separation necessary for the harvesting of electrical energy from light energy is accomplished. Basic research on the matter has been conducted earlier [59–61] but only O'Regan and Grätzel started to use the wide band gap semiconductor in a nanocrystalline form in order to increase the surface area and thus the amount of adsorbed dye, which lead to a marked increase in the achieved efficiency [13]. The nano structuring of the active layer induces an increased sensitivity for indirect light irradiation and thus a high efficiency in diffuse light conditions. The titania particles used for DSSCs are readily available, since they are produced in very high amounts and sufficient purity due to the fact that they are the basis of many other industrial products. Additionally the energy necessary to fabricate a DSSC is comparably low, enabling a short energy pay back time compared to other types of solar cells, namely silicon cells [18]. The semi-conductor scaffold which is sensitised can be semi-transparent or opaque and sensitised molecules of very different colours are available. This gives the DSSC a high degree of versatility of appearance. An additional advantage is the possibility to produce DSSCs on flexible substrates, as reviewed by Weerasinghe and coworkers in [62]. The flexibility and transparency enables the introduction of DSSCs in daily objects such as bags (as has been done by G24 Innovations Limited, Cardiff, Wales, UK), lamp shades to produce self-charging lamps (Sony Corporation Ltd., Japan) and many more. Additional examples can be found in chapter 9 of Ref. [22]. In addition to

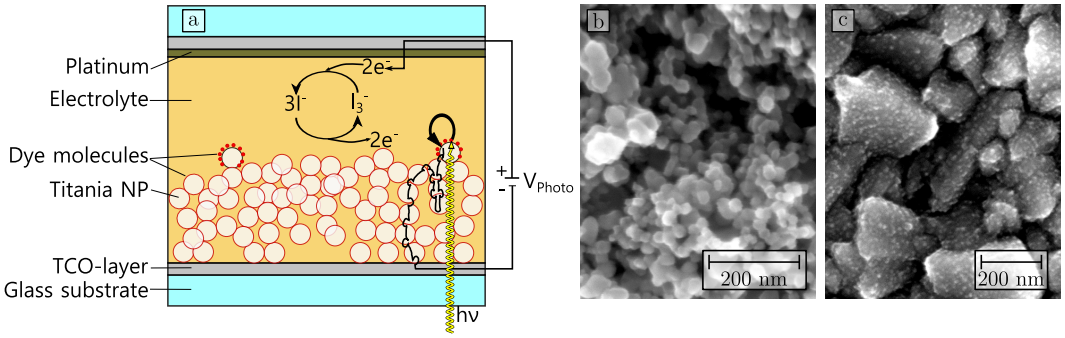

Figure 2.1.: *a) Outline of the structure of a DSSC. The layers thicknesses are not to scale but are around* 2 mm*, 10 to* 15 µm *and* 700 nm *for the glass, titania and fluorine doped tin oxide (FTO) respectively. The platinum does not form a layer, but an assembly of nanoclusters on the FTO surface. b) and c) high magnification SEM images of the titania and the platinum respectively.*

the traditional mounting on roofs, façades or in solar-cell parks DSSCs are suitable for application as part of roofs or façades or other arts of building where semi-transparency can be desirable. Additionally they can be used for architectonic effects, as has been in the "Swiss Tech Convention Center" at the "École polytechnique fédérale de Lausanne" (EPFL) where an entire façade is equipped with semi-transparent DSSCs which not only produce electricity, but also provide solar protection and a remarkable appearance [63]. The following sections will provide an overview over the setup and general function of a DSSC, the processes occurring in a running DSSC, and a very general overview over the key components. More detailed information on all the topics can be found in Ref. [22].

2.1.1. Setup and general function of DSSCs

An overview of the setup of a DSSC together with Scanning Electron Microscopy (SEM) images of the components is shown in Fig. 2.1.

A DSSC consists of two electrodes in a sandwich-structure, at least one of which needs to be transparent and which usually consist of a TCO-layer, such as FTO, coated onto a glass-substrate. An alternative for FTO is Indium doped Tin Oxide (ITO), which however has the disadvantage of being less temperature-stable and of containing indium, a rare metal. The TCO-layer has a thickness of around 700 nm and the glass of 2 to 3 mm. The nomenclature of the electrodes follows the view of a chemist, wherefore the working electrode is called photo-anode since it oxidises the reduced electrolyte species. The photo-anode is coated with the nanostructured titania layer of 10 to 15 µm thickness, which in turn is sensitised by the adsorption of a mono-layer of dye molecules. The

counter-electrode is activated with a catalyst such as platinum which is usually present in the shape of small nanoclusters which are closely distributed over the surface. The inter-space is filled with an electrolyte or hole-transporter, which can be in a liquid, solid [24, 64] or gel-state [65]. The thickness of the electrolyte layer is in the range of 20 µm. Upon light absorption the dye molecule passes into an excited state by lifting of an electron from the Highest Occupied Molecular Orbital (HOMO) to the Lowest Unoccupied Molecular Orbital (LUMO). From the LUMO the electron is injected into the CB of the TiO_2. The electron now travels through the titania layer hopping from particle to particle to reach the electrode. After passing through the external electrical-circuit the electron reaches the counter-electrode of the DSSC. In a cell filled with liquid electrolyte the oxidised form of the redox-couple is reduced by means of the electrons and the help of the catalyst. The now reduced redox-molecule diffuses through the cell and reduces the dye-molecule which was oxidised upon transferring its electron to the titania. DSSCs are a very complex electro-chemical system and the short description above delivers only a small and very simplified overview of the components and the desired processes occurring within the cell. A qualitative overview over the key components of the a DSSC is given in the next section, while the desired processes and the loss reactions occurring within a cell are presented in the section after that.

2.1.2. Key components of DSSCs

The general structure of a DSSC was described in the previous section. Here the key components and their requirements are shortly presented. The nanoporous titania layer forms the heart of the DSSC. An SEM-image of a nanoporous titania layer is shown in Fig. 2.1. TiO_2 has multiple crystal forms, the most common being anatase and rutile. The first has a band gap of 3.2 eV and the second one of 3 eV [22]. Thus they absorb light at wavelengths shorter than 390 nm and 410 nm respectively. For DSSCs the anatase phase is preferred, not because of the difference in the band gap, but since it shows faster electron transport and a higher adsorption of dye molecules [66].

While the deposition of titania as a layer of nanoparticles is still the most common today, other nanostructured titania shapes have been examined. Some examples are nanorods [67, 68], titania nanotubes [69] and columns [70], nanosheets [71], and combinations of titania nanoparticles with carbon nanotubes [72]. Interesting is also a study on different mixtures of nanoparticles and particle-aggregates of different sizes [73]. An extensive list can be found in [22, chapter 2] and the 182 references therein. The titania

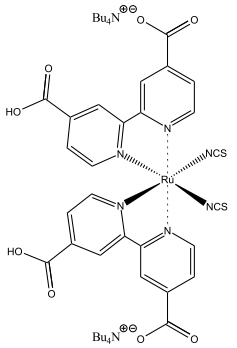

Figure 2.2.: *Chemical structure of the standard DSSC-dye N719.*

layer needs to guarantee a stable support for the dye molecules and a high conductivity in order to extract the electrons from the anode into the external circuit. Therefore a stable ohmic connection of the particles is necessary, which is established by sintering of the deposited layers as will be explained later. Homogeneous titania layers are a prerequisite to efficient cells, since interruptions of the layers by cracking diminish the conductance, and peeling off of the layers from the substrate impede the electric contact between the titania and the electrode. Peaks of higher thickness in the layer can lead to electrical short-cuts between the photo-anode and the counter electrode, and depressions will diminish the amount of absorbed light.

In order to exploit the energy-potential of the visible light, the titania is sensitised with molecules which absorb light in the visible spectrum. An example is the ruthenium complex N719, whose chemical structure is shown in Fig. 2.2.

The requirements of a useful sensitiser are not only a high absorption coefficient of light over a large part of the visible spectrum ideally, starting at its lower wavelength end and extending into the near infra-red, but also a good alignment of the HOMO with the redox potential of the electrolyte to ensure efficient dye regeneration and of the LUMO levels respective to the titania CB, which is necessary to enable an efficient injection of the excited electrons. To the same purpose are a stable connection of the dye-molecules with the titania, ideally by covalent bonding of one or multiple anchoring groups to the TiO_2. Furthermore the dye molecules need to be chemically stable with respect to the conditions in the cell.

The electrolyte needs to provide a fast regeneration of the dye-molecules to prevent recombination and damaging of the molecules by reactions with other species in the electrolyte. Since the movement of the redox-molecules through the electrolyte occurs

by diffusion, a low viscosity solvent increases their speed and thus rate at which they can be supplied. The energy level of the CB of the titania and the redox-potential of the electrolyte pose the limits to the maximal voltage generated by the cell. Thus the redox-potential of the electrolyte needs to be as low as possible. On the other hand an adequate driving force for the regeneration (thus reduction) of the dye molecule needs to be present, thereby necessitating a redox potential higher than the HOMO of the dye. Finally the electrolyte should not react with electrons in the titania and the TCO to minimise loss-effects by recombination. The electrodes and substrate need to ensure the smallest possible loss of light and thus be as transparent as possible over the entire range of light-absorption by the dye molecules. Additionally they need to provide a stable scaffold with a small resistance (below $15\,\Omega/\square$), a chemical stability towards the electrolyte and the smallest possible recombination from the anode to the electrolyte. Finally they need to withstand all the processes necessary for the fabrication of the DSSC, in particular the sintering of the titania layers, or the high pressure treatment if non-sintered layers are desired.

In the previous section the general setup and working principle of the DSSC was presented. In this section the setup was discussed more closely by giving more detailed explanation of the key components. In the next section the processes taking place within a working DSSC will be treated more closely to give a deeper insight into the working-principle of the cell.

2.1.3. Processes in DSSCs

In the last two section the general working principle of a DSSC was described, and its setup and components were explained in more detail. The current section will focus on the processes occurring in a DSSC in order to complete the description of the components and working principle of this interesting kind of solar cell. An overview of the processes occurring in a DSSC is shown in Fig. 2.3. The desired reactions are marked by blue arrows and numbers, the loss reactions by red dashed arrows and letters. The desired electron transfer processes are: (1) The excitation of the dye molecule by an incoming photon of energy $h\nu$ and the thereby induced lifting of an electron from the HOMO to the LUMO. This process occurs in the femtosecond range [74]. (2) The injection of the electron from the LUMO of the dye-molecule into the CB of the semiconductor and thereby oxidation of the dye-molecule, which was studied extensively and is summarised in [21] and in chapter 11 of Ref. [22]. It can be studied by sub-picosecond transient

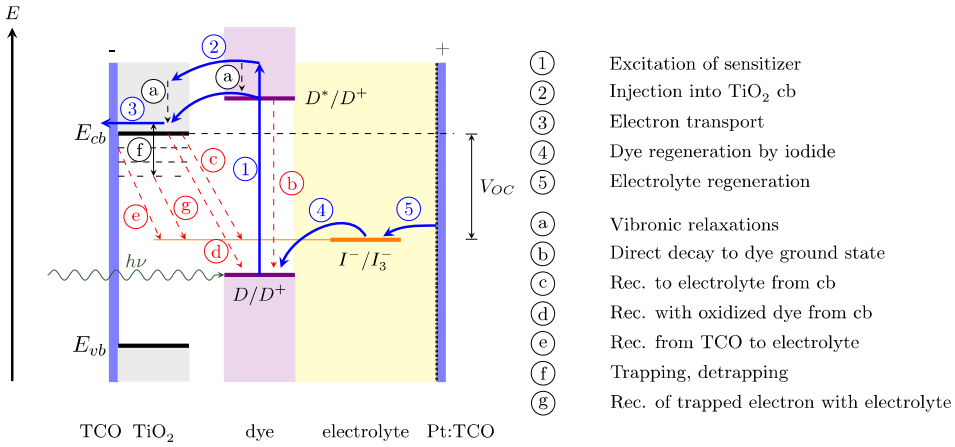

Figure 2.3.: *Outline of the processes in a DSSC under working conditions with arbitrary energy scales of the respective potentials. Desired electron transfer processes: blue arrows. Recombination pathways: dashed red arrows. Figure by Res Jöhr [74]*

absorption spectroscopy as was done by Tachibana and coworkers [75] who found the process to be bi-phasic with time-constants below $\sim 150\,\text{fs}$ (50 %) where the resolution was limited by the instrument, and a second time-constant of $1.2 \pm 0.2\,\text{ps}$ (also 50 %). Asbury and coworkers who studied the process by femtosecond infrared spectroscopy and who claim their setup to be more reliable on the other hand found the time-constants of the bi-phasic process to be $50 \pm 25\,\text{fs}$ (84 %) and $1.7 \pm 0.5\,\text{ps}$ (16 %) [76].

The charge transfer of the electrons through the semiconductor layer into the TCO-electrode (3) is not as straight forward as might be expected. The apparent high efficiency of the charge transfer is astonishing, since the conductivity of the nanocrystalline film is low and the particles are too small to support an internal electrical field [21]. Thus the driving force for the electron transport is diffusion rather than drift and its origin lies in a concentration gradient as proposed by O'Regan and coworkers [77] and proofed by Nakade et al. [78] and Kambe et al. [79]. Even though the exact mechanism of the charge transfer is a matter of discussion in the DSSC community [21], the most widely assumed option is a multiple trapping de-trapping model as proposed by Cao et al. [80], further studied by Dloczik and coworkers [81], analytically treated by van de Lagemaat and Frank [82] and discussed in Hagfeldt's review [21]. According to said model the electrons get caught in defect states underneath the conduction band edge, from where they can be de-trapped by excitation due to temperature or other energy inputs. The expected movement is a hopping from trap to trap and from particle to particle until they reach the electrode, or recombine with the electrolyte or an oxidised

dye molecule. This implies a dependence of the transport from the light intensity, or more accurately from the electron concentration, which in turn depends on the light intensity. The reason is a filling of the traps and thus a reduced trapping probability for additional electrons.

The reduction of the oxidised dye molecule by a redox molecule (4) was extensively studied and is reviewed in [21]. Therein the time scale of the process is given as 0.1 to 10 µs. The mechanism of the regeneration is described as a multi-step reaction starting with the formation of a sensitiser-iodine-complex (Eq.: 2.1), its transformation into a sensitiser-di-iodide-radical complex by the addition of an iodide ion (Eq.: 2.2), the subsequent dissociation into a regenerated sensitiser-molecule and the di-iodide radical (Eq.: 2.3) and the disproportionation of two such radicals into an iodide and a tri-iodide ion (Eq.: 2.4) [83, 84].

$$S^+ + I^- \longrightarrow S\cdots I \tag{2.1}$$

$$S\cdots I + I^- \longrightarrow S\cdots {I_2}^{-\cdot} \tag{2.2}$$

$$S\cdots {I_2}^{-\cdot} \longrightarrow S + {I_2}^{-\cdot} \tag{2.3}$$

$$2\,{I_2}^{-\cdot} \longrightarrow {I_3}^- + I^-. \tag{2.4}$$

The dependence of the process from many different factors such as temperature and light intensity [85], applied bias voltage [85, 86] and cations in the electrolyte [87] was studied. Various dependences were shown, which indicates a high complexity of the entire process. See Ref. [21] for a more extensive description.

The loss processes in a DSSC are: (b) the relaxation of the excited state of the dye molecule back to its ground state by radiative decay. For Ru-dyes such as the bipyridyl-Ru-complex N3 this process occurs on a relatively slow time scale (∼20 to 60 ns [21, 88]) compared to the injection of the electron into the titania (∼50 fs [76]). Therefore, it was assumed to be rather rare. Since these fast injections were measured on sensitised titania layers and not in complete cells, and Koops and coworkers detected a much slower injection (∼150 ps) upon examination of an complete DSSC sensitised with N719 [89] it is however not clear, whether the relaxation of the excited dye can be safely ignored.

After the injection of the electron into the conduction band it can still recombine with oxidised dye or electrolyte molecules ((c), (d) and (g)). Both processes are possible along the entire path of the electron through the titania layer, since dye and electrolyte are present throughout the entire layer. The first depends on the presence of oxidised dye

molecules, and thus the reaction kinetics for the regeneration of the dye as described above and in Ref. [21]. Despite a large number of studies concerned with the loss-reaction of the electrons in the titania with the oxidised dye which are summarised in [21] there seems to be no consensus on the dependence of the process. It might or might not depend on the driving force for the electron transfer from the titania to the oxidised dye. And the dependence might be direct (increasing rate constant with increasing driving force) [90], indirect [85, 91] or not dependent at all e.g. [92]. Also dependences on the applied bias and the concentration of electrons in the titania NPs are mentioned in the review. The latter shows an increase in the recombination with increasing electron concentration in the NPs which may lead to a competition off the recombination with the dye-regeneration, since under working conditions the electron-concentration is rather high [21].

The time constant for the recombination from electrons to the electrolyte is called electron lifetime. It seems to be in the range of 1 to 20 ms and thus rather long and to depend from many factors such as the electron concentration in the titania NPs (shorter lifetimes with increasing concentration), electrolyte concentration (shorter lifetime with increased concentration of reduceable species), the dye bound to the surface, and NP-size [21]. Finally a recombination of the electron from the TCO to the electrolyte is also possible (e), which can however be reduced by the deposition of a blocking-layer, thus a compact titania layer covering the FTO [93, 94].

The heart of the dye sensitised solar cell is the sensitised nanoporous titania layer. It influences not only the amount of dye ready to absorb light, but also the injection of the electrons into the semiconductor which depends on the phase of the titania, the binding of the dye to the titania determined by the anchoring groups, the distance of the location of the excited dye-state to the titania and the alignment of the corresponding states in terms of energy. The titania layer interacts with all the other DSSC components, thus the dye, the electrolyte and the TCO. Recombination reactions between titania and electrolyte strongly depend on the properties of the titania and the porosity of the layer limits the diffusion of the electrolyte molecules through the active layer. Furthermore, the titania layer needs to provide a high conductivity for the collected electrons despite it consisting of nanoparticles.

All these interactions depend on the microscopic properties of the titania layer. Therefore measurement-methods providing information on the nanoscale about the topographic and electrostatic properties of titania layers employed in DSSCs in air and the native

electrolyte environment of a working DSSC are necessary to gain further insight in the working principle of this fascinating solar cell type. In the next part of this chapter the measurement techniques AFM and KPFM which provide the necessary nanoscale resolution of both the topography and the surface potential in air and vacuum, and were shown to do the same in liquids and even electrolyte solutions, will be presented and explained in detail.

2.2. Methods for the nanoscale investigation of surfaces

The last section presented the setup and working principle of dye sensitised solar cells. It showed the importance of the nanostructured titania layer for the function of the cell. This implies the necessity to have tools to study the electronic properties of the titania layers with nanoscale resolution, not only in air but also in electrolyte solutions. In this section AFM and KPFM will be presented and discussed in detail. They are both SPM techniques for the detection of the topography and the surface potential in the nanoscale respectively.

While AFM is commonly applied not only in air but also in liquid and electrolyte environments e.g. for the study of biological samples [95], the use of KPFM was limited to liquid-free environments for a long time. Only in recent years methods have been presented to apply KPFM in non-polar liquids [53] and also in polar-liquids or electrolytes [54].

Since KPFM is an advanced form of AFM the latter will be presented first, before two KPFM-modes will be discussed, the one making use of a control-loop which is denoted CL-KPFM and is traditionally applied in air and vacuum, and the other without control-loop, which is denoted OL-KPFM and which can also (but not only) be applied in liquids.

2.2.1. Atomic Force Microscopy (AFM)

In this section AFM will be presented. After a short introduction into the history and setup of the AFM, the forces introduced by the interaction of the measurement tip and the examined sample are shortly described. Depending on the interaction principle AFM can be run in different modes, namely contact, intermittent contact and non-contact mode, which will be shortly introduced at the end of the current section.

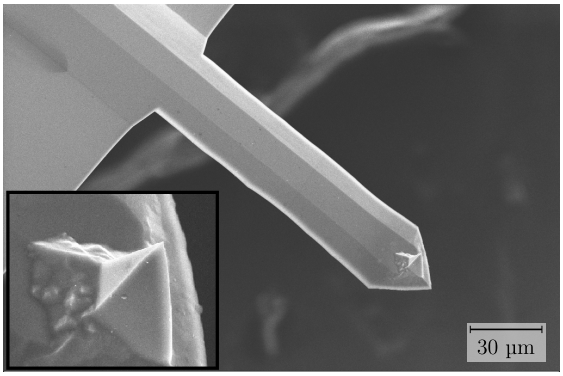

Figure 2.4.: *SEM image of an AFM cantilever. Inset: Close-up of the tip. Cantilever-beam-width:* 30 µm.

When in 1982 the STM was invented by Binnig, Rohrer, Gerber and Weibel [30] a whole new field of science toward the nanorange was established. The STM allowed imaging of nanoscale structures, which had not been revealed to the human eye before. The STM measures the topography of a sample by scanning a sharp tip over the sample surface, while measuring the tunnelling-current of the electrons tunnelling through the vacuum gap between tip and sample. Since the tunnelling-current is strongly dependent on the gap-width and thus the tip-sample distance a very accurate topographical map of the surface is received. However due to the necessity of a tunnelling-current which only occurs between conductors, the range of samples is limited to metals and other conducting materials.

This limitation of the nanoscale study to conductors was overcome in 1986 when the AFM was invented by Binnig, Gerber and Quate [31]. Also the AFM measures the topography of a sample with nano- or even sub-nanometre resolution, by scanning a probe over the sample surface and is therefore an SPM technique. To determine the topography the tip-sample distance is regulated by measurement of the interaction forces between cantilever-tip and sample surface. The nature of these interactions between tip and sample will be explained in the next section. The probe used in an AFM are cantilevers, thus a beam which has a sharp tip on its lower side and which acts as measuring instance. An SEM image of a cantilever showing the beam and the tip is shown in Fig. 2.4.

The cantilever is a very sensitive force sensor which is deflected upon interaction with a sample surface, or as reaction to the influence of forces. The deflection of the cantilever is employed to measure the surface topography. In order to detect the deflection a

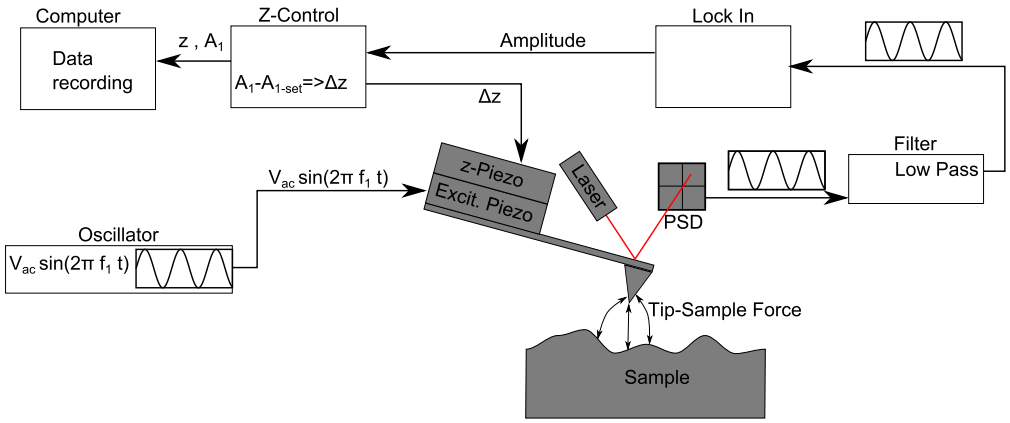

Figure 2.5.: *Outline of the basic instrumentation of an AFM.*

laser is focused onto the reflecting back of the cantilever, and the reflected laser-beam is detected on a Position Sensitive Detector (PSD). Usually four-quadrant PSDs are employed, which enables the registration of vertical and horizontal deflection of the laser-beam, and thus the detection of bending- as well as twisting of the cantilever. Depending on the measurement-mode the deflection signal is appropriately processed and fed into a control-loop, which adjusts the relative z-position of cantilever and surface by means of a piezo, in order to enable an accurate measurement of the surface topography. An outline of an AFM setup is shown in Fig. 2.5

In contrast to the STM the AFM does not employ the tunnelling effect, but other tip-sample interactions for the measurement, which will be explained more closely in the next section.

Forces

Interaction between two bodies cause variations in the potential. Such variations in a potential cause forces, which are defined as derivative of the potential. For a system consisting of a cantilever oscillating above a sample perpendicular to the sample surface the essential force component is the one parallel to the cantilever oscillation and thus perpendicular to the sample surface. Thus the force between tip and sample (F_{ts}) is the derivative of the potential between tip and sample (V_{ts}) with respect to the direction perpendicular to the sample surface (z):

$$F_{\mathrm{ts}} = \frac{\partial V_{\mathrm{ts}}}{\partial z}. \tag{2.5}$$

Therefore models of potentials can be used to describe the forces present in a system. Forces between tip and sample are the foundation of AFM. Between two bodies in close proximity, such as a cantilever-tip and a sample, multiple interactions exist. Some of the interactions are specific for bodies of certain properties, such as magnetic interactions which occur for magnetic bodies. Others such as van der Waals interactions are more general. Each interaction between the sample and the tip introduces a force acting on both and the sum of these forces induces the bending of the cantilever, which is used as measurement signal. The forces induced by the interactions between two neutral, polarisable bodies in short proximity (such as a tip the sample) can be divided in short and long range forces. Examples for short range forces are repulsive forces due to the Pauli exclusion principle, and attractive chemical binding forces, while long range forces include van der Waals forces (F_{vdW}) and electrostatic forces (F_{es}). The following paragraphs will shortly introduce the forces which are of importance in AFM in the setup used for the present work, namely the F_{vdW}, the F_{es} and the short range forces, which will be treated by approximation with a Lennard-Jones-Potential.

Van der Waals Forces

Van der Waals forces are forces between neutral particles (atoms or molecules or larger particles or bodies) without permanent dipole. Nevertheless they are dipole-interactions. The dipoles on the particles arise from fluctuations of charge on the particle surface, or are induced by electric fields wherein the particles are located. As explained by Israelachvili in the book "Intermolecular and Surface Forces" [96] and based on the work of London and Polanyi [97] and Hamaker [98] the potential of a single atom above a flat surface is given by

$$V_{vdW}(r) = -\frac{\rho\pi g}{6r^3}, \tag{2.6}$$

where r is the distance of the atom, g is a constant depending on the object, and ρ the density of atoms in the sample surface. For a macroscopic system such as a cantilever tip (which can be approximately treated as a sphere) over a sample, the potential and thus the force can be gained by integrating over the sphere, as is shown by [98] and explained by Koch in [99]. The resulting F_{vdW} upon integration over the sphere, derivation of the resulting potential and simplification into one dimension is:

$$F_{\mathrm{vdW}} = -\frac{A_H R}{6z^2}, \tag{2.7}$$

where A_H is the Hamaker constant which is depending on the material and usually lies in the range of 10^{-19} to 10^{-20} J [100], R is the radius of the sphere as which the cantilever-tip was treated, and z the tip-sample distance. Since the presented model takes only attractive forces into account an application to very small separation distances is not possible, since there short-range repulsive forces due to the overlap of electron-clouds and repulsion of atom-cores need to be considered. These will be treated later on, after discussing the second considered long-range force, the electrostatic force, in the next paragraph.

Electrostatic Forces

Two charged or a charged and an uncharged but conducting particle have different electrostatic potentials. Therefore an electrostatic force acts on the two. The tip-sample system present in an AFM can be treated as a plate capacitor. The potential in a capacitor is given by $V_{es} = \frac{1}{2}CV^2$ where C is the capacitance and V the total voltage, thus potential difference between the capacitor plates. As before the system can be treated in one dimension and the capacitance is dependent on the tip-sample separation ($C = C(z)$), which yields the resulting electrostatic force F_{es} as:

$$F_{es} = -\nabla V_{es} = +\frac{1}{2}\frac{\partial C}{\partial z}V^2. \tag{2.8}$$

Thus the distance dependence of the electrostatic force depends on the distance dependence of the capacitance. The distance dependence of the capacitance is not easily accessible, since the entire probe consisting of the cantilever-beam, the cone of the cantilever-tip and the tip-apex forms one of the capacitor plates, while the sample forms the other. The complex geometry of the probe makes an analytical solution of the capacitance impossible [101]. Based on the model shown by Hudlet et al. [101] and in combination with experimental results Law and coworkers show a dependence of the form $C(z) \propto \frac{1}{z}$ for small tip-sample separations and $C(z) \propto \ln(z)$ for large tip-sample separations [102]. The transition between large and small tip-sample separations depends on the exact geometry but seems to be in the region of 100 nm according to Fig. 4 of Ref [102]. Also the derivation of the electrostatic force does not take into account repulsive short-range forces. It can therefore not be applied to very short tip-sample-separations, since it would falsely indicate an increasing attractive force. However overlap of electron wave-function and the repulsion of the atom-cores counter-balance the attractive forces and induce a repulsion

at very small separations. These effects can be described by a Lennard-Jones-Potential, which will be explained in the next paragraph.

Lennard-Jones-Potential

The long-range forces introduced in the last paragraphs can not be applied without a balancing counter-part, since they do not consider short-range repulsive forces arising due to the Pauli-principle (overlap of electron-clouds and repulsion of the charged cores of atoms). Therefore short-range forces need to be introduced as balancing counter part, which will be done in this paragraph. The short range forces consist of an attractive component, which can be attributed to chemical-bonding and thus favourable overlap of atomic or molecular orbitals, and of a repulsive component due to the overlap of electron wave-functions and highly-charged atom-cores. The short-range forces are often described by the empirical Lennard-Jones potential (V_{LJ}) [103], since it gives an adequate approximation to the real interactions and is still easy to comprehend and to calculate. The Lennard-Jones potential has the following shape:

$$V_{LJ} = 4\epsilon \left[\left(\frac{\sigma_0}{z} \right)^{12} - \left(\frac{\sigma_0}{z} \right)^{6} \right]. \tag{2.9}$$

While the first term describes the strong repulsion mentioned before, the second describes weak attractive forces. At longer tip-sample separations the Lennard-Jones potential is dominated by the long-range forces, and becomes relevant only at very small distances below $\sim 5\,\text{Å}$ [104].

An overview over the potential components described in the last paragraphs is shown in Fig. 2.6. For the operation of an AFM various of the here described forces are taken advantage of and the cantilever is operated in different regimes of the potential. This enables the operation of the AFM in different modes, which will be described in the next section.

Operation modes

An AFM can be operated in different measurement modes, which will be described in this section. Depending on the measurement mode an AFM is operated in the repulsive regime (contact mode) thus at a distance smaller 1 in the outline of the resulting curve in Fig. 2.6, in a regime around the minimum of the potential-curve reaching the first

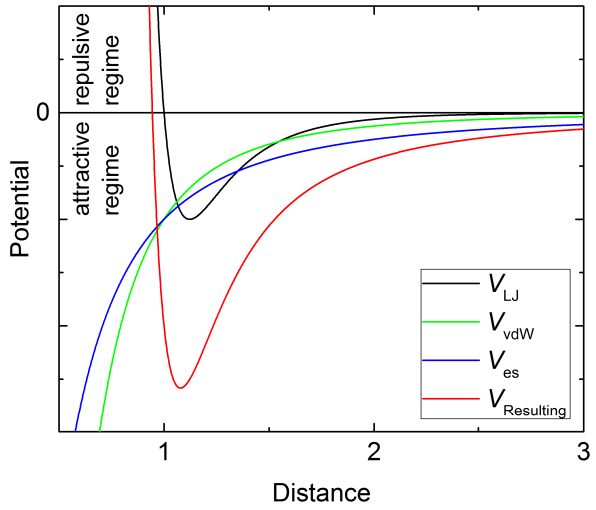

Figure 2.6.: *An outline of the different potential components described in Sec. 2.2.1, and the resulting potential as the sum thereof.*

edge of the repulsive interaction (Amplitude Modulation Atomic Force Microscopy (AM-AFM)), or in the slope at distances larger than the potential-minimum in the case of Frequency Modulation Atomic Force Microscopy (FM-AFM). These three modes will be explained in the next paragraphs.

Contact Mode

The contact-mode was the first mode for an AFM to be operated in. In contact mode the steady cantilever is approached and brought into contact with the sample surface. The repulsive force between cantilever-tip and sample induces a bending of the cantilever, which is registered. If the setup is run in constant height mode the cantilever is now scanned over the surface and the deflection is measured. Since the cantilever height is not changed and the deflection is proportional to the sample-height the deflection signal contains the entire topographic information. In constant force mode however the deflection is registered, fed into a control loop and the cantilever height is adapted by means of a piezo in order to keep the force acting on the cantilever and thus the deflection constant. In constant force mode the deflection signal contains only the error signal of the control loop, while the topographic information is carried by the height signal, thus the piezo-extension signal. While a constant height mode AFM is easy to setup, since it does not need a height-controller and can be run very fast since it has no slow controlling

mechanism, it always bears the danger of the tip crashing hard into a prominence on the sample. Therefore it is only suitable for very flat and hard samples, such as the cleavage of crystals.

Dynamic Mode

In FM-AFM and AM-AFM the cantilever is not steady, but is oscillated, ideally at its fundamental resonance frequency. The oscillation can be excited by different techniques. The most widely used is the excitation by means of a piezo-electric element on which the cantilever is mounted. The piezo-electric element is oscillated and its oscillation transmits itself to the cantilever. This piezo is usually denoted "shaking-piezo". Other possibilities are the excitation by laser or an electrostatic excitation as shown by Umeda et al. in Refs. [105] and [106] respectively. The latter two are particularly interesting in a liquid environment, where the excitation via a shaking-piezo does not only excite the cantilever, but also the entire liquid droplet around it to oscillate and thus excites many undesired modes. The oscillating cantilever can be described as a harmonic oscillator. By considering the cantilever-tip as a point mass, and the cantilever as a spring its oscillation can be described by an equation of motion. Since the cantilever beam is vibrating only along one axis the equation of motion can be simplified to a one dimensional problem:

$$m\ddot{z} + \frac{m\,\omega_0}{Q}\dot{z} + kz = F_{ts} + F_0\cos(\omega_d t) \tag{2.10}$$

where k is the spring constant of the cantilever, F_{ts} are the forces between tip and sample, and F_0 and ω_d are the driving force and angular frequency respectively and ω_1 is the angular resonance frequency of the free cantilever. Q is the quality factor of the cantilever, which is defined as the ration between the resonance frequency and the width of the resonance peak of the mechanical cantilever resonance at full-width-half-maximum (FWHM):

$$Q = \frac{f_0}{f_{FWHM}}, \tag{2.11}$$

where f_0 and f_{FWHM} are the free resonance frequency (without tip-sample interaction, thus with $F_{\mathrm{ts}} = 0$ and the width of the resonance peak at half the maximum height respectively. The resonance frequency and angular resonance frequency are converted by: $f_0 = 2\pi\omega_0$.

In AM-AFM the cantilever is not brought into contact with the sample surface, but it is excited to oscillate, ideally at one of the cantilevers resonance frequencies. The

oscillation is visible in the signal from the PSD and detected by a lock-in amplifier. Upon approaching of the oscillating cantilever to the surface an interaction arises and the oscillation amplitude diminishes due to a shift of the resonance frequency. This frequency-shift has its origin in the change of the spring constant of the cantilever upon interaction with the sample surface. The closed-loop z-controller controls the tip-sample distance in order to keep the amplitude constant, at a pre-set value. Since the reduction of the amplitude occurs if the cantilever comes into close-contact with the surface at the lower turning point of its oscillation the AM-AFM mode is also called intermittent contact or tapping mode.

In FM-AFM or non-contact mode the cantilever is also oscillated at its resonance frequency. Unlike in AM-AFM mode however the oscillation is locked upon by a Phase Locked Loop (PLL) and the excitation is controlled to keep the oscillation-amplitude and the phase shift between oscillation and excitation signal constant by varying the excitation amplitude and frequency respectively, thus locking the oscillation to the resonance, even if the resonance frequency shifts. Upon approach of the oscillating cantilever to the surface the resonance frequency shifts, and this frequency-shift is used as control signal. The height-controller adjusts the height such as to retain a pre-set frequency-shift and thus a constant distance between tip and sample. Since the frequency-shift occurs even if no contact between tip and sample is established, the FM-AFM-mode is also called non contact Atomic Force Microscopy (nc-AFM).

When the AFM is used to measure the topography the total tip-sample force is usually used as measurement signal. Therefore, this kind of measurement contains not only information about the topography of a sample, but also about the surface potential of the sample, which induces the F_{es}, about the polarisability of the sample, which influences the F_{vdW}. If the measurement takes place in close proximity to the sample surface also effects of the surface-chemistry and the chemical potential of the surface can influence the resulting force acting on the cantilever. Different enhancements of the basic AFM-setup exist, which separate the different force components from each other and thereby enable the extraction of additional information from the measurement. An example of such an enhancement is the Kelvin Probe Force Microscopy (KPFM) technique, by which the F_{es} component is separated from the resulting tip-sample force (F_{ts}) and thereby the surface potential of the sample is measured. The KPFM technique will be described in the next section.

2.2.2. Kelvin Probe Force Microscopy (KPFM)

KPFM is an advanced SPM technique based on intermittent or non-contact AFM. It enhances the AFM functionality by allowing the measurement of the CPD of conducting samples in vacuum, air and non-polar liquids with nanometre, or even sub-nanometre resolution [53, 107, 108]. By means of calibration of the used tip against a sample of known work function, the work function can be calculated from the gained CPD. The measurement is based on the isolation of the F_{es}-force component from the F_{ts}. In this section an overview over the background of KPFM-measurements and of the CPD is given. The electrostatic force which was already presented in the last section is explained in more detail and it is shown how it can be used to measure the CPD. It has to be noted, that in the present work only the CPD and local variations thereof will be studied. This differs from the local-CPD which can be determined by KPFM in UHV and which denotes the CPD on an intra-molecular, atomic or even sub-atomic level.

The CPD is defined as the difference in the work function Φ of two metals:

$$\mathrm{CPD} = \Phi_{Sample} - \Phi_{Tip} = \Delta\Phi = V_{\mathrm{CPD}} \cdot e \tag{2.12}$$

with e being the elementary charge, thus a positive charge corresponding in the magnitude to the charge of an electron or proton($e = \oplus 1.602 \times 10^{-19}\,\mathrm{C}$), and V_{CPD} the voltage necessary to compensate the CPD. The polarity of the CPD is obviously defined by the definition of said difference. In the present work the difference is defined as $\Delta\Phi = \Phi_{Sample} - \Phi_{Tip}$, since this definition leads to equal contrast in the (measured) CPD and the work function of the sample. It corresponds to an experimental setup where the tip is grounded and the dc-voltage is applied to the sample.

KPFM is a combination of AFM and the surface potential measurement technique called Kelvin probe, which was developed by Lord Kelvin in 1898 [109]. In his setup Lord Kelvin used a known metal as first plate in a parallel plate capacitor, while the sample to be tested formed the second plate. Upon vibration of the plates at a certain frequency the resulting change of distance between the plates induces a change in the capacitance, and thus an alternating current flows through the circuit connecting the plates. By application of a dc-voltage corresponding to the CPD to one of the plates the current is nullified and thus the CPD is detected. KPFM is also based on this principle of compensating the CPD between a known capacitor plate (the tip) and an unknown one (the sample) by application of a dc-voltage. However the controlling parameter is not a

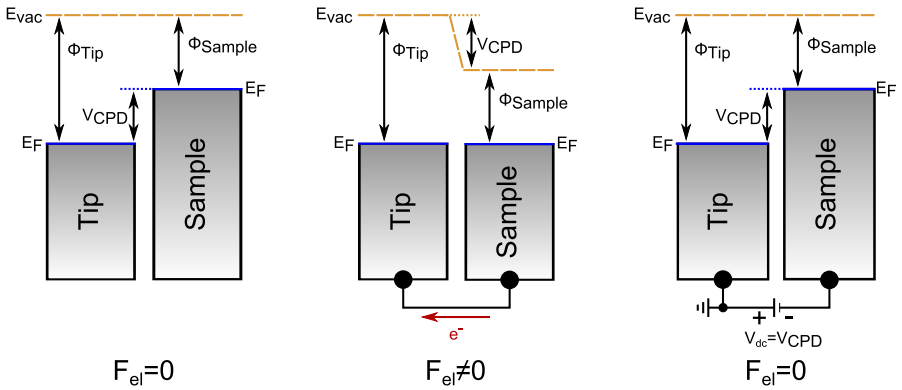

Figure 2.7.: *Origin and elimination of the force due to the CPD: Two not connected metallic samples have equal vacuum energy levels (E_{vac}) but different Fermi energy levels (E_F) (left). Upon connection of the two samples the Fermy energies align by an electron transfer from the sample with the higher E_F to the one with the lower E_F. This leads to a mismatch in the E_{vac} and an electrostatic force between the two samples (centre). By application of a dc-voltage the vacuum levels re-align, if $V_{dc} = V_{CPD}$ and thus the force can be nullified.*

current flowing through the circuit, but the electrostatic force. The general principle of the CPD and of its use for KPFM is depicted in Fig. 2.7

The detection of the force is accomplished by means of the cantilever which is an excellent force-sensor and thus is able to detect CPDs very sensitively despite its small size. Unlike the current in Lord Kelvin's setup the electrostatic force in KPFM is not excited by the oscillation of the cantilever. In order to measure the CPD, electrostatic interactions between the conducting tip and sample are excited by the application of an ac-voltage of frequency $1\omega_{\mathrm{ac}}$ and magnitude V_{ac}. The resulting F_{es} is nullified by the application of a dc-voltage. The potential of the dc-voltage necessary to nullify the F_{es} corresponds to the CPD ($V_{\mathrm{dc}} = V_{\mathrm{CPD}} = \frac{1}{e} \cdot \mathrm{CPD}$). The dc-voltage is applied by a PI-controller, which is commonly called Kelvin-controller.

As shown before the interaction between a metallic AFM tip and a conducting sample can be approximated as a capacitor. Since the potential in a capacitor can be described as $V_{es} = \frac{1}{2}CV^2$ the corresponding electrostatic force in three dimensions is:

$$F_{es} = -\nabla V_{es} = +\frac{1}{2}\frac{\partial C}{\partial r}V^2, \tag{2.13}$$

with $C = C(z)$ being the capacitance of the capacitor, V the total voltage and r the radius. The application of a voltage to a capacitor induces an attractive force between the two capacitor plates, since they are oppositely charged. By convention attractive

forces are negative. In the first part of Eq. 2.13 the attractive nature of the force is achieved by the $\ominus$. However, Sadeghi et al. show that the derivative of the capacitance is always negative by itself [110], thus $\partial C/\partial z < 0$ and thus the addition of a $\ominus$ results in a positive force. However the negative derivation of the capacitance is not always considered, thus the $\ominus$ is often added. Therefore, the formulae presented in the present work may differ (by the sign) from derivations found in other sources.

In a KPFM-setup the electrostatic force perpendicular to the sample surface is the most significant. Thus Eq. 2.13 can be reduced to one dimension. Assuming the sample to be in the xy-plane the thereto perpendicular force lies in the z-direction. Thus Eq. 2.13 becomes

$$F_{\mathrm{es}} = \frac{1}{2}\frac{\partial C}{\partial z}V^2, \tag{2.14}$$

where $\partial C/\partial z$ is the capacitance gradient in the capacitor consisting of the tip and the sample. The total voltage consists of the applied ac-voltage ($V_{\mathrm{ac}} \cdot \sin(\omega_{ac})$), the applied dc-voltage (V_{dc}) and the voltage corresponding to the potential of the CPD (V_{CPD}), the voltage originating in the CPD, and thus the resulting force can be written as:

$$F_{\mathrm{es}} = \frac{1}{2}\frac{\partial C}{\partial z}(V_{\mathrm{dc}} - V_{\mathrm{CPD}} + V_{\mathrm{ac}} \cdot \sin(\omega_{ac}t))^2, \tag{2.15}$$

Considering $\cos(2x) = \cos(x)^2 - \sin(x)^2$ and $\cos(\frac{a}{2}) = \sqrt{\frac{1}{2}(1+\cos(a))}$ which transforms into $\cos(x)^2 = \frac{1+\cos(2x)}{2}$ by substituting $\frac{a}{2} = x$, Eq. 2.15 can be split up in its spectral components $F_{\mathrm{es}} = F_{\mathrm{dc}} + F_{1\omega_{\mathrm{ac}}} + F_{2\omega_{\mathrm{ac}}}$ which are the components of the force activated by the dc-voltage and the first and second harmonic of the ac-voltage respectively:

$$F_{\mathrm{dc}} = +\frac{\partial C}{\partial z}\left[\frac{1}{2}(V_{\mathrm{dc}} - V_{\mathrm{CPD}})^2 + \frac{V_{\mathrm{ac}}^2}{4}\right], \tag{2.16}$$

$$F_{1\omega_{\mathrm{ac}}} = +\frac{\partial C}{\partial z}(V_{\mathrm{dc}} - V_{\mathrm{CPD}}) \cdot V_{\mathrm{ac}} \cdot \sin(\omega_{ac}t), \tag{2.17}$$

$$F_{2\omega_{\mathrm{ac}}} = -\frac{\partial C}{\partial z}\frac{V_{\mathrm{ac}}^2}{4} \cdot \cos(2 \cdot \omega_{ac}t). \tag{2.18}$$

The dc component of the electrostatical force (F_{dc}) contributes to the topography signal, since it induces a constant bending of the cantilever. On the other hand the $F_{1\omega_{\mathrm{ac}}}$ component of the force induces an oscillation of the cantilever at the frequency of the excitation. Throughout this work the amplitude of this oscillation induced by $F_{1\omega_{\mathrm{ac}}}$ will be denoted $A_{1\omega_{\mathrm{ac}}}$. The amplitude $A_{1\omega_{\mathrm{ac}}}$ can be used to determine the CPD, since it

depends on both the CPD (via V_{CPD}) and the V_{dc}. Considering Eq. 2.17 it is obvious that $F_{1\omega_{\mathrm{ac}}}$ becomes zero if the potential of the dc-voltage equals the CPD, thus $V_{\mathrm{dc}} = V_{\mathrm{CPD}}$ since then $V_{\mathrm{dc}} - V_{\mathrm{CPD}} = 0$ and $F_{1\omega_{\mathrm{ac}}} = 0$, thus also $A_{1\omega_{\mathrm{ac}}}$ becomes zero. Hence V_{CPD} can be determined by applying dc-voltage in a way to nullify $A_{1\omega_{\mathrm{ac}}}$, which is the basic principle of the CPD measurement applied in KPFM. The force component $F_{1\omega_{\mathrm{ac}}}$ can also be used directly by measuring $A_{1\omega_{\mathrm{ac}}}$ without nullifying it by a controller, to measure qualitative electrostatic properties of the surface. This kind of measurement (excitation of F_{es} by the application of an ac-voltage and measurement of the resulting $A_{1\omega_{\mathrm{ac}}}$) is called EFM and is described in references [35] and chapter 6 in [36]. The $F_{2\omega_{\mathrm{ac}}}$ component of the force can be used for capacitance microscopy which is described in [37] and in [36, chapter 5]. It induces a cantilever oscillation at the frequency $2\omega_{\mathrm{ac}}$, thus at twice the frequency of the excitation. This amplitude will be denoted $A_{2\omega_{\mathrm{ac}}}$. In capacitance microscopy $A_{2\omega_{\mathrm{ac}}}$ is measured. It contains only information about the derivative of the capacitance in the tip-sample capacitor and since the tip is always the same the signal holds information about the capacitance of the sample. Additionally $F_{1\omega_{\mathrm{ac}}}$ and $F_{2\omega_{\mathrm{ac}}}$ are used to determine the CPD in the OL-KPFM mode as will be described in the next section but one.

In the present section the theoretical background of KPFM measurements was explained. It was shown why the CPD induces a force between tip and sample, how it can be brought forward and how this electrostatic force component can be isolated from the F_{ts}. In the next sections two measurement technique to determine the CPD from the isolated F_{es} are shown. The first is based on the compensation of the electrostatic force and the thereby determination of the CPD. Thereto it employs a control-loop and hence it is denoted CL-KPFM. The second is based on the measurement of both the electrostatic- and the capacitative force components acting between tip and sample, wherefrom the CPD can be calculated. Since this mode does not employ a control-loop it is denoted OL-KPFM.

Closed Loop Kelvin Probe Force Microscopy

The CPD determined by CL-KPFM is denoted $\mathrm{CPD}_{\mathrm{CL}}$ throughout this thesis. To determine the $\mathrm{CPD}_{\mathrm{CL}}$ the $F_{1\omega_{\mathrm{ac}}}$ force component is nullified by the application of a dc-voltage. The nullifying is done by feeding of the measured $A_{1\omega_{\mathrm{ac}}}$ into the Kelvin-controller, which then applies the dc-voltage (V_{dc}) until the measured amplitude is zero ($A_{1\omega_{\mathrm{ac}}} = 0$), showing that $F_{1\omega_{\mathrm{ac}}} = 0$ and thereby $V_{\mathrm{dc}} = V_{\mathrm{CPD}} = \frac{1}{e} \cdot \mathrm{CPD}$. This includes a

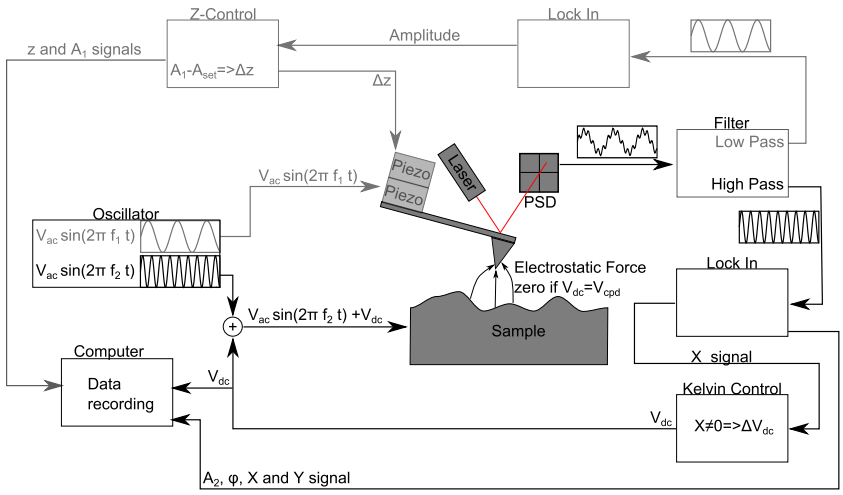

Figure 2.8.: *Outline of the CL-KPFM instrumentation. The AFM part of the instrumentation is shown in grey for clarity.*

closed control loop (signal measurement, feeding into controller, application of voltage, measurement of remaining signal,...) and thus this KPFM-mode is called CL-KPFM. The determined CPD gives a relative measure of the work function of the sample in relation to the work function of the used tip, as described by Eq. 2.12. In order to determine the absolute work function of the sample Φ_{sample} a calibration of the tip against a calibration-standard with known work function is necessary (e.g. HOPG with a reference work function in air of $4.475 \pm 0.005\,\mathrm{eV}$ [111] and in UHV of $4.4\,\mathrm{eV}$ [112]). By measurement of the CPDs of the calibration-standard and the unknown sample with the same tip, and application of Eq. 2.12 the absolute work function of the tip Φ_{Tip} and subsequently of the sample Φ_{Sample} can be determined.

An outline of a CL-KPFM setup is shown in Fig. 2.8. It is based on an AFM for the measurement of the topography, which is depicted in the upper part of the figure. The AFM-instrumentation consists of an oscillator generating the excitation signal at the first cantilever resonance, a shaking-piezo to transfer the excitation signal to the cantilever, a lock-in (lock-in amplifier) or PLL to record the resulting cantilever oscillation and a control-loop usually based on a PI-controller to keep the control signal constant by adapting the tip-sample separation by means of a z-piezo and thus to measure the topography. Additionally the CL-KPFM-setup contains a second oscillator which generates the excitation at the second cantilever resonance. It is electronically connected to the sample and the excitation takes place by the application of an ac-voltage. The electrostatic force is detected by the cantilever and thus part of the cantilever oscillation

signal. The first and second resonance oscillations (and thus the signals for topography and CPD) are separated by a set of low- and high-pass filters (not mandatory). The oscillation corresponding to the information of the electrostatic force is detected by a second lock-in. The detected oscillation amplitude (or more precisely the $X_{1\omega_{ac}}$-signal of the lock-in amplifier) is passed on to a Kelvin-controller, which applies a dc-voltage such as to nullify the amplitude and thus the force. The necessary dc-voltage can be applied to the tip or the sample. Application to the sample yields the same contrast for the dc-voltage as it does for the work function, while the contrast is inverted during the calculation of the work function from the dc-voltage by the calibration of the tip to a known standard, if the dc-voltage is applied to the tip.

To determine the CPD in a single point without the necessity to enable the control-loop a sweep of the applied dc-voltage and a simultaneous measurement of $A_{1\omega_{ac}}$ can be performed in a bias-sweep measurement. Due to the linear dependence of $A_{1\omega_{ac}}$ on the absolute value of V_{dc} shown in Eq. 2.19 the resulting $A_{1\omega_{ac}}(V_{dc})$-signal is a $\bigvee$-shaped curve with its minimum at $V_{dc} = V_{CPD}$.

Open Loop Kelvin Probe Force Microscopy

The CPD determined by OL-KPFM will be denoted CPD_{OL} throughout this thesis. No dc-voltage is applied to measure in, but the CPD_{OL} is determined by calculation from the $F_{1\omega_{ac}}$- and $F_{2\omega_{ac}}$-components of the electrostatic force as shown by Kobayashi et al. in Ref. [54]. From Eqs. 2.17 and 2.18 one can calculate the amplitude of the cantilever oscillation $A_{1\omega_{ac}}$ and $A_{2\omega_{ac}}$ induced by the two spectral force components to be:

$$A_{1\omega_{ac}} = \frac{|F_{1\omega_{ac}}|}{k} = \left|\frac{\partial C}{\partial z} V_{CPD}\right| \frac{V_{ac}}{k}, \tag{2.19}$$

$$A_{2\omega_{ac}} = \frac{|F_{2\omega_{ac}}|}{k} = \left|\frac{\partial C}{\partial z} V_{CPD}\right| \frac{V_{ac}^2}{4k}, \tag{2.20}$$

containing k as the spring constant of the cantilever and $\frac{\partial C}{\partial z}$ as the capacitance gradient in the z-direction, thus perpendicular to the sample surface. $A_{1\omega_{ac}}$ and $A_{2\omega_{ac}}$ are recorded during the OL-KPFM measurement. Therefore by combining Eqs. 2.19 and 2.20 and inputting the measured amplitudes the absolute value of the CPD can be calculated as

$$|V_{CPD}| = \frac{A_{1\omega_{ac}}}{A_{2\omega_{ac}}} \frac{V_{ac}}{4}. \tag{2.21}$$

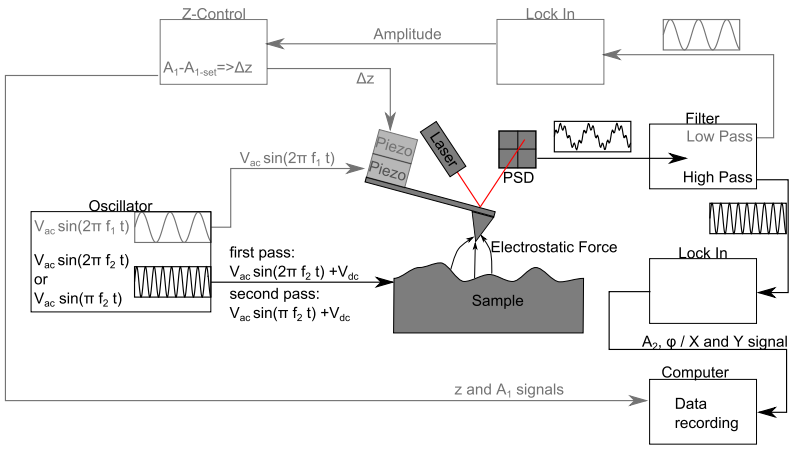

Figure 2.9.: *Outline of the OL-KPFM instrumentation, AFM part in grey.*

The polarity of the calculated CPD can be determined by the phase of $A_{1\omega_{\mathrm{ac}}}$:

$$V_{\mathrm{CPD}} = \frac{A_{1\omega_{\mathrm{ac}}}}{A_{2\omega_{\mathrm{ac}}}} \frac{V_{\mathrm{ac}}}{4} \cos(\phi_{1\omega_{\mathrm{ac}}}) = \frac{X_{1\omega_{\mathrm{ac}}}}{A_{2\omega_{\mathrm{ac}}}} \frac{V_{\mathrm{ac}}}{4}, \tag{2.22}$$

where $X_{1\omega_{\mathrm{ac}}}$ is the X-signal determined by the lock-in amplifier in $F_{1\omega_{\mathrm{ac}}}$-setting and is defined as $X_{1\omega_{\mathrm{ac}}} \equiv A_{1\omega_{\mathrm{ac}}} \cos(\phi_{1\omega_{\mathrm{ac}}})$.

The instrumentation of an OL-KPFM-setup is shown in Fig. 2.9. It is based on the same system as the CL-KPFM presented in the last section. The differences are only the missing (or not employing) of a Kelvin-controller, and the necessity to perform measurements in 2-pass-mode despite the presence of two lock-in amplifiers. Thus every line of the recorded image is scanned twice, once in $F_{1\omega_{\mathrm{ac}}}$-setting (where the excitation frequency (f_{ex}) is equal to the detection frequency (f_{det})) to record $A_{1\omega_{\mathrm{ac}}}$, and a second time in $F_{2\omega_{\mathrm{ac}}}$-setting (thus with the detection tuned to the second harmonic of the excitation, thus to twice the excitation frequency ($f_{\mathrm{det}} = 2 \cdot f_{\mathrm{ex}}$)) to record $A_{2\omega_{\mathrm{ac}}}$. This increases the time necessary for a measurement by a factor of 2. It can however be avoided by the employment of a third lock-in amplifier.

Equations 2.19 and 2.20 show that $A_{1\omega_{\mathrm{ac}}}$ and $A_{2\omega_{\mathrm{ac}}}$ depend on the applied excitation voltage in a linear and quadratic fashion respectively, if the applied model is applicable for a studied system in a particular setup and under the chosen settings. Therefore, the applicability of the assumed model can be verified by measuring the dependence of said amplitudes from the excitation voltage V_{ac} in excitation voltage spectroscopy (V_{ac}-spectroscopy) measurements. The resulting data can be fitted by a non-linear function

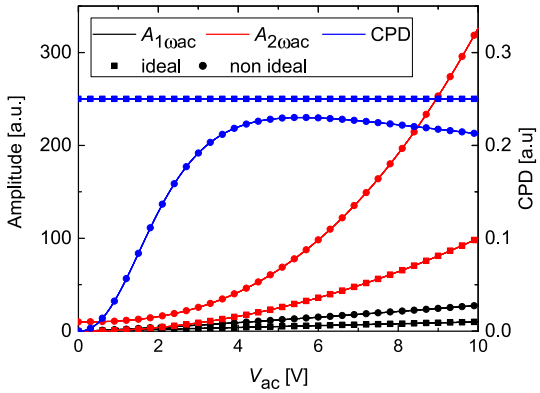

Figure 2.10.: *Outline of an ideal (squares) and a non-ideal (circles) theoretical data set of $A_{1\omega_{ac}}(V_{ac})$- (black) and $A_{2\omega_{ac}}(V_{ac})$-spectra (red) and the thereof calculated CPD (blue). All values in arbitrary units (a.u.)*

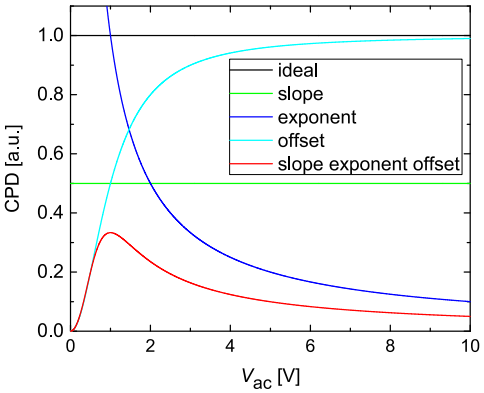

Figure 2.11.: *Outlines of the CPD calculated from theoretical excitation-spectroscopy data sets. Variations from the ideal curve are an increased slope, an increased exponent and an increased intercept all of $A_{2\omega_{ac}}$, and a combination of the three.*

of the form

$$A = m \cdot V_{\mathrm{ac}}^{n} + o, \tag{2.23}$$

where A is the amplitude of the respective signal ($A_{1\omega_{\mathrm{ac}}}$ or $A_{2\omega_{\mathrm{ac}}}$) and m, n and o are fitting parameters corresponding to the slope, exponent and intercept of the respective curve. An outline of two sets of theoretical $A_{1\omega_{\mathrm{ac}}}(V_{\mathrm{ac}})$- and $A_{2\omega_{\mathrm{ac}}}(V_{\mathrm{ac}})$-signals is shown in Fig. 2.10 together with the thereof calculated CPDs. The ideal curves which depend linearly and quadratically from the V_{ac} ($n_{1\omega_{\mathrm{ac}}} = 1$ and $n_{2\omega_{\mathrm{ac}}} = 2$), have a slope-ratio of $\frac{m_{1\omega_{\mathrm{ac}}}}{m_{2\omega_{\mathrm{ac}}}} = 1$, intercepts of $o_{1\omega_{\mathrm{ac}}} = o_{2\omega_{\mathrm{ac}}} = 0$ yield the expected constant CPD. On the other hand the non-ideal curves with values differing from the ideal ($m_{1\omega_{\mathrm{ac}}} = 1.75$; $n_{1\omega_{\mathrm{ac}}} = 1.2$; $o_{1\omega_{\mathrm{ac}}} = 0$ and $m_{2\omega_{\mathrm{ac}}} = 1$; $n_{2\omega_{\mathrm{ac}}} = 2.5$; $o_{2\omega_{\mathrm{ac}}} = 10$) show a characteristically different shape. In Fig. 2.11 the influence of the different factors on the resulting curve is illustrated. It identifies the slopes to influence the value of the resulting CPD, but not the general shape of the curve. An increase of $n_{2\omega_{\mathrm{ac}}}$ above 2 (or a decrease of $n_{1\omega_{\mathrm{ac}}}$ below 1) yields a decreasing CPD with increasing V_{ac}, and the intercept of $A_{2\omega_{\mathrm{ac}}}$ is responsible for a depression of the CPD at low excitation voltages, while an intercept of $A_{1\omega_{\mathrm{ac}}}$ yields a high CPD at low V_{ac} and thus a curve similar to the one at increased $n_{2\omega_{\mathrm{ac}}}$. Thus the resulting curves of all the three effects combined in both the Figs. 2.10 and 2.11 own their shape mainly to the intercept of $A_{2\omega_{\mathrm{ac}}}$ which causes the rising slope at low excitation voltages, and the increase of the exponent of $A_{2\omega_{\mathrm{ac}}}$ which causes the depression of the CPD at high voltages. In measured curves as shown in chapter 4 the depression of the CPD towards higher voltages is seldom reached

and the shape of the curves is dominated by the intercept.

It needs to be pointed out that the $A_{1\omega_{ac}}(V_{ac})$-spectroscopy data has a very similar appearance as the data from bias-sweep measurements used to determine the CPD by the sweep of the dc-voltage as explained in the previous section. They have however a different physical meaning. The bias-sweep shows the dependence of the $F_{1\omega_{ac}}$ from the applied bias, thus from the difference in the present potential of tip and sample and thereby determines the CPD. The V_{ac}-spectroscopy on the other hand shows the dependence of the $F_{1\omega_{ac}}$ from the excitation voltage. Its minimum is always located at $V_{ac} = 0$ and does not hold information about the CPD.

Multiple experimental approaches to record the necessary signals exist. In the original publication in which Kobayashi et al. present the open loop technique [54] they present Single-Frequency Open Loop Kelvin Probe Force Microscopy (SF-OL-KPFM). Therein the electrical excitation is performed at a constant frequency, and $A_{1\omega_{ac}}$ and $A_{2\omega_{ac}}$ are detected at the first and second harmonic of the excitation frequency respectively, thus at two different frequencies. Advantages of this approach are an easier experimental implementation and the possibility to measure $A_{1\omega_{ac}}$ and $A_{2\omega_{ac}}$ simultaneously with two lock-ins tuned to the two frequencies. Furthermore, a possible dependence of F_{es} from the excitation-frequency ($F_{es} = F_{es}(\omega_{ac})$) will not distort the measured results. However, when detecting at two different frequencies the result may be influenced by variations of the mechanical oscillation response of the cantilever, such as by the presence or proximity of a cantilever resonance. While in air the oscillation-response of the system is mainly based on the cantilever, in a liquid environment many more factors such as oscillation of the liquid's molecules come into play. Therefore, the response in air shows a rather flat background signal except in close proximity to a cantilever resonance, while in a liquid environment many variations of the background appear. Additionally the resonance peaks are much less distinct due to the increased damping, therefore the ratio of background to resonance decreases, and also the relative variations of the background increase. This necessitates the introduction of a correction factor for the oscillation response, as explained in Ref. [55]. Furthermore SF-OL-KPFM does not allow the use of a cantilever resonance to increase the sensitivity and signal to noise ratio of the measurement, which would be desirable. Therefore, Half Harmonic excitation Open Loop Kelvin Probe Force Microscopy (HH-OL-KPFM) was presented by Guo et al. [57]. In this mode the detection of $A_{1\omega_{ac}}$ and $A_{2\omega_{ac}}$ occurs at the same frequency, preferably a resonance frequency, while the excitation occurs at two different frequencies. The excitation frequencies of the corresponding amplitude f_{ex} are $f_{ex\text{-}1\omega_{ac}} = \omega_{ac} = f_{det\text{-}1\omega_{ac}}$ thus the

detection frequency of $A_{1\omega_{ac}}$, and $f_{\text{ex-}2\omega_{ac}} = \frac{\omega_{ac}}{2}$, thereby enabling the detection of $A_{2\omega_{ac}}$ at $f_{\text{det-}2\omega_{ac}} = \omega_{ac}$ as well, since $f_{\text{det-}2\omega_{ac}} = 2 \cdot f_{\text{ex-}2\omega_{ac}} = 2 \cdot \frac{\omega_{ac}}{2} = \omega_{ac}$ with f_{det} being the detection frequency of the corresponding amplitude. While the advantage of this mode is resonance enhanced measurement, the disadvantages are a possible distortion of the results if a frequency dependence of the electrostatic force occurs and the impossibility of measuring both signals at the same time. After the completion of the measurements for this work we solved the latter problem in our lab by using a multi lock-in system and detecting both $A_{1\omega_{ac}}$ and $A_{2\omega_{ac}}$ at the same resonance, but not exactly on the centre of the peak, but slightly shifted towards higher and lower frequencies respectively. Thereby we retained the resonance enhancement and enabled the simultaneous measurement of both $A_{1\omega_{ac}}$ and $A_{2\omega_{ac}}$ overcoming both disadvantages.

An interesting enhancement was again presented by Kobayashi et al. [56]. They presented a technique which they denote Dual-Frequency Open Loop Kelvin Probe Force Microscopy (DL-OL-KPFM). Therein the excitation occurs at two different and independent frequencies. Unlike in SF-OL-KPFM and HH-OL-KPFM, where the $F_{1\omega_{ac}}$ and $F_{2\omega_{ac}}$ components of the F_{es} are measured, in DL-OL-KPFM the $F_{1\omega_{ac}}$ component is measured at two different frequencies and thereof the $F_{2\omega_{ac}}$ component and thus the CPD can be calculated. This enables the use of two independent frequencies, which may lie close together and thus diminish the frequency-range between the lowest excited and the highest detected frequency. This is advantageous since the large frequency range required by the detection of $A_{2\omega_{ac}}$ at the second harmonic of the excitation frequency imposes restriction on the measurement. It either necessitates the detection at high frequencies and thus a detection system with a high bandwidth, or the excitation at low frequencies. The latter is problematic when measuring in electrolyte solutions due to the diffusion of ions and other processes interfering with the OL-KPFM measurement.

Polarity of CPD_{OL}-Data

The polarity of the CPD derived from OL-KPFM is determined by the phase of $A_{1\omega_{ac}}$ which is denoted ($\phi_{1\omega_{ac}}$) [55] as is explained in Eq. 2.22:

$$\text{sign}(CPD) = \text{sign}(cos(\phi_{1\omega_{ac}})) \tag{2.24}$$

The phase shift of the signal is the shift between the excitation- and the response signal, thus in the case of an electrical excitation of a cantilever oscillation the phase shift between the applied ac-voltage and the oscillation of the cantilever. The phase shift

consists of multiple components aside from the surface potential. They have their origin in different parts of the system. Some of the components are unchanging. Examples are internal circuits in the devices, the wiring and cable-connections, filters such as the high-pass filter used to separate the topography signal from the CPD signal (which does not change its phase shift as long as the filter-settings are not changed) and the cantilever and its connection to the microscope. Others are more variable such as the measurement environment (air, water, electrolyte).

Figure 2.12c shows traces of the $X_{1\omega_{ac}}$ plotted against the reference phase at different bias-voltages and at different settings of the high pass filter. The measured curves simulate the influences of the setup on the phase shift (simulated by changes in high pass filter) and measurements on regions with different CPDs (simulated by different applied V_{dc}). The curves show that the polarity of the $X_{1\omega_{ac}}$-signal changes upon change of the CPD (compare solid red with solid black or dashed red with dashed black line) or upon change of the measurement setup (compare solid black with dashed black or solid red with dashed red line). Thirdly the curves imply a dependence of the polarity from the reference phase indicating the influence of the phase adjustment on the polarity.

The phase shift induced by the setup and the environment holds no information about the polarity of the CPD. It can thus be discarded, which is achieved by introducing a reference phase shift, which is subtracted from the phase shift thus adjusting the phase to $\phi = 0°$.

In order to understand the phase adjustment it is helpful to introduce the measurement-mode of a lock-in amplifier. The lock-in describes the measured amplitude by a point in a polar- and a cartesian coordinate system. In the first the relevant information to describe a point is the distance from the centre, and the angle to a defined direction, thus a radius (R) and a phase (ϕ). In the second a point is described by a set of X and Y coordinates which describe the distance from the centre in the direction of the defined x- and y-axes. Assuming orthogonal x- and y-axes and a correspondence of the polar axis with the cartesian x-axis the X and Y coordinates correspond to the projection of the amplitude onto the respective axis. Thus a conversion is achieved by

$$X = R \cdot \cos(\phi) \tag{2.25}$$

$$Y = R \cdot \sin(\phi) \tag{2.26}$$

$$R = \sqrt{x^2 + y^2} \tag{2.27}$$

The phase adjustment is performed by adjusting the x-axis (and thus the polar axis) such as to bring the currently measured point onto the axis. It keeps its radius R, but its Y and ϕ values become zero and its X and R values become equal ($X = R$). This phase adjustment necessarily also includes the information about the CPD polarity. In order to separate the two (polarity of the CPD and phase shift due to influences by the system and the environment) it is necessary to determine the CPD polarity at the point of the phase adjustment. In vacuum, air and non-polar liquids this is done by the application of a dc-voltage. Sweeping of the dc-voltage will reveal the V_{CPD} and thus the CPD of the currently measured point by the nullification of the F_{es} as shown by the decrease of the corresponding oscillation amplitude to zero.

However in polar liquids and electrolytes the application of a dc-voltage is not applicable, since it may introduce polarisation of the liquid, migration of ions or even electrochemical reactions. Therefore no non-trivial method exists to determine the polarity of the surface potential in the point of the phase adjust, and the information of the CPD-polarity is lost in the phase adjustment process. The not assessable component of the phase shift is the one due to the measurement-environment. Since neither the phase shift induced by the system, nor the phase shift induced by the environment will change during a measurement, changes in the polarity of the CPD can easily be determined by measuring the phase shift along with $A_{1\omega_{\mathrm{ac}}}$. However without a method to determine the polarity of the CPD in one measurement point, and thus gain a reference for the phase shift, its absolute polarity can not easily be determined. Possible approaches to determine the CPD of the measurement point might be the introduction of a reference that is known not to be influenced by the environment, as it was used in non-polar liquids by Domanski et al. [53], or a fast dc-voltage sweep. However they were not evaluated for this work. Therefore, for all OL-KPFM measurements performed in liquid the polarity of the data measured with OL-KPFM was established manually, in a way for it to be consistent to other measurements and for the contrast of the sample to correspond to the contrast measured in air. To that end a positive or negative sign was added to Eq. 2.24 and thus the formulae to calculate the OL-KPFM data including the correct polarity were:

$$CPD = \oplus \mathrm{sign}(cos(\phi_{1\omega_{\mathrm{ac}}})) \frac{V_{\mathrm{ac}} A_{1\omega_{\mathrm{ac}}}}{4 A_{2\omega_{\mathrm{ac}}}} \tag{2.28}$$

$$CPD = \ominus \mathrm{sign}(cos(\phi_{1\omega_{\mathrm{ac}}})) \frac{V_{\mathrm{ac}} A_{1\omega_{\mathrm{ac}}}}{4 A_{2\omega_{\mathrm{ac}}}} \tag{2.29}$$

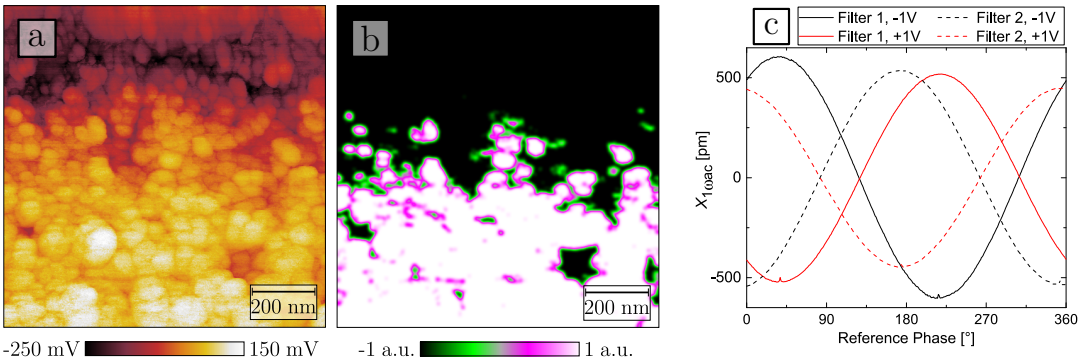

Figure 2.12.: *a) OL-KPFM-measurement on a sample with positive and negative CPD values, calculated taking the phase shift into account and b) the corresponding sign of the $X_{1\omega_{ac}}$-signal filtered in order to have smoother transitions. c) $X_{1\omega_{ac}}$-signal plotted against the reference phase simulating different setups and CPDs by changes of the high pass filter and an applied dc-voltage. Solid and dashed curves correspond to equal filter settings, red curves to a positive- and black curves to a negative bias. Thus comparing curves of different colour but equal line corresponds to comparing signals of samples with different CPDs. Scan Parameters: $f_{1st} = 171\,\mathrm{kHz}$; $A_{1st} = 14\,\mathrm{nm}$; $f_{2nd} = 1051\,\mathrm{kHz}$; $V_{ac} = 2\,\mathrm{V}$*

An example of a measurement containing both positive and negative CPD-values is shown in Fig. 2.12 together with the corresponding sign of the $X_{1\omega_{\mathrm{ac}}}$-signal, to illustrate the positive and negative polarity of the CPD.

The measurement was performed with a reference phase of $\phi_{ref} = 97.25°$. Both the cosine of the phase and the $X_{1\omega_{\mathrm{ac}}}$-signal show a simultaneous change of the sign where the CPD changes its polarity. However the change is obviously dependent on the set reference phase. Comparison of $A_{1\omega_{\mathrm{ac}}}$- and $A_{2\omega_{\mathrm{ac}}}$-data and the sign of the cosine of the phase of the measurement in $F_{1\omega_{\mathrm{ac}}}$-setting ($cos(\phi_{1\omega_{\mathrm{ac}}})$) with the simultaneously measured $\mathrm{CPD_{CL}}$ show that Eq. 2.28 needs to be employed to calculate the $\mathrm{CPD_{OL}}$. Since the system-parameters do not change this holds true for all measurements performed in air.

In the present chapter the theoretical and experimental background necessary to understand the performed work described in this thesis, was presented. In the first part the DSSC was explained. Its general setup and working principle was presented, and the key components and the desired processes and loss-reactions occurring in a DSSC under working conditions were treated in more detail. The importance of the nanoporous titania layer was pointed out, and the importance of the nanostructuring was stressed together with the resulting necessity for adequate examination methods to determine the nanoscale properties of the titania layer. Examples for examination methods able

to determine surface-properties are AFM and its enhancement KPFM, which can be applied to measure the topography and the surface potential of a sample respectively, with a nanoscale resolution for both. These techniques were presented in the second part of the chapter. After a short introduction into the working-principle of AFM the forces acting in the tip-sample system of an AFM were presented and described in more detail and the different modes in which an AFM can be operated and which depend on different components of these forces, were shown. Finally it was explained that by isolation of certain components of the F_{ts} these force components can be determined and used to gain information about additional surface properties, such as the contact potential difference, which can be measured by isolating the F_{es}, as it is done in KPFM. In order to understand the surface potential measurement the theoretical background of the CPD was explained. The modelling of the tip-sample-system as a capacitor was introduced in order to show the resulting forces acting on tip and sample upon the application of an ac-voltage and it was shown that the CPD can be determined by excitation of these forces in two modes, by either compensation of the $F_{1\omega_{\mathrm{ac}}}$ component which depends on the CPD, or by measurement of the $F_{1\omega_{\mathrm{ac}}}$ and $F_{2\omega_{\mathrm{ac}}}$ components and subsequent calculation of the CPD from the measured data sets.

After providing the background information to DSSCs and the measurement techniques applied to examine them for the present work in the last chapter, in the following chapter the experimental details will be presented and explained.

3. Materials and Methods

After providing of the background information and the working principles of the DSSC and the measurement techniques employed to examine them in the last chapter, this chapter focusses on the applied experimental methods and the setups used for the measurements.

A large component of the experimental work performed in the course of this thesis, was the implementation of DSSC-fabrication and examination into a research group whose core-competence is the examination of single molecules on single-crystals in UHV. The fabrication of highly efficient DSSCs is well described in the literature, e.g. in [113] and [22, chapter 8]. Compared to the fabrication of other solar-cells or highly specialised electronic devices the fabrication steps necessary to produce DSSCs are not very complex. Within a short time and with manageable effort cells which are not very efficient, but nonetheless work can be fabricated. However, more sophisticated cells with a high efficiency and durability are necessary for the proper study of DSSCs. The key prerequisite however is the ability to fabricate highly efficient and overall highly reproducible cells. Despite the detailed descriptions and the manageable experimental effort necessary to produce simple cells, highly reproducible cell require a large expertise, know-how and experience. Many fabrication steps, which seem to be trivial from the description turn out to be not trivial at all. Furthermore, it is not always clear whether a certain step in the instruction was carefully evaluated and optimised, or whether it established itself as standard due to common practice alone. An example is the fabrication of the nanoporous titania layer, which is usually deposited by screen-printing from a viscous paste, but which might also be deposited by other techniques such as spray-deposition from liquid suspensions.

To gain the necessary know-how every fabrication step of the procedure had to be performed, practised and evaluated separately, thereby adapting it to the present equipment, as e.g. the sintering of the titania layers which could not be performed according

to the procedure described in [114], since the heating-rates of the furnace present in our department were not high enough.

In the first part of this chapter some of the evaluations performed to implement a specialised fabrication of efficient and highly reproducible DSSCs are presented and discussed. The main focus lies on the fabrication of the nanoporous titania layers, which we are particularly interested in since they not only form the heart of the DSSC but also offer many interesting open question which can be examined by a physical rather than a chemical approach, such as the distribution of the work function.

In order to convey a complete overview first a short summary of the fabrication of DSSCs is provided in Sec. 3.1. The deposition and examination of the titania layer is treated in more detail in Secs. 3.1.3, 3.1.4, 3.1.5. Also the deposition of compact layers necessary to impede the recombination of electrons from the FTO to the electrolyte is examined (Sec. 3.1.2).

Even though DSSCs are solar cells and are characterised by techniques used for the characterisation of silicon solar cells, these techniques need to be adapted to the properties of DSSCs, as is shown in the second part of this chapter in Secs. 3.2.1 and 3.2.2. Finally possibilities for the fabrication of DSSCs with sensitive dyes are presented in Sec. 3.2.3

In the third part of this chapter the instrumentation employed for the nanoscale topography and surface potential measurements is introduced.

3.1. Dye Sensitised Solar Cells - Fabrication

The fabrication of DSSCs is described in the literature, e.g. in chapter 8 of Ref. [22] or in Ref. [113]. Even though the methods mainly described by the Grätzel group from the EPFL in Lausanne have established themselves as standard procedures this does not mean, that other techniques might not bring equal or even better results, along with faster or easier cell preparation or other advantages. DSSCs can be fabricated in a laboratory without the need of countless highly specialised and expensive devices and processes. Nevertheless a large experience, know-how and expertise are necessary for the fabrication of high-quality solar cells of high reproducibility. Therefore the implementation of DSSC building in a group mainly concerned with the study of surfaces in UHV was a long task. Important tasks to evaluate were the different steps of the cell fabrication, such as titania paste fabrication and titania layer deposition and evaluation

of the deposited layers, but also characterisation aspects, such as the influence of diffuse light in the measurement setup or frequency of the measurements of single points in a measurement curve. Additionally the influence of the fabrication of cells in an inert glove box atmosphere was tested in view of the sensitisation of layers with sensitive natural organic dyes.

These evaluations are discussed in this section. The main focus lies on the fabrication and evaluation of the titania layers. After explaining the general fabrication procedure applied to produce the DSSCs the production of pastes for the deposition of these layers is discussed and three different techniques for the deposition of titania layers, namely screen printing, doctor blading and spray deposition, are introduced. The fabricated layers need to be of outstanding quality which implies an excellent control and reproducibility of the layer thickness and the ability to deposit homogeneous layers of a high integrity. Therefore different methods to examine the layer thickness, homogeneity and integrity were evaluated and are compared in this chapter.

Depending on the sensitiser and electrolyte employed in a DSSC, the recombination from the TCO at the photo-anode to the electrolyte is not negligible [74]. But it can be reduces by the application of a blocking layer to the TCO before the deposition of the titania [93, 94]. Different types of blocking-layers were examined and will be discussed in the corresponding section, Sec. 3.1.2.

DSSCs are solar cells. Therefore examination methods commonly applied to investigate and characterise solar cells are applied for the characterisation of DSSCs. However, DSSCs are different from traditional silicon solar cells in many ways. The active layer is inherently nano and micro structured and therefore predestined to harvest not only light irradiated perpendicular to the cell, but also scattered and diffuse light with varying angles of incidence. The reaction mechanism in DSSCs is a complex combination of physical and electrochemical processes and even diffusion. Thus DSSCs react more slowly to external stimuli (e.g. irradiated light) compared to silicon solar cells. When examination methods developed for silicon solar cells are applied to DSSCs such differences have to be born in mind and investigated in order to adapt the applied measurement methods to the changed behaviour of the DSSC. This will be shown by the evaluation of the composition of irradiated light in terms of its content of scattered light, and by an evaluation of the reaction kinetics of a DSSC in the sections IV measurements and Reaction times respectively. In the first the measurement of the efficiency of a solar cell by the recording of current-voltage-characteristics (IV-curves) will be introduced. Many

other differences occur and come to mind, such as the possible cell transparency

DSSCs can be sensitised with very different kinds of dyes. Natural organic molecules promise not only a cheap and easy alternative to dyes containing rare metals such as ruthenium, and who require an extensive and elaborate synthesis, but they have been used and optimised for light-absorption processes by nature and have very high extinction coefficients [115]. Many kinds of natural molecules have been studied before. We examined different carotenoic acids for their suitability as sensitisers in DSSCs. While the results of this evaluation is not part of this work, but is presented by Res Jöhr in his master thesis [74], the experimental work showed decomposition of the sensitisers during the cell-fabrication upon irradiation of light. The decomposition could be averted by protection of the dye-titania interface from light and oxygen by implementing cell fabrication in a glove box. This will be described in the final section of the first part of this chapter.

3.1.1. General fabrication procedure for DSSCs

In this paragraph a very short description of the fabrication process is given. A step by step instruction of the procedure applied for the fabrication of the cells used for this work is given in Appendix A. The procedure is based on the detailed description given in Refs. [22, 113]. The basic materials used for the fabrication of DSSCs in our lab is FTO coated glass (TCO22-7, Solaronix SA, Rue de l'Ouriette 129, CH-1170 Aubonne, Switzerland). "Titanium diisopropoxide bis(acetylacetonate)" (TAA) was used for the deposition of compact layers by spray-pyrolysis, $TiCl_4$ was used for pre- and post-treatment of the deposited titania layers and thereby deposition of compact layers as well. Both TAA and $TiCl_4$ were purchased from Sigma-Aldrich. Be aware that $TiCl_4$ reacts explosively with water whereby HCl is released. Even air-humidity might be enough to trigger a reaction. It is therefore advisable to prepare a stock-solution (e.g. 1 M in nanopure water) which can be stored in a fridge and further diluted for daily use without further danger. Titania pastes were home-made using NPs produced by flame-spray pyrolysis (AEROXIDE® TiO_2 P25, provided by Evonik Industries AG, Hanau, Germany) as described in Sec. 3.1.3. While all the cells and layers in this work were produced with home-made pastes, for other measurements we also applied commercial pastes (Solaronix Nanoxide T/SP, Solaronix SA). Two types of sensitisers were employed. The standard sensitiser N719 (Ruthenizer 535-bisTBA, Solaronix SA) or natural organic carotenoic acids, which were provided by "DSM" (DSM Nutritional

Products Ltd., NRD CH, Kaiseraugst, Switzerland). Platinum precursor solution was purchased from Solarnoix (Platisol-T, Solaronix SA).

The next paragraph shortly describes the general fabrication procedure for dye sensitised solar cells. For the fabrication of DSSCs the TCO-glass needs to be cut to the desired shape and size. The photo-anodes are cleaned and dried and remaining organic adsorbates are removed by UV/Ozone treatment. Compact-layers are deposited on the FTO either by immersion in an aqueous $TiCl_4$ solution, or by spray-deposition of TAA. After the preparation of the compact layers, the nanoporous titania layers are deposited as described in Sec. 3.1.4 and finalised by sintering as described in Sec. 3.1.6. The sintered layers are post-treated by immersion in an aqueous $TiCl_4$ solution and sintered again. After that they are sensitised by immersion in a solution of the dye overnight and rinsed with the solvent of the dye solution. A hole is drilled into the counter electrodes by sand-blasting to enable the filling of the assembled cells with electrolyte. For the drilling the FTO-layer is protected with a scotch-tape attached to its surface. The counter-electrodes are cleaned and the platinum-catalyst is added onto the surface by means of deposition of the precursor solution and subsequent firing to 400 °C in air. The cells are assembled and sealed by a surlyn® foil of 25 µm thickness. The sealing is performed by heating of the cell through the counter-electrode by means of a soldering iron with a home-made tip adapted to match the cell-design. The cell is filled with the electrolyte by vacuum back-filling. Thereto the tip of a syringe-needle is removed from its base-part leaving only 1 to 2 mm of the needle and thereby forming a minuscule funnel. The filling-hole is sealed by a surlyn® foil and the needle-part of the funnel is pierced through the foil into the hole. A drop of electrolyte is introduced in the funnel, and a vacuum is applied around the cell. Upon re-establishing of environmental pressure the electrolyte is pushed into the cell. Finally the filling-hole is sealed by a cover-glass. The contact-areas can be coated by silver-paint (alternatively a glass-solder can be used) but we found this not to be mandatory for most applications.

After introducing the general fabrication procedure in the last paragraph, in the next sections some of the steps will be discussed in detail, starting with the compact-layers, followed by the discussion of the fabrication of the home-made titania pastes and the sintering process.

3.1.2. Compact Layers

Compact or blocking layers are applied in DSSCs in order to reduce the parasitic loss-reaction of electrons from the FTO electrode in the anode with oxidised redox-molecules, in the present case tri-iodide (I_3^-) molecules [93, 94]. Different deposition techniques of blocking layers have been described. A simple pre-treatment by immersion in an aqueous solution of $TiCl_4$ for 30 min at 70 °C of the cleaned FTO glass before the titania depositions is supposed to result in a compact TiO_2 layer of a few nanometres thickness [88, 116, 117]. Our comparison of SEM images of $TiCl_4$ treated and untreated FTO glass did not show any difference hinting to the presence of a layer covering the entire surface. The structure of the FTO layer on the glass are identical in both cases, as shown by the comparing images in Figs. 3.1a and 3.1c. Both samples show the characteristic surface structure off small crystals (≈300 nm diameter), and also the striped pattern on the FTO crystals is present in both samples. Even though we have not examined the source of the stripes, we assume that they would have vanished or diminished upon covering of the FTO layer with a compact titania layer, especially since no stripes have been observed on any titania particles. Upon performing of the $TiCl_4$ treatment clusters appeared, mainly in the grain-boundaries between the FTO crystals (Fig. 3.1c), which were attributed to the $TiCl_4$ treatment and assumed to be titania nanoclusters.

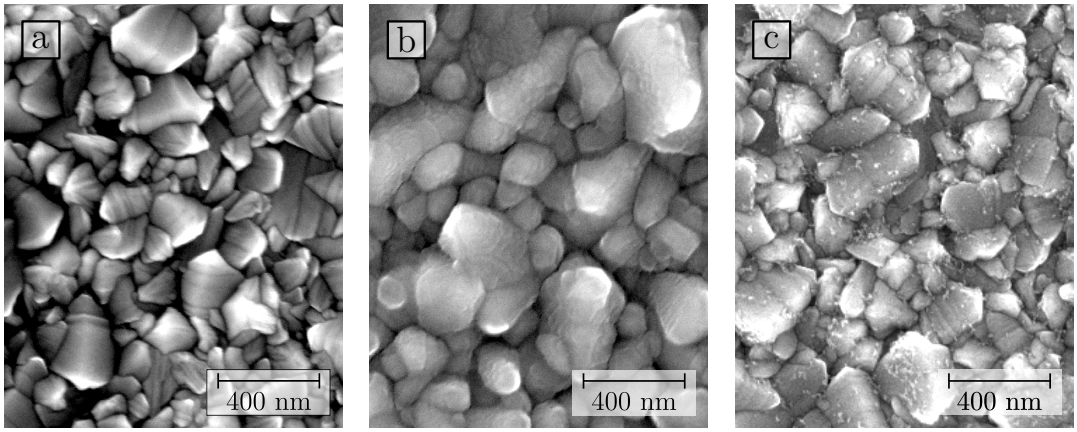

Figure 3.1.: *SEM images of the surface of the FTO after different pre-treatments. a) bare FTO, b) FTO with a compact layer deposited by TAA pyrolysis, c) FTO treated with $TiCl_4$. No layer but small TiO_2 clusters appear.*

A second possibility to deposit a compact layer is by spray pyrolysis of TAA which was presented by Andreas Kay in his Ph.D.-thesis [118], the technique was described by Kavan [119] and blocking layers were discussed in [93]. In the spray pyrolysis the TAA

acts as precursor, which decomposes into TiO_2 upon spraying of a solution of TAA onto an FTO glass heated to 500 °C. The process is said to yield highly reproducible layers of defined thickness [114]. Our experience shows that the fabrication of the layers is not as straight forward as described in the literature. The first difficulty is the spraying of a small glass sample which constantly moves away but can not be fixed due to the hot heating plate. Additionally upon deposition of the layer the conductivity of the FTO glass strongly diminishes. Our measurements show an increase of the resistivity from around $\approx 12\,\Omega/\square$ to $\approx 40\,\Omega/\square$. Careful removal of the deposited compact layer by mild sanding nearly re-established the original resistance, showing that the conductivity of the FTO layer was not altered. In order to make efficient contact between the cell and the external circuit possible, the contact area of the FTO needs to be protected from the TAA spraying. Covering of the contact-area with an aluminium sheet (thickness of the sheet 1 mm) did not yield satisfactory results. The resistivity increased despite the covering. Presumably the TAA was pulled between the cover and the sample by capillary forces. Wrapping of the contact areas in aluminium foil during the deposition yielded a marked improvement. However, the border between coated and uncoated FTO was very broad and not well defined at all. Examination of the deposited layers by top-view SEM revealed a markedly altered surface structure compared to the blank FTO, as is shown in Fig. 3.1b. The images show a sample coated by deposition of 0.1 M TAA dissolved in ethanol (EtOH) and isopropanol. The sample temperature during deposition was 400 °C. The deposition was achieved by 10 spray depositions of 5 s each, in intervals of 35 s at a nitrogen pressure of 1 bar and a nozzle aperture of 1/2 turn. The masking of the contact area was accomplished by wrapping of the contact areas in aluminium foil.

The crystal structure is still present, however in the coated part the grain boundaries are less pronounced, shallower and less steep. The striped fine structure is not visible anymore. Instead the flakes show a distinct structure reminding of a tortoiseshell. Overview images show a clear distinction between the coated and uncoated part of the FTO sample . At equal brightness and contrast settings the uncoated part is of a much lighter grey. However images recorded in the light part of the image still show the tortoiseshell structure in approximately the first third, thus the first ≈ 1 to 2 mm after the apparent transition.

Despite the highly visible difference between blank FTO glass and FTO glass coated by TAA pyrolysis in top-view SEM images, we did not succeed in imaging the coating in “side-view” SEM, thus images showing the cross section of the layers coating the glass-substrate. All cross-section images we recorded show only one layer deposited on

the glass. Possible explanations are that the spray-deposited compact layers show equal contrast as the FTO layer, or that they are very thin and thus can not be distinguished from the FTO layer at the magnifications employed in our studies. It has to be annotated, that larger magnifications were difficult to obtain during cross-section imaging due to the charging of the glass in close vicinity of the FTO and due to the necessity of a larger working distance as a precaution since the relative position of the sample and the SEM-cone was difficult to asses. However, to our knowledge in no publications describing the deposition and application of compact layers cross-section images of the layers are shown, except by Wu et al. ([120]) who, however, used a deposition by application of an anodic current and not by pyrolysis of TAA.

3.1.3. Titania pastes

Titania-pastes were home-made according to the procedure described by Ito et al. [121], where it is described in detail. Therefore only a short outline stressing the most important points will be given here. For the home-made pastes TiO_2 NPs produced by flame-spray pyrolysis (AEROXIDE® TiO_2 P25, provided by Evonik Industries AG, Hanau, Germany) were placed in a porcelain-mortar. Acetic-acid was added and the nearly dry mixture was pestled for a few minutes. During the pestling of the nearly dry and thus very viscous mixture extreme shear forces occur, which induce a decomposition of the particle-aggregates. The acid induces a charging of the particle-surfaces and thus a coulomb repulsion, which inhibits their re-agglomeration. Ultrapure water (Milli-Q, Merck Millipore, Merck KGaA, Darmstadt, Germany) was added drop wise while pestling over a time-span of 30 to 45 min to receive an even paste of very viscous consistency. The pestling of a few grams of titania-particles, which correspond to volume of around 100 cm^3 yields only a few millilitres of pestled paste, thus the volume is reduced by a factor of around 20. The resulting viscous paste was dissolved in ethanol, and the liquid ethanol-suspension was sonicated before adding terpineol. As organic stabilisers two kinds of ethyl-cellulose (the first with a viscosity of 30 to 70 $mPa \cdot s$ and the second with a viscosity of 5 to 15 $mPa \cdot s$) dissolved in ethanol were added. The dissolution of the ethyl-cellulose takes longer than expected, so it is started before the pestling. Finally the ethanol was evaporated using a rotary evaporator and evacuating until no lower pressure could be reached ($\approx$ 10 mbar) and continuing to evaporate for $\approx$30 to 60 min.

Different attempts to further improve the pastes by milling in a three roll mill (Exact 50i)

were undertaken, since no particulars are given about the milling step in the reference. They were all unsuccessful in that no finer structures could be obtained than without milling. Additionally the milling resulted in material losses. Attempts to disintegrate a larger fraction of the particle-aggregates in the paste by prolonged or repeated milling (30 min or 15 × 2 min) at the smallest possible gap between the rolls of the mill yielded an increase of the viscosity of the paste which ended up having the consistency of a chewed chewing gum. Shorter milling or fewer repetitions did not influence the consistency of the paste notably, but neither was a decrease of aggregates visible in the thereof deposited layers. If deposited by screen printing, thin layers of 2 to 4 µm thickness of the non-milled, or shortly milled pastes prepared from P25 yielded transparent or nearly transparent layers with a slightly white-blue colouring, similar to Fig. 4a in Ref. [121]. Therefore, the additional milling step was not employed any further. For spray deposition of titania layers the resulting home-made or purchased pastes were diluted with ethanol in order to receive a titania content of ≈3 % by weight. After the dilution they were stirred for 3 h or more, ideally overnight, and finally sonicated for 2 h. The thus finalised layers were stored at room temperature (RT) in glass-flasks or small bottles. The containers were tightly sealed using para-film.

The thus prepared titania-pastes were used for the deposition of nanoporous titania layers. Different deposition techniques will be explained and the resulting layers will be compared in the next section.

3.1.4. Deposition of Layers

It can be expected that even, integer and high-quality titania layers provide the best basis for high-efficiency dye sensitised solar cells and a highly reproducible cell fabrication. The porosity of the film is a compromise between different processes. Since a binding of the dye molecules to the titania by covalent bonds or strong hydrogen bonds is necessary to enable an efficient charge transfer from the dye to the substrate, only mono layer adsorption of dye molecules is desired. Thus the largest possible surface area is desirable in order to enable a large amount of dye to bind and thus a correspondingly high light absorption. On the other hand efficient charge transfer is only possible, if the density of the nanoporous film is high enough to minimise dead-ends and to enable unhindered and non-limiting conduction [122]. Thirdly the titania layer should not hinder the diffusion of the electrolyte through the layer in order to allow a fast regeneration of the dye molecules. Standard nanoparticle sizes used today are around $d \approx 20\,\text{nm}$, which yields transparent

layers up to layer thicknesses of 10 to 15 µm [21]. The ideal thickness of the film depends on different factors. While the conduction through the film is more efficient for low film-thicknesses the amount of adsorbed dye increases with increasing film-thickness (at equal porosities). Thus a maximum efficiency is expected at intermediate film-thicknesses with lower efficiencies above and below [113, 123]. The ideal thickness can be lowered by the use of opaque titania layers or the application of a scattering-layer additionally to the generally used transparent layer [23, 124]. Presumably the ideal film-thickness also depends on the sensitiser and the sensitiser absorption coefficient. In order to produce nanoporous titania layers different deposition techniques were tested, which will be described in this section. Foreclosing it can be mentioned, that at the end of our testing we ended up using the screen-printing technique, which is the standard technique generally used in DSSC-fabrication. The reason for this were the high reproducibility of the deposited layers and the easy availability of the necessary materials.

The next sections will describe the three techniques applied for the deposition of the titania layers, before the resulting layers will be compared.

Doctor blading

For doctor blading of titania layers a double-layer of scotch-tape was fixed to an overhead transparency, and a hole of the desired size (usually 6 mm in diameter) was punched through by means of a helve picker. The holy scotch was moved from the transparency to the prepared glass-slide and the top scotch layer was removed (its only function was to stabilise the scotch and to keep the resulting hole round). Afterwards a drop of titania-paste was placed on the scotch next to the hole-mask and it was coated onto the glass by means of a plastic squeegee. If necessary the printing was repeated, after drying the layer on a hot plate for 6 min at 125 °C. The scotch-mask was left on during drying and only removed after the second printing pass. Afterwards the layers were sintered in a box-type-furnace according to a heating-program based on the one described by Jessica Krüger in her Ph.D. thesis and adapted to our furnace [114]. An outline of the heating-program is shown in Fig. 3.14 on page 70.

Doctor blading is the simplest of the used deposition techniques. It is outlined in Fig. 3.2. The necessary tools are limited to a simple doctor blade or spatula, ideally made of a non-metallic material in order to prevent the introduction of iron atoms and ions into the layer. Additionally a helve picker or alternatively a hole puncher present in every office to punch the hole into the scotch tape. The advantage of a helve picker are slightly

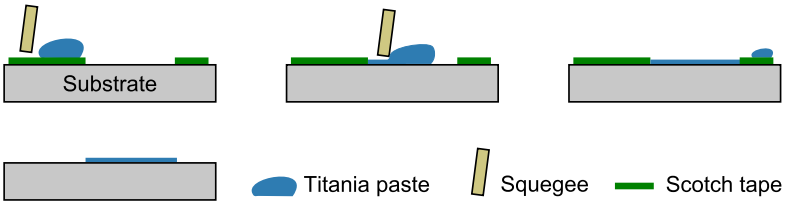

Figure 3.2.: *An outline of the doctor blading process.*

more even margins of the scotch mask and variable titania layer sizes since helve pickers of different diameter are easily available. For doctor blading titania pastes designed for screen printing can be used, thus they are easily available commercially or can be home-made according to established procedures [121]. The deposition of layers is very simple and fast. Layers of multiple microns thickness can be produced within minutes, making the printing time negligible compared to the sintering and the deposition of blocking layers and other preparation steps.

Disadvantages are the missing control of the layer thickness. For one the thickness of the scotch and thus the thickness of the deposited layer can not be influenced. It is unknown, whether the scotch has always the same thickness, and what the thickness-tolerance of the scotch is, so the final layer thickness suffers from unknown and non-influenceable factors. Additionally the printing of layers is reduced to producing masks of multiple scotch layers, or to print multiple layers into one scotch-mask. With very few exceptions the first resulted in damaged and mostly unusable layers. The second might be an adequate means of producing thicker layers by doctor blading. But also here a large part of the produced layers suffered from cracking and pealing off the substrate.

Spray Deposition

For the spray deposition a simple air-brush (Revell, standard class, Nr. 39101) was used. It was connected to a standard nitrogen pressure bottle via a decompression valve and the titania emulsion was sprayed on an FTO glass sample. In order to receive the desired layer-shape the sample was covered with a mask made of an aluminium sheet (thickness: 1 mm) into which a hole with a diameter of $d = 5.5\,\text{mm}$ had been drilled.

The spraying-parameters available in this setting are N_2 pressure at the air brush input and aperture of the needle-valve at the titania suspension connection to the air brush. While the pressure is accurately displayed at the decompression valve, the aperture was “measured” by turns of the valve-screw and thus estimated rather coarsely. Additional

parameters of the spray-deposition technique were the distance of the air brush to the sample, the spraying-mode (continuous spraying or spraying with intervals), the temperature of the sample and whether the air brush was held by hand or fixed to a support. In combination with the solvent used to suspend the titania particles from these particles two deposition-modes evolved. Either the spraying was performed dry (titania formed a dry layer on the surface) or wet (titania formed a wet layer and was left to dry before spraying again).

The deposition of titania layers via spray deposition seemed/is a promising, future-safe technique, since it can easily be scaled up and introduced in industrial production lines. In a sophisticated setup it should also easily enable the production of layers of different shape and thickness without the necessity of stencils and masks.

In our setup the spray deposition produced nice and uniform layers. Early layers deposited on cold glass-substrate showed drop-like patterns on the surface, and consequent variations in the layer thickness. A uniform layer thickness over the entire layer diameter and without large peaks or grooves and only minor variations around the average were observed by profilometer. Upon determining of more ideal settings and deposition of the layers from an ethanol based suspension on a glass-substrate heated to 500 °C during the entire deposition process, the drop-pattern diminished resulting in an even more uniform layer thickness. SEM overview images of layers deposited by spraying on hot and cold substrates are shown in Fig. 3.3.

Layers produced by spray-deposition yielded comparably high efficient cells with efficiencies up to 3.5 % while the simultaneously produced cells with doctor-bladed layers yielded efficiencies of up to 3 %. The general low efficiency is due to the fact, that the layers produced by spray-deposition and doctor-blading were fabricated in the very beginning of this work, when the general production method had yet to be improved. The main drawback of the spray deposition, which led to its dismissal, is the high ratio of damaged and unusable layers and a missing thickness control. Both had their origin in a clogging of the nozzle. Presumably nanoparticles aggregate at the nozzle and thus clog it, thereby leading to an interruption of the flow of the sprayed suspension. Since we assumed a constant material flow and a thus a spray-time dependence of the layer thickness as single thickness-control, this clogging interfered with the reproducibility of the technique. Additionally damaged and unusable layers resulted from impact of clogging-debris and large amounts of spray material upon flaking of the clogging aggregates.

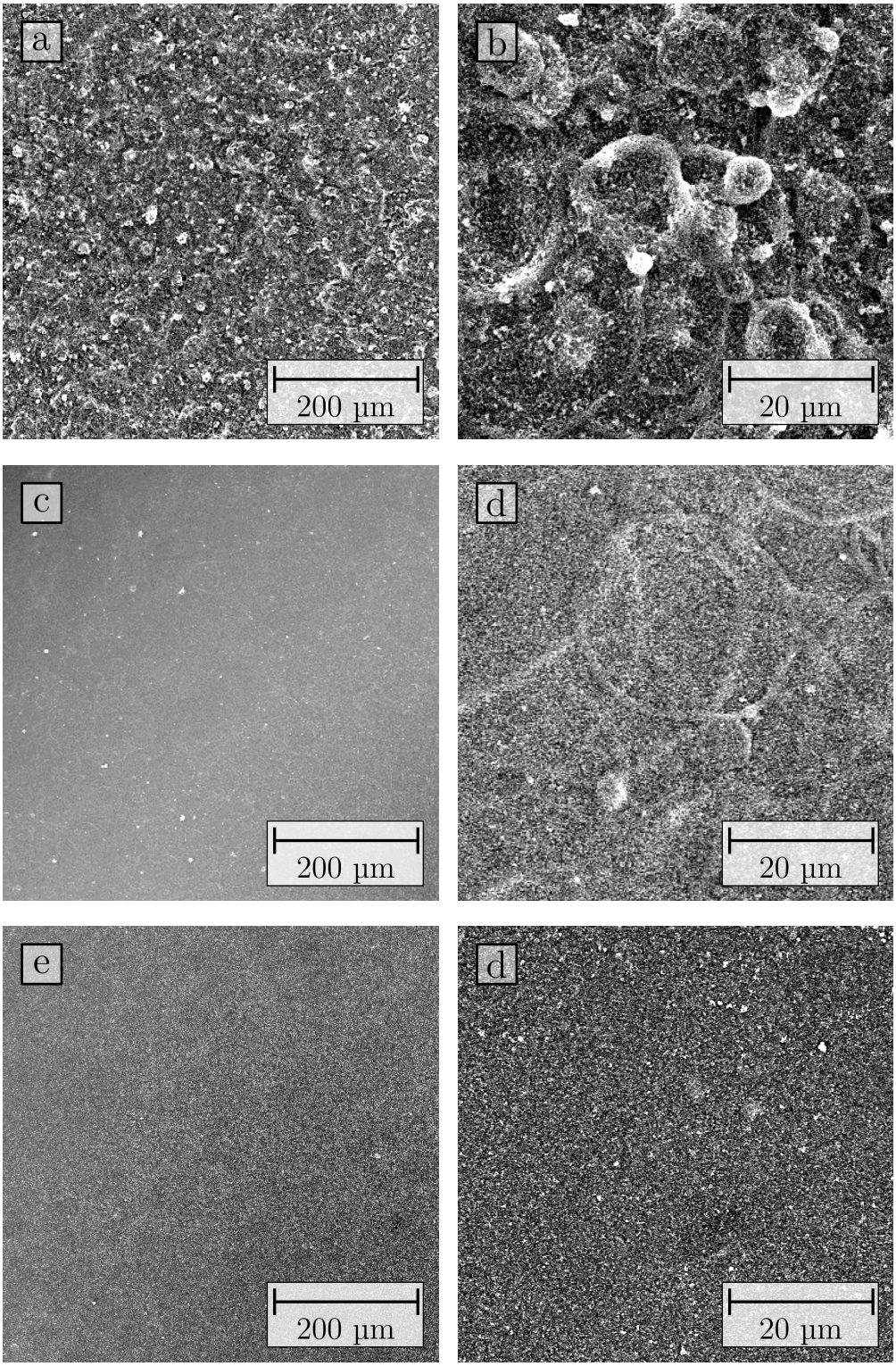

Figure 3.3.: *Comparative images of the layers produced by spray-deposition of suspensions containing P25 particles. Different magnifications of one layer (left and right) and different sample-temperatures:* 25 °C *for (a) and (b),* 100 °C *for (c) and (d),* 500 °C *for (e) and (f).*

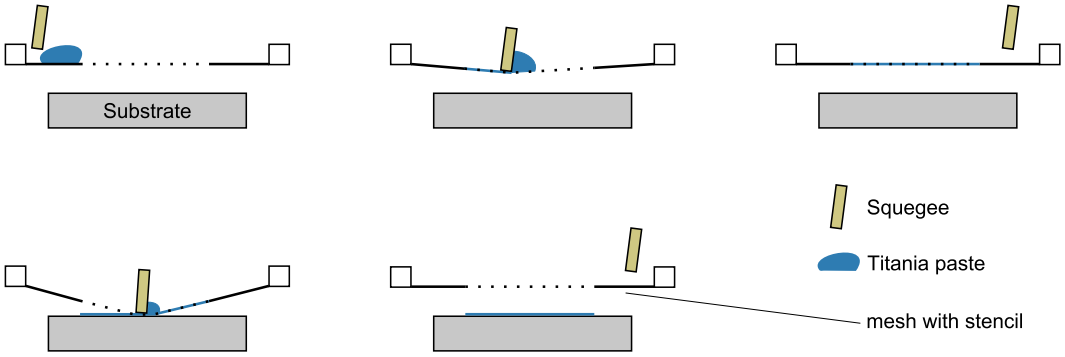

Figure 3.4.: *Outline of the screen-printing process: Loading of the mesh with titania-paste by application of the paste with the squeegee without contact between mesh and sample (top); transfer of the paste from the mesh to the sample by repetition of the printing with increased pressure and thus contact between mesh and sample (bottom).*

Screen Printing

Screen printing is the standard deposition technique for nanoparticle based titania layers. The NPs are prepared in a paste of viscosity comparable to semi-liquid honey. In addition to the NPs and the solvent the pastes contain a combination of (organic) stabilisers, which provide not only the desired viscosity but additionally support and thus enable the sponge like structure of the nanoporous layer during the drying and sintering and in the final layer. The screen-printing device consists of a cloth mesh (the screen) of defined thread thickness and spacing. In order to enable printing of defined features the mesh is transformed into a stencil by "closing" the non-printing part with a polymer. Screen-printing was performed according to [22] where it is described in more detail in chapter 8. The printing is a two-step process. The paste is loaded to the mesh by dispersion of the paste with a rubber squeegee at low pressure. In the second step the paste is transferred from the mesh to the substrate by applying more pressure to the squeegee. After printing, the deposited layer consists of many dots resulting from the printing-mesh which relax into an even layer upon storage in an EtOH atmosphere. Thereafter the layer is dried on a hot plate, and the printing can be repeated to create layers of the desired thickness. A single casting process is outlined in Fig. 3.4

The used printing setup consists of a 90T-mesh (Mesh-type: 90-48Y, specification: mesh-count 90 threads/cm; thread thickness: 48 µm) and squeegee from Serilith (Serilith AG, CH-6275 Ballwil, Switzerland) and a home-built base plate which holds the mesh-frame and aligns the stencil with the glass-substrates. For the relaxation a crystallising dish was covered with a watch-glass. The bottom of the crystallising dish was filled with EtOH

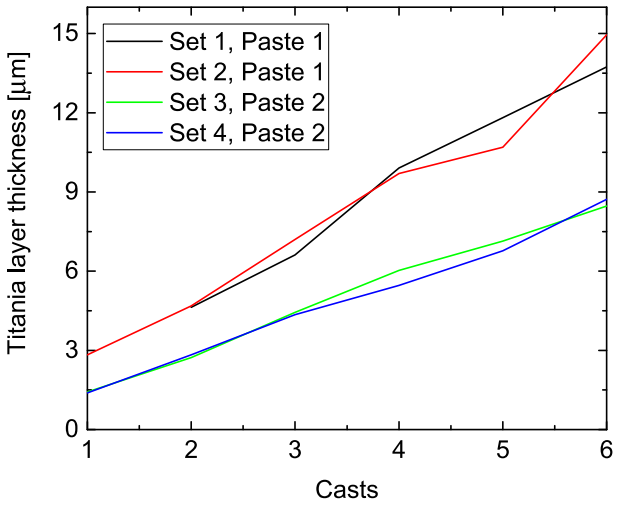

Figure 3.5.: *Evolution of the layer thickness depending on the number of screen printing casts for samples printed with two home-made pastes.*

and the sides furnished with blotting paper in order to provide the Ethanol atmosphere. A petri-dish in the crystallising dish served as stage for the glass-substrates to avoid contact with the Ethanol. The relaxation was monitored "by eye" and was aborted when the layers looked even over the entire surface, but did not start to form a "donut"-shaped structure. Drying of the printed layers was performed on a hot-plate in a fume hood at 125 °C for 6 min. After finishing the entire printing procedure the layers were sintered in a box-type-furnace. In order to evaluate the reproducibility and the thickness-control experienced by the screen-printing technique, layers consisting of 1 to 6 casts or sublayer were produced, and the increase in thickness with each additional sub-layer was determined by Laser Scanning Microscope (LSM) at a magnification of 200 ×. The resulting thickness per cast depends on different factors, such as the screen printing mesh (which was constant in our measurements), but also properties of the used paste, such as its viscosity and titania content.

The evaluation of the total layer thickness depending on the number of casts of four sets of layers made with two home-made pastes is shown in Fig. 3.5.

The data shows a clear separation of the two pastes in terms of resulting layer thickness. The average thickness per print of "Paste 1" is 2.4 ± 0.2 µm, while the average thickness per print of "Paste 2" is only 1.40 ± 0.05 µm. Both pastes were prepared according to the same instruction with the same materials and with the same amount of starting materials. The only differences between the two were that during the evaporation of

the solvent of "Paste 1" a skin like film formed on the surface of the paste. This skin might have formed a barrier hindering the evaporation of the solvent from the paste, which could result in a decreased paste viscosity. If present at all the effect had to be very small, since it was not noted. However no viscosity measurements of the pastes were performed. The second difference was the time of year. While the first two sets using "Paste 1" were printed within a few days of each other in summer, the second two sets using "Paste 2" were printed within a few days of each other in autumn. The temperature difference between the two was around 5 °C. With increasing temperature the viscosity decreases which results in a more liquid paste. It was shown by Jabbour and coworkers [125] as well as by Alias and Shapee [126] that a decrease in the viscosity of a screen-printing paste results in a decreased thickness of the deposited layer. Thus the combination of these two very small viscosity reducing influences might have been enough to induce the remarkable change in layer thickness.

This finding indicates the need for further evaluation of the factors influencing the thickness of deposited titania layers. It also shows the necessity to evaluate the produced pastes carefully in terms of their viscosity and titania content. In terms of the thickness of deposited layers it shows the importance of evaluating each used paste separately. Whether the influence of external factors such as the temperature is enough to bring about a marked change in the thickness of screen-printed layers can not be concluded from the present data and needs to be further investigated.

Independently of the used paste the maximal printable layer thickness we achieved was around ≈10 to 12 µm for layers without scattering layer in our setup. Thicker layers started to crack and peel off the surface during the sintering process as is described in more detail in Sec. 3.1.6.

Comparison of the Deposition Techniques

All the examined deposition techniques yield integer and homogeneous layers. Therefore, appearance of the layers produced by all the different deposition techniques is very similar if adequate deposition settings are chosen. Layers deposited by spray deposition on a hot sample, by doctor-blading and by screen-printing of home-made titania pastes containing P25 nanoparticles are shown in Fig. 3.6.

The layers deposited by screen printing are the most uniform. Some cracking of the layers may occur at anomalies, such as particle-aggregates, which introduce additional

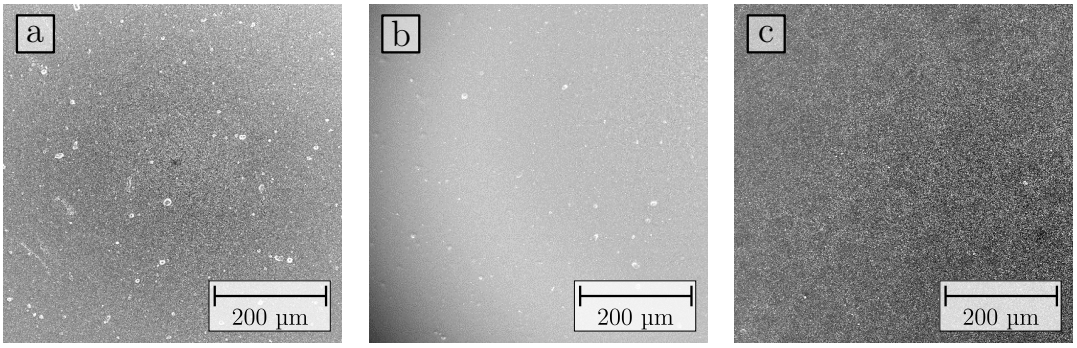

Figure 3.6.: *SEM images of titania layers of home-made pastes containing P25-particles deposited by different techniques. a) screen-printing, b) doctor-blading, c) spray deposition on a hot (*500 °C*) sample.*

strain into the layer, but large cracks are rare at layer thicknesses below 12 µm. The aggregates still present in the particle-paste after the paste-fabrication are clearly visible in the micrograph as protrusions in the layer surface. Since they are a characteristic of the used paste they are present in all the deposited layers independent of the deposition method. Thickness evaluations of screen-printed layers show a dependence of the relaxation process. If the layer was left to relax too long, the layer assumes a "donut" shape, with a relative depression in the centre and an elevation towards the outside. Properly relaxed layers show a uniform thickness over the entire layer, especially excluding high peaks at the edge which occur in doctor bladed layers.

Doctor bladed layers do not need to be relaxed, since they are printed in entire layers and not in many dots. Therefore the "donut" shape is not encountered here. However the scotch mask is much thicker than the freshly printed layer. Therefore, at the mask-edge the paste rises to the scotch top forming a peak. This peak is often visible in the finished layer. Also the doctor bladed layer is much more dependent from irregularities which occur during the printing process, since the paste is directly dispersed on the substrate with a hard blade. In screen printing on the other hand it is first deposited in the mesh and afterwards on the substrate with a softer squeegee. Examples of irregularities are variations of pressure and speed of the blade during the printing or irregular blade-edges, which can prevent an even layer and introduce grooves perpendicular to or along the printing direction.

Spray deposited layers can show a drop-like pattern on the surface if the solvent is non-volatile compared to the substrate temperature. Spray deposited layers seldom show any peaks or deep grooves but usually show a rather uniform height distribution which can have a maximum depending on the alignment of the airbrush and the sample. Optical

examination of the fine-structure of the layers deposited by the different techniques by SEM reveals that the fine-structure mainly depends on the used nanoparticles. Commercially available nanoparticles for DSSCs are often produced by sol-gel processes which yields a very uniform particle-size distribution. Particles produced by flame-spray pyrolysis (such as the P25 particles) have a broader particle-size distribution. Additionally they can contain aggregates which could not be completely disintegrated during the production of the pastes. Furthermore, the commercially available pastes contain only titania in the desired Anatase phase, while nearly a third of the titania in the P25 is Rutile [127, 128]. These differences are obvious upon examination of the layers by high resolution SEM. Only round particles of ≈20 nm diameter can be found in layers produced from titania-pastes purchased from Solaronix , while two kinds of particles can be detected in the layers produced from home-made pastes containing P25 (see Fig. 2.1 on page 12) . The distribution of large and small particles suits the relation of anatase:rutile which was stated to be ≈ 70 : 30 by Jensen et al [127]. As conclusion from the comparison to literature data of the phase distribution, the smaller, rounder particles are the anatase phase and the larger, more angular particles are in the rutile phase.

3.1.5. Examination of the Layer-thickness and uniformity

In order to characterise the layers deposited with the techniques described in the last section the layer thickness needs to be reliably measured and the appearance of the layer inspected. Therefore we compared different measurement methods to determine the thickness of a nanoporous titania layer with expected thicknesses in the range of 2 to 15 µm. The used methods were measurement by profilometer, by Laser Scanning Microscope (LSM) and on appropriately prepared layers by SEM.

All the used methods have their advantages and draw-backs, which will be presented in the next paragraphs.

Profilometry

Profilometry measurements were performed with an ALPHA-STEP ® 500 surface profiler (Tencor Instruments, Mountain View, California). A profilometer is a device calling to mind a record player or gramophone. It consists of a needle like tip which is brought in contact with a surface and then moved across the sample with a constant force recording

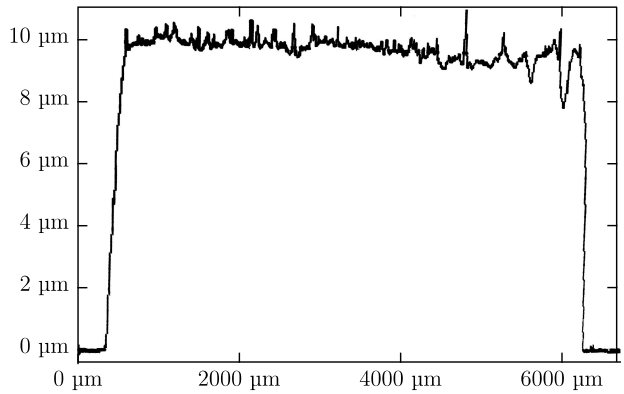

Figure 3.7.: *Example profile of a titania layer measured with the profilometer. The data was extracted from a photo of the screen.*

the relative sample-height and the distance of movement. The device yields a profile of the sample surface along the travelled distance of the tip.

The α-step is a rather ancient device. It runs on a computer without graphical interface and provides no possibility to export the data except for graphical export via the recording of a screen-shot. An example of a curve extracted from a photo of the screen is shown in Fig. 3.7.

The profile looks less noisy than the ones measured in the laser-microscope. Since the data is not available in any form other than graphically the errors can only be estimated. The curve has a thickness of around 500 nm resulting in an error for a single point of around 250 nm. The variation of the sample thickness is around 1.3 µm excluding the single very high peak and the two low depressions. The main body of values lies within a band of around 1 µm width, which can reasonably be assumed as error for the layer presented in the figure. The variations of measurements on other samples lies somewhat above the presented values, since the presented layer shows a rather even topography. A reasonable assumption for the variations of the layer thickness measured with the profilometer is ± 0.75 µm around the determined average for normal titania layers of around 10 µm thickness deposited by screen-printing corresponding to a variation of around ± 7.5 %. This corresponds well with the variations determined by the other methods. The relatively small error of the profilometry measurement compared to the LSM measurement can be explained by the much larger tip which "smooths" the measurement by dividing of one point over a larger surface area. Probably also the lower sensitivity of the measurement reduces the noise. The impact of the profilometer tip onto the sample is described by a tip-weight acting onto the measured surface, from which the force can be

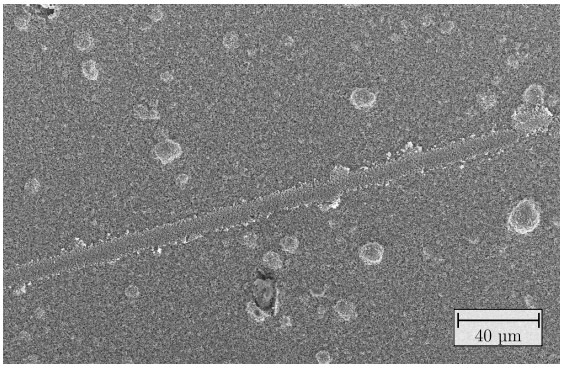

Figure 3.8.: *SEM image of a TiO_2-layer with a groove from a profilometer measurement.*

calculated as $F_{tip} = m_{tip} \cdot g = 13\,\text{mg} \cdot 9.81\,\text{m/s}^2 = 127\,\mu\text{N}$. Estimating the impact-radius of the tip on the titania layers by the groove resulting from the profilometry measurements yields a radius of $R_{Tip} = 5\,\mu\text{m}$ and thus an estimated pressure on the layer of $P_{tip} = \frac{F_{tip}}{A_{tip}} \approx 1.6\,\text{MPa}$. An SEM image of a sample surface with a groove resulting from a profilometer measurement is shown in Fig. 3.8

Scanning Electron Microscopy Measurements

SEM measurements were performed on a "Zeiss Supra 35"-SEM. The general settings were an acceleration voltage of 10 kV and a work distance of 5 to 10 mm for top view imaging and up to 15 mm for layer thickness estimation, thus cross section imaging. The samples were mounted with double-sided carbon-tape disks onto aluminium pin-stub holders, and a conducting bridge of carbon tape connected the conducting TCO layer on the glass with the sample holder base, as is outlined in Fig. 3.9.

Titania layer thickness estimation images were recorded by breaking a titania-coated TCO-glass in two parts parallel to the sample-width. The breakage line ran through the titania layer and was achieved by scribing of the backside. After the deposition and the sintering of the layer the glass was broken by means of glass pliers. The thus prepared sample was mounted on the sample-holder as described before. In addition to the conducting bridge a carbon tape was stuck to the glass-part of the breakage below the titania in order to reduce charging of the sample and thus to facilitate the imaging. For the imaging of the breakage the entire stage was tilted by 90° to orientate the breakage towards the electron-beam as is outlined in Fig. 3.9.

While the cross-section of the broken layer was oriented perpendicularly to the electron

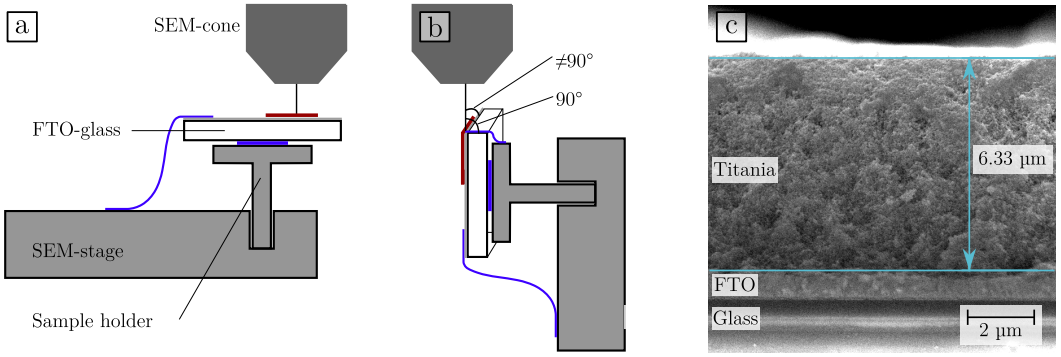

Figure 3.9.: *Outline of the layer evaluation in an SEM. a) top view onto the titania layer; b) cross-section imaging mode, stage with sample tilted by 90°; c) Example of a thickness-measurement performed by cross-section imaging by SEM; Blue and red features indicate conductive carbon tape and titania layer respectively.*

beam the breakage-plane of the tilted sample (thus the width of the glass-slide, not its thickness) was not necessarily oriented normal to the beam and the relative position between SEM-cone and sample was difficult to asses in our SEM setup. Therefore a somewhat larger working distance was chosen as a precaution to prevent contact of the sample with the highly damageable SEM-cone. Thereby the achieved magnifications were limited. But since the goal of the cross-section imaging was mainly the estimation of the layer thickness and secondly to see the layering of the samples, and not to examine single titania particles this should not be crucial, except maybe for the studies of the compact blocking layers as described in Sec. 3.1.2.

Thickness measurements by SEM were performed by measuring the thickness of the layers cross-section at multiple points. An example is shown in Fig. 3.9c. Compared to the other measurement techniques only a small number of points were measured on each sample (around 5). The accuracy of the measurement of a single point in the SEM is in the range of a few tens of nanometres and thus negligible compared to the variations of the sample thickness. The variations detected between multiple measurement points lie around $\pm 5\,\%$ of the layer thickness. It thus is rather lower than the ones determined for the profilometer and the LSM. This can be explained by the manual selection of the measurement points, which were usually performed at flat regions of average height. Thereby peaks and depressions in the layer were excluded without however unduly influencing of the determined average. The thickness value determined by SEM is the most easy to grasp, and the error on a single measurement point is very small. Due to the coarseness of the sample-preparation it could not be excluded that the

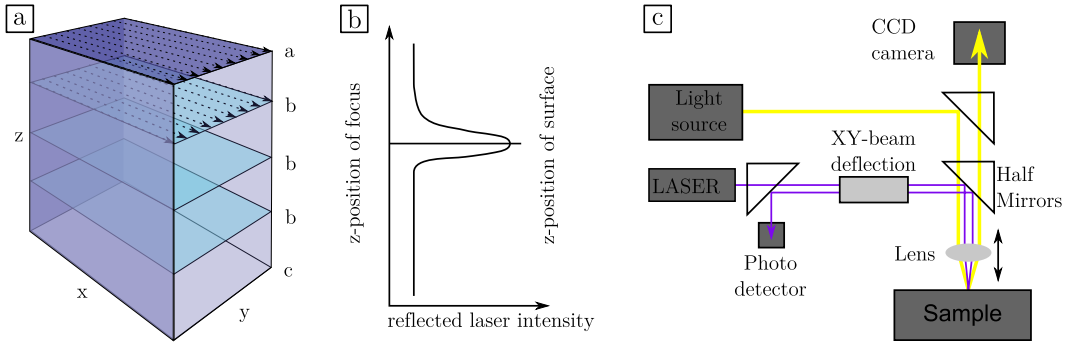

Figure 3.10.: *Outline of the measurement mode and setup of the light path in a LSM, adapted from the VK-210 manual.*
a) Measurement mode: layer-wise measurement of laser intensity in each point, repetition for the entire z-measurement range; b) subsequent generation of reflected-laser-light-intensity vs z curve for each pixel, and extraction of z-position of sample surface (intensity-maximum). c) Light path in the LSM.

layer thickness is not altered. It often results in breaking off of shards of the layer and might also lead to its compression. However comparison of the data with the data from other methods showed not only a good agreement, but put the SEM thicknesses on the average of the other two thereby indicating no alteration of the layer thickness by the sample-preparation. Therefore the values determined by SEM were used as reference for the comparison of the methods due to its high precision and easy grasp.

Laser Scanning Microscopy Measurements

LSM measurements were performed with a "Keyence VK-X210" equipped with an electronic stage "Keyence VK-S105" (both KEYENCE INTERNATIONAL (BELGIUM) NV/SA, Mechelen, Belgium). A laser scanning microscope is a combination of an optical microscope, a confocal laser microscope and the scanning technique of a scanning electron microscope which provides optical- and absolute height data of the studied sample. An outline of the setup and the light path within adapted from the VK-X210 manual is shown in Fig. 3.10.

It is based on a digital light microscope employing a CCD-camera as ocular (magnification 10 ×) and an objective revolver with a set of objectives of different magnification, namely 10×, 20×, 50×, 150×. The objective revolver can be moved in the z-direction in order to change the focal point of the system. Illumination is only provided from the top through the objective. In addition to the optical microscope the LSM is equipped with a laser source (violet, $\lambda = 408\,\mathrm{nm}$). The working principle is as follows: The laser-beam

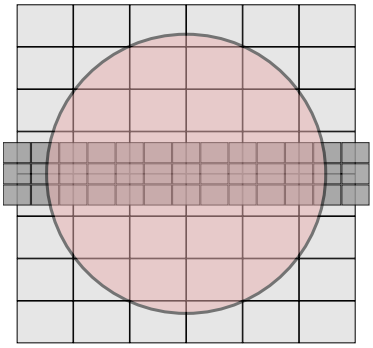

Figure 3.11.: *Imaging pattern of the two measurement types performed in the LSM. The round circle represents the titania layers, the light grey rectangles the images recorded at a magnification of* 100 × *for the overview and the dark grey rectangles the images recorded at a magnification of* 200 × *for the profile along the centre of the titania.*

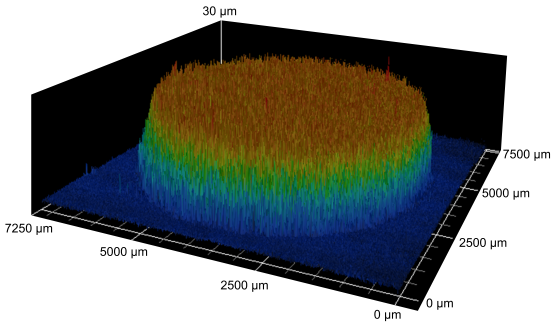

Figure 3.12.: *3D-image of a layer recorded with the LSM at a magnification of* 100 ×.

passes from the source through a deflection system and through the objective onto the sample. The deflection system enables the scanning of the beam in the xy-plane of the sample. The laser-beam is reflected from the sample surface, passes back through the optical system of the microscope and is collected by a photomultiplier. The intensity of the reflected laser light is dependent of the relative position of the focal-distance of the optical system and the sample, having a maximum when the sample surface is in focus. Thus the concurrence of the sample surface with the focal point is indicated by an increase of reflected laser light and the absolute height of the sample surface in a certain point can be determined by recording a curve of the light-intensity depending on the focal point of the optical system.

As outlined in Fig. 3.10 during the recording of height-data the laser is scanned over the sample pixel-wise with a fixed focal-point. Thereby the intensity of the reflected laser is measured in each pixel. Upon completion of the scan the focal point is changed by changing of the objective-height and a new scan is performed. This step is repeated until an adequate z-range is scanned which yields a light-intensity versus focal-length curve for each pixel. Thus a 3D-image of the surface is received by extracting the focal-length at maximum reflected laser intensity for each point.

Two types of measurement were performed for the evaluation of the titania layers. They are outlined in Fig. 3.11. Firstly an imaging of the entire titania layer by stitching of low-magnification images to one overview and secondly an imaging of a profile over

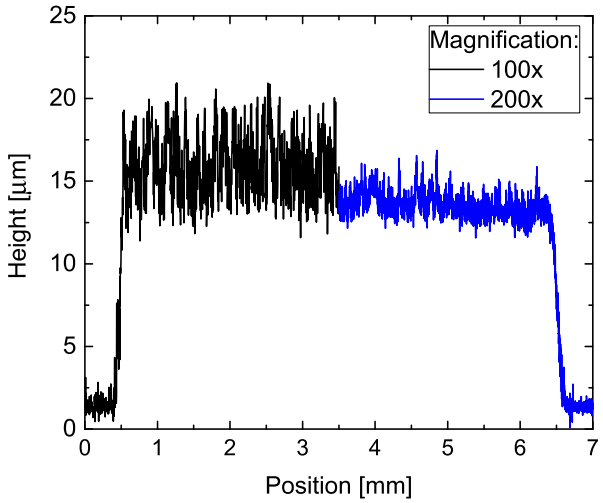

Figure 3.13.: *Two profile-parts recorded with different magnification at equal positions on the same titania layer. The lower magnification and the higher depth of focus lead to a lower accuracy at* 100 × *magnification.*

the entire width of the titania layer but covering not the entire layer-height, but only a stripe in the layer-centre. For the first 48 (6 × 8) images at magnification of 100 × were automatically recorded and stitched together to one large measurement. For the stitching the images were first raw-aligned according to the expected stage-position and then aligned based on the content by the Keyence-Software. The alignment algorithm worked quite well, but sometimes introduced a blurry area at the intersection between images. This overview image usually shows a rather large amount of noise in the height data, but a nice overview of the integrity of the layer. In a second step a stripe of 39 images (13 × 3) at a magnification of 200 × was recorded such as to have the horizontal middle-line of the layer in the centre of the imaging-area. The images were recorded and stitched as described for the overview image. An outline of the image recording pattern with the laser microscope is given in Fig. 3.11. An example image of an entire layer is shown in Fig. 3.12.

Thickness-evaluation by means of the LSM-data can be accomplished by multiple ways. Either a profile can be drawn across the sample (example shown in Fig. 3.13) or an average height of the entire or part of the areas on the layer-top and on the glass can be compared. While the first takes into account only a small amount of the data it leaves more opportunity to evaluate the result, since irregularities in the layer are easily visible and can be excluded if desired. The comparison of average heights on the other hand includes all the data points. Only large irregularities can be excluded by adaptation

of the chosen area. If not explicitly stated differently all the values presented in and used for this work were measured by averaging over the area of the layer-top excluding only the outer most part of the layer. It can however be noted, that the differences between the two measurements are small. The profiles shown in Fig. 3.13 were used to estimate the accuracy of the measurements performed by LSM. For the measurement at a magnification of 200 × the relative standard deviation of the values on the layer-top is 5 % including not only the true variation of the layer thickness, but also the not inconsiderable noise. The profile compares to the one recorded by profilometer (Fig. 3.7), but the noise seems about 2 to 3 × as large, thus the uncertainty of a measurement point lies around 500 nm. The variation within a layer was estimated to be around 1 µm corresponding to 7 % and thus barely larger than the noise-level. For the measurement at a magnification of 100 × the error increases to 12 %. In the low magnification measurement the variation of the layer thickness is lost in the noise, while at higher magnification it seems visible by eye.

Concluding it can be said that the LSM can be used only at a magnification of 200 × to measure reliable layer thickness-data. The calculated error is somewhat larger than the error estimated for the profilometry-data. Reasons for this are the larger number of measurement points, the smaller diameter of the laser beam (500 nm) compared to the profilometry tip (10 µm), and refraction of the laser at the rough surface. The detected thickness-variation of 7 % compares well to the values measured by profilometry despite the increased noise, and is somewhat higher than the one measured in the SEM due to the already filtered range of values therein. The agreement of the detected thickness-variation with the other two measurement methods shows the compatibility of the LSM with the measurement of thicknesses of titania layers.

However the increased noise and the much longer measurement time are disadvantages of this method, which is therefore less recommended for the thickness-measurement and more for the imaging of entire layers which enables an estimation of the cracking and general inhomogeneities.

Comparison

Each of the employed techniques for the measurement of the layer thickness and homogeneity has its advantages and disadvantages. The measurement by SEM requires the largest amount of sample preparation and the samples are not functional anymore after the measurement. The measurement is a measurement of a few single points, and

not of the entire layer or a profile over the entire layer diameter. Additionally before the comparison of the methods it was not certain, whether the layer preparation for the SEM measurements decreases the layer thickness by compression of the layer during the breaking process. However the measurements show, that this is not the case. No further effects that influence the result, such as scattering of the laser or depression of the layer by a measurement probe are to be expected. SEM is the only applied method which provides information about all aspects of the layer, thus the thickness (if appropriately prepared and measured), the evenness of the sample surface, a clear view of defects such as cracks and dust on the sample surface, and also of their origin with respect of the localisation. In addition to the layer thickness the size, shape and distribution of particles on the surface and throughout the profile exposed by the sample-preparation can be studied. Extreme defects of the conductivity are exposed, since they show as charging-effects during the imaging.

The profilometer measurements need no extra sample preparation. The measurement provides profiles over the entire layer diameter and is very fast and easy to handle. However the tip of the profilometer is always in contact with the sample and digs a groove in its surface. The resulting groove is not very deep and the profiles show even needle-shaped protrusions, which indicates a low impact, since else these would break away and not appear in the profile (example profile see Fig. 3.7). However, the groove is clearly visible in SEM as is shown in Fig. 3.8. A diminution of the applied tip-sample force might reduce the impact on the sample, but the used device did not offer an easy possibility to achieve it. Additionally due to the dinosaur-status of the measurement-device it did not provide the possibility to export the data in any other way than by means of a screen-shot or sketch.

Also the LSM measurements require no extra sample preparation and do not impact the usability of the studied samples. The laser irradiation has no measurable influence on the prepared layers. Further advantages of the laser microscope are easy accessible data and the possibility to measure the entire sample and not only single points or lines. Furthermore it also gives clear evidence of defects which can get lost using other measurement techniques. Drawbacks are the comparably long measurement time (10 min each for an overview and a more precise profile measurement) and the comparably high noise compared to the profilometer, especially when measuring at a magnification of 100 ×. Reasons for the noise are the large size of the laser-spot which additionally becomes reflected on the nanoporous surface. The noise can be markedly reduced by increasing the magnification to 200 ×, as is shown by the comparative profile in Fig. 3.13,

Table 3.1.: *Layer thicknesses measured by the different techniques, normalised to the thickness measured by SEM. The given errors are variations of the normalised layer thickness compared to the SEM thickness (e.g. the average thickness measured by profilometry is* $96 \pm 7\,\%$ *of the thickness measured by SEM). The variation within a single layer was determined to be around* 5 *to* 7 %*.*

Technique	normalised thickness [%]	Deviation from SEM-thickness [%]	N
LSM, 100x	119 %	8 %	13
LSM, 200x	105 %	6 %	12
Profilometer	96 %	7 %	11
SEM	100 %	-	17

but this disables the possibility to measure an overview of the entire layer within a short time, or necessitates the recording of two images at different magnification for overview and accurate thickness measurement purposes. Further increase of the magnification is not practical anymore, due to overly long measurement time.

The layer thickness of different layers were measured with all the three devices in order to compare the resulting thickness of the various methods. In order to compare the different measurement techniques the measured thickness of each layer was normalised to the thickness measured of the same layer by SEM. Errors of the measurement-method were determined as variation in the measured thickness compared to the SEM value. The resulting data is shown in Tab. 3.1

The thickness measured with the LSM at low magnification is the highest and nearly 20 % higher than the SEM value. In comparison the thickness measured with the LSM at a higher magnification is only 5 % higher than the value measured by SEM. This was to be expected from the profile shown in Fig. 3.13 where it can be clearly seen, that the high-magnification curve shows not only less noise, but is located at the lower end of the noise-level of the low-magnification curve. The thickness determined by the profilometer is 5 % lower than the one measured by SEM. An underestimation of the layer thickness by profilometer is well explainable by the groove induced by the measurement. Except for the LSM-measurement at low magnification all the measurement techniques yield very similar thicknesses for the layer. It can be assumed, that the true thickness value lies somewhere in the range of the thickness of the three. Since the SEM data is located right at the average of the three it seems like its fixing as a reference was justified. It also indicates, that the breaking of the sample does not unduly influence the thickness of the layer. Since cross-section SEM measurements call for more sample preparation, are expensive in terms of expenditure of time and yield the samples useless for the fabrication

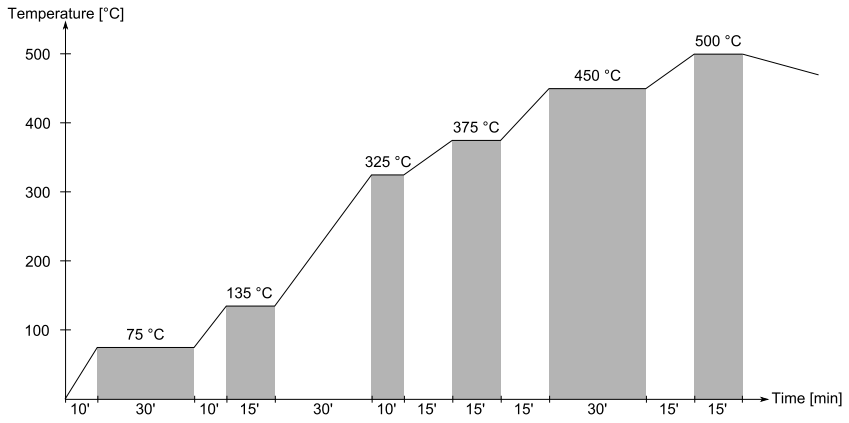

Figure 3.14.: *Outline of the heating program used for the sintering of all the deposited titania layers.*

of solar cells, measurements by LSM or profilometer are more advisable. Especially the profilometry measurements are very fast and easy and are thus the advisable option for layers produced with a known deposition method, if a profilometer which provides the data in a numeric form is available. For the comparison of new deposition methods the LSM has the advantage of showing the entire surface, and can therefore give additional insights.

3.1.6. Sintering

Sintering of the deposited layers by heating of the samples to temperatures around $\approx$500 °C is applied in order to receive a durable, compact and interlinked nanoparticle layer. Sintering was performed according to the heating program described by Jessica Krüger in her Ph.D. thesis [114], which had to be adapted to the maximum heating rates of our furnaces. An outline of the used heating-program is shown in Fig. 3.14

During the sintering the solvents present in the pastes evaporate yielding a dry layer consisting of titania and the organic stabilisers, e.g. ethyl cellulose. At increasing temperatures the ethyl-cellulose is decomposed as well resulting in a layer containing only the titania. The decomposition of the stabilisers is indicated by a brown colouring of the layer, which vanishes upon completion of the decomposition and evaporation of the decomposition products, leaving the layer white or blueish-white if it is a transparent one. Even though the nanoparticles do not melt during the sintering, they are assumed to become “sticky” at the surface and thus interconnect to form electrical contacts. In order to determine the influence of the sintering device two box-type furnaces and a

heating plate were used to sinter equally prepared titania layers. The resulting layers showed little differences.

One of the main problems we observed in the fabrication of titania layers is the cracking and peeling off the surface of the layers at increasing layer thicknesses. Kay describes cracking of titania films deposited by hydrolysis of $TiCl_4$ in his Ph.D. Thesis [118]. He assumes the cracking to be due to stress provoked by capillary forces of liquids in pores of the layers. Thinner layers don't crack, since they only shrink vertically. A similar model might be assumed in the drying of nanocrystalline layers. Capillary forces of remaining liquid lead to cracking of the already dried parts of the layer. Additionally in layers composed of home-made pastes the aggregates in the paste induce additional stress-centres. This can be shown by the fact, that thinner layers which do not peal off the surface show small cracks which can always be found at a particle aggregate. The assumption, that the box-type furnace could increase the cracking problem by heating the samples equally from all sides thereby inducing the solvent in the top-part of the layer to evaporate first and thus trapping solvent in the layer bottom was impaired by the layers sintered on the heating plate, which showed similar cracking-patterns.

3.2. Dye Sensitised Solar Cells - Examination

3.2.1. IV measurements

The main parameter of interest in the characterisation of solar cells including DSSCs is the efficiency of the cell. The efficiency η is defined as the ratio of the energy output to the energy input. Taking into account the cell-area this is described by:

$$\eta = \frac{\frac{P_{\text{ph}}}{A_{\text{cell}}}}{I_{light} * A_{\text{cell}}} \tag{3.1}$$

Where P_{ph} is the photo power generated by the solar cell, I_{light} is the light intensity of the irradiated light and A_{cell} is the active area of the solar cell. It has to be mentioned, that the solar cell does not generate energy, which is impossible according to the law of conservation of energy, but it transforms the radiation energy of the irradiated light into electrical energy. Nevertheless one speaks of generated energy keeping in mind that the energy is in fact only transformed. The electrical power generated by a solar cell depends on the produced current and voltage. It is calculated as $P_{\text{ph}} = V * I$ where I is the current

produced by the solar cell and V is the voltage against which the current was produced. One of the basic techniques to characterise solar cells is the measurement of the IV-curve, thus the measurement of the (photo)-current produced by the cell, depending on the applied voltage. In a basic approach the IV-measurements is an IR-measurement, and the setup consists of the tested solar cell, an ampere meter and a set of resistances. The current produced by the cell depending on the resistance in the circuit is measured and the power output P_{ph} is calculated from $P_{\mathrm{ph}} = V * I = R * I^2$ by introduction of $V = R * I$. In a potentiostatic approach a source meter is used to measure the current produced by the cell depending on a voltage applied over the cell instead of inserting the resistance into the circuit. The IV-curve shows a characteristic shape of decreasing current with increasing voltage. The interesting points of the IV-curve are the short circuit current (I_{sc}), where the resistance or voltage is zero, and the open circuit voltage (V_{oc}) where the resistance is infinite or the voltage large enough to allow the solar cell to produce zero current. At both points the power generated by the cell is zero. Between these two points the power curve has a maximum, the maximum power point where: $P_{MPP} = I_{MPP} \cdot V_{MPP}$. Another interesting parameter of the IV-curve is the fill factor (FF) Fill-Factor (FF). It is a quality factor and compares the maximum power generated by the cell to the theoretical maximum power which would be generated by an ideal (but practically impossible) solar cell. It is defined as the ratio of the P_{MPP} and the product of I_{sc} and V_{oc}: $FF = \frac{P_{MPP}}{I_{\mathrm{sc}} \cdot V_{\mathrm{oc}}} = \frac{I_{MPP} \cdot V_{MPP}}{I_{\mathrm{sc}} \cdot V_{\mathrm{oc}}}$.

Physically an ideal solar cell can be modelled by the one-diode model which describes it as a current source in parallel with a diode. Therein the current is given as::

$$I = I_{ph} - I_D = I_{ph} - I_0 \left[\mathrm{e}^{\frac{eV_D}{nk_bT}} - 1 \right], \tag{3.2}$$

where I_D is the diode current, I_0 the dark saturation current, e the elementary charge ($e = \oplus 1.602 \times 10^{-19}\,\mathrm{C}$), V_D the voltage over the cell, n an ideality factor, k_b the Boltzmann-constant ($k_b = 1.38 \times 10^{-23}\,\mathrm{J/K}$) and T the temperature in Kelvin. I_{ph} is the photo current produced by the cell which is usually, but not always equal to the I_{sc}. This is especially true for high quality solar cells at short circuit condition [129]. The diode current is described by the Shockley diode equation:

$$I_D = I_0 \left[\mathrm{e}^{\frac{eV_D}{nk_bT}} - 1 \right]. \tag{3.3}$$

Since no solar cell is ideal, the deviations of this ideal model are considered by including

a series- and a parallel or shunt-resistance. The series resistance corrects the ideal diode for resistances in the semi-conductor material, at the contacts and in other parts of the circuit . The influence of an increasing series resistance is a shallowing of the IV-curve near the open circuit condition. The shunt resistance on the other hand describes errors in the cell which provide an alternative route for the current and thus enable a part of the current to deviate from the desired path out of the contacts of the cell thereby reducing the usable cell current. The effect of a decreasing of the shunt-resistance is a steepening of the current around short circuit condition and thus a lowering of the flat-upper part of the curve. Considering the resistances formula 3.2 transforms to:

$$I = I_{ph} - I_D - I_{SH} = I_{ph} - I_0 \left[\mathrm{e}^{\frac{eV_D + IR_S}{nk_bT}} - 1 \right] - \frac{V_D + IR_S}{R_{SH}}, \tag{3.4}$$

where I_{SH} is the shunt current and R_S and R_{SH} are the series- and shunt resistance respectively. While the diode equation can not be solved analytically it is usually fitted to measured IV-curves in order to extract the parameters for I_0, I_{SH}, R_S and R_{SH} and thus characterise the solar cell.

In order to characterise the DSSCs, an IV-measurement-setup was implemented as part of this work. The setup is based on a solar simulator from Abet (Sun2000, Model 10016, Abet Technologies, Inc., Milford, Connecticut, USA). It uses a 550 W Xenon Arc lamp and a system of filters and lenses in order to generate a light output with an AM1.5G spectrum. It is specified to provide Class AAB simulated sun light, thus a class A spectral match, a class A temporal stability (time dependent light intensity variation of less than 1 %) and a class B light uniformity, thus a variation of the light intensity over the entire illuminated area of less than 5 %. The light intensity of the solar simulator is calibrated using a calibrated reference-cell with a short circuit current of $I_{sc_{Ref}} = 91.7\,\mathrm{mA}$ under illumination of simulated sunlight with an AM1.5G spectrum and an intensity of $I_{light} = 1000\,\mathrm{W/m^2}$.

A Keithley 2400 Series SourceMeter (Keithley Instruments, Inc. Cleveland, Ohio, USA) is used to measure the current and apply the voltage over the cell. Alternatively a home-built IV-curve-tracer is used for the measurement. While the Keithley comes pre-calibrated and is easy to handle all the way from the first setup to the measurement the home-built tracer is easily extendable and adaptable, so it perfectly fits the needs and design of the entire setup. Besides the possibility to measure IV-curves of 1 to 4 cells simultaneously it was extended with a relay-circuit in order to enable the measurement of the contact-resistances. For home-made solar cells based on a glass-substrate cables for

an external connection can not easily be soldered to the cell. Thus the cells are usually connected via clamps or contact fingers. While experience shows that the contact-fingers used in our setup usually provide an ohmic contact and a contact resistance $< 10\,\Omega$, in some cases an undesirably contact resistance was detected, which leads to an increase of the series resistance and thus decreases the measured efficiency and falsifies the measurement. Therefore an adequate DSSC-measurement setup needs to provide a possibility to measure the contact resistance, ideally in an automated manner. We implemented this by disconnecting the two probes for the four-terminal IV-measurement and thus providing two separate contacts per electrode. During the IV-measurement one of the probes is used to measure the current and the other for the voltage. However, by measuring the resistance from one probe to the other, the combined resistance of the two contacts can be measured and therefore an estimation of the contact resistance can be acquired. Thereto the relays are switched in a way to either apply the voltage between anode and cathode of the solar-cell for the IV-curve measurement, or to apply the voltage between the two probes of one cell-electrode to determine its contact resistance.

The setup additionally contains a home-built cell-holder combined with a TeTech peltier element and a corresponding temperature controller (CP-061 and TC-36-25, TE Technology, Inc., Traverse City, Michigan, USA). It allows a simple and durable clamping of up to 4 cells despite their sandwich structure and thus the opposite orientation of their contacts. It ensures a solid connection of the cell-holder and the peltier-element and thus a high quality temperature control, a low-resistance connection of the cell-electrodes to the measurement-electronics established by one plug for all the four cells. It also includes the described contact-resistance measurement and ensures a non-varying alignment of each cell-measurement position relative to the sun-simulator light-beam. The measurement-device is designed to take up cells of a specific design, which poses certain limitation to the use of cells produced by other protocols. However, it can be unmounted easily, enabling the connection of cells of a arbitrary design by contact-finger terminated measurement cables.

The entire setup is controlled either by the software Tracer 2 by Rera (ReRa Solutions BV, Wijchen, Netherlands), or by a home-built labview program. The commercial software provides easy access to all the newly acquired and already saved data, advanced data processing and fitting and various measurement modes such as measurement of short circuit current or open circuit voltage vs. time. The home-built software on the other hand is easily adaptable to changes and peculiarities in the setup. It provides an easy possibility to measure long-time measurements under constant or interrupted

illumination. The data is provided in a standard ASCII format and in single or complete data sets and an automatically generated LaTeX-based overview report is generated at the end of each measurement. Overview data of complete measurement-sets or parts of them can be displayed, and the software features a simple temperature control enabling the measurement at constant temperature or with easily definable temperature programs. An outline of the home-made labview softwares is shown in Appendix C.1

The light-output of the Abet solar simulator is perpendicular to the ground. The light is collimated before exiting the device and the last part of the light path is through the open air, thus the light-path and also the sample are not enclosed during the measurement. Therefore the amount of indirect light irradiated onto the sample due to scattering of the light-beam of the solar-simulator is reduced compared to box-type solar-simulators in which the entire light-path is enclosed in a box, as e.g. the Solaronix SolarSim150.

Comparative measurements we performed suggest this to be of importance when studying DSSCs. While silicon solar cells mainly respond to direct sunlight irradiated perpendicularly to their surface and perform feebly under indirect light irradiation, DSSCs are much more responsive to indirect irradiation due to the nano- and microsstructuring of their surface. Additionally the glass-sandwich structure of home-made DSSCs makes them transparent, allowing light to enter not only from the top-side, but also from the sides, and through the cell-surface located around (and not belonging to) the active area, if the cell is not appropriately masked.

IV-measurements of a home-made DSSC were performed in an open and a box-type solar simulator in order to evaluate the influence of the additional indirect light. The light-intensity was calibrated using a mono crystalline silicon reference cell. The DSSC was measured unmasked, masked with a black mask of ≈0.75 mm thickness and with a multilayer black mask of ≈2.5 mm thickness. The resulting IV-curves are shown in Fig. 3.15 and the corresponding parameters in Tab. 3.2. The data shows marked discrepancies between the behaviour of the two compared cells. While the silicon-cell generates the same current in both solar simulators, thus implying an equal light intensity, the unmasked DSSC's efficiency in the box-type simulator is higher by a factor of nearly 1.5. Applying a mask has a larger influence on the performance of the DSSC in the box-type simulator. Its efficiency decreases by a factor of ≈ 2 if masked by a thin mask, and by a total factor of ≈ 4 if the thicker mask is applied. In the open solar-simulator the efficiency decreases by a factor of 1.4 and 1.5 respectively upon application of the thin- and the thicker mask compared to the unmasked cell. Thus at light intensities pronounced

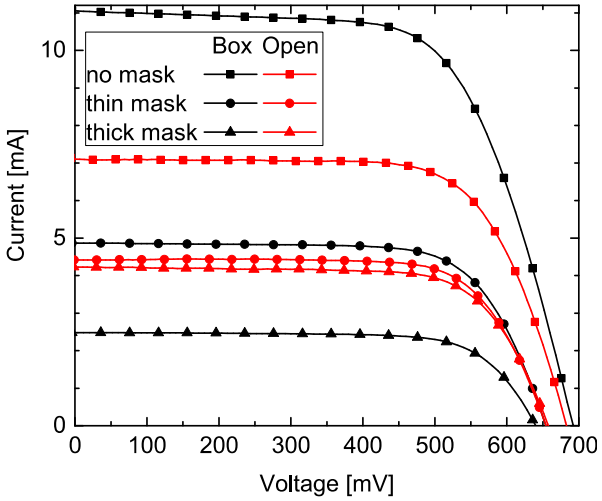

Figure 3.15.: *IV-curves measured for the comparison of open and box-type solar simulators. Equal colours are measured in equal simulator types, symbols express the kind of the applied mask.*

equal by the calibration the unmasked cell performs better in the box-type simulator, the cell performs equally in both simulators when it is masked with a thin mask, and it performs better in the open-type solar simulator upon application of the thicker mask.

This suggests a masking of not only the heavily diffuse-, but also the slightly diffuse light by the thick mask, which unduly influences the light calibration. The highly diffuse light is only converted by the DSSC and not by the silicon cell. Therefore it does not appear in the light intensity calibration performed by means of an unmasked silicon cell leading to an underestimation of the light-intensity present for an unmasked DSSC. On the other hand the slightly diffuse light is also converted by the silicon cell and thus increases the light-intensity measured during the calibration. Upon application of the thick mask, the lightly-diffuse light's path is blocked and thus it is no longer present for the examined DSSC resulting in a decreased effective light intensity and therefore an underestimation of the DSSC's-efficiency. Therefore in a solar simulator with a high proportion of diffuse light the application of a thick mask to a DSSC leads to an underestimation of the efficiency, if the light-calibration was performed by an unmasked silicon solar cell. This over- and underestimation of the cell-efficiency depending on the masking-conditions indicates that characterisation and fabrication of DSSCs can show a different dependence from various factors than is expected due to the study of silicon solar cells. Thus all steps of the fabrication and characterisation of DSSCs, also those which seem trivial such as the calibration of the light intensity in measurement devices, need to be thoroughly and systematically investigated in order to prevent systematic errors.

Table 3.2.: *Short circuit current density and efficiency data of the IV-curves measured for the comparison of the open- and box-type solar simulators for the evaluation of the importance of the amount of diffuse light in a measurement setup used for the characterisation of DSSCs.*

Sun Simulator	Mask	J_{sc} [mA/cm^2]	η [%]
Box	no mask	11.1	5 %
Box	thin mask	5.7	2.6 %
Box	thick mask	2.9	1.3 %
Open	no mask	7.1	3.4 %
Open	thin mask	5.2	2.4 %
Open	thick mask	4.9	2.3 %

3.2.2. Reaction times

Another point demonstrating interesting differences in the behaviour of silicon- and dye sensitised solar cells is the reaction time of the cell to external stimuli, which is far slower in a DSSC. This is eminent when comparing the current response generated by a DSSC and an silicon-cell upon stimulation with light modulated at different frequencies as shown in Fig. 3.16. The data was measured in a quantum efficiency setup, in which white light generated by a halogen lamp is modulated by an optical-chopper (Thorlabs MC2000) before passing through a monochromator (Omni-300, LOT Oriel). The modulated monochromatic light is irradiated on the solar cell. Optionally an additional illumination with an unmodulated white light from a home-built LED bias light is available. The current response of the cell is recorded by means of a Keithley 2400 Series SourceMeter. The data presented in Fig. 3.16 was measured with a DSSC sensitised with N719 and a silicon-reference cell. The cells were illuminated with monochromatic light at a wavelength of 600 nm and with a white bias light of $\approx 1000\,\mathrm{W/m^2}$ intensity.

The curves show a marked difference between the DSSC and the silicon-cell. While the silicon-cell (upper set of curves) shows a perfectly rectangular current response at all the measured frequencies (up to 80 Hz) and presumably also at even higher frequencies, the DSSC shows a distinct rounded shape of the curve already at 1 Hz. At 3 Hz the plateau is hardly visible anymore, while at 6 Hz the block-shape of the signal is completely absent and the response-curve is triangular. The reason for the distortion of the current-response curve is assumed to be the slow reaction of the DSSC to the external stimulus. Which part of the DSSC is the limiting factor can not be determined without further studies, e.g. by Electrochemical Impedance Spectroscopy (EIS), which is used

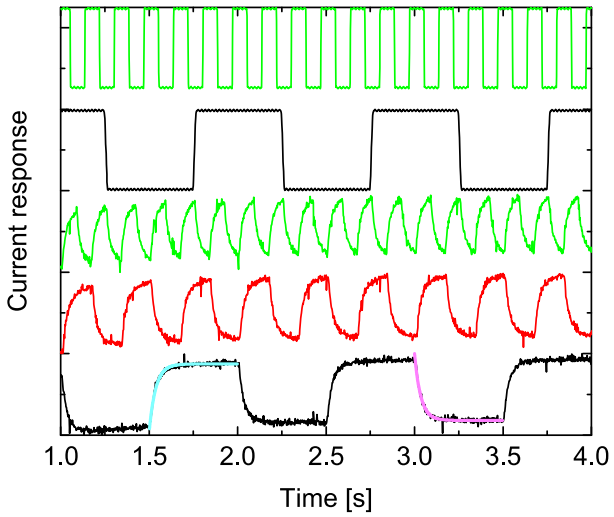

Figure 3.16.: *Current response curves of a DSSC (lower curve-set) and an Si-cell (upper curve-set) to light modulated at different frequencies. The current was normalised to a fixed amplitude of* 1*, curves were shifted for clarity. Frequencies: black:* 1 Hz*, red:* 3 Hz*, green:* 6 Hz*. Examples of an exponential decay- and growth fit for the determination of the time-constants are shown in magenta and cyan respectively.*

to measure the frequency dependent impedance of DSSCs and thus allows conclusions about frequency dependent properties of the cells. Fitting of an exponential growth or decay function to the current-response curve yields the time-constant of the reaction. The average time-constant for the current onset upon irradiation of light was determined as $\tau_{on} = 39 \pm 2\,\text{ms}$, and for the current decay as $\tau_{off} = 33 \pm 4\,\text{ms}$. The time-constant of an exponential decay describes the time in which the signal decays to $\frac{1}{e}$ of its initial value, thus to approximately 37 %. After the duration of 3 time constants the signal decayed by more than 95 % of its initial value, thus less than 5 % are left. Thus the DSSC will generate more than 95 % of its maximum possible current only at modulation frequencies below 5 Hz, where the current-response curve will no longer have a plateau, but exhibit only the saw-tooth shape shown in the figure (Fig. 3.16).

By increasing of the light-intensity to $2000\,\text{W/m}^2$ the block signal is present up to much higher frequencies, thus it speeds up the reaction of the DSSC. This indicates the limiting factor to be light-intensity dependent. This probably excludes the diffusion of the ions in the electrolyte, which would have been a first assumption for a limiting factor in terms of speed, and hints towards the charge transport in the titania layer, which has been described to be light-intensity dependent [21]. For both the silicon-reference cell, and the DSSC under illumination with a light of an intensity of $2000\,\text{W/m}^2$ the determination of the time constant is limited by the instrumentation. The light-modulation by a chopping-

wheel leads to a gradual onset of the light, which is visible upon close examination of the response-curve of the silicon-reference cell at a modulation-frequency of 1 Hz, while already at 6 Hz the current-onset is faster than the shortest measurement interval achievable with the source meter employed for the measurements.

For the study of DSSCs this indicates, that the reaction times of the cells need to be determined or assessed and the measurements need to be adapted to the decreased speed of the cells. Examples are the measurement of IV-curves, where the settling time between the application of a voltage and the measurement of the corresponding current response needs to be adapted in order to allow for the solar cell to react to the new environment and produce its maximum current. Otherwise the measurement might be falsified due to under (or over) estimation of the DSSC's response.

3.2.3. Glove Box

N719 and other ruthenium complexes which are used as standard sensitisers, as well as highly specialised organic molecules serving the same purpose are dependent on rare metals and their synthesis can be very complex, which makes them expensive and rare. Furthermore they often have low extinction coefficients. Natural organic sensitisers on the other hand are expected to be abundant, easy to obtain and to have a low environmental impact, thereby countering these disadvantages. Additionally they have been developed by nature for the absorption of light over a very long period and thus have extinction coefficients which are higher by a factor of ~ 10. Therefore, we produced dye sensitised solar cells sensitised with the natural organic molecules "crocetin", "bixin", and "torularhodin", which can be gained from the flower "Crocus Longiflorus", the tree "Bixa Orellana", and the yeast "Rhodotorula Glutinis" respectively. Their chemical structures are shown in Fig. 3.17.

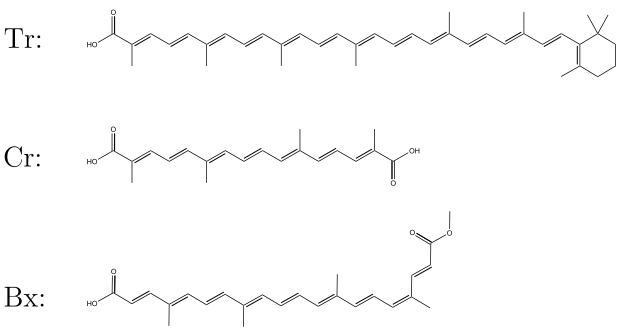

Figure 3.17.: *Natural organic sensitisers torularhodin (Tr), crocetin (Cr) and bixin (Bx).*

Table 3.3.: *Parameters of the IV-curves of crocetin sensitised cell prepared in the glove box and in air. IV-curves shown in Fig. 3.18.*

	J_{sc} [$\frac{\text{mA}}{\text{cm}^2}$]	V_{oc} [V]	FF [%]	η [%]
Glove box	8.2	530	52	2.3
Air	3.7	517	28	0.5

First attempts of producing the cells were not successful. The sensitised layers bleached and lost their colour within minutes of removing them from the sensitiser solutions, even before the assembly of the cells was accomplished. Further examination of the bleaching revealed that extreme bleaching only occurs when cells sensitised in dye solution produced of non-anhydrous solvent are simultaneously exposed to an oxygen and water containing environment and to UV-light. The bleaching was therefore attributed to catalytic self cleaning of TiO_2 [130]. In order to avoid the degeneration of the dye molecules, cells were first produced in a nitrogen filled glove bag under red-light, and subsequently in a nitrogen environment in a glove box (Unilab, mBraun, Germany) under normal light. The dye-solutions used for sensitisation were produced with anhydrous solvents and were stored in the glove box. The titania layers were still produced in a normal environment up until the post-treatment of the finished layers with aqueous $TiCl_4$ (see Sec. 3.1.1). Directly after the ensuing sintering the still hot titania layers and counter-electrodes (T>400 °C) were introduced into the glove box transfer chamber, which was evacuated and refilled with nitrogen three times. Subsequently the layers were left to cool down in the nitrogen filled transfer chamber. The remaining assembly of the DSSCs was performed in the glove box. The assembled and sealed cells were then studied outside the glove box under air. The taken measures have a large effect on the resulting cells. Unlike the cells produced in air with non-anhydrous solvents the water and oxygen free surrounding yields intensely coloured cells. Comparing the crocetin sensitised cells the efficiency could be markedly increased from 0.4 % to 1.0 % by improving the fabrication from single doctor-bladed layers of around 7 µm thickness prepared in air with dye solutions based on non-anhydrous solvents to preparation with the same layers in a nitrogen filled glove bag and solutions based on anhydrous solvents. A further increase in efficiency to a record value of 2.3 % was achieved by further improving the preparation and using screen-printed layers of 12 µm thickness and sensitisation in dye-solutions based on anhydrous solvents within the nitrogen environment of the glove-box. A set of IV-curves of crocetin sensitised DSSCs prepared by the first method in air and by the third in a glove box are shown in Fig. 3.18 with their parameters in Tab. 3.3.

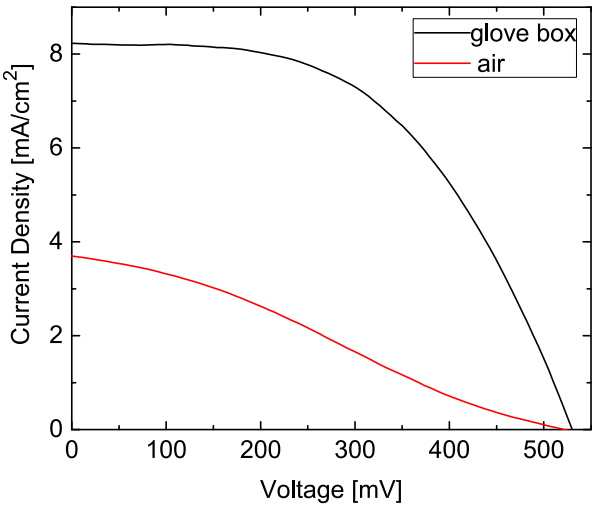

Figure 3.18.: *IV-curves of crocetin sensitised cells prepared in the glove box and in air. Parameters of the IV-curves are presented in Tab. 3.3*

Compared to efficiencies of 11 % and 12 % accomplished by cells sensitised with Ru-complexes and porphyrines respectively [131, 132] the efficiencies of our natural organic dyes are very low. However, compared to the previously published record efficiency of crocetin of 0.56 % [133] they are higher by a factor of 4 and thus promising. Even though the fabrication procedure of our cells was improved there is still lots of room for further improvements and adaptations. The utilised electrolyte was a very simple, easy to handle electrolyte based on the relatively non-volatile 3-metoxipropionitrile as solvent. For other dye-types far higher efficiencies have been reached by employing less viscous solvents such as acetonitrile-valeronitrile mixtures, which might also lead to an increased efficiency in our cells. Furthermore the electrolyte was neither tailored nor optimised for the organic dyes in terms of solvent, type and concentration of redox-molecules and additives. The same is true for the dye solutions, where different solvents, dye concentrations and sensitisation time and temperature could have an influence on the achieved cell efficiency. Also only few layer thicknesses and layer-structures were tested. The addition of a scattering layer, or of mixed layer structures including for example a transparent bottom layer of small titania nanoparticles ($d \approx 20\,\text{nm}$), a partly opaque middle layer of mixed small and large nanoparticles or aggregates of small particles as can be achieved by home-made particle pastes of particles produced by spray-pyrolysis (such as P25), and a scattering top-layer of larger particles ($d \approx 200\,\text{nm}$) might both bring further improvements of the cell-efficiency. Despite further possibilities for adaptation and optimisation of our crocetin sensitised cells it is to be assumed, that our organic

sensitisers will never reach the efficiencies achieved by other dyes. However they might be well suited for applications in which highest possible efficiency is not called for. Examples could be a partly transparent roof-tops of a store-house or industrial buildings. Other possible applications might be for design reasons, where their bright and intensive colours are appealing.

3.3. Nanoscale Examination of Surfaces

In the first two sections of this chapter the implementation of a fabrication procedure for reproducible DSSCs was presented. In the next section the instrumentation of the methods applied to investigate the topography and surface potential of the nanoporous layers will be described. Both AFM and KPFM measurements were performed with the same "Flex-AFM" microscope. The used microscope proved to be very sensitive to all kinds of external influences such as changes in the temperature, which expressed itself by a large drift between the tip and the sample not only in the xy-plane, but mainly in the z-direction. The drift could be decreased but not entirely suppressed by positioning of the microscope in an isolation chamber within an air-conditioned room and by allowing long acclimatisation times of multiple hours after having opened the isolation-chamber. In the first part of this section the microscope, the used cantilevers and measurement cell are described. In the second part the instrumentation of the different KPFM-modes is explained.

3.3.1. AFM Measurements

AFM measurements were performed on a Flex-AFM equipped with a 100 µm scan-head and a new PSD with a bandwidth of 3 MHz. Measurements were performed using a Liquid/Air cantilever holder. The Flex-AFM was placed in an acoustic enclosure box (AES300) on a Nanosurf Isostage vibration isolation device (all Nanosurf AG, CH-4410 Liestal, Switzerland) in a air conditioned room. The Flex-AFM was controlled by Nanonis-control electronics (Nanonis RC4 with two Nanonis OC4 Oscillation controllers) in combination with the Nanonis software via a home-built signal-adaptor box. Two different kinds of platinum-iridium coated cantilevers were used (PPP-EFM, nominal resonance frequency in air: 75 kHz, and PPP-NCL-Pt, nominal resonance frequency in air: 190 kHz, both from NanoAndMore GmbH, De-35578 Wetzlar, Germany). Upon immersion into water the resonance frequencies diminished to around 45 % of the nominal

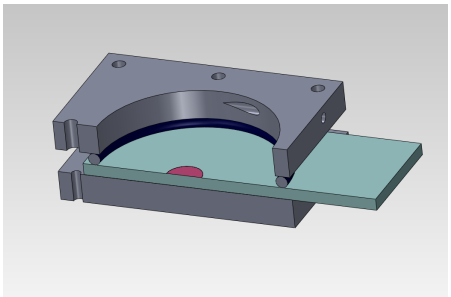

Figure 3.19.: *Outline of the liquid cell used for the KPFM measurements with a DSSC titania layer mounted for examination. The glass substrate forms part of the liquid cell and protrudes on the side, enabling easy electrical contacting outside the electrolyte.*

resonance frequency in air resulting in the following fundamental resonance frequencies in liquid: $f_{1-EFM-liquid} \approx 34\,\text{kHz}$ and $f_{1-NCL-liquid} \approx 78\,\text{kHz}$, respectively. The second resonance frequencies of the cantilevers was found at around $f_2 \approx 6.3 * f_1$ and thus resulting in frequencies of $f_{2-EFM-liquid} \approx 212\,\text{kHz}$ and $f_{2-NCL-liquid} \approx 478\,\text{kHz}$ for the measurements in liquids. All topography measurements were performed in AM-AFM mode (tapping-mode) with shaking-piezo excitation of the cantilever at its first resonance frequency, with amplitudes of the oscillation at the first resonance frequency in the range of $A_{1\text{st}}$=1 to 25 nm. All samples were introduced in a home-made liquid cell outlined in Fig. 3.19.

Therein the sample is fixed to the cell in a sandwich structure. The backplate acts as bottom, while the top plate has a hole into which the liquid is introduced, and into which the cantilever holder of the microscope can be lowered to reach the sample in the bottom. A viton-O-ring applied between sample and top-plate ensured a tight sealing of the reservoir. In order to ensure electrical contact the samples were mounted onto FTO glass by means of silver paint or a conductive epoxy. Titania layers for DSSC samples were directly printed on the glass. The glass was designed in a way for it to protrude from the cell such as to easily enable electrical contact without contact of the contact strip and the electrolytes.

3.3.2. KPFM Measurements

KPFM measurements were performed on the Flex-AFM-system described in Sec. 3.3.1. All necessary potentials (V_{ac} and V_{dc}) were applied to the sample while the tip was grounded.

Two different samples were used for the measurements. The first test-sample was a silicon-wafer on which gold and indium dots had been deposited. It will be denoted "AuIn-sample". The two metals were deposited by evaporation and were deposited through the same stencil. Since the deposition sources were mounted in slightly different places of the deposition chamber the resulting dots were not superimposed, but slightly shifted. In all the presented images of the "AuIn-sample" the gold dots are the low-left and the indium dots are the top-right dot. Due to the need of extensive cleaning of the "AuIn-sample" with aggressive agents such as hydrochloric acid, the indium dots were more and more dissolved. Thus in early images two kinds of dots are visible on the sample, while in later ones only small fragments of the indium-dots remain.

Secondly measurements were performed on titania layers deposited by the screen printing method as described in Sec. 3.1.4. They were made of home-made titania-pastes as described in Sec. 3.1.3 and were either non-sensitised or sensitised with N719.

3.3.3. Close-Loop Kelvin Probe Force Microscopy

Traditional CL-KPFM measurements were performed by excitation at the second resonance frequency of the cantilever by application of an ac-voltage to the sample. The resulting cantilever oscillation was detected by means of a lock-in amplifier tuned to the excitation frequency and the lock-in $X_{1\omega_{ac}}$-signal was nullified by the application of a dc-voltage by the Kelvin-controller integrated in the Nanonis software. The dc-voltage for the nullification was applied to the sample in addition to the ac-voltage. CL-KPFM measurements were performed in single-pass mode measuring the topography in AM-AFM mode using the fundamental cantilever resonance, and simultaneously measuring the CPD-signal using the second cantilever resonance. This implies a two lock-in system as the one used for this work.

3.3.4. Open-Loop Kelvin Probe Force Microscopy

OL-KPFM measurements were performed in half harmonic excitation mode as described by Guo et al. [57] and in Sec. 2.2.2, OL-KPFM being described by Kobayashi et al. [54]. The instrumentation and the setup was used as described in Secs. 3.3.3 and 3.3.1. For the measurement of $A_{1\omega_{ac}}$ the electrical excitation and the detection occurred at the second resonance frequency of the cantilever $f_{\text{ex-}1\omega_{ac}} = f_{\text{det-}1\omega_{ac}} = f_2$ ($F_{1\omega_{ac}}$-setting). For the measurement of $A_{2\omega_{ac}}$ the excitation frequency was intended to be set to half of

the second resonance ($f_{\text{ex-}2\omega_{\text{ac}}} = \frac{f_2}{2}$) and the detection to the second harmonic of the excitation ($f_{\text{det-}2\omega_{\text{ac}}} = 2 * f_{\text{ex-}2\omega_{\text{ac}}} = f_2$, $F_{2\omega_{\text{ac}}}$-setting). Since the maximum of the $A_{2\omega_{\text{ac}}}$ resonance peak did not always exactly correspond to half the frequency of the maximum of the $A_{1\omega_{\text{ac}}}$ resonance peak, the excitation frequency for the $A_{2\omega_{\text{ac}}}$ measurement was independently determined and thus the basic conditions of the $F_{2\omega_{\text{ac}}}$-setting changed to $f_{\text{ex-}2\omega_{\text{ac}}} \approx \frac{f_2}{2}$ and $f_{\text{det-}2\omega_{\text{ac}}} = 2 * f_{\text{ex-}2\omega_{\text{ac}}} \approx f_2$. The OL-KPFM measurements were performed in two-pass mode. Every line of the SPM image was scanned twice forward and backward. In the first pass the signals at the first harmonic of the excitation (thus in $F_{1\omega_{\text{ac}}}$-setting) and in the second pass the signals at the second harmonic of the excitation (thus in $F_{2\omega_{\text{ac}}}$-setting) were detected with the second PLL. These signals consist of $A_{1\omega_{\text{ac}}}$ and $A_{2\omega_{\text{ac}}}$, but also of the corresponding phase-signals. Simultaneously the topography was always measured using the first PLL locked to the first resonance frequency of the cantilever. Thereby a constant tip-sample separation during the KPFM measurements was accomplished. Combined OL- and CL-KPFM measurements were performed in three-pass mode, where the OL-KPFM measurement was performed on the first two, and the CL-KPFM on the third pass respectively. In order to use the multi-pass functionality provided by the Nanonis software to perform the OL-KPFM-measurements a Labview software controlling the settings of the lock-in during the multi-pass scanning was written. It is outlined and explained in Appendix C.2

Excitation Voltage Spectroscopy

While the measurement of correct data is desirable, the applicability of the used model needs to be proved. The derivation of Eq. 2.22 and thus the calculation of the CPD_{OL} is based on the model of the tip and sample forming a plate capacitor, and the fact that in that case the electrostatic force consists of the spectral components $F_{1\omega_{\text{ac}}}$ and $F_{2\omega_{\text{ac}}}$ described in Eqs. 2.17 and 2.18. Therefore, the applicability of the model is shown by a linear and quadratic V_{ac} dependence of the oscillation amplitudes induced by the corresponding spectral force components ($A_{1\omega_{\text{ac}}}$ and $A_{2\omega_{\text{ac}}}$ respectively). In order to show this dependence, spectroscopy measurements of the oscillation amplitude depending on the excitation voltage were performed in $F_{1\omega_{\text{ac}}}$-setting and $F_{2\omega_{\text{ac}}}$-setting. The data of these V_{ac}-spectroscopies was recorded by sweeping of the V_{ac} twice while recording $A_{1\omega_{\text{ac}}}$ during the first and $A_{2\omega_{\text{ac}}}$ during the second sweep. The sweep-range of the V_{ac} was set to -3 to 3 V or to -5 to 5 V depending on the surrounding and the measured effects. In order to determine the dependence and prove the applicability of the assumed model the

measured data was performed fitted with a non-linear function of the form $A = m \cdot V_{\mathrm{ac}}^{n} + o$ with $A = A_{1\omega_{\mathrm{ac}}}$ or $A_{2\omega_{\mathrm{ac}}}$, and where m, n, o are fitting parameters as shown in Eq. 2.23.

All the CPD(V_{ac}) spectra presented in this work, show the absolute of the CPD. The polarity of the CPD is shown by the CPD-images recorded on the different samples in the different environments and at different settings.

3.4. Measurement Environments

Measurements were performed in different environments, namely in air, water (MilliQ with a Resistance of $R_{\mathrm{H_2O}} \geqslant 18\,\mathrm{M\Omega}$), in two salt solutions of different concentrations in MilliQ water (c_{NaCl} =1 and 10 mM), and in a simplified DSSC electrolyte, also of different concentrations. The simplified electrolyte is based on the standard electrolyte described in Sec. 3.1.1. However, it was fabricated containing only the solvent and redox-molecules. All additional ingredients, namely the methylbenzimidazole, were discarded in order to keep the system as simple as possible. Compared to normal cell conditions the electrolyte was used diluted by factors of $\frac{1}{10}$ and $\frac{1}{100}$. The compositions and resulting concentrations of the used electrolytes are given in table 3.4.

Table 3.4.: *Concentrations of redox molecules in the simplified electrolytes diluted by factors of $\frac{1}{10}$ and $\frac{1}{100}$ from the standard electrolyte employed in DSSC fabrication and the salt solutions. Throughout this thesis the electrolytes will be denoted as in this table. The concentration of I_3^- is estimated. Since the reaction $\mathrm{I_2} + \mathrm{I^-} \rightleftharpoons \mathrm{I_3^-}$ has a reaction constant of $k = 6.76\,\mathrm{l/mol}$ a nearly complete conversion of I_2 to I_3^- can be assumed [134] and the introduced concentration of I_2 was used as tri-iodide concentration.*

Electrolyte:	El10	El100	NaCl10	NaCl1
LiI	50 mM	5 mM	-	-
$\mathrm{I_3^-}$	5 mM	0.5 mM	-	-
NaCl	-	-	10 mM	1 mM

4. Results and Discussion

In the previous two chapters the background information for the understanding of the working principle of dye sensitised solar cell and the implementation of solar cell fabrication was provided. The structures and processes found in a DSSC were pointed out and explained. In this chapter the results and findings of the KPFM measurements are presented and discussed. In the text only a selection of the recorded data is presented and the size of the images is limited. Larger scale images and full data sets of all the measurements can be found in Appendix B.

Open loop KPFM measurements in half harmonic excitation mode as described by Guo et al. [57] and explained in Secs. 3.3.4 and 2.2.2 were performed on the "AuIn-sample" and on bare as well as sensitised (N719) titania layers in air, water, salt solutions (1 mM and 10 mM) and in two diluted DSSC-electrolytes (dilution factors 100 and 10). In air perfect measurements with a high resolution were performed in both CL-KPFM and OL-KPFM-mode, which are presented, compared and discussed in the first section of this chapter. They will not only verify the applicability of the assumed plate capacitor model for the tip-sample system in air, but will also confirm the independence of the OL-KPFM-mode from capacitative cross-talk and thereby recommend it for application in systems suffering thereof.

The data measured in ultra-pure water is presented and discussed in the second section of this chapter. The CL-KPFM-mode can not be employed in polarisable liquids or electrolyte due to the necessity of the application of a dc-voltage. Therefore, no direct comparison of data recorded in the two modes is possible. However the data recorded in water is compared to the data recorded in air and also in water it is shown that the application of the chosen model is justified.

The third section presents the data recorded in the salt solutions on the "AuIn-sample". While in air and water the excitation voltage independence of the CPD warrants the treatment of the tip and sample as an ideal plate capacitor, even in weak salt solutions this is not the case anymore. Therefore possible explanations for the non-linear behaviour

of the system are discussed and it is assigned to the movement of the ions in the solution between the tip and the sample, and to Electrostatic Double Layers (EDLs) which are formed on the surface of both the sample and the cantilever and thereby screen the electrostatic forces. The non-linearity affects mainly the $F_{2\omega_{ac}}$, which is much smaller in the salt solutions compared to water and air. This is also expressed by a missing contrast in the $A_{2\omega_{ac}}$-images. The $F_{1\omega_{ac}}$ on the other hand is less affected which is expressed by the missing diminution of $A_{1\omega_{ac}}$ and the still present contrast in the $A_{1\omega_{ac}}$-images. This enables a qualitative interpretation of the measured data which can be used to discern areas of different CPD on a sample.

The fourth section focuses on the measurements performed in diluted DSSC-electrolytes on bare and sensitised titania layers. The same non-linear effects already encountered in the salt solutions are observed. However more qualitative information can be gained from the recorded data, since bare and sensitised layers were measured in the same environment and can therefore be compared. The comparison confirms the dipole orientation of N719 bound to titania proposed by Henning et al. based on measurements performed in a nitrogen-environment [38]. Thereby the measured data indicates a conservation of the general structure of the dye-titania system and its prevailing dipoles upon immersion in the electrolyte and thus the possibility to transfer findings made on titania layers to entire DSSCs.

4.1. Open Loop Kelvin Probe Force Microscopy in air

In order to introduce the OL-KPFM technique in our lab measurements in air were performed to test the setup, the implementation and the technique. When measuring in air OL- and CL-KPFM measurements were always performed in a combined measurement, thereby enabling the comparison of the “calculated” and the “measured” CPD data. Complete measurement data sets consisting of topography data with amplitude-data as error signal to the topography, $A_{1\omega_{ac}}$- and $A_{2\omega_{ac}}$-data sets and the $\mathrm{CPD_{CL}}$ and $\mathrm{CPD_{OL}}$ are shown for a bare titania layer in Fig. 4.1. A corresponding data set measured on the “AuIn-sample” is shown in Fig. 4.4.

Even though at a first glance it could be assumed that Fig. 4.1 resolves the single nanoparticles of the titania layer, this is not the case. The particles visible in the images have diameters of around 200 nm. Thus they are around 10 × bigger than the expected

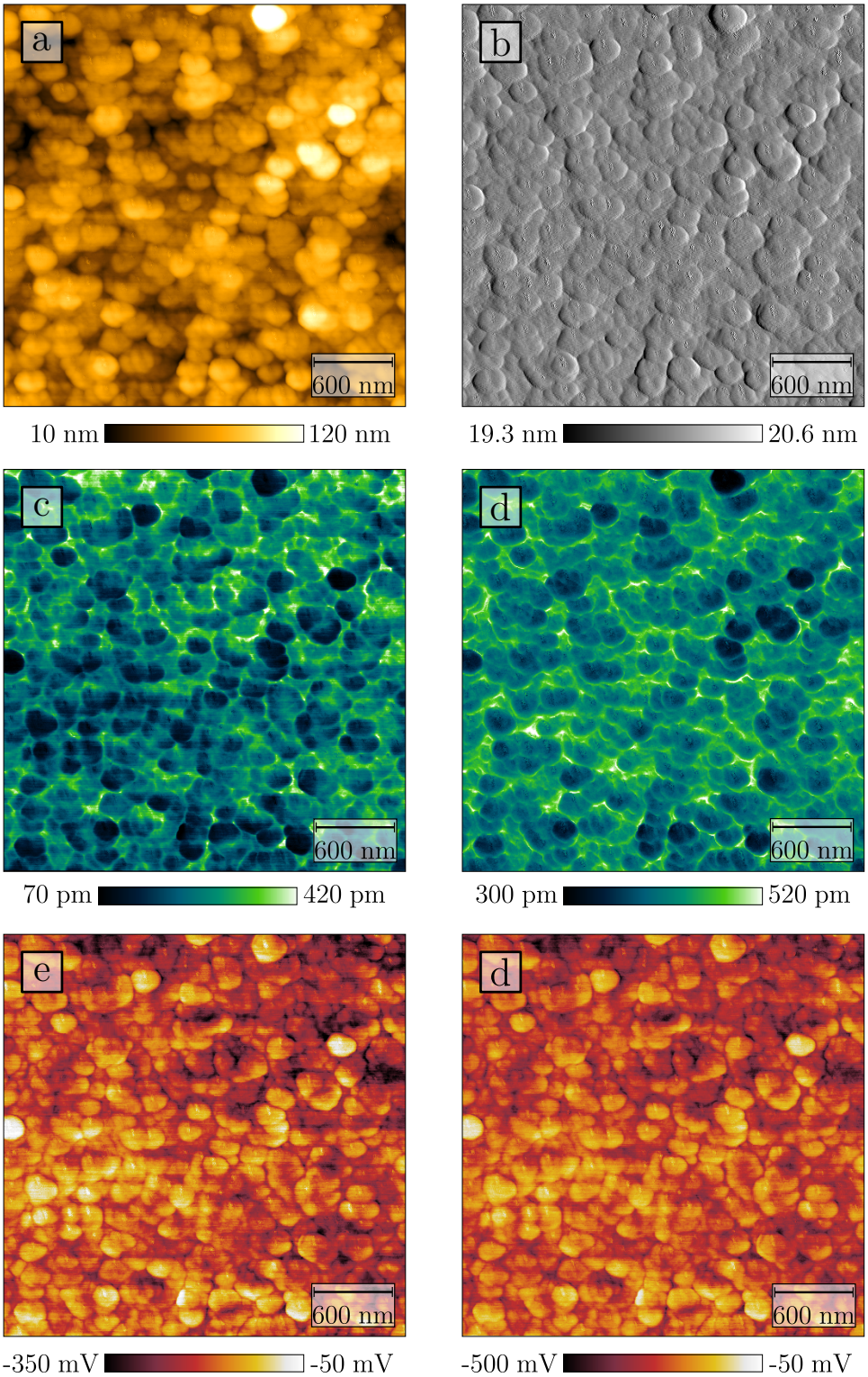

Figure 4.1.: *The full data set of a representative measurement performed on a bare titania layer in air with an PPP-NCL-Pt-cantilever. Signals are: a) Topography, b) A_{1st}, c) $A_{1\omega_{ac}}$, d) $A_{2\omega_{ac}}$, e) CPD_{CL}, f) CPD_{OL}. Scan Parameters: $f_{1st} = 149\,\mathrm{kHz}$; $A_{1st} = 20\,\mathrm{nm}$; $f_{2nd} = 9309\,\mathrm{kHz}$; $V_{ac} = 2\,\mathrm{V}$.*

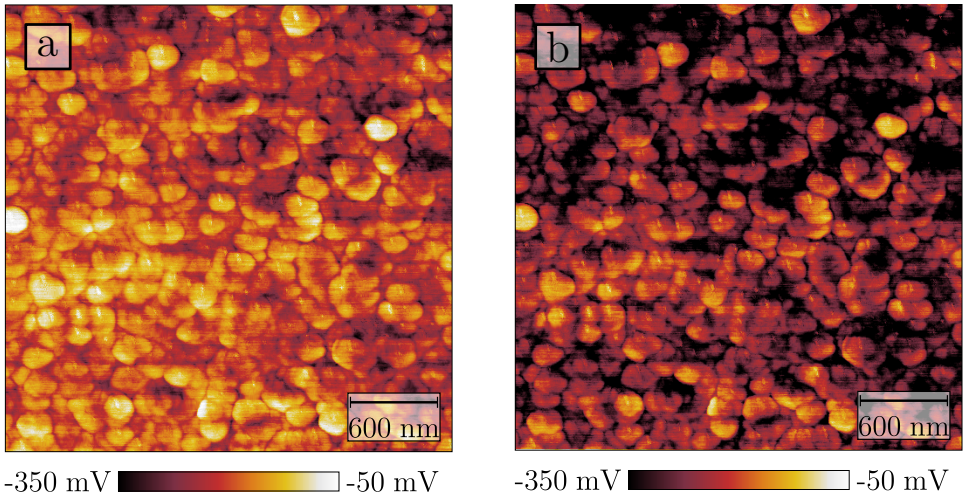

Figure 4.2.: *The same CPD_{CL} (a) and CPD_{OL} -data (b) as shown in Fig. 4.1 but with equal scales. A shift of the CPD_{CL} to higher CPDs is obvious.*

particle size. Probably the image shows aggregates of particles. This assumption is supported by smaller, roundish structures visible on the aggregates at close inspection of the data. The amplitude of the first resonance oscillation (shown in grey) is the error signal of the topography, since the z-control is set in a way to keep the amplitude constant. It should therefore show as little variation as possible. Compared to measurements performed on nearly perfectly flat samples, the amplitude variation on the titania layer samples is rather large. However this is not due to wrong controller-settings, but mainly due to the roughness of the sample, especially at large scan-ranges where not only the single nanoparticles but also particle-aggregates and the general porous structure of the layer shape the surface.

Since the CPD_{OL} and the CPD_{CL} measurements were performed combined, the tip had the same properties and the same work function for both, therefore a relative comparison of the data is directly possible. The two CPD-measurements look very similar, many details in the data are similarly present in both data sets. The CPD_{CL} is shifted towards higher CPDs compared with the CPD_{OL} by 78 mV, as can be observed in Fig. 4.2. This shift is assigned to capacitative cross-talk influencing the measurements in closed-loop mode only, as will be explained in the next paragraph. These results show that the setup works as intended and even highlight the desirable independence of cross-talk by the open-loop mode.

Shifts between the CPD_{OL} and the CPD_{CL} can occur even if the model is accurate due to an error introduced into the CL-KPFM measurement by capacitative cross-talk as

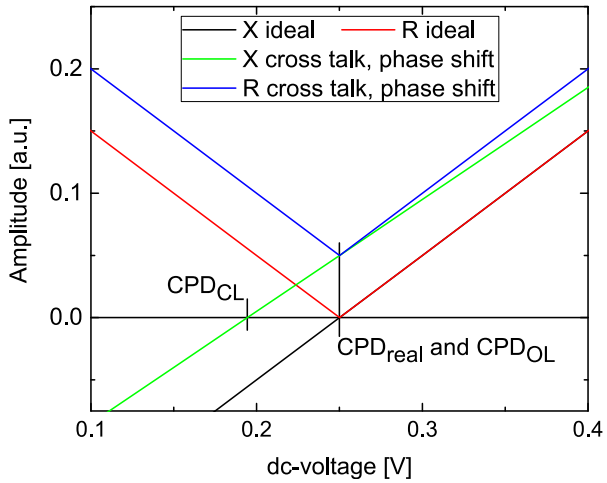

Figure 4.3.: *An outline of the theoretical lock-in amplifier signals of $A_{1\omega_{ac}}(V_{dc})$-curves on a substrate with $V_{CPD} = 250\,\mathrm{mV}$. The introduced vertical shift of 50 au of the blue/green curves describes the effect of capacitative cross-talk and the introduced phase shift of $\approx 26^{\circ}$ induces the shift between the blue (X) and the green (R) curve at $V_{dc} > V_{CPD}$. Both do not change the minimum of the amplitude-curve (R), but shift the zero crossing of the corresponding X-curve by 56 mV. 50 mV are due to the capacitative cross-talk and 6 mV due to the phase shift.*

described by Diesinger et al [135]. Capacitative cross-talk is the evocation of a cantilever oscillation by the excitation ac-voltage directly, and not by the F_{es}. It is therefore also present when the CPD is zero. Therefore it induces a non-zero $A_{1\omega_{\mathrm{ac}}}$ when the CPD is zero and $A_{1\omega_{\mathrm{ac}}}$ should be zero. When performing a sweep of the applied dc-voltage around the CPD the resulting curve shows a $\bigvee$-shape with its point at zero, thus on the x-axis. Capacitative crosstalk leads to a vertical shift of said curve away from the x-axis, as is shown in Fig. 4.3. The minimum of said $A_{1\omega_{\mathrm{ac}}}$ curve is still at $V_{\mathrm{dc}} = V_{\mathrm{CPD}}$. The reason for the falsification of the CPD measured in CL-KPFM is the working-principle of the lock-in amplifier and the Kelvin-controller. As explained in Sec. 2.2.2 the lock-in describes the measured amplitude by a point in a polar- and a cartesian coordinate system. In the first the relevant information to describe a point is the distance from the centre, and the angle to a defined direction, thus a radius (R) and a phase (ϕ). In the second a point is described by a set of X and Y coordinates which describe the distance from the centre in the direction of the defined x- and y-axes. Assuming orthogonal x- and y-axes and a correspondence of the polar axis with the cartesian x-axis the X and Y coordinates correspond to the projection of the amplitude onto the respective axis.

Thus a conversion is achieved by

$$X = R \cdot \cos(\phi) \tag{4.1}$$

$$Y = R \cdot \sin(\phi) \tag{4.2}$$

$$R = \sqrt{x^2 + y^2} \tag{4.3}$$

Assuming an ideal phase adjustment ϕ and thus y become zero and R corresponds to the absolute value of X, thus $R = |X|$. The spectral force component $F_{1\omega_{ac}}$ (Eq. 2.17) depends linearly on the CPD and the applied dc-voltage. Therefore the X signal shows the same linear dependence and its response to a sweep of the applied DC-bias is a straight. Hence the amplitude's response is the absolute of the straight and thus shows a $\bigvee$-shape. A straight is ideally suited as controlling signal for a PI-control-loop, since it has only one slope, while the absolute of the straight is not due to its changing slope, therefore the X signal is usually used as input for the Kelvin-controller. In the presence of capacitative cross-talk the minimum of the R signal and the zero-crossing of the X signal are not at the same dc-voltage and the zero-crossing of the X signal differs from V_{CPD}, as is outlined in Fig. 4.3. Since the X signal is used as input for the PI-controller this will induce an error in the measured CPD. The effect can be increased if capacitative cross-talk coincides with an improper phase adjust (if there is no capacitative cross-talk an improper phase adjust will not influence the value of the measured CPD, but only decrease the signal to noise ratio). The latter leads to a Y component which differs from zero and thus a discrepancy between the R and the X signal of the lock-in, which can increase the difference between the minimum of R and the zero-crossing of X. An outline illustrating said shift is shown in Fig. 4.3. Since OL-KPFM measurements do not rely on the X signal of the lock-in, the CPD determined in open-loop mode is not influenced by capacitative crosstalk and thus can be applied in systems suffering from capacitative cross-talk to determine an non-falsified CPD.

The measurement on the "AuIn-sample" are presented in Fig. 4.4. The structures and the image-size being much larger the images do not hold any information about the obtainable resolution. However, in the topography image small structures within- and on the borders of the dots are visible. The indium dots are the top-right ones of each dot-couple. They have a much rougher surface and show more structures, while the gold dots are smoother. The dirt particles in the top right corner of the image have a rather triangular shape. Whether they are really this triangular, or the apparent shape is an effect of the tip can only be guessed. Since the rest of the structures is not

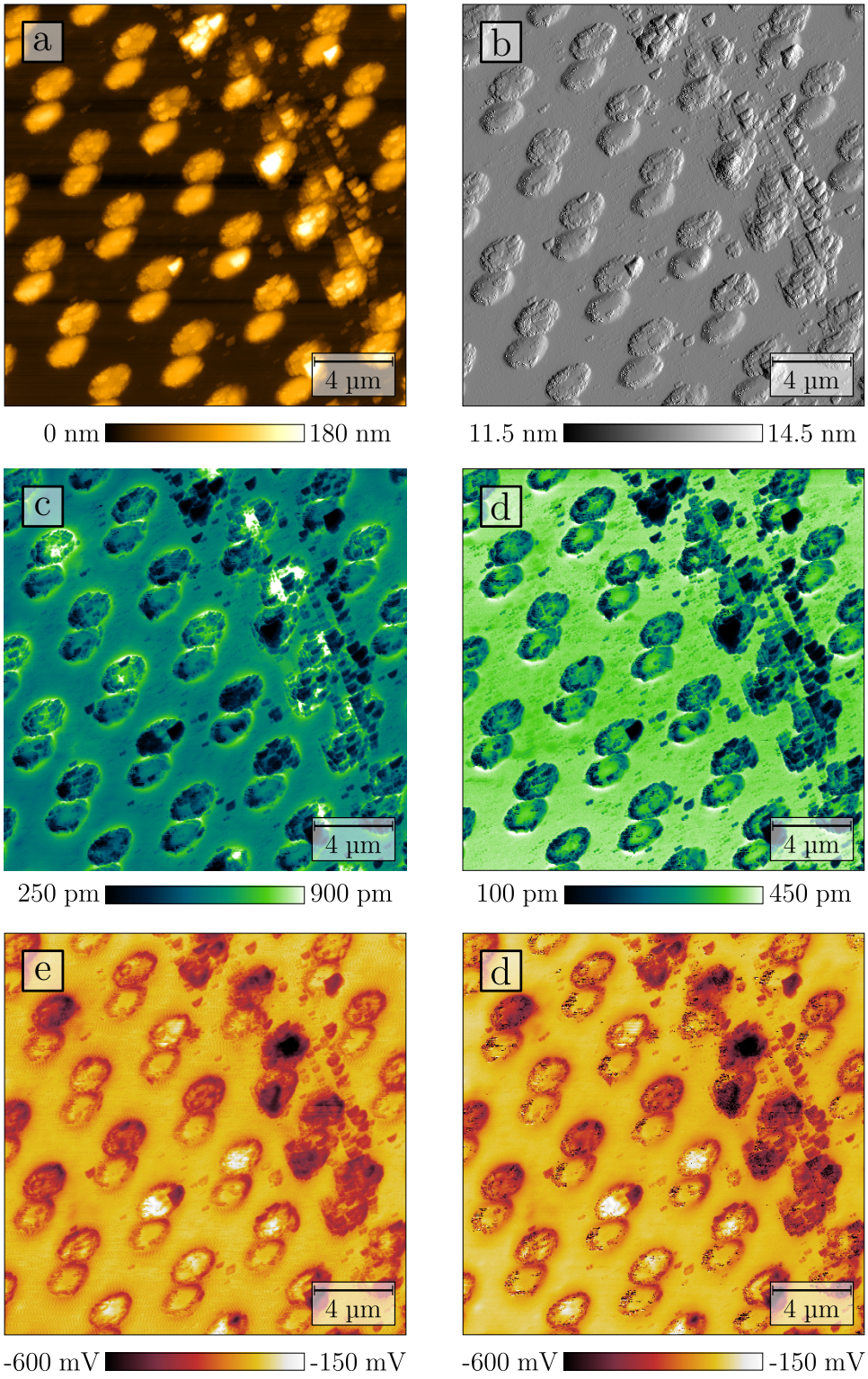

Figure 4.4.: *The full data set of a representative measurement of the "AuIn-sample" recorded in air with an EFM-cantilever. Signals are: a) Topography, b) A_{1st}, c) $A_{1\omega_{ac}}$, d) $A_{2\omega_{ac}}$, e) CPD_{CL}, f) CPD_{OL}. Scan Parameters: $f_{1st} = 76\,\mathrm{kHz}$; $A_{1st} = 13\,\mathrm{nm}$; $f_{2nd} = 477\,\mathrm{kHz}$; $V_{ac} = 700\,\mathrm{mV}$.*

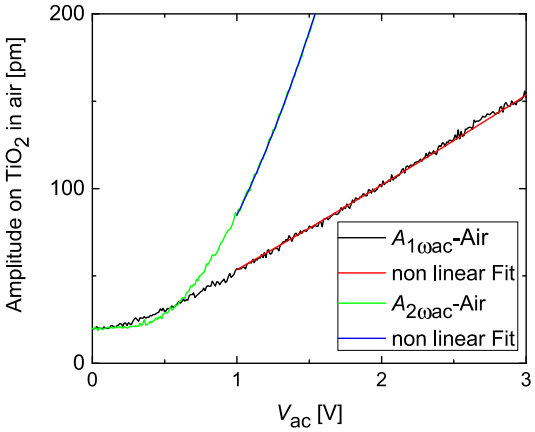

Figure 4.5.: *V_{ac}-spectroscopy data measured on TiO_2 with non-linear fits (Eq. 2.23). Scan Parameters: $f_{1st} = 149\,\mathrm{kHz}$; $A_{1st} = 24\,\mathrm{nm}$; $f_{2nd} = 930\,\mathrm{kHz}$; z-control off.*

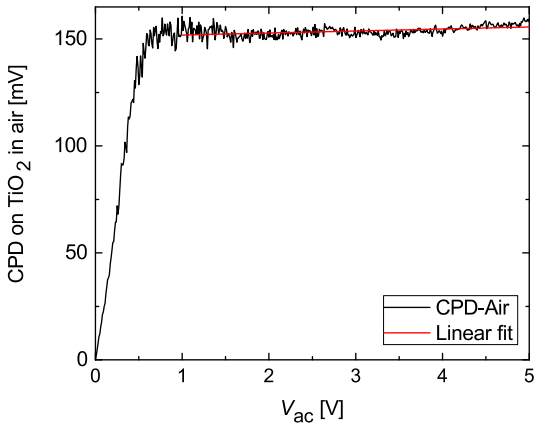

Figure 4.6.: *The CPD_{OL} calculated from the V_{ac}-spectroscopies recorded on TiO_2 in air with a linear fit to the data at $V_{ac} > 1\,\mathrm{V}$. Scan Parameters: $f_{1st} = 149\,\mathrm{kHz}$; $A_{1st} = 24\,\mathrm{nm}$; $f_{2nd} = 930\,\mathrm{kHz}$; z-control off*

triangular however they are assumed to have this curious shape. Both the $A_{1\omega_{\mathrm{ac}}}$- and $A_{2\omega_{\mathrm{ac}}}$-signals are very clear and show much contrasts. The structures are very similar to the topography. Even tough most of the structures show inverse behaviour (higher topography and lower $A_{1\omega_{\mathrm{ac}}}$- and $A_{2\omega_{\mathrm{ac}}}$ coincide) some of them do not, e.g. the indium dot near the top left corner of the image, which has a very large $A_{1\omega_{\mathrm{ac}}}$ but a rather even topography. The $\mathrm{CPD_{OL}}$ and the $\mathrm{CPD_{CL}}$ are in very good agreement. Not only the general contrast, but also the distribution of the values is nearly equal. The gold- and indium dots are expected to have CPDs differing from the silicon surface. This is the case for some of the indium dots, but the gold dots only show a different CPD at the borders while in the centre it matches the CPD of the silicon. The indium CPD seems rather random. In some cases it is higher- in others it is lower than the CPD of the silicon. Since this behaviour is equal in the closed loop and in the open loop data it can not be assigned to a defect in the measurement. The most probable explanation is a coverage of the surface with a rather even, thin layer of substance over the entire surface. Edges and steps are known to reduce the work function, which can also be observed at the borders of the islands, where the surface potential is reduced by approximately $90 \pm 10\,\mathrm{mV}$.

Data from V_{ac}-spectroscopy measurements performed on titania in air and the thereof calculated $\mathrm{CPD_{OL}}(V_{\mathrm{ac}})$ curve is shown in Figs. 4.5 and 4.6. All the $\mathrm{CPD}(V_{\mathrm{ac}})$ data presented in this work shows the absolute value of the measured CPD. Fitting of a non-linear function as shown in Eq. 2.23 to the $A_{1\omega_{\mathrm{ac}}}$- and $A_{2\omega_{\mathrm{ac}}}$-data respectively

Table 4.1.: *Overview over the important parameters from the fitting of the non linear function (Eq. 2.23) to the $A_{1\omega_{ac}}$- and $A_{2\omega_{ac}}$-signals of the V_{ac}-spectroscopy data measured on TiO_2 in the different environments.*

		bare Air	bare Water	bare El100	dyed El100	bare El10	dyed El10
$A_{1\omega_{ac}}$	Slope [pm/V]	41	25	54	26	107	92
$A_{1\omega_{ac}}$	**Exponent**	**1.12**	**1.10**	**0.92**	**0.96**	**1.01**	**0.98**
$A_{1\omega_{ac}}$	R^2	0.9993	0.9981	0.9996	0.9983	1.0000	0.9999
$A_{2\omega_{ac}}$	Slope [pm/V]	85	25	0.08	0.01	0.06	0.72
$A_{2\omega_{ac}}$	**Exponent**	**1.99**	**2.02**	**3.20**	**4.80**	**3.42**	**2.34**
$A_{2\omega_{ac}}$	R^2	1.0000	0.9997	0.8366	0.5200	0.8498	0.9672

shows good agreement at $|V_{ac}| > 0.5\,V$. The resulting exponents are $n_{1\omega_{ac}} = 1.12$ and $n_{2\omega_{ac}} = 1.99$. At excitation voltages closer to zero the response signal is larger than expected. This is especially obvious for the $A_{1\omega_{ac}}$-signal, where the thereto linear signal shows a marked levelling of the slope and assumes a roundish "$\bigcup$" shape as opposed to the expected pointed "$\bigvee$" shape. This is due to a decreased signal to noise ratio and thus "loosing" of the signal in the noise. Since the signal is detected by a lock-in amplifier and even the noise has a spectral component at the locked frequency the lock-in amplifier always detects a signal within the noise and thus the measured signal is never zero. This intercept differing from zero mainly determines the shape of the $CPD_{OL}(V_{ac})$ curve, which has a depression at small excitation voltages, a steep slope in the intermediate region, and is constant at $Vac > 700\,mV$. A linear fit to said data reveals a slope of only $0.94\,mV/V$ at a $CPD_{OL} \approx 150\,mV$. These values prove the proper working of our setup and the applicability of the chosen model to the titania system in air.

Similar results are true for the V_{ac}-spectroscopy on the "AuIn-sample" in air. The fitting parameters of the V_{ac}-spectroscopies performed in the different environments on titania and the "AuIn-sample" are shown in Tabs. 4.1 and 4.2 respectively. On the "AuIn-sample" the fitting to the data measured in air shows exponents even closer to the expected values, especially the $A_{1\omega_{ac}}$-signal is more linear.

As a short conclusion for the measurements performed in air it can be said, that the chosen model works well on both sample systems in air which supports the assumption that it is generally applicable on conducting and semi-conducting samples. For non-conducting samples or samples with a very low conductivity the applicability of the model

might need to be tested again. The assumed model of a plate capacitor in which the tip forms one plate and the sample the other depends on a conductive sample. It might not be applicable else since non-conductive samples can be assumed to behave (more) like a dielectric than like a capacitor plate, which would render the main assumption of the model untrue.

Summarising it can be said that by means of the measurements performed we can prove the working principle of the OL-KPFM technique in general and of the used setup in particular. The CPD of both titania layers and the "AuIn-sample" were determined and the open loop measurements yielded data with equal contrast, but more accurate CPD values due to its independence of capacitative cross-talk. This recommends the application of OL-KPFM in systems which suffer from capacitative cross-talk.

Table 4.2.: *Overview over the important parameters from the fitting of the non linear function (Eq. 2.23) to the $A_{1\omega_{ac}}$- and $A_{2\omega_{ac}}$-signals of the V_{ac}-spectroscopy data measured on the "AuIn-sample" in the different environments.*

		Air	NaCl1	NaCl10
$A_{1\omega_{\mathrm{ac}}}$	Slope [pm/V]	126	112	142
$A_{1\omega_{\mathrm{ac}}}$	**Exponent**	**0.98**	**1.20**	**1.20**
$A_{1\omega_{\mathrm{ac}}}$	R^2	0.9998	0.9999	0.9998
$A_{2\omega_{\mathrm{ac}}}$	Slope [pm/V]	46	13	5
$A_{2\omega_{\mathrm{ac}}}$	**Exponent**	**2.01**	**1.00**	**1.94**
$A_{2\omega_{\mathrm{ac}}}$	R^2	0.99994	0.99254	0.99279

4.2. Open Loop Kelvin Probe Force Microscopy in water

Open Loop Kelvin Probe Force Microscopy measurements and V_{ac}-spectroscopies of $A_{1\omega_{\mathrm{ac}}}$ and $A_{2\omega_{\mathrm{ac}}}$ on titania layers were performed in ultra-pure water. In water no reference in terms of the CPD-polarity exists, since no $\mathrm{CPD_{CL}}$ can be measured. Therefore the contrast of the $\mathrm{CPD_{OL}}$ was compared to the CPD contrast of a similar sample measured in air and the polarity was calculated by Eq. 2.29 which yields a contrast of the same polarity.

Figure 4.7 shows a topography and a CPD image of an OL-KPFM measurement of a titania layer in water. The measurement shows the same nanoparticle aggregates visible in air. At the top border of the image the particle-aggregates look somewhat stretched.

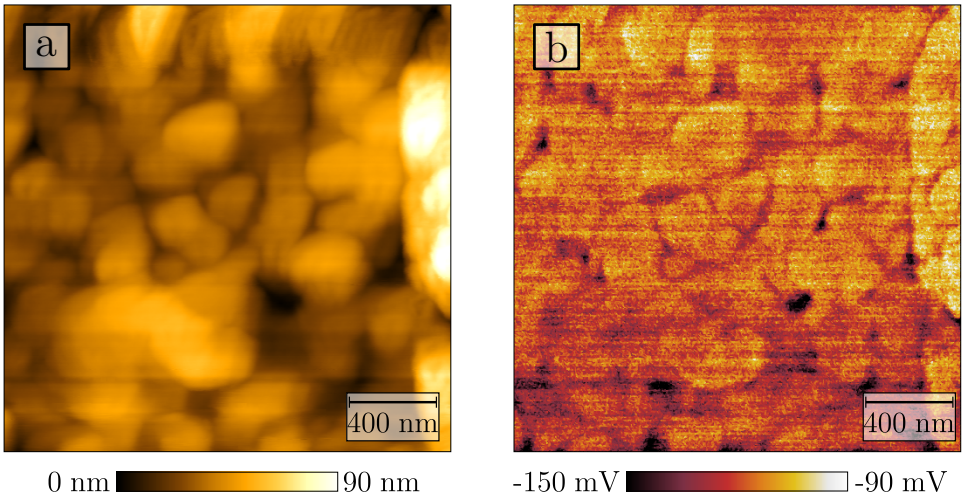

Figure 4.7.: *Data measured on a titania sample in water. a) Topography, b) CPD_{OL}. Scan Parameters: $f_{1st} = 74\,\text{kHz}$; $A_{1st} = 1\,\text{nm}$; $f_{2nd} = 487\,\text{kHz}$; $V_{ac} = 3\,\text{V}$*

This is due to a drift between tip and sample. The recorded CPD is comparable to the data measured in air in magnitude. The distribution of the CPD values is significantly narrower in water. This might be due to different samples, but also due to a shielding of the surface by the water molecules which form an electronic double layer on the surface, due to water molecules adsorbed onto the titania or since molecules are adsorbed everywhere to the titania and not only in some places. The V_{ac}-spectroscopy measurements recorded in water show similar trends as the ones recorded in air. The fitting of a non-linear function as presented in Eq. 2.23 yields perfect fit-results. The yielded exponents are in close but not in perfect agreement with the expectations, as shown in Tabs. 4.1 and 4.2.

The CPD(V_{ac}) spectra on titania (Fig. 4.8) in water show a perfect curve with a steep slope at an excitation close to zero followed by a plateau of nearly perfectly excitation independent CPD at excitations between 1 and 3 V. The curves in air and water show a nearly identical general shape, excluding the plateau-height coming from the different CPD due to the changed cantilever, and possibly effects of adsorption of molecules and screening by the water layer. The only difference is the length of the steep slope. While in air the plateau is reached at around $V_{\text{ac}} = 0.7\,\text{V}$, in water the steep slope continues up to $V_{\text{ac}} \approx 1.1\,\text{V}$ thereby reaching the CPD of $\approx 300\,\text{mV}$ compared to $\approx 150\,\text{mV}$ measured on TiO_2 in air with a different cantilever.

Concluding it can be said, that the model holds true not only for measurements in air but also in water. Perfect CPD data can be recorded by the open loop technique and

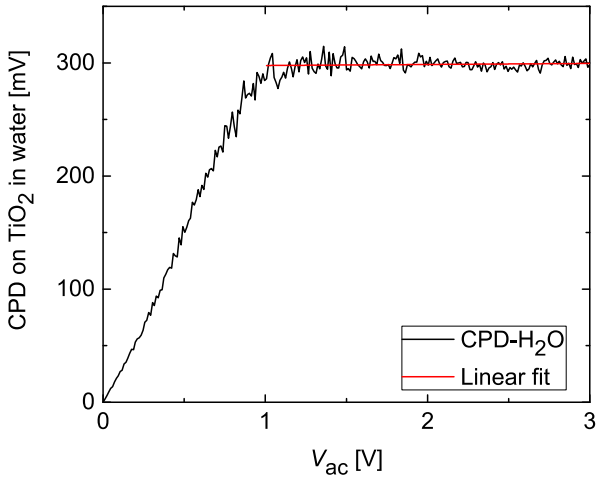

Figure 4.8.: *$CPD_{OL}(V_{ac})$ determined from V_{ac}-spectroscopies measured on titania in water, with a linear fit at $V_{ac} > 1\,\mathrm{V}$. Scan Parameters: $f_{1st} = 74\,\mathrm{kHz}$; $A_{1st} = 1\,\mathrm{nm}$; $f_{2nd} = 487\,\mathrm{kHz}$; z-control off*

the results seem not to be influenced by the water. High resolutions are more difficult to obtain in a liquid environment due to the reduced Q-factor, especially in a system with piezo-excitation. Also the setup is appropriate to measure CPD data not only in air, but also in water. The measurements show that the recording of excellent data with high resolution in terms of CPD and topography becomes even more demanding. This includes the requirements posed on the measurement setup which not only needs to be built for measurements in liquid environments and possibly aggressive solvents, but ideally includes an oscillation excitation such as photo-thermal excitation in order to achieve high quality-factors despite the liquid surroundings. The determination of work function data from the measured CPD is depending on the availability of secured work function data which can be used as references to calibrate the tip. The work function being defined as the energy necessary to bring an electron from a material to the vacuum in close proximity of the sample surface, a work function measurement in a non-vacuum environment is somewhat inordinate. However, we will treat the measured data as an "apparent" work function keeping in mind, that we are measuring a kind of difference in Fermi levels between tip and sample or between two systems consisting of the tip and adsorbates from the electrolyte on the tip surface on one hand, of the sample and adsorbates from the electrolyte on its surface on the other hand, and a connecting layer of electrolyte between the two systems.

4.3. Open Loop Kelvin Probe Force Microscopy in NaCl-solution

OL-KPFM- and V_{ac}-spectroscopy measurements on the "AuIn-sample" were performed in two aqueous NaCl solutions of different salt concentrations, namely 1 mM and 10 mM. The measurements showed a strong dependence of the measured CPD on the applied V_{ac} with increasing excitation voltages leading to increasing CPD_{OL}-values. The effect was studied by Umeda et al. and Collins et al. [136–138] who identified ion diffusion, voltage division at the inner-most layer of ions, and surface stress originating in a voltage drop over the electronic double layer surrounding the cantilever (but not the one surrounding the sample) as possible reasons.

4.3.1. Low concentration salt solution

Measurements on the "AuIn-sample" in 1 mM NaCl were performed at different excitation voltages, namely 1 and 2 V. Two are shown in Figs. 4.9a and 4.9b.

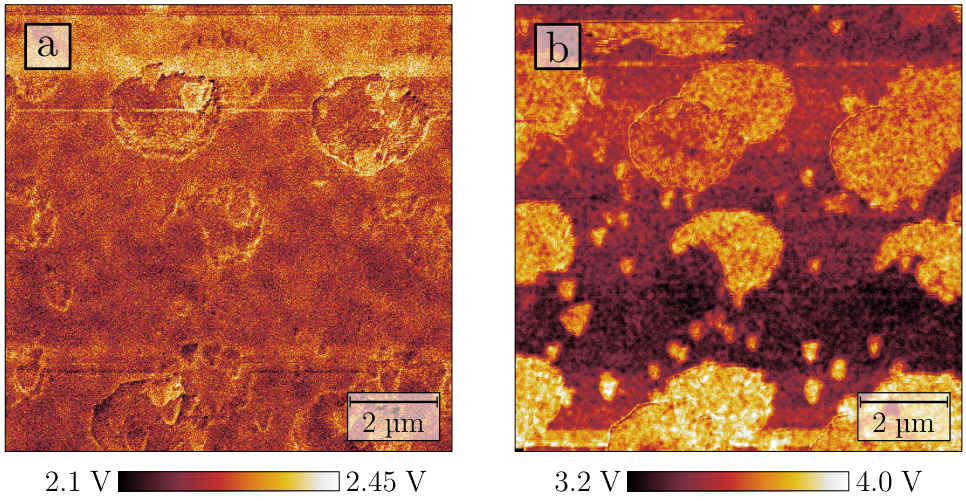

Figure 4.9.: *CPD_{OL}-images recorded on the "AuIn-sample" in* 1 mM *NaCl solution with different excitation voltages. a) $V_{ac} = 1$ V, b) $V_{ac} = 2$ V.*
Scan Parameters: $f_{1st} = 75$ kHz; $A_{1st} = 14$ nm; $f_{2nd} = 496$ kHz; $V_{ac} = 1$ and 2 V.

The calculation of the CPD proved strange. In order to receive $CPD_{Gold} > CPD_{background}$ at an excitation voltage of $V_{ac} = 2$ V the CPD_{OL} needs to be calculated by Eq. 2.28 and is positive. At an excitation voltage of $V_{ac} = 1$ V the CPD of the gold is very similar to the one of the background and sometimes even changes from being lower to being

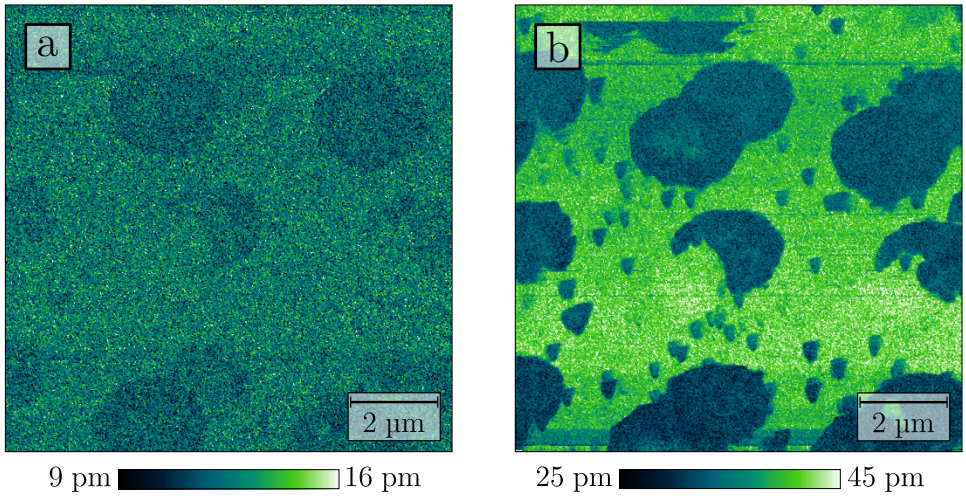

Figure 4.10.: *$A_{2\omega_{ac}}$-images recorded on the "AuIn-sample" in* 1 mM *NaCl solution with different excitation voltages. a)* $V_{ac} = 1\,\mathrm{V}$*, b)* $V_{ac} = 2\,\mathrm{V}$*.*
Scan Parameters: $f_{1st} = 75\,\mathrm{kHz}$; $A_{1st} = 14\,\mathrm{nm}$; $f_{2nd} = 496\,\mathrm{kHz}$; $V_{ac} = 1$ *and* $2\,\mathrm{V}$*.*

higher. If it is calculated in a way that it is generally larger it needs to be calculated by Eq. 2.29 and the CPD of the entire measurement is negative. Since the images were recorded consecutively and the only change was the excitation voltage (same cantilever, same frequencies, same electrolyte, same sample and position, not even the box enclosing the microscope was opened) this change in CPD-polarity could only be explained if a particle got stuck to the cantilever tip thereby changing its work function. However this would have been visible in the image as a sudden change of signal (not only in CPD but also in topography). Comparing the two $A_{2\omega_{\mathrm{ac}}}$-signals, which are shown in Fig. 4.10, leads to a second explanation. While the $A_{2\omega_{\mathrm{ac}}}$-signal recorded at an excitation voltage of 1 V is mainly noise and shows only a very small amount of contrast, the $A_{2\omega_{\mathrm{ac}}}$-signal recorded at $V_{\mathrm{ac}} = 2\,\mathrm{V}$ shows a very clear contrast between gold and background with gold having lower amplitudes than silicon. Upon calculation of the CPD this lower amplitude in the denominator leads to a higher CPD. This discrepancy is visible in the recorded $A_{2\omega_{\mathrm{ac}}}(V_{\mathrm{ac}})$ spectra whose parabolic shape is distorted and has a much flatter bottom than the ones recorded in air. Overall $A_{2\omega_{\mathrm{ac}}}$ in the salt solution is very small compared to $A_{2\omega_{\mathrm{ac}}}$ in water and air.

The fitting of the spectroscopy data yields interesting results. If fitting is performed in the same excitation voltage range (1 to 3 V) as for the previous measurements which were performed in air and water, the $A_{2\omega_{\mathrm{ac}}}$-signal shows a perfectly linear behaviour. If fitting is performed at lower excitation voltages (0 to 2 V) the fitting yields an exponent

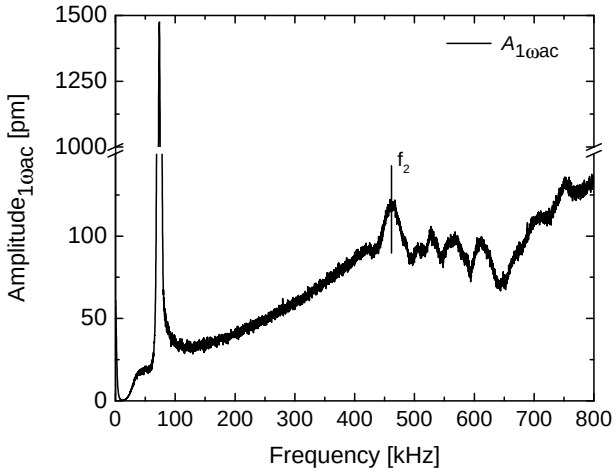

Figure 4.11.: *$A_{1\omega_{ac}}$ recorded against the excitation frequency ($A_{1\omega_{ac}}(1\omega_{ac})$) at an electrostatic excitation of $V_{ac} = 500\,\mathrm{mV}$. Additional mechanical excitation at f_1. The high pass filter was set to a cut-off frequency of 30 kHz explaining the dip of the signal at lower frequencies.*

of 2.59 and in the full range of the measurement (0 to 3 V) the fitted exponent is 1.76. The slope of the $A_{2\omega_{\mathrm{ac}}}$-signal as determined by the non-linear fit in the voltage range from 1 to 3 V is lower by a factor of ≈ 2 compared with the slopes of the same signal measured in air and water. This decrease of the slope is not only a sign of a higher CPD, but also shifts the plateau of CPD-independence to higher excitation voltages and thus possibly out of the measurement range.

These results indicate, that the present setup is not ideally suited for KPFM measurements in electrolyte solutions, even if the electrolyte concentration is as low as 1 mM. The linear dependence of $A_{2\omega_{\mathrm{ac}}}$ on V_{ac} disagrees with the applied model, which requires a quadratic dependence. Reasons for this are probably to be found in the formation of electrical double-layers, electrochemical reactions and rearrangement of ions in the liquid and on the sample and the tip. It was however expected, that their influence would be negligible at such low concentrations and with the use of the present setup, since Kobayashi et al. state that the spurious forces in low concentration electrolytes in their system interfere only at frequencies below 30 kHz [55]. In reference [56] the same authors show the spurious forces by conducting a frequency sweep in $F_{1\omega_{\mathrm{ac}}}$-setting- and $F_{2\omega_{\mathrm{ac}}}$-setting, in which the amplitudes are very visibly enhanced due to said forces upon excitation of the oscillation by a ac-voltage at low frequencies. Therein the authors claim their presence at f_{ex} below $f_{\mathrm{ex}} = 50\,\mathrm{kHz}$ and $f_{\mathrm{ex}} = 300\,\mathrm{kHz}$ for 1 and 10 mM salt solutions respectively. In our own frequency sweeps we did not observe this effect. A representative frequency sweep in 10 mM salt solution with an electrostatic excitation

of $V_{ac} = 500\,mV$ performed in $F_{1\omega_{ac}}$-setting is shown in Fig. 4.11. The graph shows the first resonance at 73 kHz which was additionally excited mechanically by the shaking piezo, and the second resonance at 464 kHz but no enhanced amplitude due to spurious forces at low frequencies. If the spurious forces were present at very low frequencies $f_{ex} < 30\,kHz$ they were filtered by the high pass filter, whose lowest setting was said frequency. If they were present in the range from 30 to 100 kHz they were overlaid by the first mechanical cantilever resonance located around 75 kHz. Kobayashi et al. further show the possibility of OL-KPFM measurements at concentrations up to 1 mM at modulation frequencies as low as $f_{ex} = 30\,kHz$ and in solutions of 10 mM at modulation frequencies of $f_{ex} \approx 600\,kHz$. Thus it was expected that the measurements in both environments should also be possible in our setup.

While Kobayashi et al. focus on OL-KPFM [54–56], Gramse et al. study Dynamic Electrostatic Force Microscopy (DEFM) in electrolyte solutions and the critical frequency below which the examination of $F_{1\omega_{ac}}$ by means of the measurement of $A_{1\omega_{ac}}$ is impeded by the effects of the electrolyte [139]. They assume the same plate capacitor model for the interaction between tip and sample as for KPFM, but include the capacitance and voltage drop over the electrolyte. Thereby they roughly estimate frequencies of $\approx 10\,MHz$ and $\approx 100\,MHz$ for measurements on a $SiO_2\backslash Si_2{}^+$ sample in 1 mM and 10 mM aqueous $KClO_4$-solutions respectively. There seems to be a mistake in the reference. Calculation of the critical frequencies with the therein presented equations and parameters yields a value of $f_{crit-1\,mM-wrong} \approx 3\,GHz/m^3$ which does not correspond to the described and measured data, and has a wrong unit. Assuming the molar conductivity to be $\Lambda = 13.3\,mSm^2/mol$ [140] yields the described frequencies and has a proper unit for a molar conductivity. Assuming the relative permittivity (sometimes called the dielectric constant as in the reference) of both the salt solutions to be very close to that of water ($\varepsilon_{H_2O} \approx \varepsilon_{NaCl_{Aq}} \approx 80$) [141], the sample surface to be silicon dioxide and thus its relative permittivity being $\varepsilon_{SiO_2} = 3.9$ [142], a molar conductivity of $96 \times 10^{-4}\,Sm^2/mol$ [140, table 5-73] and the sample thickness and tip-sample-separation to be $h = z = 10\,nm$ as in the reference, the calculated critical frequencies for our systems are $f_{crit-1\,mM} \approx 2\,MHz$ and $f_{crit-10\,mM} \approx 21\,MHz$ for the two salt solutions respectively. As the $A_{1\omega_{ac}}$-signal shows contrast in all the present measurements and the measurements in $F_{1\omega_{ac}}$-settings in liquids were all performed at $\approx 480\,kHz$ the assumptions don't seem to be true for our setup. In the measurements accompanying these predictions, Gramse et al. demonstrate some visible contrast starting from 100 kHz in 1 mM and from 500 kHz in 10 mM solutions [139]. This compares closer to the present settings, however our measurements

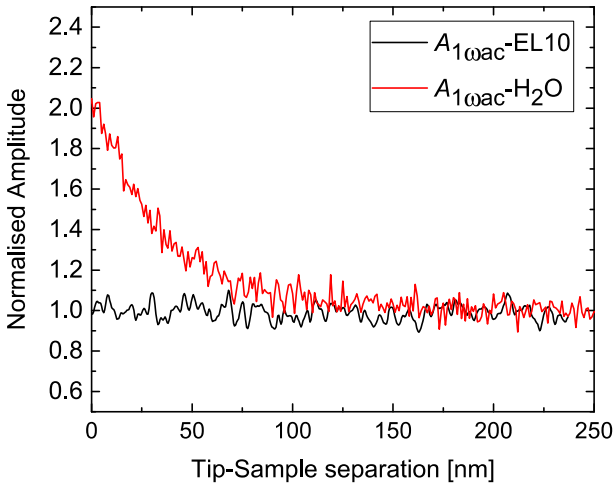

Figure 4.12.: *$A_{1\omega_{ac}}$-curves plotted against the tip-sample separation, normalised to 1 at values far from the surface. The curves were measured in water and the electrolyte El10.*

still seem to show a lot more contrast than the ones in the reference. However, this might also be due to a larger difference in the surface potential of gold and SiO_2 and within the titania layers presented later.

Umeda et al. studied capacitive forces acting on cantilevers, thus measurements at $F_{2\omega_{ac}}$-setting-settings [136]. They compare the $A_{2\omega_{ac}}$-signal and its dependence on the tip-sample separation and excitation frequency in different media. They show a strong tip-sample separation dependence in air and apolar media, where $A_{2\omega_{ac}}$ strongly increases with decreasing distance (increase by a factor of ≈6 and 8 in air and aprotic liquid respectively). The effect does not appear in an electrolyte solution (KCl, 1 mM in water) at low and high frequencies (10 and 180 kHz) and in protic and aprotic polar media without added ions (acetonitrile and acetic acid) at low frequencies. At high frequencies a very small effect (increase by a factor of ≈ 2) is visible in the polar media without added ions. Our own measurements show a similar behaviour. While in pure water an increase of $A_{2\omega_{ac}}$ by a factor of around 2 is visible, in the electrolyte no dependence of $A_{2\omega_{ac}}$ on the tip-sample-separation is detected as shown in Fig. 4.12. This compares perfectly to the data presented by Umeda and coworkers.

Raiteri and Butt show that a cantilever in an electrolyte solution experiences a surface stress which causes a bending of the cantilever by the application of an external potential [143]. Bearing in mind this surface stress Umeda et al. show that the oscillation of cantilevers exited by a V_{ac} as in the setup used for the here presented measurements

consists of a surface stress component and an electrostatic component [106]. Taking into account the EDL forming on the sample and the tip and the conductance of the bulk electrolyte they model the tip-electrolyte-sample system by a combination of resistances, capacitances and impedances, as shown in Fig. 4.13 which was copied from [137] with permission from AIP Publishing LLC and the authors.

The easiest applicable model depends on the tip-sample separation and the frequency of the applied V_{ac}. The modelling is based on the Guoy-Chapman-Stern model (GCS), which describes the border at a surface in an electrolyte by an EDL consisting of a well ordered layer directly at the border (Stern-layer) and a subsequent diffusive layer, throughout whose thickness the ordering decreases [144]. If the tip-sample separation is large, the two EDLs do not overlap. In this case each EDL's impedance C_{EDL} can be described by a capacitance for the Stern layer (C_{S}) and one for the diffusive layer (C_{d}) which are connected in series and parallel to the two a series of a charge transfer resistance (R_{CT}) and a Warburg impedance (Z_{W}). The bulk electrolyte solution is described as an impedance consisting of a bulk resistance (R_{B}) in parallel to a bulk capacitance (C_{B}). Upon application of a voltage the EDL is charged and discharged by a current consisting of a flow of ions from the bulk solution. The surface stress originates in the EDL and is large at low frequencies. It is filtered by the "low-pass filtering" effect of the RC-element consisting of the bulk impedance (R_{B} and C_{B} in parallel) in series to the capacitances of the EDL (C_{S} and C_{d}) [136]. Its cut-off frequency $f_{\mathrm{SS\_C}}$ depends on the characteristic dielectric relaxation frequency f_{C} and the inverse Debye length of the electrolyte, and the cantilever-sample separation and is proportional to the square root of the electrolyte concentration due to the Debye length's equal proportionality. The dielectric relaxation frequency depends on the resistivity of the electrolyte and its relative permittivity. The two are calculated as following [136]:

$$f_{\mathrm{C}} = \frac{1}{2\pi R_B C_B} = \frac{1}{2\pi\varepsilon_0\varepsilon_r\rho_B} \propto n_\infty \tag{4.4}$$

$$f_{\mathrm{SS\_C}} = \frac{1}{1\pi R_B(\frac{C_{\mathrm{EDL}}}{2})} = \frac{1}{\pi\kappa_D\varepsilon_0\varepsilon_r\rho_B(z+h)} = \frac{2f_{\mathrm{C}}}{\kappa_D(z+h)} \propto n_\infty^{\frac{1}{2}} \tag{4.5}$$

For our own system, the calculated values for a 1 mM NaCl-solution are $f_{\mathrm{C}} \approx 2.78\,\mathrm{MHz}$ and $f_{\mathrm{SS\_C}} \approx 5410$ to $3610\,\mathrm{Hz}$ depending on the length of the cantilever tip ($h + z$ =10 and 15 µm respectively). The resistivity ρ_B for the calculations were calculated from the molar conductivities given in reference [140, table 5.76]. The parameters used for the calculation were: $\varepsilon_0 = 8.85\,\mathrm{F/m}$ and $\varepsilon_{NaCl_{aq}} = 80$ and $\rho_{\mathrm{NaCl-1\,mM}} = 80.85\,\Omega\,\mathrm{m}$

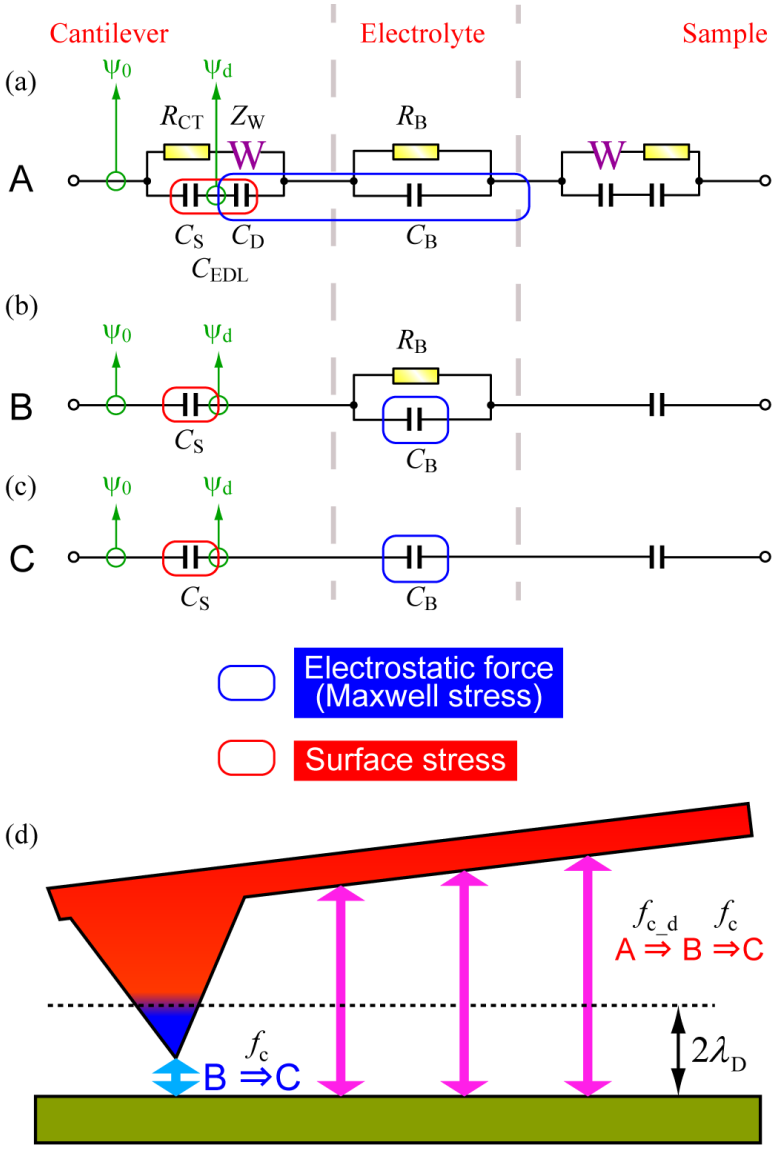

Figure 4.13.: *Equivalent circuit for an electrolyte solution between a cantilever with its tip and a sample based on a Randel's circuit. a) Actual equivalent circuit applicable at large tip-sample separations and low excitation frequencies ($f_{ex} < f_{c\_d}$ and $z > 2\lambda_D$). b) Simplification of a) applicable at high tip-sample separations and intermediate frequencies ($f_{c\_d} < f_{ex} < f_c$ and $z > 2\lambda_D$), or at low tip-sample separations and low or intermediate excitation frequencies ($f_{ex} < f_c$ and $z < 2\lambda_D$). c) Further simplification applicable at very high excitation frequencies ($f_{ex} > f_c$). d) Schematic of the applicability of the equivalent circuits A, B and C depending on the excitation frequency and the distance.*
Reproduced with permission from Journal of Applied Physics 116, 134307 (2014). Copyright 2014, AIP Publishing LLC. Caption adapted from [137]

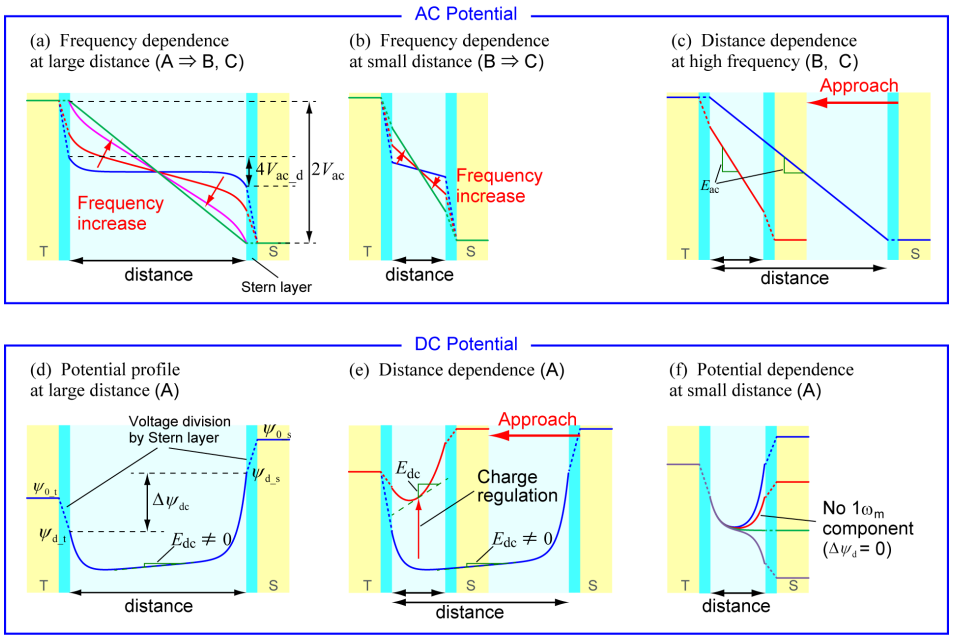

Figure 4.14.: *Top row, a-c) Schematics of ac-potential profiles in aqueous solution as a function of f_{ex} for a) electrodes with a large distance, and b) with a short distance. In c) the schematics of ac-potential profiles in a solution as function of the tip-sample distance is shown. These ac-potential profiles depict the instantaneous maximum voltages in the electrolyte, which are observed when a V_{ac} is applied to the left electrode assuming the tip-potential (T) to be higher than the sample-potential (S).*
Bottom row, d-e) Schematics of dc-potential profiles for electrodes with a large distance in d), and with a short distance in e). f) shows schematics of dc-potential profiles for electrodes with a short distance as a function of the V_{dc} applied to the sample.
Reproduced with permission from Journal of Applied Physics 116, 134307 (2014). Copyright 2014, AIP Publishing LLC. Citation adapted from [137]

and $\kappa_{D-\mathrm{NaCl}-1\,\mathrm{mM}} = \frac{1}{\lambda_{D-\mathrm{NaCl}-1\,\mathrm{mM}}} = \frac{1}{9.74\,\mathrm{nm}}$ using that the Debey length for a monovalent salt at 25 °C is $\lambda_D = \frac{3.04\,\text{Å}}{\sqrt{c\frac{1}{\mathrm{mol}}}}$ [145]. For a 10 mM NaCl-solution the critical frequencies are $f_C \approx 26.6\,\mathrm{MHz}$ and $f_{SS\_C} \approx 16.4$ to 10.9 kHz. The parameters used for the calculation were: $\varepsilon_0 = 8.85\,\mathrm{F/m}$ and $\varepsilon_{NaCl_{aq}} = 80$ and $\rho_{\mathrm{NaCl}-10\,\mathrm{mM}} = 8.44\,\Omega\,\mathrm{m}$ and $\kappa_{D-\mathrm{NaCl}-10\,\mathrm{mM}} = \frac{1}{\lambda_{D-\mathrm{NaCl}-10\,\mathrm{mM}}} = \frac{1}{3.08\,\mathrm{nm}}$. If the excitation frequency f_{ex} is higher than f_{SS_C} the equivalent circuit can be simplified. The C_{EDL} now consists of the C_S alone while C_d, R_{CT} and Z_W can be ignored. The same holds true if the tip sample separation becomes so small, that the two EDLs overlap.

By further increasing the excitation frequency until $f_{\mathrm{ex}} > f_C$ also the impedance of the bulk can be simplified and expressed by C_B alone without R_B resulting in a series of three capacitances for the entire equivalent circuit model.

The calculated potential profiles from Ref. [137] between tip and sample at three different

settings are shown in Fig. 4.14. They largely differ from each other. As is shown in Fig. 4.14 (a) at a large distance and a low excitation frequency hardly any potential drop occurs over the bulk. The potential over the bulk is nearly constant and changes of the potential only occur in the EDLs, thus just at the tip and sample surface. Therefore the potential gradient is very steep in the vicinity of the tip/sample but very flat in between. Since the desired electrostatic force originates in the potential drop in the bulk electrolyte, and the surface stress originates in the potential drop at the EDL this shows the domination of the force at low frequencies by the surface stress. Since the EDL at the cantilever is very localised it has no connection to the sample and thus contains no sample information. Additionally the EDL is present on the entire cantilever and thus the surface of the tip in close proximity to the sample is negligible compared to the rest, resulting in an overlaying of the very small amount of useful signal that might have been generated by the tip by the much larger influence of the surface stress on the entire cantilever. Upon increasing of the frequency the potential drop over the EDL decreases and levels out. Assumingly this is because the EDL is not rearranged in every cycle of the V_{ac}. Thus there is a constant potential gradient throughout the bulk of the electrolyte and no potential change throughout the EDL, and a useful measurement becomes possible. Fig. 4.14 (b) shows the behaviour at smaller tip-sample separations. Now the potential profiles show a linear potential drop throughout the overlapping diffusive layers which now correspond to the electrolyte bulk even at slow excitation frequencies, and an also linear drop through the Stern-layers. Increasing the frequency leads to an increase in the potential gradient outside the Stern-layers and a decrease within and thus to an enhancement of the electrostatic signal. The result of a decrease of the tip-sample separation at a constant frequency is shown in Fig. 4.14 (c). The potential gradient throughout the bulk-electrolyte becomes steeper. However also the potential drop over the Stern-layer increases since the capacitance of the Stern layer and of the tip (both per unit area) become comparable. This induces a voltage division by the Stern-layer capacitance and thus a decrease of the voltage over the bulk-layer. Since the latter induces the electrostatic force containing the sample information this yields to a decrease of the measurement signal. Thereby it diminishes the spatial resolution of the electrostatic measurements since the electrostatic force ceases to act on the tip due to the potential-loss over the Stern-layers.

Thus Umeda et al. [136, 137] show that very large excitation frequencies higher than the dielectric relaxation frequency ($f_{\mathrm{ex}} > f_{\mathrm{C}}$) are necessary in order to enable the measurement of local electrostatic properties. Additionally, the capacitance of the tip and

sample underneath it must be lower than the one of the Stern layer covering said surfaces in order to avoid the division of the applied voltage by the Stern-layer capacitance.

Also Collins et al. studied the measurement of electrostatic properties of surfaces in polar liquids [138]. They stress the importance of ion dynamics and describe the processes occurring upon application of a low voltage pulse as following. The first step is electro-migration in which the ions move according to the applied potential towards the electrodes. This movements leads to the formation of the EDL which screens the electrode from the bulk of the electrolyte. The resulting gradient of the ion concentration induces the ions to diffuse towards the electrodes. This leads to a charge transfer from the bulk solution to the EDL. Finally the charge in the diffuse layer of the EDL relaxes. Of the three steps the first one is limiting in terms of time. Its time constant is called the Debye time (τ_D) and describes the diffusion of an ion through the EDL. It is calculated as $\tau_D = \lambda^2/D$ using the Debye screening length λ and the ion diffusivity across λ denoted as D and is in the range of $\tau_D \approx 5\,\mathrm{ns}$ for a 10 mM 1 : 1 electrolyte. Thus it generates the necessity of high excitation frequencies for measurements in electrolytes, similar to the ones described by Umeda et al. [137]. The measurements performed by Collins et al. are based on the application of bipolar V_{dc} pulses with a length of 50 ms and increasing voltages from 0 to $\pm 1.5\,\mathrm{V}$. The time dependent $A_{1\omega_{\mathrm{ac}}}$- and $A_{2\omega_{\mathrm{ac}}}$-signals are measured upon application of the pulse and thus a set of two dimensional data is gathered for both harmonics. The two dimensions are the applied voltage and the time evolution of the signal.

The experimental data by Collins et al. [138] shows a linear behaviour in air, but already in water there are deviations from the linearity which are claimed to be incompatible with closed loop KPFM. However, the data is such that open loop KPFM is possible due to the linear response at short reaction times, which indicates a dominating electrostatic interaction. This agrees well with our own results presented in Sec. 4.2. However their measurement becomes inconsistent at longer reaction times. Despite the low excitation frequency of $f_{\mathrm{ex}} = 17.8\,\mathrm{kHz}$ Collins et al. were able to measure a CPD comparable to a KPFM measurement in a 1 mM K_2SO_4 solution, but not at higher concentrations, since there the response was highly non-linear and indicates electrochemical reaction on the tip or the sample.

Summarising it can be said that in the literature there is no consensus whether or not OL-KPFM is possible in electrolyte solutions, which are the critical electrolyte concentrations making OL-KPFM impossible, and at which experimental settings measurements can be

performed. Effects interfering with the measurements are claimed to be surface stress due to a force caused by the voltage drop over the Stern-layer, long range electrostatic interactions between the large cantilever surface and the sample which dominate the attenuated signal from the tip, general ion dynamics and diffusion into the EDLs and ultimately chemical reactions on the surfaces. All sources giving specific data agree, that our measurement settings are well below the critical frequencies necessary to prevent an interference of ion dynamics and Stern-layer impedance with the attempted OL-KPFM measurement, even though surface stress should have a negligible influence. This interference explains the V_{ac} dependence of the $\mathrm{CPD_{OL}}$ we observed in our measurements. The original model of a plate capacitor requires the inter-space between the tip and sample to behave as a dielectric. In electrolyte solutions below the critical frequency this is not the case due to the formation of the EDLs and the described diffusions of the ions within the bulk and the EDLs, but also between the two. The EDLs screen the capacitor plates from each other and the diffusion of ions can be assumed to result in a frequency and voltage dependent change of the voltage drop over the different regions of the electrolyte layer between tip and sample. The forming and reforming of the EDLs induces a high amount of movement of the ions in the electrolyte. Thus the voltage drop between the two plates becomes non linear and the resulting force acting on the cantilever tip depends not only on the desired factors, namely the CPD, the capacitance gradient due to the tip and the sample, and the V_{ac}, but also on the electrolyte. Assuming the Stern-layer on the positively charged capacitor plate to consist of negatively charged ions and the ion uptake of the diffusive layer described by Collins et al. to be true this would lead to a supercharging of the capacitor due to "attracting" of the positive ions from the bulk electrolyte by the negative charge of the Stern layer. All these processes occur in time frames of few tens of ns and thus well below the period of the excitation signal which is in the range of a 2 to 4 µs. However Umeda et al. describe a voltage division due to the capacitance of the Stern-layer. Assuming an influence of the charging of the sample on the Stern-layer and therefore on its impedance would lead to a diminution of the voltage drop in the bulk electrolyte. A combination of these effects, which might be time dependent but with different dependences makes the original capacitor-model inapplicable and therefore leads to the observed V_{ac}-dependence of the $\mathrm{CPD_{OL}}$. The observed stronger influence on $A_{2\omega_{\mathrm{ac}}}$ might be a real stronger influence due to the lower frequency, the weaker dependence of $A_{1\omega_{\mathrm{ac}}}$ from V_{ac}, or might be ascribed to differences in the fit especially due to a larger signal to noise ratio and a smaller influence of the low signal region around zero excitation in the $A_{1\omega_{\mathrm{ac}}}$-signal. Further possibilities would be an onset of chemical reactions at lower voltages at lower frequency which might also

explain the levelling of the $A_{2\omega_{ac}}$-curve at higher excitation voltages. The presence of chemical reaction upon application of excitation voltages in the described ranges was obvious in the measurements in electrolyte on the "AuIn-sample", where the gold on the sample disappeared during a measurement. Despite the lack of comparability due to the different environment this shows a high probability of further chemical processes.

Despite the non-linearity of the system, the contrast within single measurements is comparable to previous data if sufficiently high excitation voltages are applied. This shows that even though no quantitative information can be drawn from the measurements it is possible to obtain qualitative information from the data.

In order to enable quantitative measurements different possible ideas for solutions arise. An increase of the excitation frequency is the first, most obvious and while it might be a practical solution for measurements in low-concentration electrolytes, the strong increase of the critical frequency with increasing electrolyte concentrations makes it impractical as a general solution. We tried to conduct measurements at higher frequencies employing the third mechanical resonance of our cantilevers at a frequency of around $f_{3-NCL-liquid} \approx 1\,\mathrm{MHz}$. However, the try did not succeed and the measurements consisted of only noise and hardly any contrast. The employment of a different kind of cantilever might rectify this, but is would still be necessary to work at frequencies in the GHz regime, which is not feasible due to limitations of the PSD bandwidth. An interesting technique to study surfaces and processes in liquids and electrolyte solutions is the combination of AFM and SECM called AFM-SECM, as described in references [49–51]. Therein special cantilevers are employed, which are electrically insulated at the cantilever beam and the cone, and only the apex of the tip is conducting. Thereby the sensing of electro-chemical processes is limited to the tip-apex and parasitic effects from processes taking place on the beam and cone are minimised. An application of insulated cantilevers might also have an advantageous effect onto OL-KPFM measurements. Additionally further theoretical and experimental background research of OL-KPFM in electrolyte solutions is necessary. This might yield highly accurate and even quantitative models of the employed system by means of which quantitative information could be gained from the non-linear data.

After this discussion of the data recorded in the lowly concentrated salt solution the next section will focus on the measurements performed in a solution with increased NaCl-concentration.

4.3.2. High concentration salt solution

Measurements in a salt solution with a concentration of 10 mM were performed to evaluate the influence of increasing ion-concentrations in an environment less reactive as the DSSC-electrolyte. These measurements are presented and discussed in the present section.

Three CPD_{OL} images measured in a 10 mM NaCl solution are shown in Fig. 4.15, together with cross-section profiles measured through the images. They were recorded at different excitation voltages, namely V_{ac} = 1, 2 and 3 V.

The measurements do not exhibit the contrast inversion seen in the low concentration salt solution, but they exhibit a strong dependence of the CPD from the excitation voltage. As in the previous measurements the reasons are expected to be the diffusion of ions through the electrolyte resulting in the formation of EDLs on the tip and sample surface, changing gradients of ion-concentrations through the bulk electrolyte depending on the voltage and excitation frequency, and maybe other processes such as chemical reactions or the onset thereof. These undesired interactions result in an impediment of the assumed model of a plate capacitor filled with an ideal dielectric.

Comparison of the measurements in lowly- and highly concentrated salt solution shows far higher CPD-values at equal V_{ac} with higher salt concentration. At an excitation of V_{ac} = 1 V the background CPD increases from around $CPD_{SiO_2-1\,mM-NaCl-1\,V} \approx 2.2\,V$ to around $CPD_{SiO_2-10\,mM-NaCl-1\,V} \approx 4.5\,V$. The same is true for the excitation at V_{ac} = 2 V, even though especially at a larger excitation the background CPD is rather difficult to estimate, since it shows striped features and thus varies by 200 to 300 mV. Here the background CPD increases from around $CPD_{SiO_2-1\,mM-NaCl-2\,V} \approx 3.4\,V$ to around $CPD_{SiO_2-10\,mM-NaCl-2\,V} \approx 7.7\,V$.

This increase in the CPD is also obvious from the V_{ac}-spectroscopy measurements which show steeper slopes for the higher salt concentrations in both the regions at $V_{ac} < 1\,V$ ($NaCl_{1\,mM} = 3.3\,V_{CPD}/V_{V_{ac}}$; and $NaCl_{10\,mM}$=$9.5\,V_{CPD}/V_{V_{ac}}$) and at larger excitation voltages ($V_{ac} > 1\,V$), where the slopes are $1.4\,V_{CPD}/V_{V_{ac}}$ and $1.8\,V_{CPD}/V_{V_{ac}}$ for salt concentrations of 1 and 10 mM respectively. Despite the increase in CPD the fit-results for $A_{1\omega_{ac}}$ and $A_{2\omega_{ac}}$ are much closer to the expected values as for the measurements in 1 mM salt solution, as is shown in Tab. 4.2 on page 96. The non-linear fit (Eq. 2.23) to $A_{1\omega_{ac}}$ shows an increased exponent of 1.20 compared to the expected 1.00 in both salt solutions. However, the data-curve shows a strange depression at around V_{ac} = 1.5 V

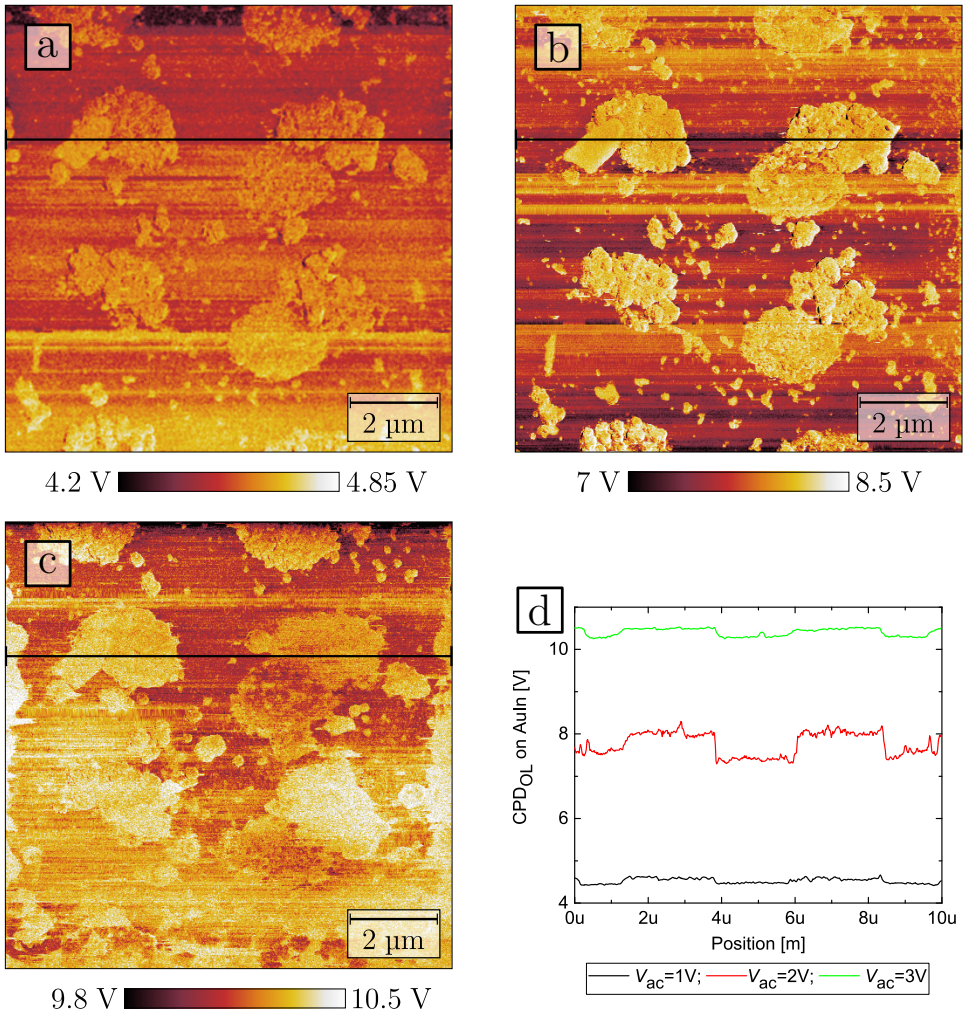

Figure 4.15.: *CPD_{OL}-data recorded on the "AuIn-sample" (same spot for all images) in a* 10 mM *salt solution with increasing excitation voltages: a) V_{ac}=1 V, b) V_{ac}=2 V, c) V_{ac}=3 V. Black line indicates measured profiles, which are displayed in d).*
Scan Parameters: f_{1st} = 73 kHz; A_{1st} = 5 nm; f_{2nd} = 499 kHz; V_{ac} = 1, 2 and 3 V

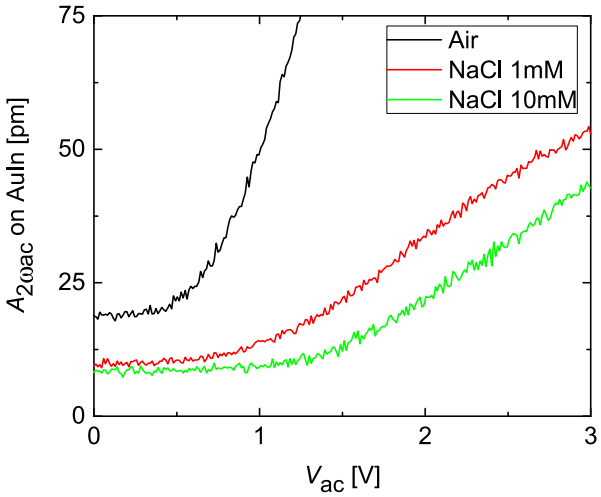

Figure 4.16.: *An overview over $A_{2\omega_{ac}}(V_{ac})$-spectra measured on the "AuIn-sample" in all the different environments.*

both at positive and negative voltages. This leads to the slight bending of the curve and the resulting increased fit parameters. The exponent of the $A_{2\omega_{ac}}$-fit agrees very well with the expected value (1.94 compared to 2.00). The intercept yielded by the fitting of the $A_{2\omega_{ac}}$-signals of all the spectroscopies recorded in liquid are "artefacts" of the fitting. This is obvious by the fact that the fitted intercepts differ largely from each other and can even be negative, while the residual amplitudes at zero excitation for all the $A_{2\omega_{ac}}$-spectra in liquids are nearly equal in the range of 10 pm, and only in air an increased amplitude of 20 pm remains. Since the amplitudes at V_{ac}=0 are presumed to be due to noise they are not expected to have any further physical meaning or influence on the measurement of the CPD. The slope of the $A_{2\omega_{ac}}$-signal measured in 10 mM NaCl is is fitted to be 10 × smaller than the slopes measured in air and water and thus even 5 × smaller than the one measured in the lowly concentrated salt solution. This explains the increased CPDs measured therein. This is nicely shown in the overview over the $A_{2\omega_{ac}}$-signals measured on the "AuIn-sample" in the different environments in Fig. 4.16

All the images recorded in the 10 mM salt solution show a clear contrast between the gold-dots and the silicon dioxide background. As can be seen in the profiles in Fig 4.15 the average difference between the CPD of the gold-dots and the background does not follow a trend. It increases from $\Delta\mathrm{CPD}_{\mathrm{Au-SiO_2;1\,V}} \approx 105 \pm 33\,\mathrm{mV}$ at an excitation voltage of $V_{ac} = 1\,\mathrm{V}$ to $\Delta\mathrm{CPD}_{\mathrm{Au-SiO_2;2\,V}} \approx 540 \pm 150\,\mathrm{mV}$ and then decreases back to $\Delta\mathrm{CPD}_{\mathrm{Au-SiO_2;3\,V}} \approx 185 \pm 20\,\mathrm{mV}$ upon increasing of the excitation to $V_{ac} = 2$ and 3 V

respectively. Considering the general increase of the CPD one would have expected to find an increased CPD difference and no plausible explanation for this strange behaviour has been found yet, except maybe the onset (or actual occurring) of chemical reactions triggered by the applied ac-voltage despite the high frequencies.

Concluding it can be said that the measurements in the 10 mM NaCl solution show the same undesired dependence of the CPD from the excitation voltage. Considering the measurements performed by Kobayashi et al. it was expected that it should be possible to perform the measurement in our system [56] despite the somewhat lower excitation-frequency applied for the $F_{2\omega_{ac}}$-setting-measurement. In order to test, whether the voltage dependence is due to too low excitation frequencies, measurements were attempted to be performed at the third mechanical resonance frequency of the cantilever, and thus at $f_{ex} \approx 1\,\text{MHz}$. The resonance could be detected by mechanical excitation of the cantilever and by excitation of the cantilever with white noise (applied to the shaking piezo and simulating a highly increased temperature and thus yielding a large signal at the resonance without excitation of other modes). However by electro-statical excitation no resonance peak could be detected, especially not in $F_{2\omega_{ac}}$-setting-settings.

The recorded CPD-data shows a consistent contrast between gold and silicon dioxide. Thus even though no quantitative measurements of surfaces are possible with the currently applied technique and setup it should be possible to gather qualitative information about surfaces or at least discern different regions with various surface properties, such as different materials in the described salt solution.

After having discussed the measurements performed in air, water and different salt solutions, thus less reactive electrolytes, the focus of the next section lies on the data recorded in the diluted DSSC-electrolytes and their discussion and interpretation.

4.4. Open Loop Kelvin Probe Force Microscopy in Electrolyte

In order to examine nanoporous titania layers in a system closely resembling their "native" environment inside a working DSSC, OL-KPFM measurements were performed in diluted DSSC-electrolytes. The cantilevers used for the measurements were coated with a PtIr layer and thus even provided an adequate counter-electrode with the same catalyst

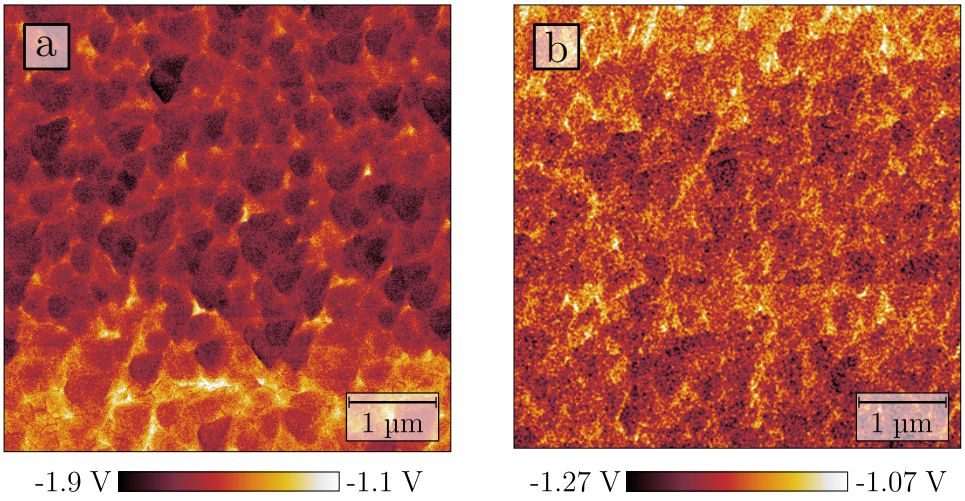

Figure 4.17.: *CPD_{OL}-images recorded on bare (a) and dyed (b) titania in the electrolyte "El100" at an excitation voltage of $V_{ac} = 1\,V$. The measurements were recorded under equal conditions. The higher CPD and lower CPD-range in the dyed sample indicate the possibility to gain qualitative information from the measurements. Scan Parameters: $f_{1st} = 75\,kHz$; $A_{1st} = 9\,nm$; $f_{2nd} = 488\,kHz$; $V_{ac} = 1\,V$.*

as is employed in DSSCs. OL-KPFM measurements were performed on bare and sensitised titania layers (sensitiser: N719) in an electrolyte containing the iodide/tri-iodide redox couple which is often used in DSSC electrolytes. We did not include any additives in the electrolyte in order to simplify the system, and we employed the electrolyte in two diluted forms of only 1/10 and 1/100 of the concentrations usual for DSSC-electrolytes. The two electrolytes are denoted "El10" and "El100" respectively, where the number indicates the dilution factor.

Preliminary tests using the "AuIn-sample" in the electrolyte did not yield any images. The measured CPD did not show any consistent contrast and an evolution of large particles during the measurements was observed. At the end of the measurements the gold dots on the sample had been dissolved, presumingly due to electro-chemical reactions taking place in the electrolyte upon applying of the V_{ac}.

The measurements in electrolyte behave similarly as those in the salt solutions. All the measured CPDs show a dependence of the excitation voltage with increasing CPD for increasing V_{ac}. Representative CPD_{OL} images recorded in electrolyte are shown in Figs. 4.17 (El100) and 4.18 (El10). An overview of the CPD(V_{ac}) spectroscopies measured in all the configurations on titania is shown in Fig. 4.19. Both the images and the spectroscopies show the dependence of the CPD_{OL} from the excitation voltage, as was expected from the results of the measurements in the salt solutions. The dependency

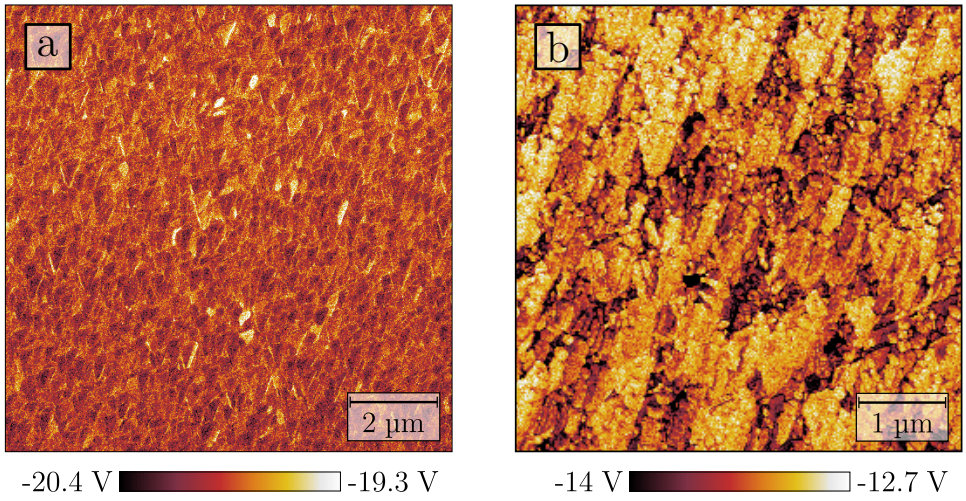

Figure 4.18.: *CPD_{OL}-images recorded on bare (a) and dyed (b) titania in the electrolyte "El10" at an excitation voltage of $V_{ac} = 2\,\mathrm{V}$. Scan Parameters: $f_{1st} = 75\,\mathrm{kHz}$; $A_{1st} = 8\,\mathrm{nm}$; $f_{2nd} = 497\,\mathrm{kHz}$; $V_{ac} = 2\,\mathrm{V}$.*

increases with increasing electrolyte concentration and is more pronounced for the bare layers where the slope of the V_{ac}-depends on the CPD increases from $5.7\,\mathrm{V_{CPD}/V_{V_{ac}}}$ to $13.5\,\mathrm{V_{CPD}/V_{V_{ac}}}$ compared to the sensitised layer where the slope increases from $2.6\,\mathrm{V_{CPD}/V_{V_{ac}}}$ to $3.4\,\mathrm{V_{CPD}/V_{V_{ac}}}$. The fit of the latter was performed starting at 1.5 V instead of 1 V since this curve shows two slopes and the transition from the first to the second occurs at around $V_{\mathrm{ac}} = 1.5\,\mathrm{V}$. The absolute values of the CPDs measured in the different electrolytes are not comparable, since the system was interrupted between the different measurements, the electrolyte was replaced and the tip was exposed to air. The CPD dependence measured on the sensitised layer in the electrolyte "El10" differs from the ones recorded in the other electrolytes. Its shape shows similarities to the CPD dependences recorded in air and water. It has two regions, the first with a steep slope comparable to the curve recorded on the bare layer, the second with a much less steep slope. The setup was slightly modified before the measurements of the sensitised layer in "El10". Even though it seems improbable this change of the setup is the first explanation coming to mind for the change of the spectroscopy-shape.

The measurements performed in the electrolyte "El10" on the bare and sensitised layer were not performed with an equal configuration. Thus the comparison is difficult and does not hold much information. However the images recorded on sensitised titania are notable because they are the nicest images recorded. The still large image does not allow the distinction of single nanoparticles since each pixel is around 20 nm large and thus of similar magnitude as the particles. However despite the rather blunt tip small particle

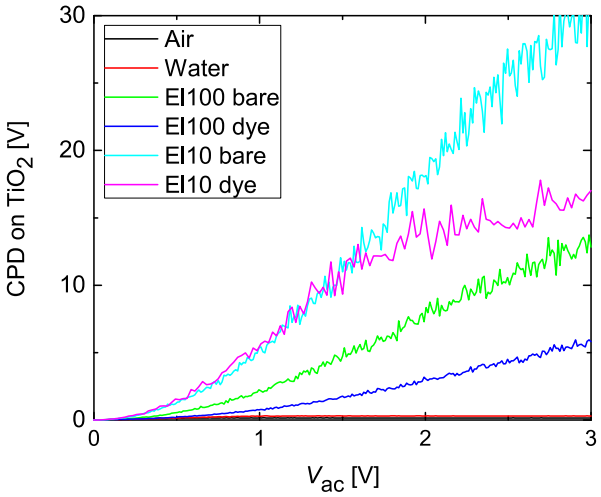

Figure 4.19.: *Overview of the CPD(V_{ac}) sweeps measured on titania in all the different configurations. The curves show the absolute of the measured CPD.*

aggregates of sizes around 100 nm were resolved among the larger structures visible in the other measurements.

The images recorded in the electrolyte "El100" on the other hand hold interesting qualitative information. Comparing the images recorded in "El100" on the bare and the sensitised titania (Fig. 4.17) which were recorded in an equal configuration without withdrawing the tip from the electrolyte between the two measurements nor changing of any parameters, shows a lower CPD on the bare titania. Also its CPD-distribution is far wider and the signal-to-noise ratio is larger, thus the images look less noisy. The more grainy appearance of the sensitised layers' CPD image is due to a filtering applied in order to reduce the noise. The lower CPD of the bare layer is consistent with the finding of Henning et al. [38] who claim this to be due to a dipole of the sensitiser molecules oriented towards the titania surface. Since in both cases the used sensitiser was N719 this effect supports their claim. It also shows that the dipole-orientation of the sensitiser molecule does not change upon introduction of the electrolyte. A change of the dipole-direction would have indicated either a change of the structure of the bound molecule, a change of the binding pattern of the molecule, or a very strong interaction and coupling of the bound molecules with the molecules in the electrolyte. The missing of said change thus suggests a consistent binding mode of the molecule, a high intermolecular stability and no joining of the sensitiser- and electrolyte molecules. This is encouraging for studies of sensitiser molecules outside the electrolyte, since it means that findings from such

measurements are not necessarily doubtable, which would have been indicated by the identification of drastic changes of the sensitisers upon contact with the electrolyte.

The small range of the CPD-values indicates a more even surface on the sensitised compared to the bare layer. This was expected and is desirable, since it shows the coverage of the surface with one single species of molecules and little other adsorbates. The values higher than the average belong to depressions in the surface at the border of the particle-aggregates. Possible reasons for this increase are different interactions between tip and sample when the tip is beside an aggregate (or between two) rather than above the surface of one aggregate. Interestingly the gaps between particles and aggregates show a lower CPD in air and water. As for the "AuIn-sample" in the salt solution a possible explanation is the strongly decreased amplitude and the missing contrast of $A_{2\omega_{ac}}$ which leads to an increased CPD above particle aggregates compared to beside the aggregates. The lower CPD values belong more to the surface of the aggregates. Some few aggregates show notably lower CPDs than the average aggregates. This might originate in the adsorption of other molecules than the dye on the surface, or of the adsorption of less dye molecules on said aggregates. A reduction of the number of these lower CPD aggregates might be achieved by baking of the sample directly before the sensitisation, sensitisation in an anhydrous dye-solution in a glove-box and subsequent measurement of the sample in the glove box without interruption of the inert atmosphere. However, in order to be able to measure bare and sensitised layers in the same configuration of the setup they necessarily need to be on the same sample. Thus the layer remaining bare needs to be protected from the dye-solution during the sensitisation process. This was achieved by sealing of the layer with a surlyn® foil and a cover glass. This made a subsequent baking of the layer impossible. Further more the measurement setup for the measurements in electrolyte could not be located in a glove box, thus prohibiting an uninterrupted inert atmosphere.

Concluding the measurements in electrolyte solutions show the same non-linear behaviour of increasing CPD with increasing V_{ac} due to a very small capacitative force which is shown by the very small $A_{2\omega_{ac}}$ which consists mainly of noise. This decreased amplitude and thereby the non-linear behaviour of the CPD is induced by the EDLs and the diffusion of ions in the electrolyte as described in Sec. 4.3. Therefore, no quantitative results can be obtained from the performed measurements. However, closer examination of the data enables qualitative observations. Henning et al. showed the N719 molecules bound to a nanoporous titania surface exhibit a dipole-moment towards the titania [38]. The lower surface potential we detected for sensitised titania layers compared to bare

titania layers examined in electrolytes support Henning's claim and indicate the retention of the dipole orientation of the bound molecules upon immersion in the electrolyte. The decrease in the surface potential variation indicates a more even surface, probably due to a high coverage with dye molecules and consequentially low amounts of undesired adsorbates on the titania. This enables further studies of dye molecules and dye-titania interfaces in environments differing from the DSSC electrolyte since it indicates a general conservation of the structure of the dye molecule and of the dye-titania interface.

4.5. Summary

In the present chapter the results of the surface potential measurement in the various environments were presented and discussed. The results of the measurement performed in air and ultra-pure water show a perfect agreement not only among each other, but also between the recorded data and the basic plate capacitor model applied to explain the governing electrostatic interactions between tip and sample.

The presence of ions in the electrolyte solution impedes with the basic model, since they form EDLs on the involved surfaces, which screen the tip sample interactions and introduce a non-linear factor into the potential landscape. In addition the applied frequencies were not high enough to generate quasi-static conditions, and the ions are expected to re-arrange by diffusion at every cycle of the applied ac-voltage, thereby introducing charge-transport dynamics, which impede the measurements even further.

These unfavourable interactions are mainly expressed by a diminution of $A_{2\omega_{\mathrm{ac}}}$. The influence on $A_{1\omega_{\mathrm{ac}}}$ is much smaller. Therefore qualitative information can still be gained from the recorded $A_{1\omega_{\mathrm{ac}}}$s and we were able to support a claim made by Henning et al. whose work indicates an orientation of the dipoles of N719 molecules adsorbed on nanostructured titania towards the titania surface [38]. Our data not only supports this claim, but thereby indicates the possibility to transfer findings made in isolated measurements outside the working conditions of a DSSC to the inside of a cell.

5. Conclusion and outlook

A large part of the work performed in the course of this Ph.D. was concerned with the implementation of the fabrication of reproducible DSSCs at our department. Despite the beautiful simplicity of DSSCs the fabrication of highly efficient and overall highly reproducible cells requires a large know-how and a far reaching expertise. The work performed on the way to getting this expertise is described in the method section of this thesis in chapter 3. Important milestones on the way to successful solar cell fabrication are the production of integer and homogeneous titania layers. Our work showed that such layers can be deposited not only from viscous pastes by screen-printing or doctor-blading, which are the standard deposition techniques generally applied in the DSSC-community, but also by spray deposition of liquid suspensions by means of an air-brush. Particularities of this deposition technique compared to the standard procedures are the expected possibility of an easy up-scaling and the independence from prefabricated masks and stencils. Hindering factors for a continuing application of spray deposition were frequent clogging of the spray-valves, which lead to an unpredictable thickness of the deposited layers. The thickness of titania layers is usually measured by profilometry. We employed further techniques, namely cross-section imaging by SEM and surface-imaging by LSM for precise evaluation of the layer thickness. The measurements showed that the best control over the thickness of the produced layers is given by the screen-printing technique. However even there variations can occur based on the viscosity and exact composition of the employed printing pastes, and maybe even the temperature. Thus regular evaluation of fabricated layers is advisable. The method of choice for the evaluation of the thickness is a compromise between time consummation and amount of gained information. All the evaluated measurement techniques provide the correct layer thickness if they are applied correctly. The advantage of the profilometer is its very fast measurement. However the output is only a single profile at one particular location of the cell. The laser-microscope on the other hand is much more time-consuming, but it yields further information about the exact shape of the layer and about possible defects.

When examining DSSCs characterisation methods developed for the examination of

silicon solar cells are often applied. Our measurements indicate that great care has to be taken, when such methods are applied to DSSCs, since even such seemingly trivial things as the calibration of the light intensity, or the setting of a measurement frequency or settling time can have large influences on the results due to differences in the working principle of DSSCs from other types of solar cells.

After the implementation of the DSSC-fabrication the second point of interest in this work was the examination of electrostatical surface properties of the photo-active layer. Since this layer is nanostructured, and the peculiar structure is bound to strongly influence the working and the properties of the DSSCs these examinations were performed at the nanoscale, and were attempted to be performed in a system resembling a working DSSC as closely as possible. Therefore starting from the techniques proposed by Kobayashi [54] and Guo [57] OL-KPFM in single-frequency half-harmonic excitation mode was used to investigate titania layers for DSSCs in different environments in order to gain deeper understandings of the relatively young measurement technique and the investigated interface. Measurements on titania layers and a model-sample of gold and indium dots on an Si-wafer were performed in air, water, salt solutions of different concentrations (NaCl; 1 and 10 mM) and in a simplified DSSC-electrolyte in two highly diluted concentrations (1/100 and 1/10 of the normal electrolyte concentration). The applicability of the model of a plate capacitor, on which the calculations of the surface potential are based was verified and found to hold true for air and water, but not for salt- or electrolyte solutions.

Our measurements show that the proposed OL-KPFM technique is applicable for measurements in air and water. In air perfect surface potential measurements were performed on both samples. Comparison of the data measured by the open-loop technique to that measured by the closed-loop technique shows nearly perfect agreement of the values on the gold-sample. On the titania the CPD measured by the closed-loop technique is shifted by around 80 mV compared to the CPD measured by open-loop technique. The reason for this shift is capacitative cross-talk, which influences only the measurement in closed-loop mode and not the one in open-loop mode, thus showing a advantage of the open-loop measurement. In water no close-loop mode measurements are possible, due to the polarisability of the solvent which would interfere with the applied dc-voltage. The performed OL-KPFM measurements yielded perfect data which in good agreement to the data measured in air. The cantilever-sample system is modelled as a plate capacitor for the derivation the KPFM in both open- and closed-loop. The applicability of this model on both test-samples was confirmed in air and water by spectroscopic measure-

ments of the dependence of the electrostatic- and capacitative force from the excitation voltage.

Also in water perfect surface potential measurements were performed and the applicability of the model was proved by the spectroscopy-data.

In all the examined electrolyte-solutions (aqueous NaCl solution of 1 and 10 mM and DSSC-electrolyte diluted by factors of 10 and 100) the recorded data showed a dependence of the surface potential from the applied excitation voltage and a strongly non-linear behaviour. This shows that the applied model is not applicable using the employed settings and setup (e.g. ion-concentration, excitation voltage, modulation frequency of the excitation voltage, highly-conducting cantilevers,...). The non-linear response was described among others by Umeda et al. [137] and was attributed to the diffusion of ions in the electrolyte and the forming of electronic double layers on the cantilever and the sample surface.

Qualitative information can be gained from the present data. It shows differences in the absolute values and the distribution of the CPD of bare- and sensitised titania layers and thus indicates the possibility to discern between surfaces with different surface-properties. The observed negative shift of the surface potential of sensitised layers compared to bare ones supports our claims made in [38] where we assume a shift of the surface potential due to the dipole of the adsorbed sensitisers. It indicates that the structure of the TiO_2-N719 interface does not completely change and is not entirely screened by the immersion into the electrolyte and the interaction with the redox-ions therein. This is a very positive finding, since it enables the transfer of data measured on said interface in air and vacuum to the complete dye sensitised solar cell system.

In order to enable the gaining of quantitative data either the instrumentation needs to be adapted to the non-linear behaviour, e.g. by increasing of the modulation frequency, by insulating of the cantilever beams, or by further dilution of the electrolytes. Other possibilities would be the development of a model taking into account and correcting for the non-linearities, and thus enabling the calculation of qualitative information from the present data.

Further insight into the studied systems might also be gained by examining them with additional measurement techniques such as SECM, Electro Chemical Force Microscopy (ECFM), AFM-SECM and others.

6. Acknowledgements

This work would not have been possible without the help and support of all the people surrounding me.

In particular I want to thank *Prof. Ernst Meyer*, for giving me the opportunity of doing this work in his research group. Special thanks goes to *Thilo Glatzel* for the supervision of my work, the enormous transfer on knowledge from which I profited a lot, and for an always excellent working-climate and lots of patience. I would like to thank *Res Jöhr* who worked with me during all this time. Thanks for every helping hand that was there when needed and for the providing of your beautiful figures and art-work. Another personal thanks goes to *Marcin Kisiel* for his help with the KPFM in general and the setting up of the OL-KPFM and to *Martin Mendelin* for all the proof-reading (mostly at short notice) and the helpful suggestions.

The fabrication of all the "home-built" equipment would not have been possible without all the people in the mechanical and electronic work-shop. Thanks to all of you, particularly *Heinz Breitenstein* for the drilling of all our filling holes in the counter electrode and all the other help whenever it was needed, to *Sascha Martin*, *Andreas Tonin*, *Roberto Maffiolini*, *Michael Steinacher* and *Yves Pellmont* for designing and assembling of the IV-curve measurement setup to the fulfilment of all my chaotic desires. Also a thank you to *Roland Steiner* for the help with the drawing of the liquid AFM cell.

Many thanks also to the administrative staff of the University of Basel and the physics department, particularly *Barbara Kammerman*, *Astrid Kalt* and *Germaine Weaver* for help with all the administrative work and many hours of overtime performed all around the clock, to *Beat Glatz* for support in the daily fight against the menace of computers and IT in general, and to *Peter Reimann* and *Bernd Heimann* who keep the entire department up and running.

I would like to thank all the members of the *Meyer-group* for an excellent working climate and fruitful discussions on all possible subjects, whether scientific or otherwise, and to *Monica Schönenberger* for letting me share her lab.

A very particular thank you goes to my entire family, my parents, my sisters and my friends for always supporting me, and the biggest thanks of all to *Yvonne* for always believing in and supporting me and for suffering me during the more stressful periods of this work.

7. Bibliography

[1] IEA; *Key World Energy Statistics 2014*; 2014 ed. (OECD Publishing, Paris, 2014); ISBN 9789264223998; DOI: 10.1787/key_energ_stat-2014-en.
(Cited on page 1.)

[2] P. Würfel and U. Würfel; *Physics of Solar Cells: From Basic Principles to Advanced Concepts*; Physics textbook (Wiley, 2009); ISBN 9783527408573.
(Cited on page 1.)

[3] Susan Solomon, Dahe Qin, Martin Manning, Melinda Marquis, Kristen Ayeryt, Melinda M.B. Tignor, Henry LeRoy Jr. Miller, and Chen Zhenlin (editors); *IPCC, 2007: Climate Change 2007: The Physical Science Basis. Contribution of Working Group I to the Fourth Assessment Report of the Intergovernmental Panel on Climate Change* (Cambridge University Press, United Kingdom and New York, 2007); ISBN 9780521705967.
(Cited on page 1.)

[4] Martin A. Green; «The path to 25% silicon solar cell efficiency: History of silicon cell evolution;» *Progress in Photovoltaics: Research and Applications* (**2009**); vol. 17 (3), pp. 183–189; ISSN 1099-159X; DOI: 10.1002/pip.892.
(Cited on page 1.)

[5] Arif Hepbasli; «A key review on exergetic analysis and assessment of renewable energy resources for a sustainable future;» *Renewable and Sustainable Energy Reviews* (**2008**); vol. 12 (3), pp. 593 – 661; ISSN 1364-0321; DOI: 10.1016/j.rser.2006.10.001.

[6] Ahmet Duran Sahin; «Progress and recent trends in wind energy;» *Progress in Energy and Combustion Science* (**2004**); vol. 30 (5), pp. 501 – 543; ISSN 0360-1285; DOI: 10.1016/j.pecs.2004.04.001.
(Cited on page 1.)

[7] Hans-Günther Wagemann and Heinz Eschrich; *Photovoltaik:*; 2nd ed. (Vieweg+Teubner Verlag, Wiesbaden, 2010); ISBN 9783834806376.
(Cited on page 1.)

[8] AASHE Association for the Advancement of Sustainability in Higher Education; «Solar Photovoltaic Installation @ Georgetown University;»
URL: http://www.aashe.org/resources/campus-solar-photovoltaic-installations/detail/georgetown-university-1984/ read 24.1.2015 (**2015**).
(Cited on page 1.)

[9] Philip Jackson, Dimitrios Hariskos, Erwin Lotter, Stefan Paetel, Roland Wuerz, Richard Menner, Wiltraud Wischmann, and Michael Powalla; «New world record efficiency for Cu(In,Ga)Se_2 thin-film solar cells beyond 20 %;» *Progress in Photovoltaics: Research and Applications* (**2011**); vol. 19 (7), pp. 894–897; ISSN 1099-159X; DOI: 10.1002/pip.1078.
(Cited on page 1.)

[10] Ingrid Repins, Miguel A. Contreras, Brian Egaas, Clay DeHart, John Scharf, Craig L. Perkins, Bobby To, and Rommel Noufi; «19.9 %-efficient ZnO/CdS/CuInGaSe2 solar cell with 81.2 % fill factor;» *Progress in Photovoltaics: Research and Applications* (**2008**); vol. 16 (3), pp. 235–239; ISSN 1099-159X; DOI: 10.1002/pip.822.
(Cited on page 1.)

[11] B.M. Kayes, Hui Nie, R. Twist, S.G. Spruytte, F. Reinhardt, I.C. Kizilyalli, and G.S. Higashi; «27.6% Conversion efficiency, a new record for single-junction solar cells under 1 sun illumination;» in «Photovoltaic Specialists Conference (PVSC), 2011 37th IEEE,» (2011); ISSN 0160-8371 pp. 000 004–000 008; DOI: 10.1109/PVSC.2011.6185831.
(Cited on page 1.)

[12] Mingzhen Liu, Michael B. Johnston, and Henry J. Snaith; «Efficient planar heterojunction perovskite solar cells by vapour deposition;» *Nature* (**2013**); vol. 501 (7467), pp. 395–398; ISSN 0028-0836; DOI: 10.1038/nature12509.
(Cited on page 1.)

[13] Brian O'Regan and Michael Graetzel; «A low-cost, high-efficiency solar cell based on dye-sensitized colloidal TiO_2 films;» *Letters to Nature* (**1991**); vol. 353, pp. 737 – 740; DOI: doi:10.1038/353737a0.
(Cited on pages 1, 2 and 11.)

[14] Harald Hoppe and Niyazi Serdar Sariciftci; «Organic solar cells: An overview;» *Journal of Materials Research* (**2004**); vol. 19, pp. 1924–1945; ISSN 2044-5326; DOI: 10.1557/JMR.2004.0252.
(Cited on page 1.)

[15] Serap Günes, Helmut Neugebauer, and Niyazi Serdar Sariciftci; «Conjugated Polymer-Based Organic Solar Cells;» *Chemical Reviews* (**2007**); vol. 107 (4), pp. 1324–1338; DOI: 10.1021/cr050149z.
(Cited on page 1.)

[16] Martin A. Green, Keith Emery, Yoshihiro Hishikawa, Wilhelm Warta, and Ewan D. Dunlop; «Solar cell efficiency tables (Version 45);» *Progress in Photovoltaics: Research and Applications* (**2015**); vol. 23 (1), pp. 1–9; ISSN 1099-159X; DOI: 10.1002/pip.2573.
(Cited on page 1.)

[17] Jinqing Peng, Lin Lu, and Hongxing Yang; «Review on life cycle assessment of energy payback and greenhouse gas emission of solar photovoltaic systems;» *Renewable and Sustainable Energy Reviews* (**2013**); vol. 19 (0), pp. 255 – 274; ISSN 1364-0321; DOI: 10.1016/j.rser.2012.11.035.
(Cited on page 1.)

[18] Maria Laura Parisi, Simone Maranghi, and Riccardo Basosi; «The evolution of the dye sensitized solar cells from Grätzel prototype to up-scaled solar applications: A life cycle assessment approach;» *Renewable and Sustainable Energy Reviews* (**2014**); vol. 39 (0), pp. 124 – 138; ISSN 1364-0321; DOI: 10.1016/j.rser.2014.07.079.
(Cited on pages 1, 2 and 11.)

[19] P. Poizot, S. Laruelle, S. Grugeon, L. Dupont, and J-M. Tarascon; «Nano-sized transition-metal oxides as negative-electrode materials for lithium-ion batteries;» *Nature* (**2000**); vol. 407 (6803), pp. 496 – 499; ISSN 0028-0836; DOI: 10.1038/35035045.
(Cited on page 2.)

[20] Subrahmanyam Goriparti, Ermanno Miele, Francesco De Angelis, Enzo Di Fabrizio, Remo Proietti Zaccaria, and Claudio Capiglia; «Review on recent progress of nanostructured anode materials for Li-ion batteries;» *Journal of Power Sources* (**2014**); vol. 257 (0), pp. 421 – 443; ISSN 0378-7753; DOI: 10.1016/j.jpowsour.2013.11.103.
(Cited on page 2.)

[21] Anders Hagfeldt, Gerrit Boschloo, Licheng Sun, Lars Kloo, and Henrik Pettersson; «Dye-Sensitized Solar Cells;» *Chemical Reviews* (**2010**); vol. 110 (11), pp. 6595–6663; DOI: 10.1021/cr900356p.
(Cited on pages 2, 3, 11, 15, 16, 17, 18, 52 and 78.)

[22] K. Kalyanasundaram; *Dye-sensitized Solar Cells*; Fundamental sciences : chemistry (EFPL Press, 2010); ISBN 9781439808665.
(Cited on pages 2, 3, 11, 12, 13, 15, 43, 44, 46 and 56.)

[23] Peng Wang, Shaik M. Zakeeruddin, Pascal Comte, Raphael Charvet, Robin Humphry-Baker, and Michael Grätzel; «Enhance the Performance of Dye-Sensitized Solar Cells by Co-grafting Amphiphilic Sensitizer and Hexadecylmalonic Acid on TiO_2 Nanocrystals;» *The Journal of Physical Chemistry B* (**2003**); vol. 107 (51), pp. 14 336–14 341; DOI: 10.1021/jp0365965.
(Cited on pages 3 and 52.)

[24] K Tennakone, G R R A Kumara, A R Kumarasinghe, K G U Wijayantha, and P M Sirimanne; «A dye-sensitized nano-porous solid-state photovoltaic cell;» *Semiconductor Science and Technology* (**1995**); vol. 10 (12), p. 1689.
(Cited on pages 3 and 13.)

[25] R. Kern, R. Sastrawan, J. Ferber, R. Stangl, and J. Luther; «Modeling and interpretation of electrical impedance spectra of dye solar cells operated under open-circuit conditions;» *Electrochimica Acta* (**2002**); vol. 47 (26), pp. 4213 – 4225; ISSN 0013-4686; DOI: 10.1016/S0013-4686(02)00444-9.
(Cited on page 3.)

[26] N.W Duffy, L.M Peter, R.M.G Rajapakse, and K.G.U Wijayantha; «A novel charge extraction method for the study of electron transport and interfacial transfer in dye sensitised nanocrystalline solar cells;» *Electrochemistry Communications* (**2000**); vol. 2 (9), pp. 658 – 662; ISSN 1388-2481; DOI: 10.1016/S1388-2481(00)00097-7.
(Cited on page 3.)

[27] Arie Zaban, Miri Greenshtein, and Juan Bisquert; «Determination of the Electron Lifetime in Nanocrystalline Dye Solar Cells by Open-Circuit Voltage Decay Measurements;» *ChemPhysChem* (**2003**); vol. 4 (8), pp. 859–864; ISSN 1439-7641; DOI: 10.1002/cphc.200200615.
(Cited on page 3.)

[28] Masatoshi Ikeda, Naoki Koide, Liyuan Han, Akira Sasahara, and Hiroshi Onishi; «Work Function on Dye-Adsorbed TiO_2 Surfaces Measured by Using a Kelvin Probe Force Microscope;» *The Journal of Physical Chemistry C* (**2008**); vol. 112 (17), pp. 6961–6967; DOI: 10.1021/jp077065+.
(Cited on page 3.)

[29] Harald Graaf, Carsten Maedler, Mirko Kehr, Thomas Baumgaertel, and Torsten Oekermann; «Identification of changes in the inorganic matrix of dye sensitized solar cells during preparation;» *physica status solidi (a)* (**2009**); pp. 2709–2714; ISSN 1862-6319; DOI: 10.1002/pssa.200925294.
(Cited on page 3.)

[30] G. Binnig, H. Rohrer, Ch. Gerber, and E. Weibel; «Surface Studies by Scanning Tunneling Microscopy;» *Phys. Rev. Lett.* (**1982**); vol. 49, pp. 57–61; DOI: 10.1103/PhysRevLett.49.57.
(Cited on pages 4 and 20.)

[31] G. Binnig, C. F. Quate, and Ch. Gerber; «Atomic Force Microscope;» *Phys. Rev. Lett.* (**1986**); vol. 56, pp. 930–933; DOI: 10.1103/PhysRevLett.56.930.
(Cited on pages 4 and 20.)

[32] F. Ohnesorge and G. Binnig; «True Atomic Resolution by Atomic Force Microscopy Through Repulsive and Attractive Forces;» *Science* (**1993**); vol. 260 (5113), pp. 1451–1456; DOI: 10.1126/science.260.5113.1451.
(Cited on page 4.)

[33] Takeshi Fukuma, Kei Kobayashi, Kazumi Matsushige, and Hirofumi Yamada; «True atomic resolution in liquid by frequency-modulation atomic force microscopy;» *Applied Physics Letters* (**2005**); vol. 87 (3), 034101; DOI: 10.1063/1.1999856.
(Cited on page 4.)

[34] M. Nonnenmacher, M. P. O'Boyle, and H. K. Wickramasinghe; «Kelvin probe force microscopy;» *Applied Physics Letters* (**1991**); vol. 58 (25), pp. 2921–2923; DOI: 10.1063/1.105227.
(Cited on pages 4 and 6.)

[35] J. E. Stern, B. D. Terris, H. J. Mamin, and D. Rugar; «Deposition and imaging of localized charge on insulator surfaces using a force microscope;» *Applied Physics Letters* (**1988**); vol. 53 (26), pp. 2717–2719; DOI: 10.1063/1.100162.
(Cited on pages 4 and 31.)

[36] S. Morita (editor); *Roadmap of Scanning Probe Microscopy*; NanoScience and Technology (Springer, 2006); ISBN 9783540343158.
(Cited on pages 4 and 31.)

[37] J. R. Matey and J. Blanc; «Scanning capacitance microscopy;» *Journal of Applied Physics* (**1985**); vol. 57 (5), p. 1437; ISSN 0021-8979; DOI: 10.1063/1.334506.
(Cited on pages 4 and 31.)

[38] Alex Henning, Gino Günzburger, Res Jöhr, Yossi Rosenwaks, Biljana Bozic-Weber, Catherine E. Housecroft, Edwin C. Constable, Ernst Meyer, and Thilo Glatzel; «Kelvin probe force microscopy of nanocrystalline TiO_2 photoelectrodes;» *Beilstein Journal of Nanotechnology* (**2013**); vol. 4, pp. 418–428; ISSN 2190-4286; DOI: 10.3762/bjnano.4.49.
(Cited on pages 4, 88, 117, 118, 120 and 123.)

[39] Hsue Yang. Liu, Fu Ren F. Fan, Charles W. Lin, and Allen J. Bard; «Scanning electrochemical and tunneling ultramicroelectrode microscope for high-resolution examination of electrode surfaces in solution;» *Journal of the American Chemical Society* (**1986**); vol. 108 (13), pp. 3838–3839; DOI: 10.1021/ja00273a054.

(Cited on page 5.)

[40] IlyaV. Pobelov, Chen Li, and Thomas Wandlowski; «Electrochemical Scanning Tunneling Microscopy;» in «Encyclopedia of Nanotechnology,» , edited by Bharat Bhushan; pp. 688–702 (Springer Netherlands, 2012); ISBN 978-90-481-9750-7; DOI: 10.1007/978-90-481-9751-4_46.
(Cited on page 5.)

[41] H. Siegenthaler; «STM in Electrochemistry;» *Springer Series in Surface Sciences* (**1995**); vol. 28, pp. 7–49; ISSN 0931-5195; DOI: 10.1007/978-3-642-79366-0_2.
(Cited on page 5.)

[42] Roland Wiesendanger and Hans-Joachim Güntherodt (editors); *Scanning Tunneling Microscopy II* (Springer Berlin Heidelberg, 1995); ISBN http://id.crossref.org/isbn/978-3-642-79366-0; DOI: 10.1007/978-3-642-79366-0.
(Cited on page 5.)

[43] L. A. Nagahara, T. Thundat, and S. M. Lindsay; «Preparation and characterization of STM tips for electrochemical studies;» *Review of Scientific Instruments* (**1989**); vol. 60 (10), pp. 3128–3130; DOI: 10.1063/1.1140590.
(Cited on page 5.)

[44] J. Wiechers, T. Twomey, D.M. Kolb, and R.J. Behm; «An in-situ scanning tunneling microscopy study of au (111) with atomic scale resolution;» *Journal of Electroanalytical Chemistry and Interfacial Electrochemistry* (**1988**); vol. 248 (2), pp. 451 – 460; ISSN 0022-0728; DOI: 10.1016/0022-0728(88)85106-4.
(Cited on page 5.)

[45] M. A. Schneeweiss and D. M. Kolb; «The Initial Stages of Copper Deposition on Bare and Chemically Modified Gold Electrodes;» *physica status solidi (a)* (**1999**); vol. 173 (1), pp. 51–71; ISSN 1521-396X; DOI: 10.1002/(SICI)1521-396X(199905)173:1<51::AID-PSSA51>3.0.CO;2-0.
(Cited on page 5.)

[46] Bo Han, Zhihai Li, Chen Li, Ilya Pobelov, Guijin Su, Rocio Aguilar-Sanchez, and Thomas Wandlowski; «From Self-Assembly to Charge Transport with Single Molecules - An Electrochemical Approach;» in «Templates in Chemistry III,» , edited by Peter Broekmann, Karl-Heinz Dötz, and ChristophA. Schalley; vol. 287 of *Topics in Current Chemistry*; pp. 181–255 (Springer Berlin Heidelberg, 2009); ISBN 978-3-540-89691-3; DOI: 10.1007/128_2008_152.
(Cited on page 5.)

[47] Allen J. Bard, Fu Ren F. Fan, Juhyoun Kwak, and Ovadia Lev; «Scanning electrochemical microscopy. Introduction and principles;» *Analytical Chemistry* (**1989**); vol. 61 (2), pp. 132–138; DOI: 10.1021/ac00177a011.
(Cited on page 5.)

[48] Michael V. Mirkin and Benjamin R. Horrocks; «Electroanalytical measurements using the scanning electrochemical microscope;» *Analytica Chimica Acta* (**2000**); vol. 406 (2), pp. 119 – 146; ISSN 0003-2670; DOI: 10.1016/S0003-2670(99)00630-3.
(Cited on pages 5 and 6.)

[49] Julie V. Macpherson, Patrick R. Unwin, Andrew C. Hillier, and Allen J. Bard; «In-Situ Imaging of Ionic Crystal Dissolution Using an Integrated Electrochemical/AFM Probe;» *Journal of the American Chemical Society* (**1996**); vol. 118 (27), pp. 6445–6452; DOI: 10.1021/ja960842r.
(Cited on pages 6 and 110.)

[50] Julie V. Macpherson and Patrick R. Unwin; «Combined Scanning Electrochemical-Atomic Force Microscopy;» *Analytical Chemistry* (**2000**); vol. 72 (2), pp. 276–285; DOI: 10.1021/ac990921w; pMID: 10658320.
(Cited on page 6.)

[51] Julie V. Macpherson and Patrick R. Unwin; «Noncontact Electrochemical Imaging with Combined Scanning Electrochemical Atomic Force Microscopy;» *Analytical Chemistry* (**2001**); vol. 73 (3), pp. 550–557; DOI: 10.1021/ac001072b; pMID: 11217761.
(Cited on pages 6 and 110.)

[52] Atsushi Kikukawa, Sumio Hosaka, and Ryo Imura; «Vacuum compatible high-sensitive Kelvin probe force microscopy;» *Review of Scientific Instruments* (**1996**); vol. 67 (4), p. 1463; ISSN 0034-6748; DOI: 10.1063/1.1146874.
(Cited on page 6.)

[53] Anna L. Domanski, Esha Sengupta, Karina Bley, Maria B. Untch, Stefan A. L. Weber, Katharina Landfester, Clemens K. Weiss, Hans-Jürgen Butt, and Rüdiger Berger; «Kelvin Probe Force Microscopy in Nonpolar Liquids;» *Langmuir* (**2012**); vol. 28 (39), pp. 13 892–13 899; ISSN 1520-5827; DOI: 10.1021/la302451h.
(Cited on pages 6, 19, 28 and 39.)

[54] Naritaka Kobayashi, Hitoshi Asakawa, and Takeshi Fukuma; «Nanoscale potential measurements in liquid by frequency modulation atomic force microscopy;» *Review of Scientific Instruments* (**2010**); vol. 81 (12), 123705; DOI: 10.1063/1.3514148.
(Cited on pages 7, 8, 19, 33, 36, 84, 102 and 122.)

[55] Naritaka Kobayashi, Hitoshi Asakawa, and Takeshi Fukuma; «Quantitative potential measurements of nanoparticles with different surface charges in liquid by open-loop electric potential microscopy;» *Journal of Applied Physics* (**2011**); vol. 110 (4), 044315; DOI: 10.1063/1.3625230.
(Cited on pages 7, 8, 36, 37 and 101.)

[56] Naritaka Kobayashi, Hitoshi Asakawa, and Takeshi Fukuma; «Dual frequency open-loop electric potential microscopy for local potential measurements in electrolyte solution with high ionic strength;» *Review of Scientific Instruments* (**2012**); vol. 83 (3), 033709; DOI: 10.1063/1.3698207.
(Cited on pages 7, 8, 37, 101, 102 and 114.)

[57] Senli Guo, Sergei V. Kalinin, and Stephen Jesse; «Half-harmonic Kelvin probe force microscopy with transfer function correction;» *Applied Physics Letters* (**2012**); vol. 100 (6), 063118; DOI: 10.1063/1.3684274.
(Cited on pages 8, 36, 84, 87 and 122.)

[58] Liam Collins, Jason I. Kilpatrick, Ivan V. Vlassiouk, Alexander Tselev, Stefan A. L. Weber, Stephen Jesse, Sergei V. Kalinin, and Brian J. Rodriguez; «Dual harmonic Kelvin probe force microscopy at the graphene-liquid interface;» *Applied Physics Letters* (**2014**); vol. 104 (13), p. 133 103; ISSN 1077-3118; DOI: 10.1063/1.4870074.

(Cited on page 8.)

[59] Helmut Tributsch and Melvin Calvin; «ELECTROCHEMISTRY OF EXCITED MOLECULES: PHOTO-ELECTROCHEMICAL REACTIONS OF CHLOROPHYLLS;» *Photochemistry and Photobiology* (**1971**); vol. 14 (2), pp. 95–112; ISSN 1751-1097; DOI: 10.1111/j.1751-1097.1971.tb06156.x.
(Cited on page 11.)

[60] Helmut Tributsch; «REACTION OF EXCITED CHLOROPHYLL MOLECULES AT ELECTRODES AND IN PHOTOSYNTHESIS*;» *Photochemistry and Photobiology* (**1972**); vol. 16 (4), pp. 261–269; ISSN 1751-1097; DOI: 10.1111/j.1751-1097.1972.tb06297.x.

[61] Mark T. Spitler and Melvin Calvin; «Electron transfer at sensitized TiO_2 electrodes;» *The Journal of Chemical Physics* (**1977**); vol. 66 (10), pp. 4294–4305; DOI: 10.1063/1.433739.
(Cited on page 11.)

[62] Hasitha C. Weerasinghe, Fuzhi Huang, and Yi-Bing Cheng; «Fabrication of flexible dye sensitized solar cells on plastic substrates;» *Nano Energy* (**2013**); vol. 2 (2), pp. 174 – 189; ISSN 2211-2855; DOI: 10.1016/j.nanoen.2012.10.004.
(Cited on page 11.)

[63] EPFL - Swiss Tech Convention Center; «Swiss Tech Convention center & sustainability;» URL: http://www.tstcc.ch/fileadmin/user_upload/SUSTAINABLE_STCC_english.pdf read on 31.1.2015
URL: http://www.tstcc.ch/fileadmin/user_upload/files/stcc/pdf/SUSTAINABLE_EN.pdf read on 2.3.2016 (**2015**).
(Cited on page 12.)

[64] Fei Cao, Gerko Oskam, and Peter C. Searson; «A Solid State, Dye Sensitized Photoelectrochemical Cell;» *The Journal of Physical Chemistry* (**1995**); vol. 99 (47), pp. 17 071–17 073; DOI: 10.1021/j100047a003.
(Cited on page 13.)

[65] Wataru Kubo, Kei Murakoshi, Takayuki Kitamura, Yuji Wada, Kenji Hanabusa, Hirofusa Shirai, and Shozo Yanagida; «Fabrication of Quasi-solid-state Dye-sensitized TiO_2 Solar Cells Using Low Molecular Weight Gelators;» *Chemistry Letters* (**1998**); vol. 27 (12), pp. 1241–1242; DOI: 10.1246/cl.1998.1241.
(Cited on page 13.)

[66] N.-G. Park, J. van de Lagemaat, and A. J. Frank; «Comparison of Dye-Sensitized Rutile- and Anatase-Based TiO_2 Solar Cells;» *The Journal of Physical Chemistry B* (**2000**); vol. 104 (38), pp. 8989–8994; DOI: 10.1021/jp9943651.
(Cited on page 13.)

[67] Raffaella Buonsanti, Elvio Carlino, Cinzia Giannini, Davide Altamura, Luisa De Marco, Roberto Giannuzzi, Michele Manca, Giuseppe Gigli, and P. Davide Cozzoli; «Hyperbranched Anatase TiO_2 Nanocrystals: Nonaqueous Synthesis, Growth Mechanism, and Exploitation in Dye-Sensitized Solar Cells;» *Journal of the American Chemical Society* (**2011**); vol. 133 (47), pp. 19 216–19 239; DOI: 10.1021/ja208418z.
(Cited on page 13.)

[68] Luisa De Marco, Michele Manca, Roberto Giannuzzi, Francesco Malara, Giovanna Melcarne, Giuseppe Ciccarella, Isabella Zama, Roberto Cingolani, and Giuseppe Gigli; «Novel Preparation Method of TiO_2-Nanorod-Based Photoelectrodes for Dye-Sensitized Solar Cells with Improved Light-Harvesting Efficiency;» *The Journal of Physical Chemistry C* (**2010**); vol. 114 (9), pp. 4228–4236; DOI: 10.1021/jp910346d.
(Cited on page 13.)

[69] Dae-Jin Yang, Hun Park, Seong-Je Cho, Ho-Gi Kim, and Won-Youl Choi; «TiO_2-nanotube-based dye-sensitized solar cells fabricated by an efficient anodic oxidation for high surface area;» *Journal of Physics and Chemistry of Solids* (**2008**); vol. 69 (5-6), pp. 1272 – 1275; ISSN 0022-3697; DOI: 10.1016/j.jpcs.2007.10.107; international Symposium on Intercalation Compounds.
(Cited on page 13.)

[70] Lola Gonzalez-Garcia, Irene Gonzalez-Valls, Monica Lira-Cantu, Angel Barranco, and Agustin R. Gonzalez-Elipe; «Aligned TiO_2 nanocolumnar layers prepared by PVD-GLAD for transparent dye sensitized solar cells;» *Energy Environ. Sci.* (**2011**); vol. 4, pp. 3426–3435; DOI: 10.1039/C0EE00489H.
(Cited on page 13.)

[71] Barbora Laskova, Marketa Zukalova, Ladislav Kavan, Alison Chou, Paul Liska, Zhang Wei, Liu Bin, Pavel Kubat, Elham Ghadiri, Jacques E. Moser, and Michael Grätzel; «Voltage enhancement in dye-sensitized solar cell using (001)-oriented anatase TiO_2 nanosheets;» *Journal of Solid State Electrochemistry* (**2012**); vol. 16 (9), pp. 2993–3001; ISSN 1432-8488; DOI: 10.1007/s10008-012-1729-0.
(Cited on page 13.)

[72] Patrick Brown, Kensuke Takechi, and Prashant V. Kamat; «Single-Walled Carbon Nanotube Scaffolds for Dye-Sensitized Solar Cells;» *The Journal of Physical Chemistry C* (**2008**); vol. 112 (12), pp. 4776–4782; DOI: 10.1021/jp7107472.
(Cited on page 13.)

[73] Zhong-Sheng Wang, Hiroshi Kawauchi, Takeo Kashima, and Hironori Arakawa; «Significant influence of TiO_2 photoelectrode morphology on the energy conversion efficiency of N719 dye-sensitized solar cell;» *Coordination Chemistry Reviews* (**2004**); vol. 248 (13-14), pp. 1381 – 1389; ISSN 0010-8545; DOI: 10.1016/j.ccr.2004.03.006; michael Graetzel Festschrift, a tribute for his 60th Birthday, Dye Sensitized Solar Cells.
(Cited on page 13.)

[74] Res Jöhr; *Evaluation of carotenoic acid sensitizers for use in dye-sensitized solar cells*; Master's thesis; Universität Basel (**2012**).
(Cited on pages 15, 16, 45 and 46.)

[75] Yasuhiro Tachibana, Jacques E. Moser, Michael Grätzel, David R. Klug, and James R. Durrant; «Subpicosecond Interfacial Charge Separation in Dye-Sensitized Nanocrystalline Titanium Dioxide Films;» *The Journal of Physical Chemistry* (**1996**); vol. 100 (51), pp. 20 056 – 20 062; ISSN 1541-5740; DOI: 10.1021/jp962227f.
(Cited on page 16.)

[76] John B. Asbury, Randy J. Ellingson, Hirendra N. Ghosh, Suzanne Ferrere, Arthur J. Nozik, and Tianquan Lian; «Femtosecond IR Study of Excited-State Relaxation and Electron-Injection Dynamics of $Ru(dcbpy)_2(NCS)_2$ in Solution and on Nanocrystalline TiO_2 and

Al_2O_3 Thin Films;» *The Journal of Physical Chemistry B* (**1999**); vol. 103 (16), pp. 3110–3119; DOI: 10.1021/jp983915x.
(Cited on pages 16 and 17.)

[77] Brian O'Regan, Jacques Moser, Marc Anderson, and Michael Graetzel; «Vectorial electron injection into transparent semiconductor membranes and electric field effects on the dynamics of light-induced charge separation;» *The Journal of Physical Chemistry* (**1990**); vol. 94 (24), pp. 8720–8726; DOI: 10.1021/j100387a017.
(Cited on page 16.)

[78] S. Nakade, S. Kambe, T. Kitamura, Y. Wada, and S. Yanagida; «Effects of Lithium Ion Density on Electron Transport in Nanoporous TiO_2 Electrodes;» *The Journal of Physical Chemistry B* (**2001**); vol. 105 (38), pp. 9150–9152; DOI: 10.1021/jp011375p.
(Cited on page 16.)

[79] Shingo Kambe, Shogo Nakade, Yuji Wada, Takayuki Kitamura, and Shozo Yanagida; «Effects of crystal structure, size, shape and surface structural differences on photo-induced electron transport in TiO_2 mesoporous electrodes;» *J. Mater. Chem.* (**2002**); vol. 12, pp. 723–728; DOI: 10.1039/B105142N.
(Cited on page 16.)

[80] Fei Cao, Gerko Oskam, Gerald J. Meyer, and Peter C. Searson; «Electron Transport in Porous Nanocrystalline TiO_2 Photoelectrochemical Cells;» *The Journal of Physical Chemistry* (**1996**); vol. 100 (42), pp. 17 021–17 027; DOI: 10.1021/jp9616573.
(Cited on page 16.)

[81] L. Dloczik, O. Ileperuma, I. Lauermann, L. M. Peter, E. A. Ponomarev, G. Redmond, N. J. Shaw, and I. Uhlendorf; «Dynamic Response of Dye-Sensitized Nanocrystalline Solar Cells: Characterization by Intensity Modulated Photocurrent Spectroscopy;» *The Journal of Physical Chemistry B* (**1997**); vol. 101 (49), pp. 10 281–10 289; DOI: 10.1021/jp972466i.
(Cited on page 16.)

[82] J. van de Lagemaat and A. J. Frank; «Effect of the Surface-State Distribution on Electron Transport in Dye-Sensitized TiO_2 Solar Cells: Nonlinear Electron-Transport Kinetics;» *The Journal of Physical Chemistry B* (**2000**); vol. 104 (18), pp. 4292–4294; DOI: 10.1021/jp000836o.
(Cited on page 16.)

[83] Donald J. Fitzmaurice and Heinz. Frei; «Transient near-infrared spectroscopy of visible light sensitized oxidation of iodide at colloidal titania;» *Langmuir* (**1991**); vol. 7 (6), pp. 1129–1137; DOI: 10.1021/la00054a019.
(Cited on page 17.)

[84] Ana F. Nogueira, Marco-A. De Paoli, Ivan Montanari, Richard Monkhouse, Jenny Nelson, and James R. Durrant; «Electron Transfer Dynamics in Dye Sensitized Nanocrystalline Solar Cells Using a Polymer Electrolyte;» *The Journal of Physical Chemistry B* (**2001**); vol. 105 (31), pp. 7517–7524; DOI: 10.1021/jp010420q.
(Cited on page 17.)

[85] Darius Kuciauskas, Michael S. Freund, Harry B. Gray, Jay R. Winkler, and Nathan S. Lewis; «Electron Transfer Dynamics in Nanocrystalline Titanium Dioxide Solar Cells Sensitized with Ruthenium or Osmium Polypyridyl Complexes;» *The Journal of Physical Chemistry B* (**2001**); vol. 105 (2), pp. 392–403; DOI: 10.1021/jp0025451.

(Cited on pages 17 and 18.)

[86] Saif A. Haque, Yasuhiro Tachibana, David R. Klug, and James R. Durrant; «Charge Recombination Kinetics in Dye-Sensitized Nanocrystalline Titanium Dioxide Films under Externally Applied Bias;» *The Journal of Physical Chemistry B* (**1998**); vol. 102 (10), pp. 1745–1749; DOI: 10.1021/jp973335k.
(Cited on page 17.)

[87] Serge Pelet, Jacques-E. Moser, and Michael Grätzel; «Cooperative Effect of Adsorbed Cations and Iodide on the Interception of Back Electron Transfer in the Dye Sensitization of Nanocrystalline TiO_2;» *The Journal of Physical Chemistry B* (**2000**); vol. 104 (8), pp. 1791–1795; DOI: 10.1021/jp9934477.
(Cited on page 17.)

[88] M. K. Nazeeruddin, A. Kay, I. Rodicio, R. Humphry-Baker, E. Mueller, P. Liska, N. Vlachopoulos, and M. Graetzel; «Conversion of light to electricity by cis-X2bis(2,2'-bipyridyl-4,4'-dicarboxylate)ruthenium(II) charge-transfer sensitizers (X = Cl-, Br-, I-, CN-, and SCN-) on nanocrystalline titanium dioxide electrodes;» *Journal of the American Chemical Society* (**1993**); vol. 115 (14), pp. 6382–6390; DOI: 10.1021/ja00067a063.
(Cited on pages 17 and 48.)

[89] Sara E. Koops, Brian C. O'Regan, Piers R. F. Barnes, and James R. Durrant; «Parameters Influencing the Efficiency of Electron Injection in Dye-Sensitized Solar Cells;» *Journal of the American Chemical Society* (**2009**); vol. 131 (13), pp. 4808–4818; DOI: 10.1021/ja8091278; pMID: 19334776.
(Cited on page 17.)

[90] Susan G. Yan, Janice S. Prieskorn, Youngjin Kim, and Joseph T. Hupp; «In search of the inverted region: chromophore-based driving force dependence of interfacial elecron transfer reactivity at the nanocrystalline titanium dioxide semiconductor/solution interface;» *The Journal of Physical Chemistry B* (**2000**); vol. 104 (46), pp. 10 871–10 877; DOI: 10.1021/jp001628z.
(Cited on page 18.)

[91] Jacques E. Moser and Michael Grätzel; «Observation of temperature independent heterogeneous electron transfer reactions in the inverted Marcus region;» *Chemical Physics* (**1993**); vol. 176 (2-3), pp. 493 – 500; ISSN 0301-0104; DOI: 10.1016/0301-0104(93)80257-A.
(Cited on page 18.)

[92] John N. Clifford, Emilio Palomares, Md. K Nazeeruddin, Michael. Grätzel, Jenny Nelson, X. Li, Nicholas J. Long, and James R. Durrant; «Molecular Control of Recombination Dynamics in Dye-Sensitized Nanocrystalline TiO_2 Films: Free Energy vs Distance Dependence;» *Journal of the American Chemical Society* (**2004**); vol. 126 (16), pp. 5225–5233; DOI: 10.1021/ja039924n.
(Cited on page 18.)

[93] Petra J. Cameron and Laurence M. Peter; «Characterization of Titanium Dioxide Blocking Layers in Dye-Sensitized Nanocrystalline Solar Cells;» *The Journal of Physical Chemistry B* (**2003**); vol. 107 (51), pp. 14 394–14 400; DOI: 10.1021/jp030790+.
(Cited on pages 18, 45 and 48.)

[94] P. J. Cameron and L. M. Peter; «How Does Back-Reaction at the Conducting Glass Substrate Influence the Dynamic Photovoltage Response of Nanocrystalline Dye-Sensitized Solar Cells?» *The Journal of Physical Chemistry B* (**2005**); vol. 109 (15), pp. 7392–7398; DOI: 10.1021/jp0407270.
(Cited on pages 18, 45 and 48.)

[95] Bart W. Hoogenboom; «AFM in Liquids;» in «Encyclopedia of Nanotechnology,» , edited by Bharat Bhushan; pp. 83–89 (Springer Netherlands, 2012); ISBN 978-90-481-9750-7; DOI: 10.1007/978-90-481-9751-4_108.
(Cited on page 19.)

[96] Jacob N. Israelachvili; *Intermolecular and Surface Forces*; third edition ed. (Academic Press, San Diego, 2011); ISBN 978-0-12-375182-9.
(Cited on page 22.)

[97] F. London and M. Polanyi; «Über die atomtheoretische Deutung der Adsorptionskräfte;» *Naturwissenschaften* (**1930**); vol. 18 (50), pp. 1099–1100; ISSN 0028-1042; DOI: 10.1007/BF01492533.
(Cited on page 22.)

[98] H.C. Hamaker; «The London - van der Waals attraction between spherical particles;» *Physica* (**1937**); vol. 4 (10), pp. 1058 – 1072; ISSN 0031-8914; DOI: 10.1016/S0031-8914(37)80203-7.
(Cited on page 22.)

[99] Sascha Koch; *Investigation of hexagonal 2D super structures by dynamic force spectroscopy: boron nitride and graphene on transition metals.*; Ph.D. thesis; University of Basel, Faculty of Science (**2012**); DOI: 10.5451/unibas-005976956.
(Cited on page 22.)

[100] Lennart Bergström; «Hamaker constants of inorganic materials;» *Advances in Colloid and Interface Science* (**1997**); vol. 70 (0), pp. 125 – 169; ISSN 0001-8686; DOI: 10.1016/S0001-8686(97)00003-1.
(Cited on page 23.)

[101] Hudlet, S., Saint Jean, M., Guthmann, C., and Berger, J.; «Evaluation of the capacitive force between an atomic force microscopy tip and a metallic surface;» *Eur. Phys. J. B* (**1998**); vol. 2 (1), pp. 5–10; DOI: 10.1007/s100510050219.
(Cited on page 23.)

[102] B. M. Law and F. Rieutord; «Electrostatic forces in atomic force microscopy;» *Phys. Rev. B* (**2002**); vol. 66, p. 035 402; DOI: 10.1103/PhysRevB.66.035402.
(Cited on page 23.)

[103] J. E. Jones; «On the Determination of Molecular Fields. I. From the Variation of the Viscosity of a Gas with Temperature;» *Proceedings of the Royal Society of London A: Mathematical, Physical and Engineering Sciences* (**1924**); vol. 106 (738), pp. 441–462; ISSN 0950-1207; DOI: 10.1098/rspa.1924.0081.
(Cited on page 24.)

[104] Rubén Pérez, Michael C. Payne, Ivan Štich, and Kiyoyuki Terakura; «Role of Covalent Tip-Surface Interactions in Noncontact Atomic Force Microscopy on Reactive Surfaces;» *Phys. Rev. Lett.* (**1997**); vol. 78, pp. 678–681; DOI: 10.1103/PhysRevLett.78.678.

(Cited on page 24.)

[105] N. Umeda; «Scanning attractive force microscope using photothermal vibration;» *J. Vac. Sci. Technol. B* (**1991**); vol. 9 (2), p. 1318; ISSN 0734-211X; DOI: 10.1116/1.585187.
(Cited on page 26.)

[106] Ken-ichi Umeda, Noriaki Oyabu, Kei Kobayashi, Yoshiki Hirata, Kazumi Matsushige, and Hirofumi Yamada; «High-Resolution Frequency-Modulation Atomic Force Microscopy in Liquids Using Electrostatic Excitation Method;» *Applied Physics Express* (**2010**); vol. 3 (6), p. 065 205; ISSN 1882-0786; DOI: 10.1143/apex.3.065205.
(Cited on pages 26 and 104.)

[107] S. Sadewasser and T. Glatzel (editors); *Kelvin Probe Force Microscopy: Measuring and Compensating Electrostatic Forces*; Springer Series in Surface Sciences (Springer-Verlag Berlin Heidelberg, 2011); ISBN 9783642225666.
(Cited on page 28.)

[108] Wilhelm Melitz, Jian Shen, Andrew C. Kummel, and Sangyeob Lee; «Kelvin probe force microscopy and its application;» *Surface Science Reports* (**2011**); vol. 66 (1), pp. 1 – 27; ISSN 0167-5729; DOI: 10.1016/j.surfrep.2010.10.001.
(Cited on page 28.)

[109] Lord Kelvin; «V. Contact electricity of metals;» *Philosophical Magazine Series 5* (**1898**); vol. 46 (278), pp. 82–120; DOI: 10.1080/14786449808621172.
(Cited on page 28.)

[110] Ali Sadeghi, Alexis Baratoff, S. Alireza Ghasemi, Stefan Goedecker, Thilo Glatzel, Shigeki Kawai, and Ernst Meyer; «Multiscale approach for simulations of Kelvin probe force microscopy with atomic resolution;» *Phys. Rev. B* (**2012**); vol. 86 (7), p. 075 407; ISSN 1550-235X; DOI: 10.1103/physrevb.86.075407.
(Cited on page 30.)

[111] Wilford N Hansen and Galen J Hansen; «Standard reference surfaces for work function measurements in air;» *Surface Science* (**2001**); vol. 481 (1-3), pp. 172 – 184; ISSN 0039-6028; DOI: 10.1016/S0039-6028(01)01036-6.
(Cited on page 32.)

[112] H. Ago, Th. Kugler, F. Cacialli, K. Petritsch, R.H. Friend, W.R. Salaneck, Y. Ono, T. Yamabe, and K. Tanaka; «Workfunction of purified and oxidised carbon nanotubes;» *Synthetic Metals* (**1999**); vol. 103 (1-3), pp. 2494–2495; ISSN 0379-6779; DOI: 10.1016/s0379-6779(98)01062-5.
(Cited on page 32.)

[113] Seigo Ito, Takurou N. Murakami, Pascal Comte, Paul Liska, Carole Grätzel, Mohammad K. Nazeeruddin, and Michael Grätzel; «Fabrication of thin film dye sensitized solar cells with solar to electric power conversion efficiency over 10 %;» *Thin Solid Films* (**2008**); vol. 516 (14), pp. 4613 – 4619; ISSN 0040-6090; DOI: 10.1016/j.tsf.2007.05.090; 6th International Conference on Coatings on Glass and Plastics (ICCG6)- Advanced Coatings for Large-Area or High-Volume Products.
(Cited on pages 43, 44, 46 and 52.)

[114] Jessica Krüger; *Interface engineering in solid-state dye-sensitized solar cells*; Ph.D. thesis; EPFL; Lausanne (**2003**); DOI: 10.5075/epfl-thesis-2793.
(Cited on pages 44, 49, 52 and 70.)

[115] Hubert Hug, Michael Bader, Peter Mair, and Thilo Glatzel; «Biophotovoltaics: Natural pigments in dye-sensitized solar cells;» *Applied Energy* (**2014**); vol. 115 (0), pp. 216 – 225; ISSN 0306-2619; DOI: 10.1016/j.apenergy.2013.10.055.
(Cited on page 46.)

[116] Seigo Ito, Paul Liska, Pascal Comte, Raphael Charvet, Peter Pechy, Udo Bach, Lukas Schmidt-Mende, Shaik Mohammed Zakeeruddin, Andreas Kay, Mohammad K. Nazeeruddin, and Michael Gratzel; «Control of dark current in photoelectrochemical (TiO_2/I^--I_3^-) and dye-sensitized solar cells;» *Chem. Commun.* (**2005**); vol. 34, pp. 4351–4353; DOI: 10.1039/B505718C.
(Cited on page 48.)

[117] Luigi Vesce, Riccardo Riccitelli, Giuseppe Soscia, Thomas M. Brown, Aldo Di Carlo, and Andrea Reale; «Optimization of nanostructured titania photoanodes for dye-sensitized solar cells: Study and experimentation of $TiCl_4$ treatment;» *Journal of Non-Crystalline Solids* (**2010**); vol. 356 (37-40), pp. 1958 – 1961; ISSN 0022-3093; DOI: 10.1016/j.jnoncrysol.2010.05.070; joint Conferences on Advanced Materials: Functional and Nanonstructured Materials - FNMA'09; Intermolecular and Magnetic Interactions in Matter - IMIM'09.
(Cited on page 48.)

[118] Andreas Kay; *Solar cells based on dye-sensitized nanocrystalline TiO_2 electrodes*; Ph.D. thesis; EPFL; Lausanne (**1994**); DOI: 10.5075/epfl-thesis-1214.
(Cited on pages 48 and 71.)

[119] Ladislav Kavan and Michael Grätzel; «Highly efficient semiconducting TiO_2 photoelectrodes prepared by aerosol pyrolysis;» *Electrochimica Acta* (**1995**); vol. 40 (5), pp. 643 – 652; ISSN 0013-4686; DOI: 10.1016/0013-4686(95)90400-W.
(Cited on page 48.)

[120] Mao-Sung Wu, Chen-Hsiu Tsai, and Tzu-Chien Wei; «Electrochemical formation of transparent nanostructured TiO_2 film as an effective bifunctional layer for dye-sensitized solar cells;» *Chem. Commun.* (**2011**); vol. 47, pp. 2871–2873; DOI: 10.1039/C0CC04888G.
(Cited on page 50.)

[121] Seigo Ito, Peter Chen, Pascal Comte, Mohammad Khaja Nazeeruddin, Paul Liska, Péter Péchy, and Michael Grätzel; «Fabrication of screen-printing pastes from TiO_2 powders for dye-sensitised solar cells;» *Progress in Photovoltaics: Research and Applications* (**2007**); vol. 15 (7), pp. 603–612; ISSN 1099-159X; DOI: 10.1002/pip.768.
(Cited on pages 50, 51 and 53.)

[122] K. D. Benkstein, N. Kopidakis, J. van de Lagemaat, and A. J. Frank; «Influence of the Percolation Network Geometry on Electron Transport in Dye-Sensitized Titanium Dioxide Solar Cells;» *The Journal of Physical Chemistry B* (**2003**); vol. 107 (31), pp. 7759–7767; DOI: 10.1021/jp0226811.
(Cited on page 51.)

[123] S. Ito, S.M. Zakeeruddin, R. Humphry-Baker, P. Liska, R. Charvet, P. Comte, M.K. Nazeeruddin, P. Péchy, M. Takata, H. Miura, S. Uchida, and M. Grätzel; «High-Efficiency Organic-Dye- Sensitized Solar Cells Controlled by Nanocrystalline-TiO_2 Electrode Thickness;» *Advanced Materials* (**2006**); vol. 18 (9), pp. 1202–1205; ISSN 1521-4095; DOI: 10.1002/adma.200502540.
(Cited on page 52.)

[124] Zhipan Zhang, Seigo Ito, Brian O'Regan, Daibin Kuang, Shaik Mohammed Zakeeruddin, Paul Liska, Raphaël Charvet, Pascal Comte, Mohammad Khaja Nazeeruddin, Peter Pechy, Robin Humphry-Baker, Tsuguo Koyanagi, Takaki Mizuno, and Michael Graetzel; «The Electronic Role of the TiO_2 Light-Scattering Layer in Dye-Sensitized Solar Cells;» *Zeitschrift für Physikalische Chemie* (**2007**); vol. 221 (3), pp. 319 – 327; ISSN 0942-9352; DOI: 10.1524/zpch.2007.221.3.319.
(Cited on page 52.)

[125] Ghassan E. Jabbour, Rachel Radspinner, and Nasser Peyghambarian; «Screen printing for the fabrication of organic light-emitting devices;» *Selected Topics in Quantum Electronics, IEEE Journal of* (**2001**); vol. 7 (5), pp. 769–773; ISSN 1077-260X; DOI: 10.1109/2944.979337.
(Cited on page 58.)

[126] Rosidah Alias and Sabrina Mohd Shapee; «Rheological Behaviors and Their Correlation with Printing Performance of Silver Paste for LTCC Tape;» in «Rheology,» , edited by Juan De Vincente; chap. 13, pp. 321–339 (In-Tech, 2012); ISBN 978-953-51-0187-1; DOI: 10.5772/35004; available from: http://www.intechopen.com/books/rheology/rheological-behaviors-and-their-correlation-with-printing-performance-of-silver-paste-for-ltcc-tape.
(Cited on page 58.)

[127] Henrik Jensen, Karsten D. Joensen, Jens-Erik Jørgensen, Jan Skov Pedersen, and G. Søgaard; «Characterization of nanosized partly crystalline photocatalysts;» *Journal of Nanoparticle Research* (**2004**); vol. 6 (5), pp. 519–526; ISSN 1388-0764; DOI: 10.1007/s11051-004-1714-3.
(Cited on page 60.)

[128] Jan Kehres, Jens Wenzel Andreasen, Frederik Christian Krebs, Alfons M. Molenbroek, Ib Chorkendorff, and Tejs Vegge; «Combined in situ small- and wide-angle X-ray scattering studies of TiO_2 nanoparticle annealing to 1023 K;» *J Appl Cryst* (**2010**); vol. 43 (6), pp. 1400–1408; ISSN 0021-8898; DOI: 10.1107/s0021889810041907.
(Cited on page 60.)

[129] E. Lorenzo; *Solar Electricity: Engineering of Photovoltaic Systems* (PROGENSA, 1994); ISBN 9788486505554.
(Cited on page 72.)

[130] Ralph W. Matthews and Stephen R. McEvoy; «Photocatalytic degradation of phenol in the presence of near-UV illuminated titanium dioxide;» *Journal of Photochemistry and Photobiology A: Chemistry* (**1992**); vol. 64 (2), pp. 231 – 246; ISSN 1010-6030; DOI: 10.1016/1010-6030(92)85110-G.
(Cited on page 80.)

[131] Yasuo Chiba, Ashraful Islam, Yuki Watanabe, Ryoichi Komiya, Naoki Koide, and Liyuan Han; «Dye-Sensitized Solar Cells with Conversion Efficiency of 11.1%;» *Jpn. J. Appl. Phys.* (**2006**); vol. 45 (No. 25), pp. L638 – L640; ISSN 0021-4922; DOI: 10.1143/jjap.45.l638.
(Cited on page 81.)

[132] Aswani Yella, Hsuan-Wei Lee, Hoi Nok Tsao, Chenyi Yi, Aravind Kumar Chandiran, Md.Khaja Nazeeruddin, Eric Wei-Guang Diau, Chen-Yu Yeh, Shaik M Zakeeruddin, and Michael Grätzel; «Porphyrin-Sensitized Solar Cells with Cobalt (II/III)-Based Redox Electrolyte Exceed 12 Percent Efficiency;» *Science* (**2011**); vol. 334 (6056), pp. 629–634; DOI: 10.1126/science.1209688.
(Cited on page 81.)

[133] Eiji Yamazaki, Masaki Murayama, Naomi Nishikawa, Noritsugu Hashimoto, Masashi Shoyama, and Osamu Kurita; «Utilization of natural carotenoids as photosensitizers for dye-sensitized solar cells;» *Solar Energy* (**2007**); vol. 81 (4), pp. 512 – 516; ISSN 0038-092X; DOI: 10.1016/j.solener.2006.08.003.
(Cited on page 81.)

[134] Gerrit Boschloo and Anders Hagfeldt; «Characteristics of the Iodide/Triiodide Redox Mediator in Dye-Sensitized Solar Cells;» *Accounts of Chemical Research* (**2009**); vol. 42 (11), pp. 1819–1826; DOI: 10.1021/ar900138m.
(Cited on page 86.)

[135] H. Diesinger, D. Deresmes, J.-P. Nys, and T. Mélin; «Kelvin force microscopy at the second cantilever resonance: An out-of-vacuum crosstalk compensation setup;» *Ultramicroscopy* (**2008**); vol. 108 (8), pp. 773 – 781; ISSN 0304-3991; DOI: 10.1016/j.ultramic.2008.01.003.
(Cited on page 91.)

[136] Ken-ichi Umeda, Kei Kobayashi, Noriaki Oyabu, Yoshiki Hirata, Kazumi Matsushige, and Hirofumi Yamada; «Analysis of capacitive force acting on a cantilever tip at solid/liquid interfaces;» *Journal of Applied Physics* (**2013**); vol. 113 (15), 154311; DOI: 10.1063/1.4801795.
(Cited on pages 99, 103, 104 and 107.)

[137] Ken-ichi Umeda, Kei Kobayashi, Noriaki Oyabu, Yoshiki Hirata, Kazumi Matsushige, and Hirofumi Yamada; «Practical aspects of Kelvin-probe force microscopy at solid/liquid interfaces in various liquid media;» *Journal of Applied Physics* (**2014**); vol. 116 (13), 134307; DOI: 10.1063/1.4896881.
(Cited on pages 104, 105, 106, 107, 108 and 123.)

[138] Liam Collins, Stephen Jesse, Jason I. Kilpatrick, Alexander Tselev, Oleksandr Varenyk, M. Baris Okatan, Stefan A. L. Weber, Amit Kumar, Nina Balke, Sergei V. Kalinin, and Brian J. Rodriguez; «Probing charge screening dynamics and electrochemical processes at the solid-liquid interface with electrochemical force microscopy;» *Nat Commun* (**2014**); vol. 5, p. 3871; DOI: 10.1038/ncomms4871.
(Cited on pages 99 and 108.)

[139] G. Gramse, M. A. Edwards, L. Fumagalli, and G. Gomila; «Dynamic electrostatic force microscopy in liquid media;» *Appl. Phys. Lett.* (**2012**); vol. 101 (21), p. 213 108; ISSN 0003-6951; DOI: 10.1063/1.4768164.
(Cited on page 102.)

[140] William M. Haynes (editor); *100 Year CRC Anniversary. CRC Handbook of Chemistry and Physics*; 94 ed. (Taylor & Francis, 2013); ISBN 978-1-4665-7114-3.
(Cited on pages 102 and 104.)

[141] Richard Buchner, Glenn T. Hefter, and Peter M. May; «Dielectric Relaxation of Aqueous NaCl Solutions;» *The Journal of Physical Chemistry A* (**1999**); vol. 103 (1), pp. 1 – 9; ISSN 1520-5215; DOI: 10.1021/jp982977k.
(Cited on page 102.)

[142] Paul R. Gray, Paul j. Hurst, Stephen H. Lewis, and Robert G. Meyer; *Analysis and Design of Analog Integrated Circuits*; 5 ed. (J. Wiley and Sons, New York, 2009); ISBN 978-0-470-24599-6.
(Cited on page 102.)

[143] Roberto Raiteri and Hans-Juergen Butt; «Measuring Electrochemically Induced Surface Stress with an Atomic Force Microscope;» *The Journal of Physical Chemistry* (**1995**); vol. 99 (43), pp. 15 728 – 15 732; ISSN 1541-5740; DOI: 10.1021/j100043a008.
(Cited on page 103.)

[144] Allen J. Bard and Larry R. Faulkner; *Electrochemical Methods: Fundamentals and Applications, Student Solutions Manual, 2nd Edition* (John Wiley & Sons, Inc, 2001); ISBN 978-0-471-40521-4.
(Cited on page 104.)

[145] H.J. Butt, K. Graf, and M. Kappl; *Physics and Chemistry of Interfaces* (Wiley, 2006); ISBN 9783527606405.
(Cited on page 106.)

List of Figures

List of Tables

A. DSSC fabrication procedure

For the fabrication of DSSCs FTO coated glass (TCO 22-7, Solaronix SA) was cut to the dimensions 1.5 cm × 2 cm for both electrodes. The following steps were performed to prepare various cell components and to assemble the cell:

1. For the photo-anode:
    - The glass-slide was cleaned by sonication for 15 min in a detergent solution (Sonoswiss L2) in H_2O (2 % by volume), rinsed with tap- and sonicated in MilliQ water and ethanol (5 min each). Afterwards it was dried under nitrogen flux. Directly before the deposition of the titania the substrate was further cleaned by UV/Ozone treatment for 18 min (UVO-Cleaner R, Model42-220, Jelight Company Inc.).
    - The glass-slides were pre-treated by immersion in an aqueous $TiCl_4$ solution (40 mM in MilliQ water for 30 min at 70 °C, then they were rinsed with MilliQ water and ethanol and dried under nitrogen flux.
    - Titania layers were deposited by spray-deposition, screen-printing or doctor-blading as is described in Sec. 3.1.4.
    - Gradual sintering of the deposited layers was performed in a box-type furnace and an environment of normal air. The heating program was adapted from Jessica Krügers PhD thesis to the heating-rates of our furnace. It is outlined in Fig. 3.14
    - The sintered layers were post-treated by repeating the immersion in aqueous $TiCl_4$,
    - and subsequently sintered 500 °C for 30 min on a heating plate.
    - For the sensitisation of the layers by oxygen-sensitive organic dyes they were transferred to the glove box directly from the sintering-plate (see Sec. 3.2.3). For sensitisation by less-sensitive dyes they were cooled down in air.

- The still warm (80 °C) anodes were immersed in the dye-solution for approximately 24 h.
- The sensitised layers were washed with the sensitiser-solution solvent and dried under nitrogen flux.

2. For the counter-electrode:
   - A hole for the filling of the cell was drilled (⌀ : 0.9 mm). For this step the FTO layer was protected with scotch.
   - The scotch was removed and the slide was cleaned as described for the photoanode. Subsequently it was sonicated in a 0.1 M solution of HCl in ethanol, and in acetone for 10 min each. To complete the cleaning process the layer was heated to 400 °C for 15 min.
   - A drop of platinum precursor (Platisol T, Solaronix SA) was spread on the sample, which was then heated to 400 °C for 15 min.
   - For assembly of cells with sensitive dyes the electrodes were transferred to the glove box directly from the sintering-plate (see Sec. 3.2.3).
3. Dye solutions and electrolyte
   - The dyes were dissolved in ethanol (N719) or Tetra Hydro Furan (THF) (natural organic dyes). The solvents were anhydrous and at least High Pressure Liquid Chromatography (HPLC)-grade.
   - The standard electrolyte was made according to the following recipe: Iodine (I_2) in a concentration of 0.05 M and lithium iodide (LiI) in a concentration of 0.5 M were used as redox-couple. Methylbenzimidazole in a concentration of 0.5 M was used as additive. The used solvent was 3-methoxypropionitrile.
4. Assembly of the cell
   - A round ring-gasket of an inner- and an outer diameter of 10 mm and 14 mm respectively was cut from a surlyn® foil of 25 µm thickness by means of helve pickers. The centre ring was used as sealing for the filling-hole in the counter-electrode. The surlyn® parts were prepared in advance and kept under vacuum or nitrogen, since they draw water.

- The cell components were carefully aligned and sealed by heating the gasket through the counter electrode by means of a soldering-iron with a modified tip and a temperature of 250 °C for 30 s. The filling-hole was sealed by application of its sealing onto the still hot glass.
- The cell was filled by vacuum-back-filling: A cannula was stuck through the sealed filling-hole, the air was evacuated from the cell-interior by three repetitions of an application of a vacuum and subsequent flushing with nitrogen. Then the cannula was filled with a drop of electrolyte, the vacuum was reapplied and by flushing with nitrogen the electrolyte was drawn into the cell.
- The filling hole was resealed by another surlyn® foil and a cover-glass.
- The contacts were painted with silver paint (2psi).

B. Large images of KPFM measurements

In this appendix the full data sets of all the measurements in the main body of this thesis are collected. The data sets consist of the topography data, the $A_{1\omega_{ac}}$- and $A_{2\omega_{ac}}$-signals and the CPD. For the measurements in air both the CPD_{CL} and the CPD_{OL} are presented and also additional curves such as the distribution of the two CPDs to show the observed CPD-shift. The data is completed by the V_{ac}-spectroscopy-data, which are presented for each set of measurements, but also comparative for each sample.

B.1. KPFM measurements on Titania

B.1.1. Overview

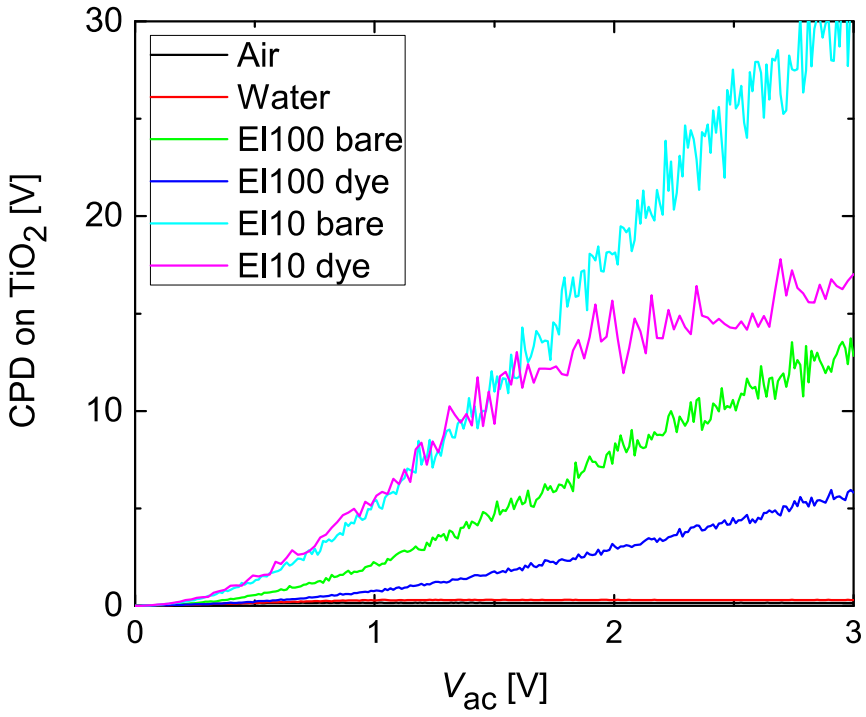

Figure B.1.: *Data of the V_{ac}-spectroscopy-measurements on titania, comparison of the dependence of the CPD on the excitation voltage (CPD(V_{ac})) in different environments. The curves show the absolute of the measured CPD.*

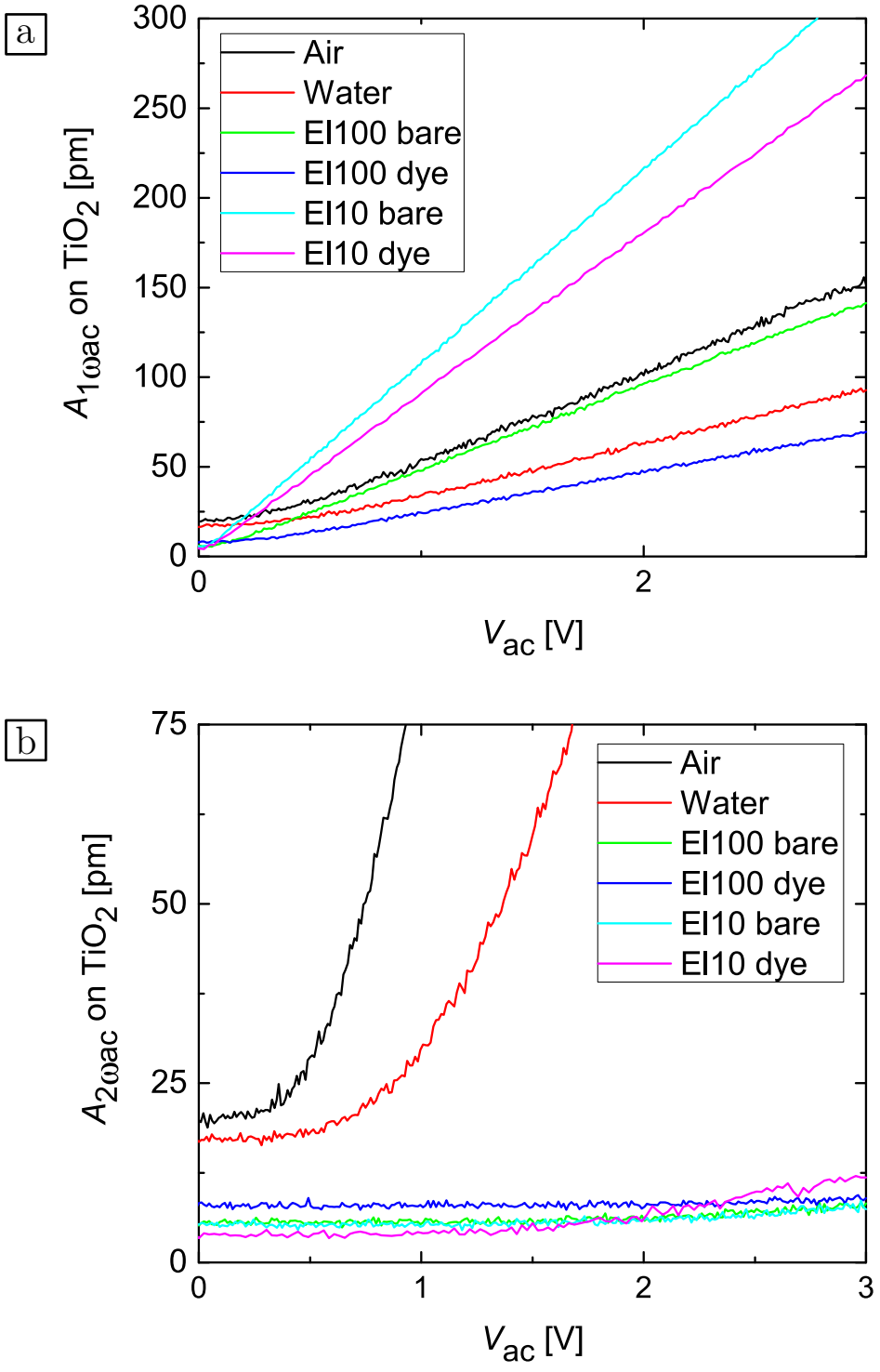

Figure B.2.: *Data of the V_{ac}-spectroscopy-measurements on TiO_2, comparison of the measurements in different environments. a) $A_{1\omega_{ac}}(V_{ac})$, and b) $A_{2\omega_{ac}}(V_{ac})$.*

B.1.2. Titania in air

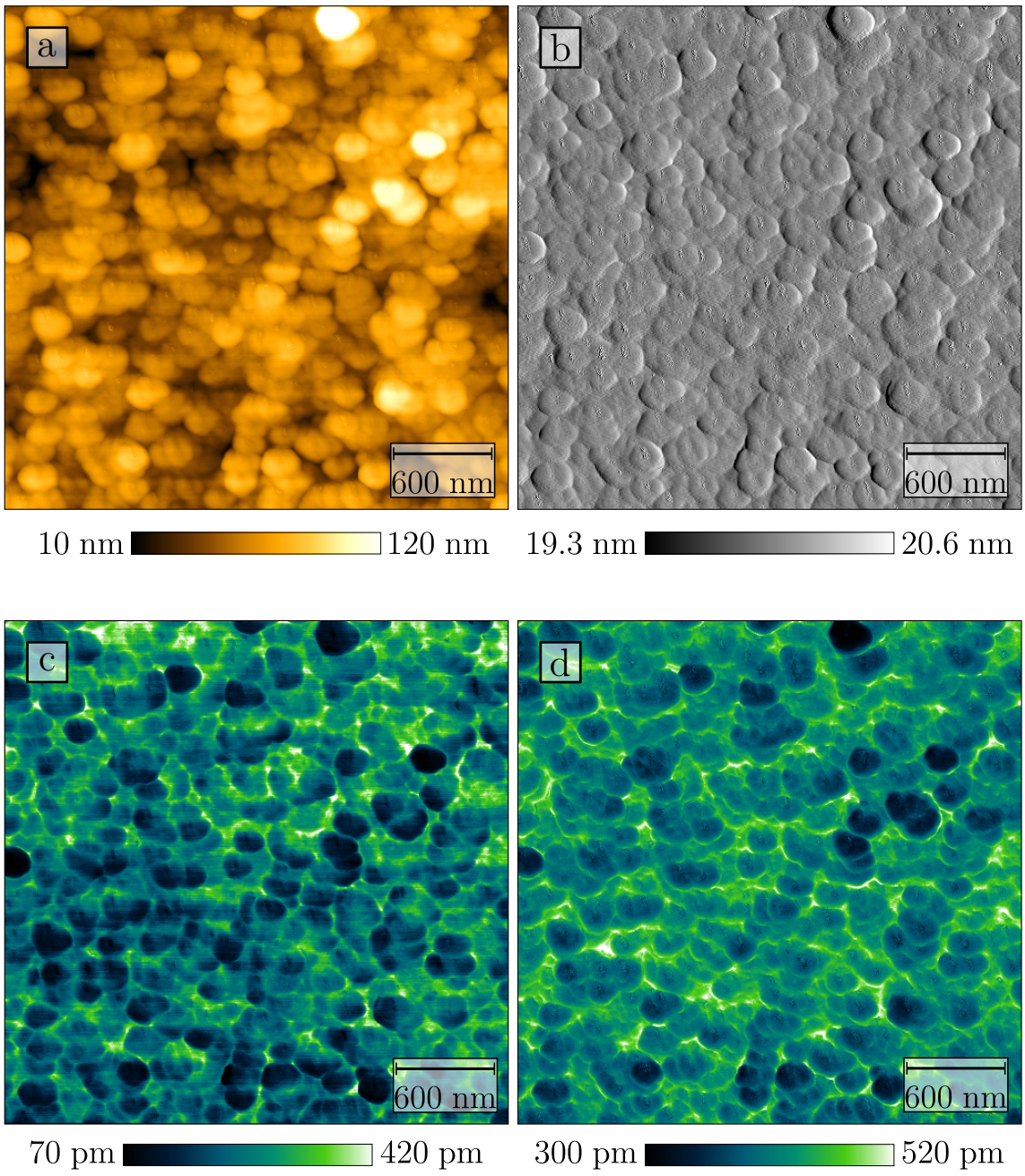

Figure B.3.: *Topography and amplitudes of the measurement performed on TiO_2 in air at an excitation voltage of $V_{ac} = 2\,\mathrm{V}$. a) Topography, b) A_{1st}, c) $A_{1\omega_{ac}}$, d) $A_{2\omega_{ac}}$.*
Scan parameters: Cantilever: NCL-Pt; $f_{1st} = 149\,\mathrm{kHz}$; $A_{1st} = 20\,\mathrm{nm}$; $f_{2nd} = 930\,\mathrm{kHz}$; $V_{ac} = 2\,\mathrm{V}$.

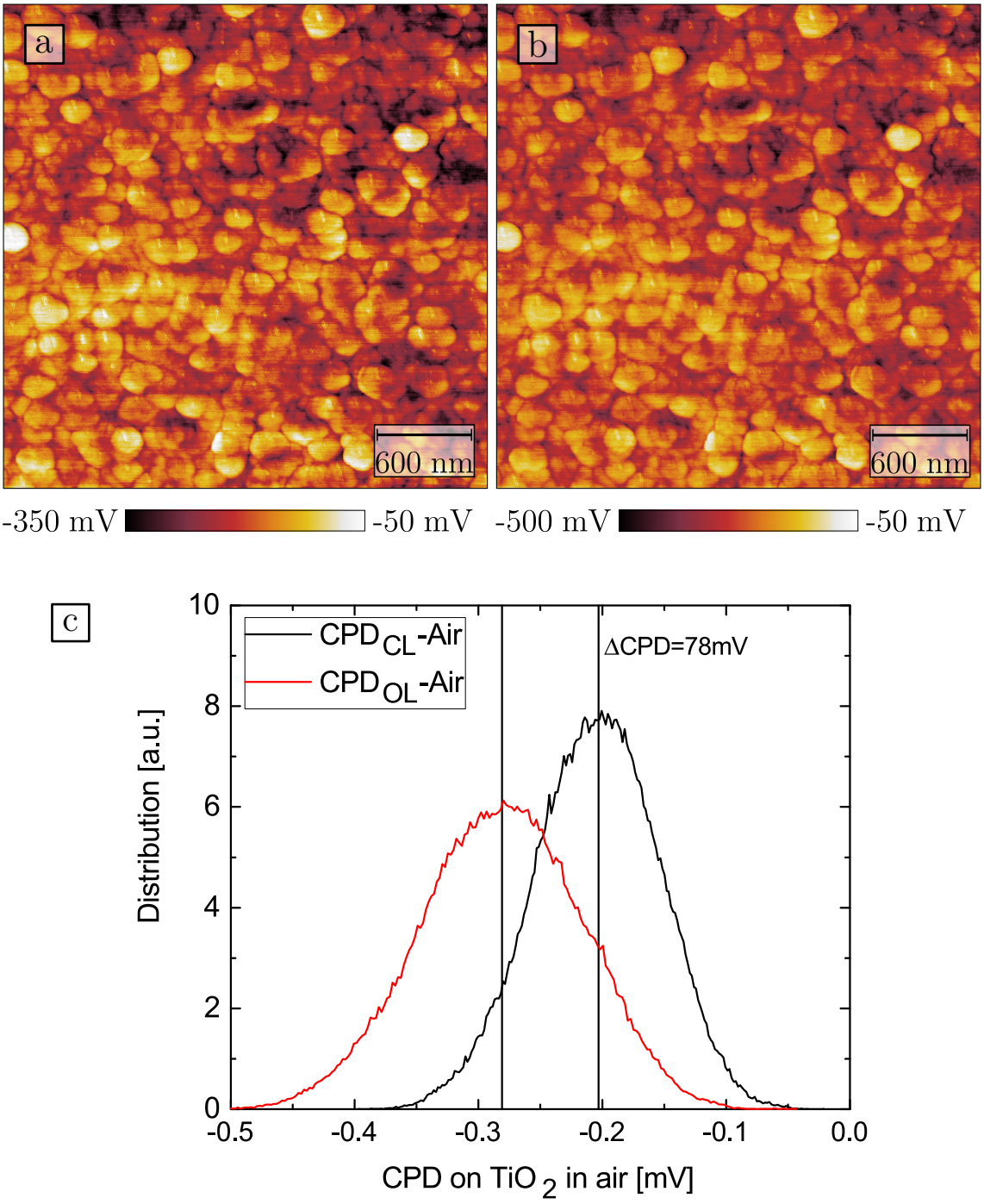

Figure B.4.: *CPD-data of the measurement on TiO_2 in air at an excitation voltage of $V_{ac} = 2\,\mathrm{V}$. a) CPD_{CL}- and b) CPD_{OL}-signal, with (c) the distribution of the values for these two images. A shift of the median CPD by $\Delta CPD = 78\,\mathrm{mV}$ and a slightly narrower distribution of the measured CPD-values in the CPD_{CL} is obvious. Scan parameters: Cantilever: NCL-Pt; $f_{1st} = 149\,\mathrm{kHz}$; $A_{1st} = 20\,\mathrm{nm}$; $f_{2nd} = 930\,\mathrm{kHz}$; $V_{ac} = 2\,\mathrm{V}$.*

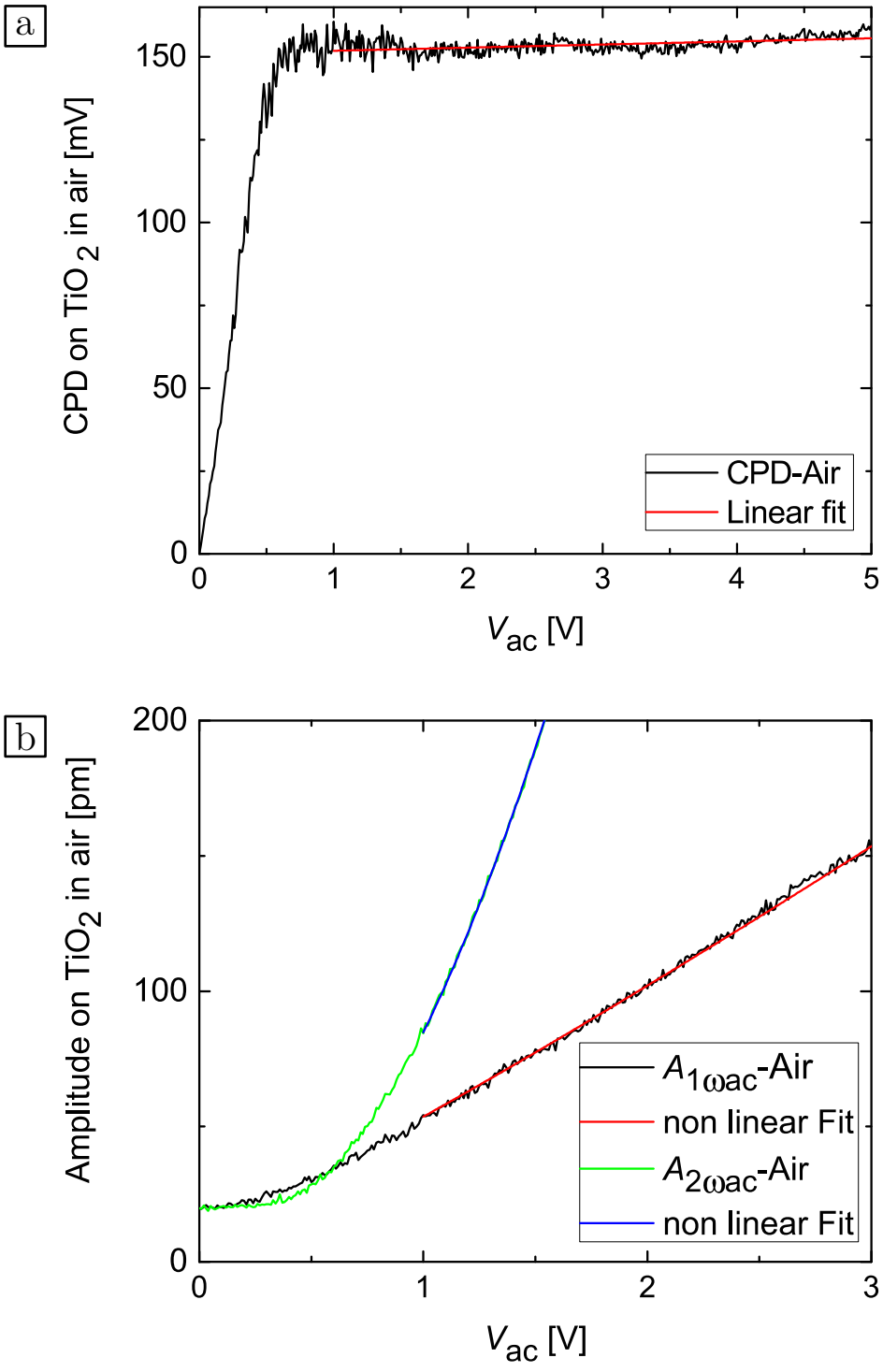

Figure B.5.: *Data of the V_{ac}-spectroscopy-measurements on TiO_2 in air. a) CPD(V_{ac}) with linear fit at $V_{ac} > 1\,\mathrm{V}$, and b) amplitude(V_{ac}) with non linear fits at $V_{ac} > 1\,\mathrm{V}$.*
Scan parameters: Cantilever: NCL-Pt; $f_{1st} = 149\,\mathrm{kHz}$; $A_{1st} = 20\,\mathrm{nm}$; $f_{2nd} = 930\,\mathrm{kHz}$; z -controller off.

B.1.3. Titania in water

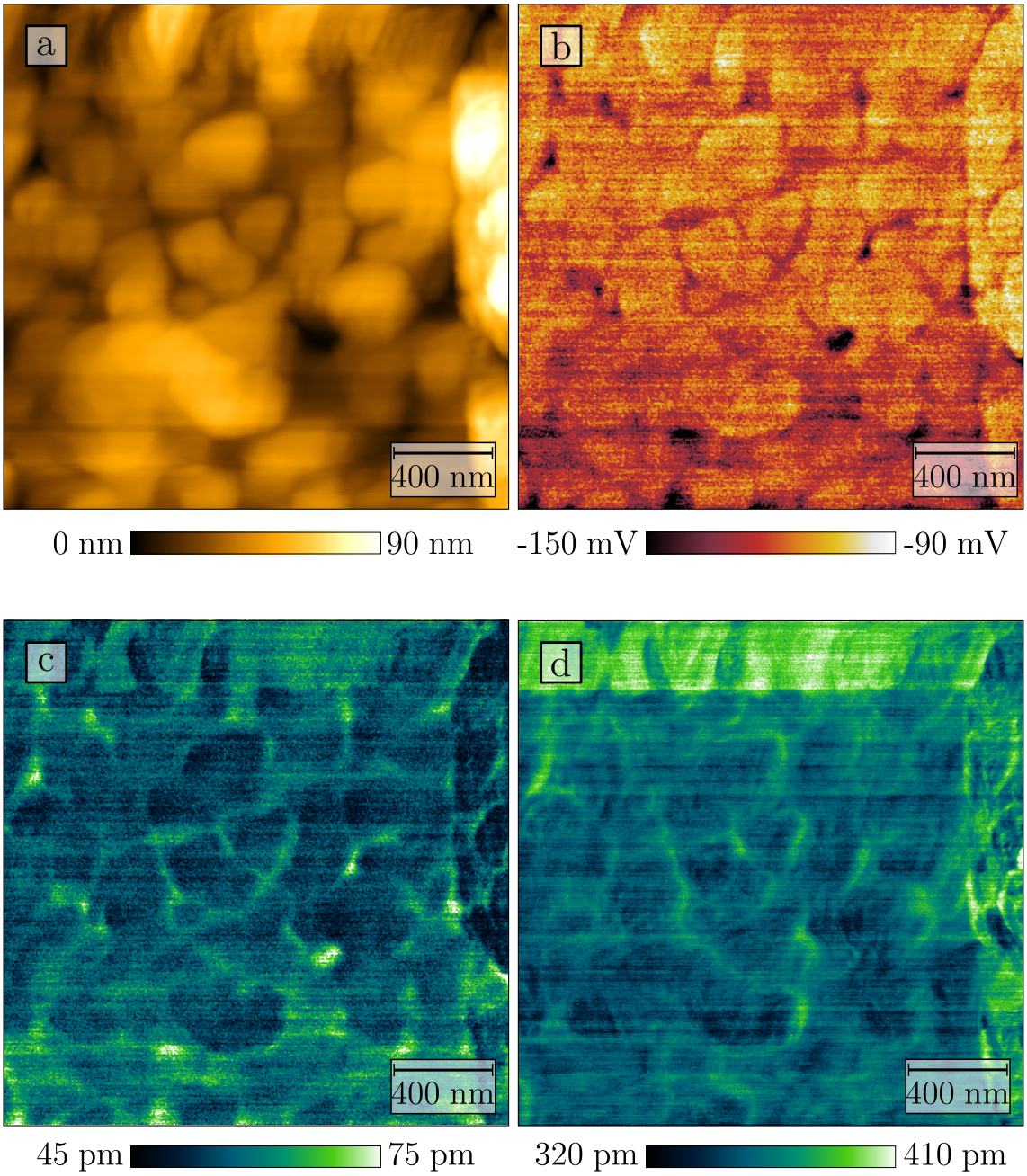

Figure B.6.: *Full data set of the measurement on TiO_2 in water at an excitation voltage of V_{ac} = 3 V. a) Topography, b) CPD_{OL}, c) $A_{1\omega_{ac}}$, d) $A_{2\omega_{ac}}$.*
Scan parameters: Cantilever: NCL-Pt; f_{1st} = 74 kHz; A_{1st} = 2 nm; f_{2nd} = 487 kHz; V_{ac} = 3 V.

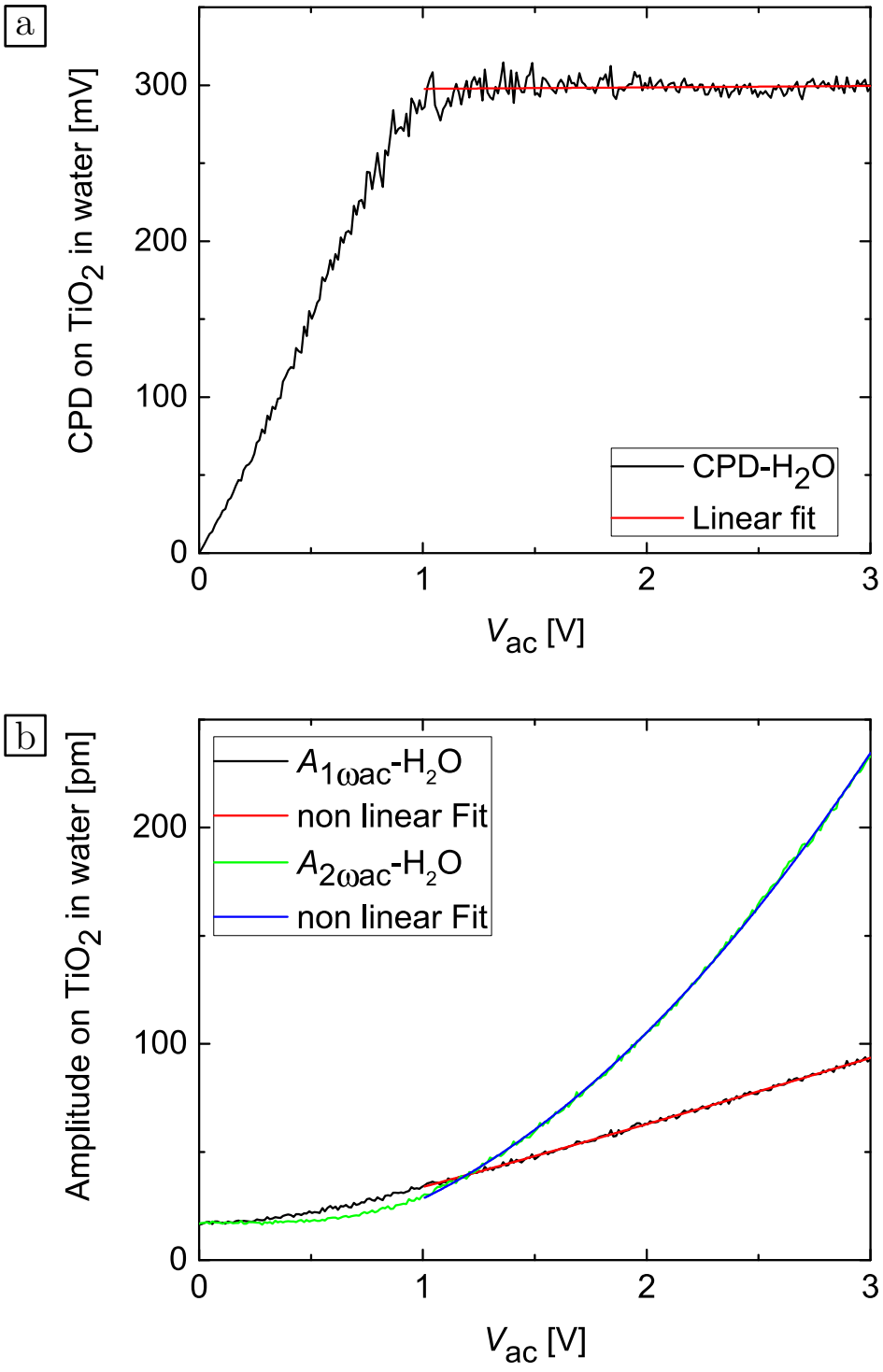

Figure B.7.: *Data of the V_{ac}-spectroscopy-measurements on TiO_2 in water. a) CPD(V_{ac}) with linear fit at $V_{ac} > 1\,\mathrm{V}$, and b) amplitude(V_{ac}) with non linear fits at $V_{ac} > 1\,\mathrm{V}$.*
Scan parameters: Cantilever: NCL-Pt; $f_{1st} = 74\,\mathrm{kHz}$; $A_{1st} = 2\,\mathrm{nm}$; $f_{2nd} = 487\,\mathrm{kHz}$; $V_{ac} = 3\,\mathrm{V}$.

B.1.4. Bare titania in El100

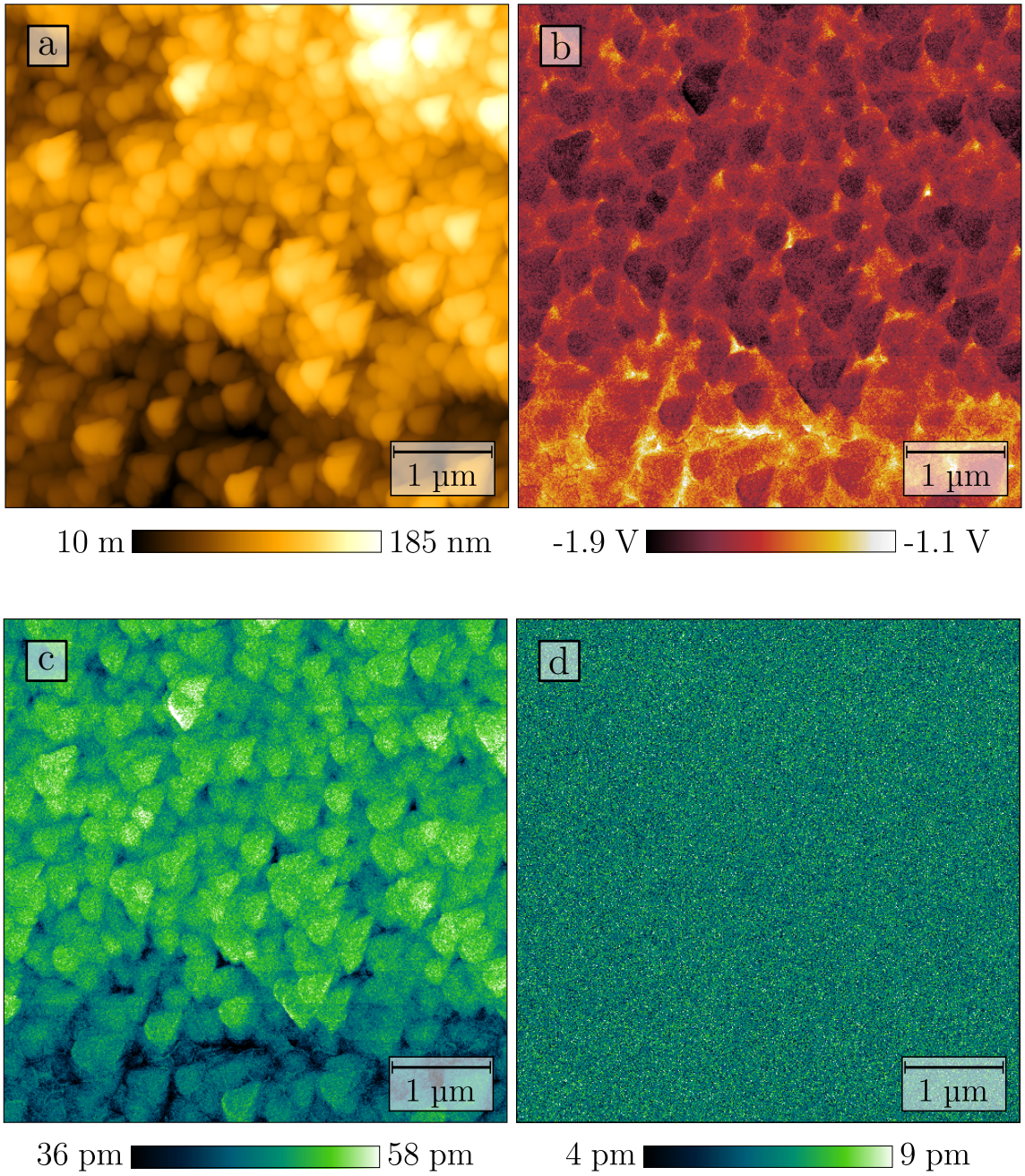

Figure B.8.: *Full data set of the measurement on bare TiO_2 in El100 at an excitation voltage of $V_{ac} = 1\,\mathrm{V}$. a) Topography, b) CPD_{OL}, c) $A_{1\omega_{ac}}$, d) $A_{2\omega_{ac}}$.*
Scan parameters: Cantilever: NCL-Pt; $f_{1st} = 75\,\mathrm{kHz}$; $A_{1st} = 9\,\mathrm{nm}$; $f_{2nd} = 487\,\mathrm{kHz}$; $V_{ac} = 1\,\mathrm{V}$.

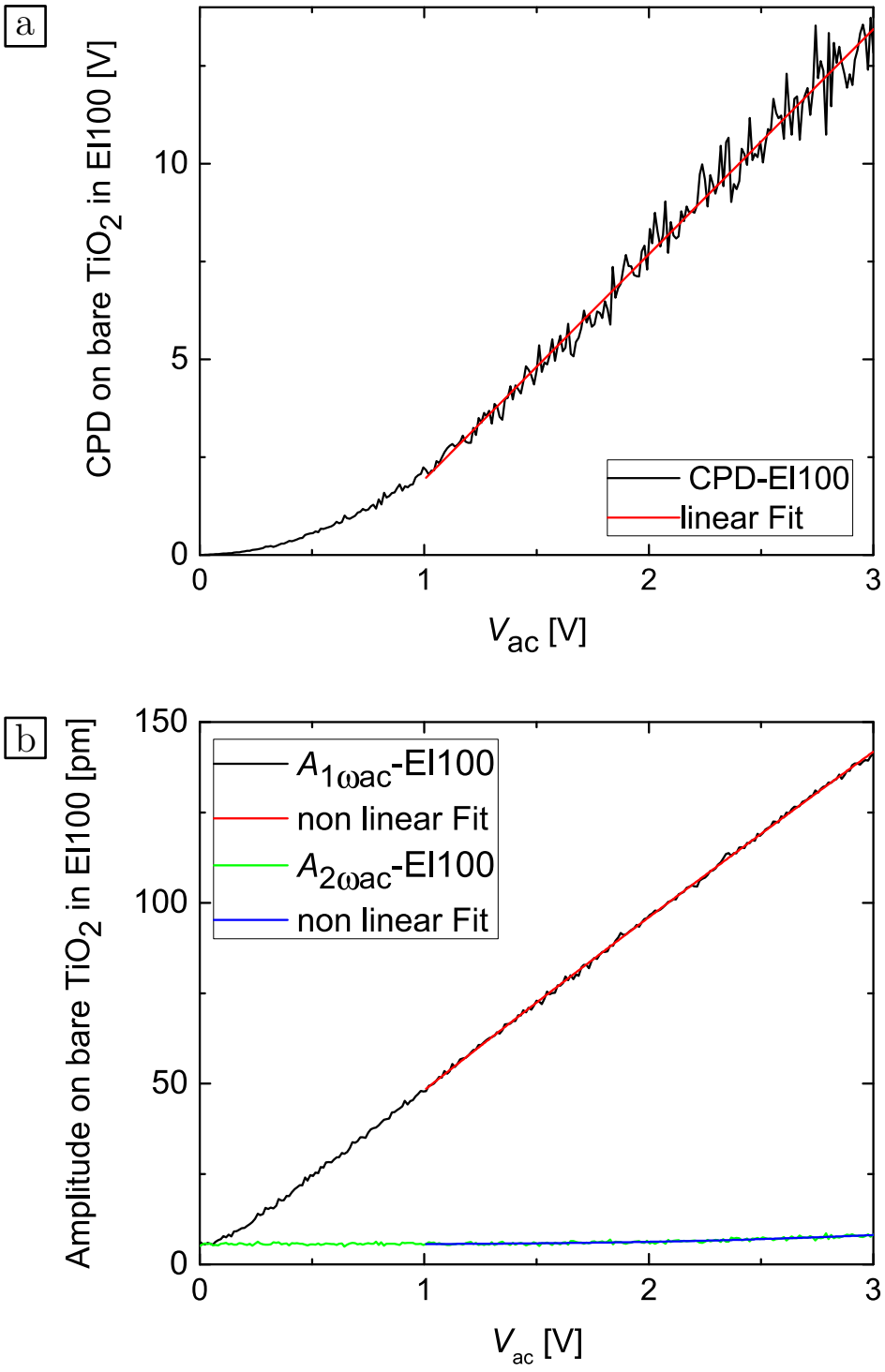

Figure B.9.: *Data of the V_{ac}-spectroscopy-measurements on bare TiO_2 in El100. a) CPD(V_{ac}) with linear fit at $V_{ac} > 1\,\mathrm{V}$, and b) amplitude(V_{ac}) with non linear fits at $V_{ac} > 1\,\mathrm{V}$.*
Scan parameters: Cantilever: NCL-Pt; $f_{1st} = 75\,\mathrm{kHz}$; $A_{1st} = 9\,\mathrm{nm}$; $f_{2nd} = 487\,\mathrm{kHz}$; z-control off.

B.1.5. Dyed Titania in El100

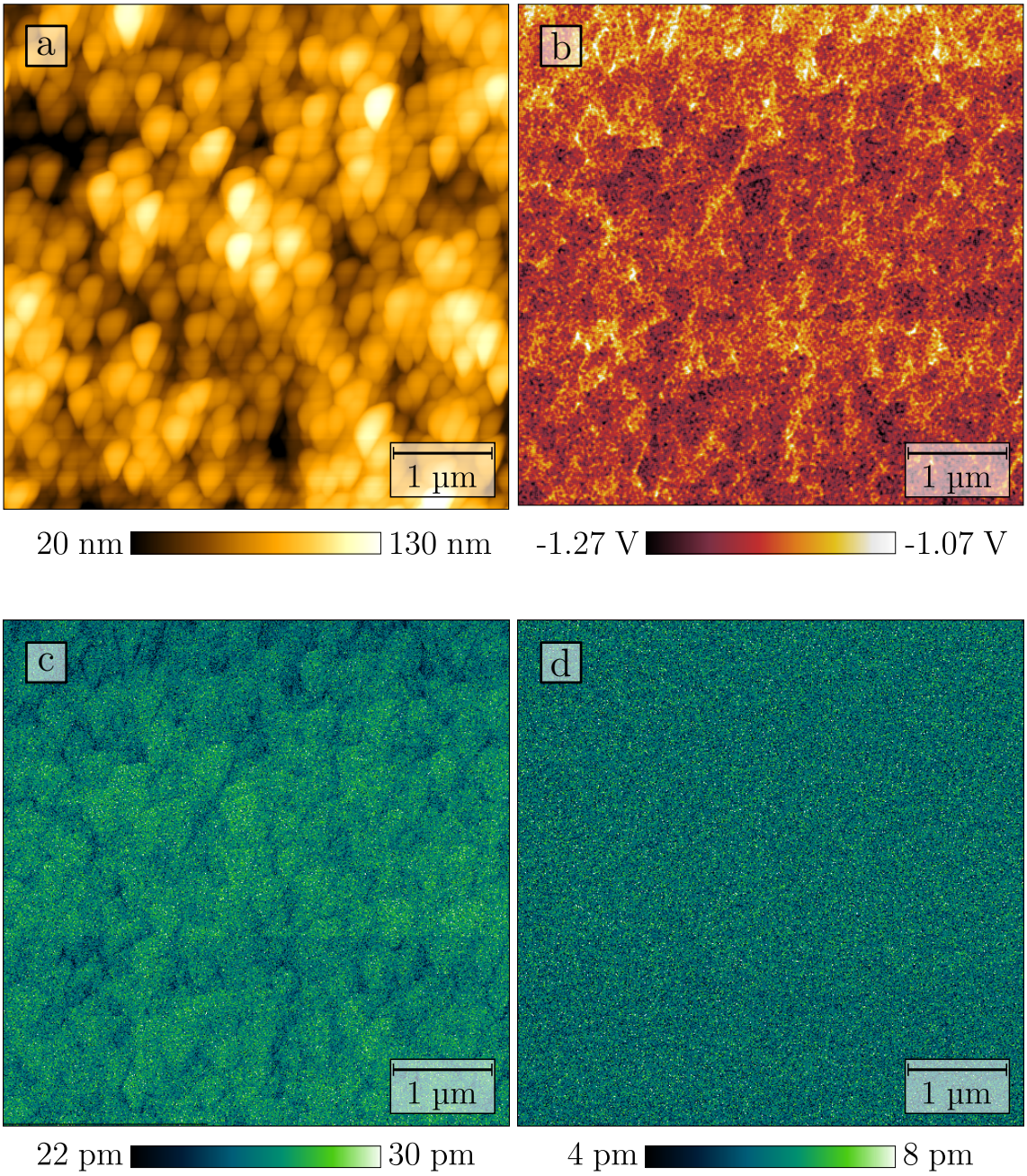

Figure B.10.: *Full data set of the measurement on dyed TiO_2 in El100 at an excitation voltage of $V_{ac} = 1\,\mathrm{V}$. a) Topography, b) CPD_{OL}, c) $A_{1\omega_{ac}}$, d) $A_{2\omega_{ac}}$.*
Scan parameters: Cantilever: NCL-Pt; $f_{1st} = 75\,\mathrm{kHz}$; $A_{1st} = 9\,\mathrm{nm}$; $f_{2nd} = 487\,\mathrm{kHz}$; $V_{ac} = 1\,\mathrm{V}$.

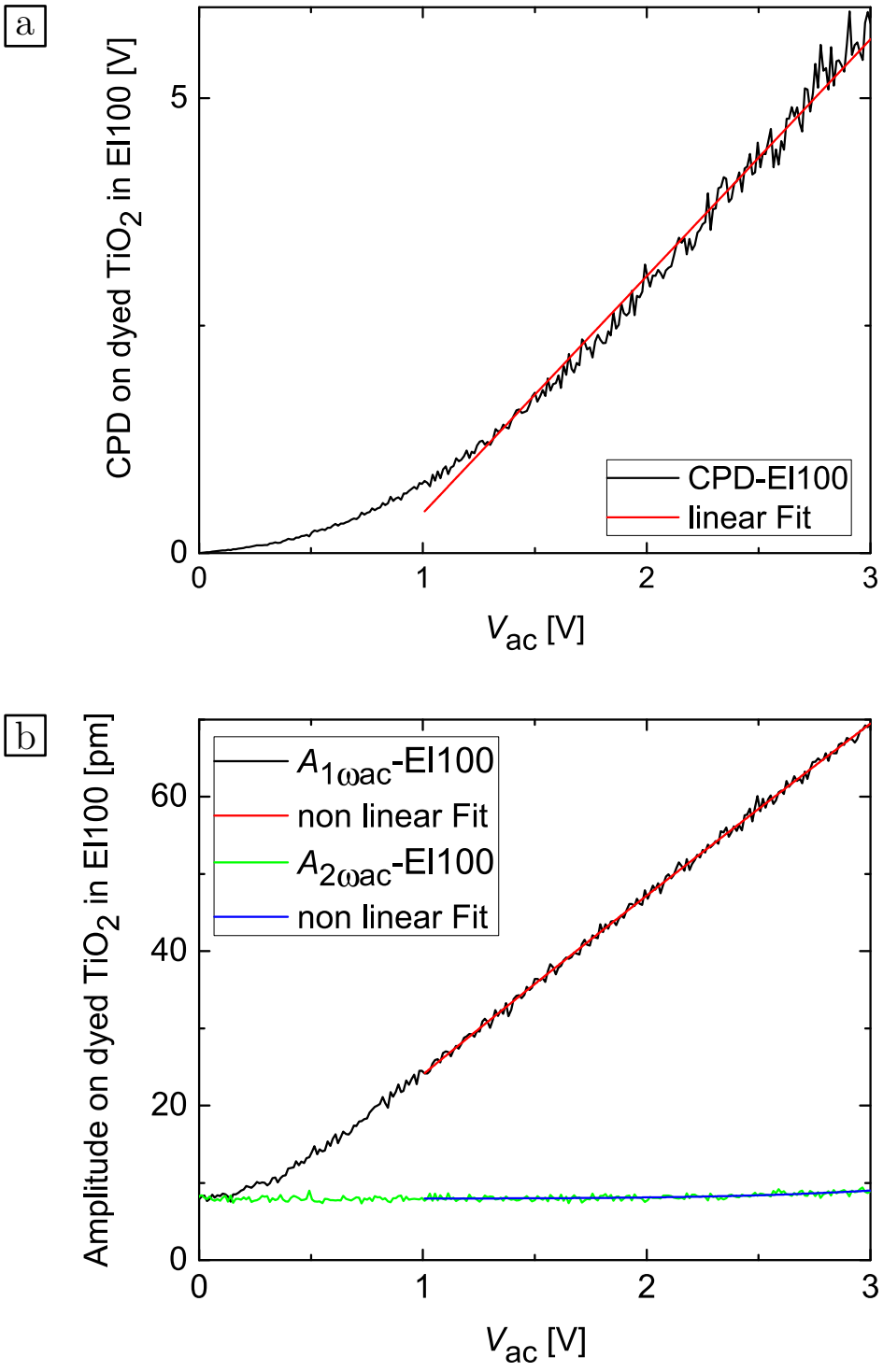

Figure B.11.: *Data of the V_{ac}-spectroscopy-measurements on dyed TiO_2 in El100. a) CPD(V_{ac}) with linear fit at $V_{ac} > 1\,\mathrm{V}$, and b) amplitude(V_{ac}) with non linear fits at $V_{ac} > 1\,\mathrm{V}$.*
Scan parameters: Cantilever: NCL-Pt; $f_{1st} = 75\,\mathrm{kHz}$; $A_{1st} = 9\,\mathrm{nm}$; $f_{2nd} = 487\,\mathrm{kHz}$; z-control off.

B.1.6. Bare titania in El10, $V_{ac} = 1\,V$

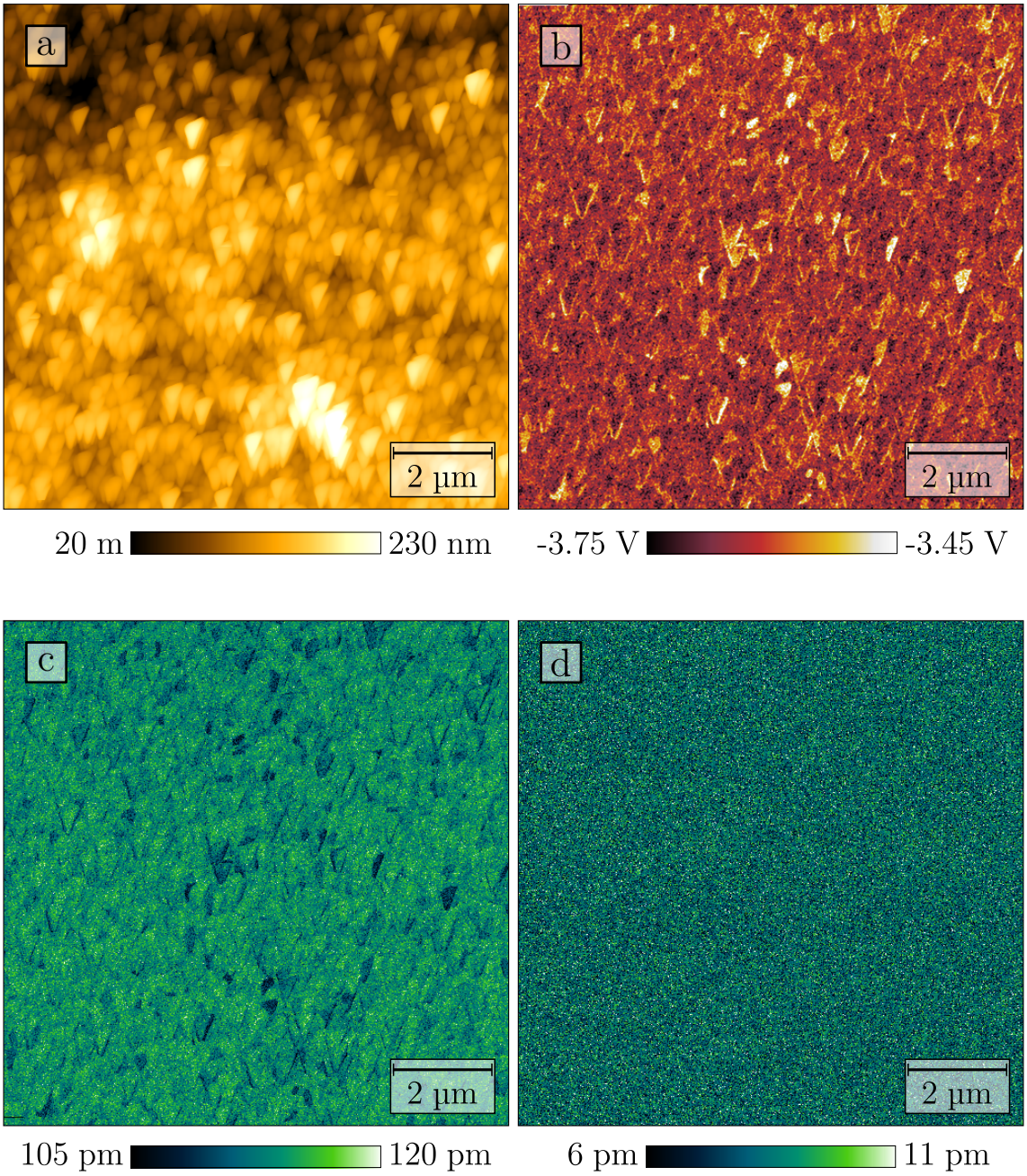

Figure B.12.: *Full data set of the measurement on bare TiO_2 in El10 at an excitation voltage of $V_{ac} = 1\,V$. a) Topography, b) CPD_{OL}, c) $A_{1\omega_{ac}}$, d) $A_{2\omega_{ac}}$.*
Scan parameters: Cantilever: NCL-Pt; $f_{1st} = 75\,kHz$; $A_{1st} = 8\,nm$; $f_{2nd} = 498\,kHz$; $V_{ac} = 1\,V$.

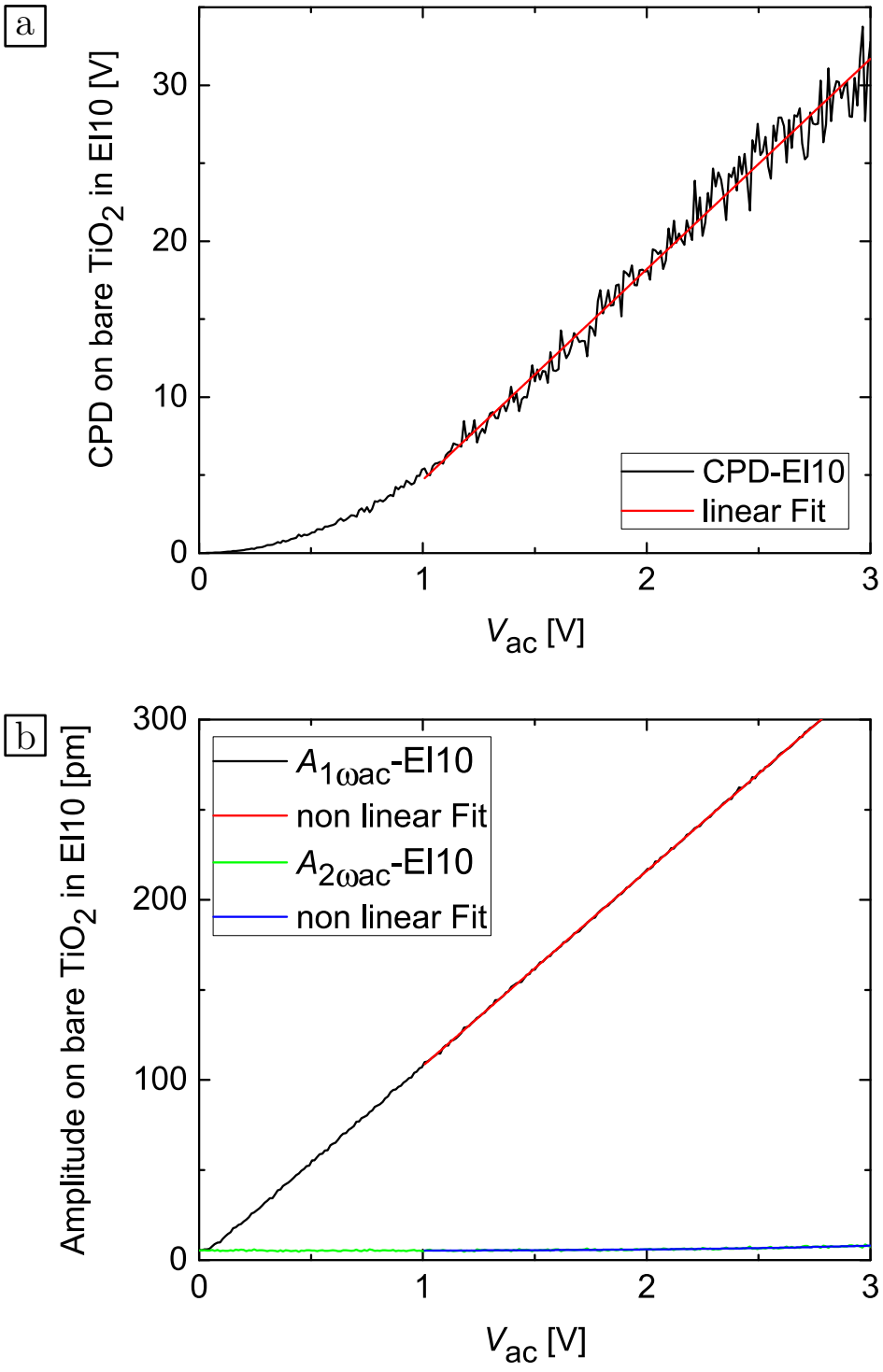

Figure B.13.: *Data of the V_{ac}-spectroscopy-measurements on bare TiO_2 in El10. a) CPD(V_{ac}) with linear fit at $V_{ac} > 1\,\mathrm{V}$, and b) amplitude(V_{ac}) with non linear fits at $V_{ac} > 1\,\mathrm{V}$.*
Scan parameters: Cantilever: NCL-Pt; $f_{1st} = 75\,\mathrm{kHz}$; $A_{1st} = 8\,\mathrm{nm}$; $f_{2nd} = 498\,\mathrm{kHz}$; z-control off.

B.1.7. Bare titania in El10, $V_{ac} = 2\,V$

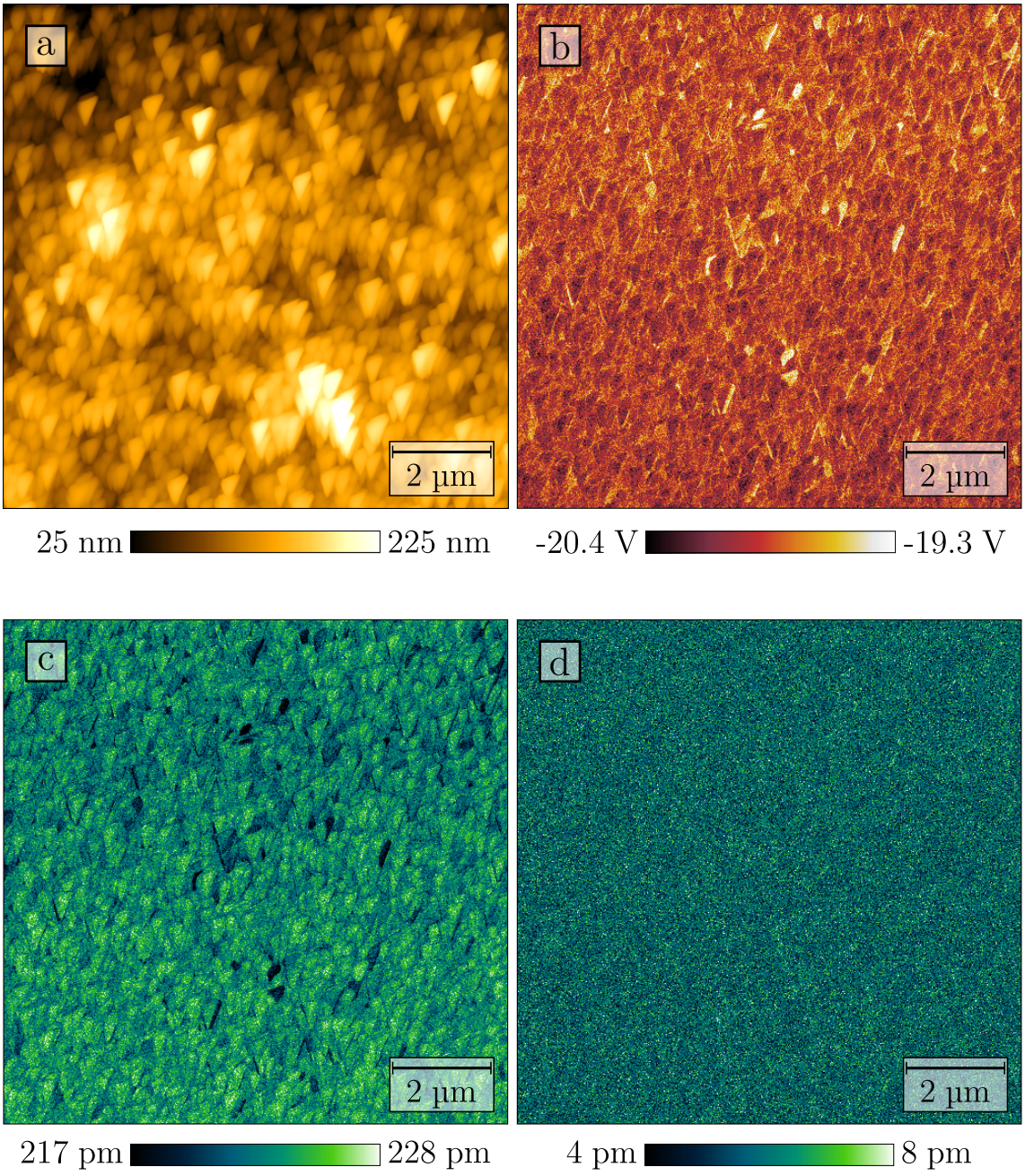

Figure B.14.: *Full data set of the measurement on bare TiO_2 in El10 at an excitation voltage of $V_{ac} = 2\,V$. a) Topography, b) CPD_{OL}, c) $A_{1\omega_{ac}}$, d) $A_{2\omega_{ac}}$.*
Scan parameters: Cantilever: NCL-Pt; $f_{1st} = 75\,kHz$; $A_{1st} = 8\,nm$; $f_{2nd} = 498\,kHz$; $V_{ac} = 2\,V$.

B.1.8. Dyed titania in El10, $V_{ac} = 1\,V$

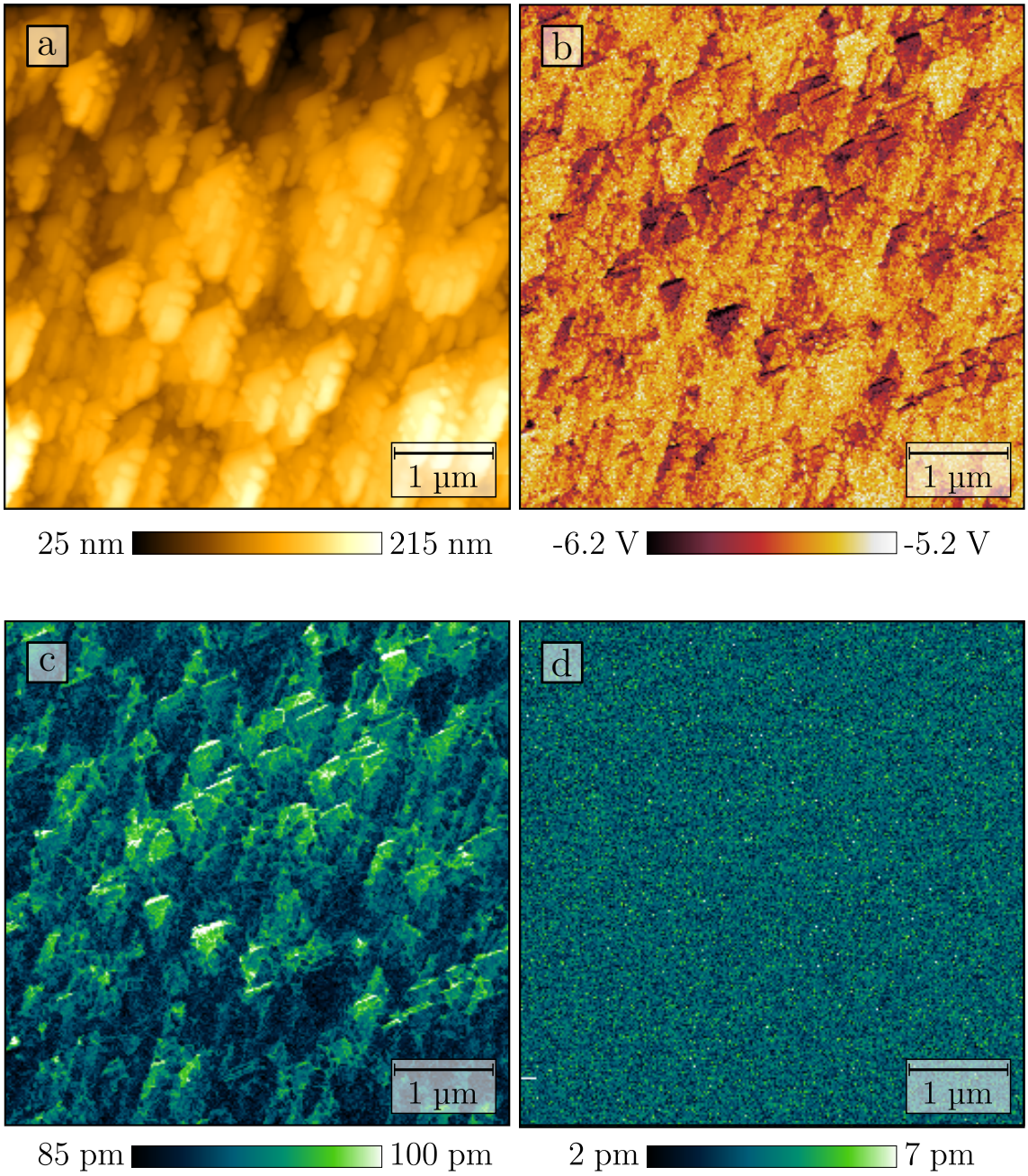

Figure B.15.: *Full data set of the measurement on dyed TiO_2 in El10 at an excitation voltage of $V_{ac} = 1\,V$. a) Topography, b) CPD_{OL}, c) $A_{1\omega_{ac}}$, d) $A_{2\omega_{ac}}$.*
Scan parameters: Cantilever: NCL-Pt; $f_{1st} = 75\,kHz$; $A_{1st} = 8\,nm$; $f_{2nd} = 497\,kHz$; $V_{ac} = 1\,V$.

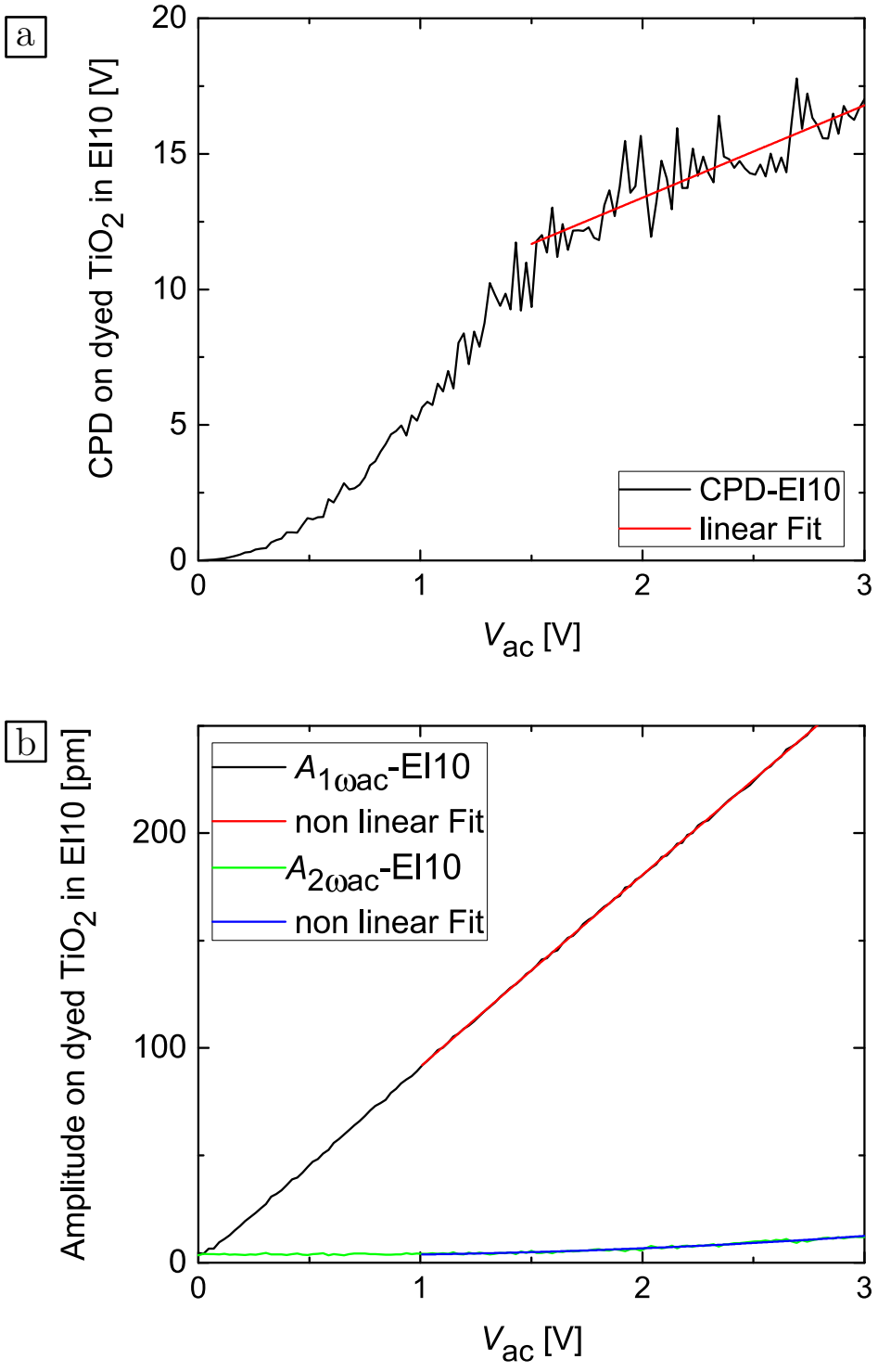

Figure B.16.: *Data of the V_{ac}-spectroscopy-measurements on dyed TiO_2 in El10. a) CPD(V_{ac}) with linear fit at $V_{ac} > 1\,\mathrm{V}$, and b) amplitude(V_{ac}) with non linear fits at $V_{ac} > 1\,\mathrm{V}$.*
Scan parameters: Cantilever: NCL-Pt; $f_{1st} = 75\,\mathrm{kHz}$; $A_{1st} = 8\,\mathrm{nm}$; $f_{2nd} = 497\,\mathrm{kHz}$; z-control off.

B.1.9. Titania in El10, $V_{ac} = 2\,V$

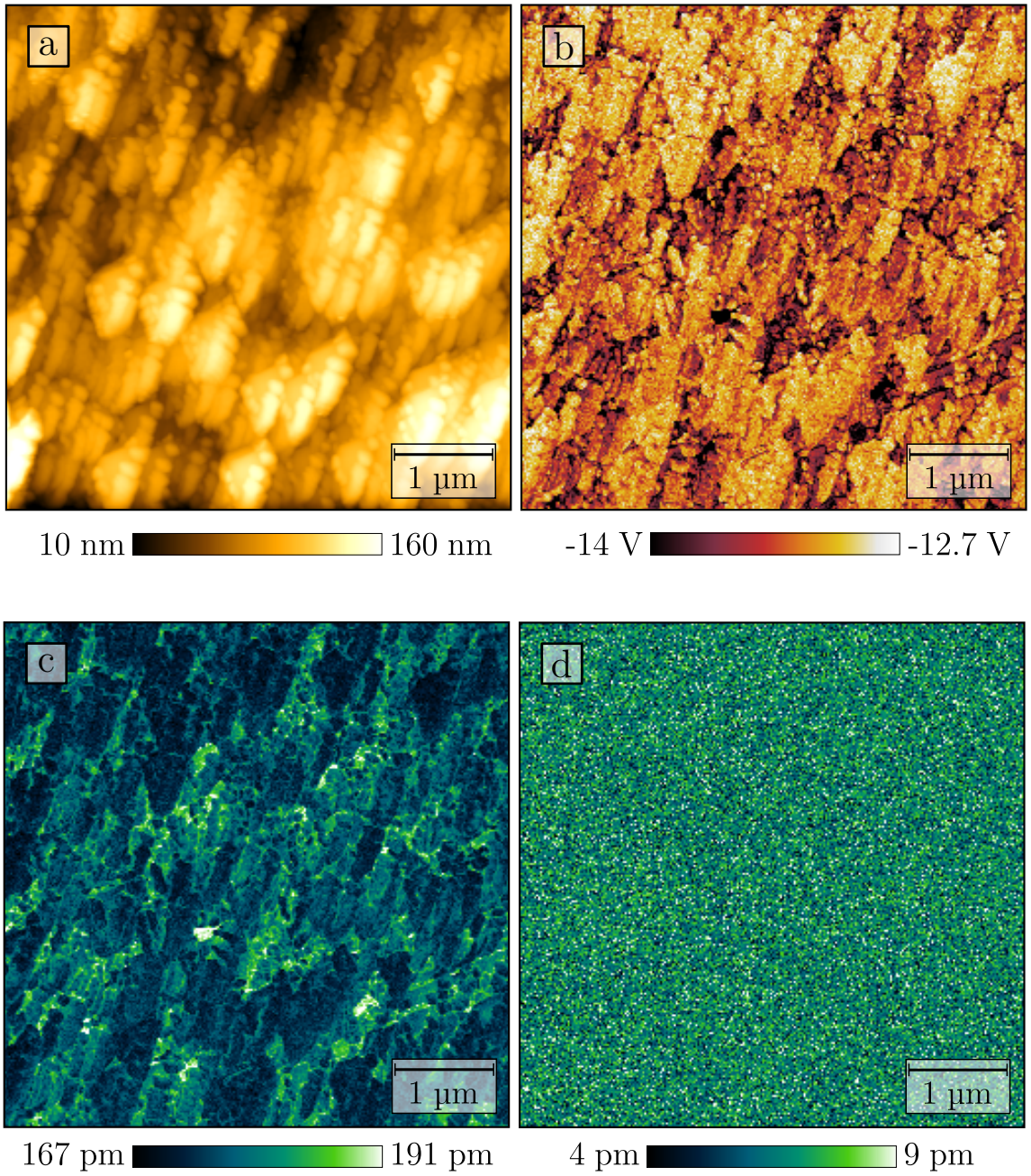

Figure B.17.: *Full data set of the measurement on dyed TiO_2 in El10 at an excitation voltage of $V_{ac} = 2\,V$. a) Topography, b) CPD_{OL}, c) $A_{1\omega_{ac}}$, d) $A_{2\omega_{ac}}$.*
Scan parameters: Cantilever: NCL-Pt; $f_{1st} = 75\,kHz$; $A_{1st} = 8\,nm$; $f_{2nd} = 497\,kHz$; $V_{ac} = 2\,V$.

B.2. KPFM measurements on the "AuIn-sample"

B.2.1. Overview

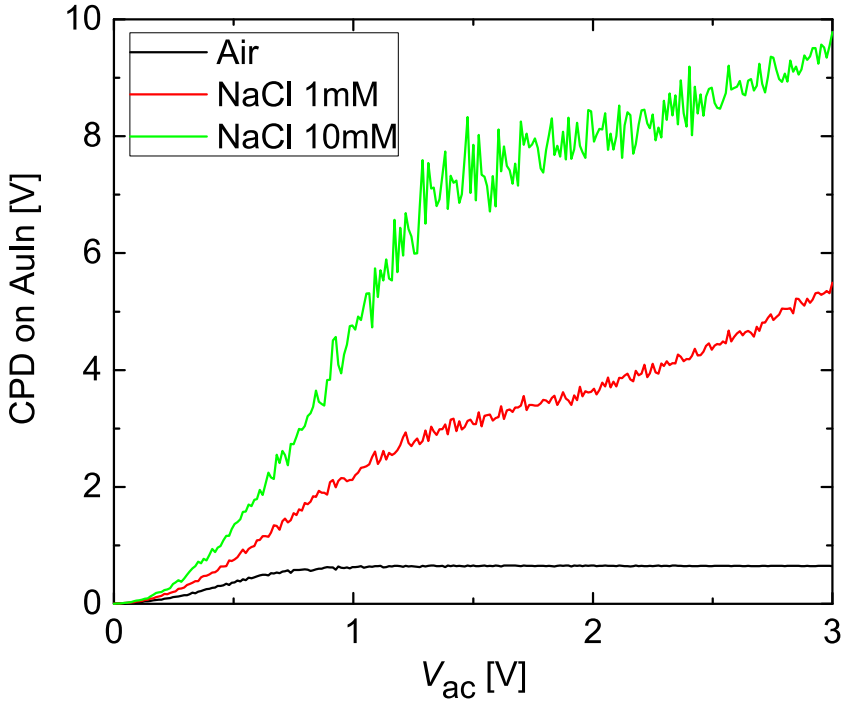

Figure B.18.: *Data of the V_{ac}-spectroscopy-measurements on the "AuIn-sample", comparison of the dependence of the CPD on the excitation voltage (CPD(V_{ac})) in different environments. The graph shows the absolute of the measured CPD.*

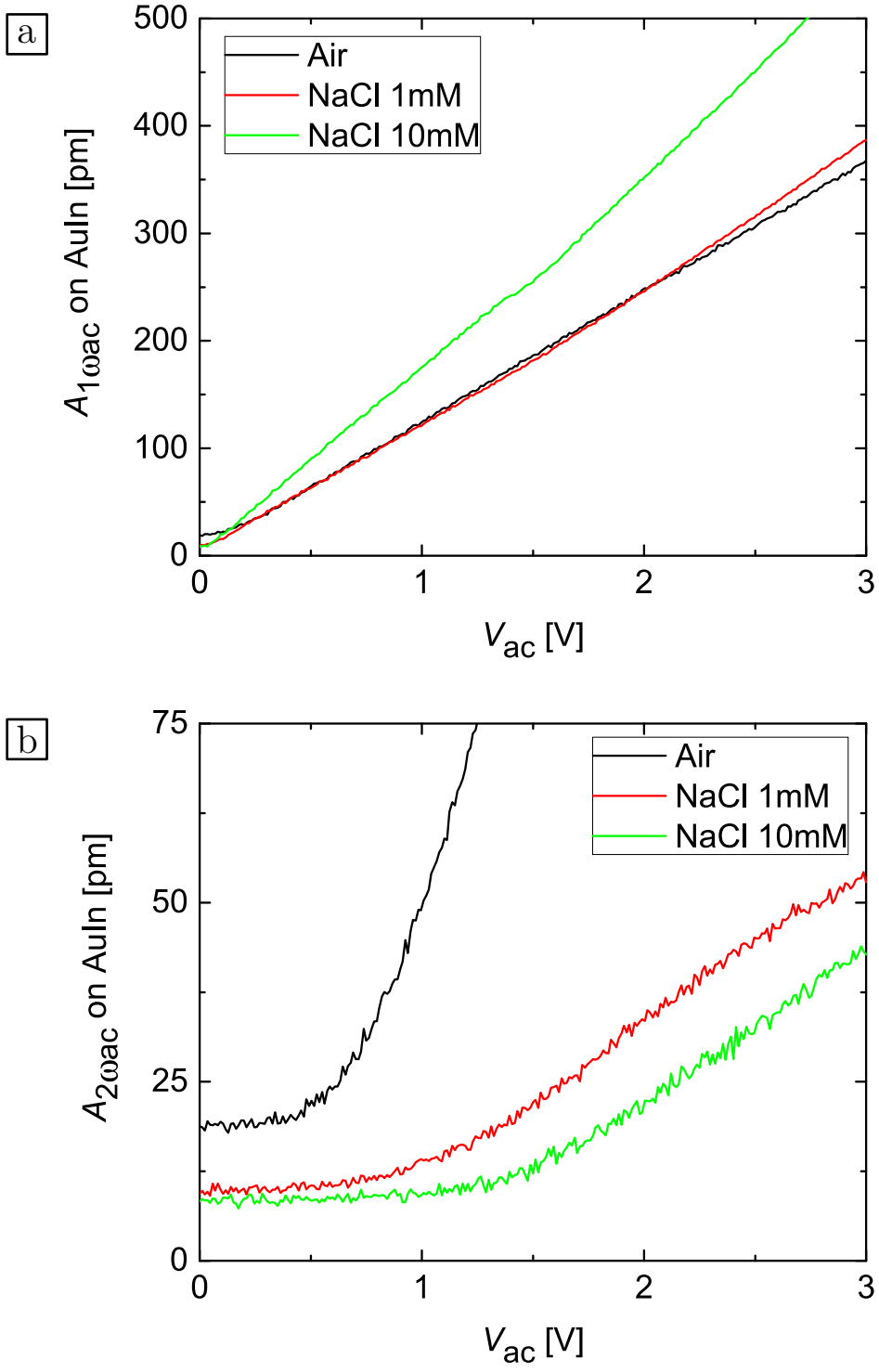

Figure B.19.: *Data of the V_{ac}-spectroscopy-measurements on the "AuIn-sample", comparison of the measurements in different environments. a) $A_{1\omega_{ac}}(V_{ac})$, and b) $A_{2\omega_{ac}}(V_{ac})$.*

B.2.2. AuIn-sample in air

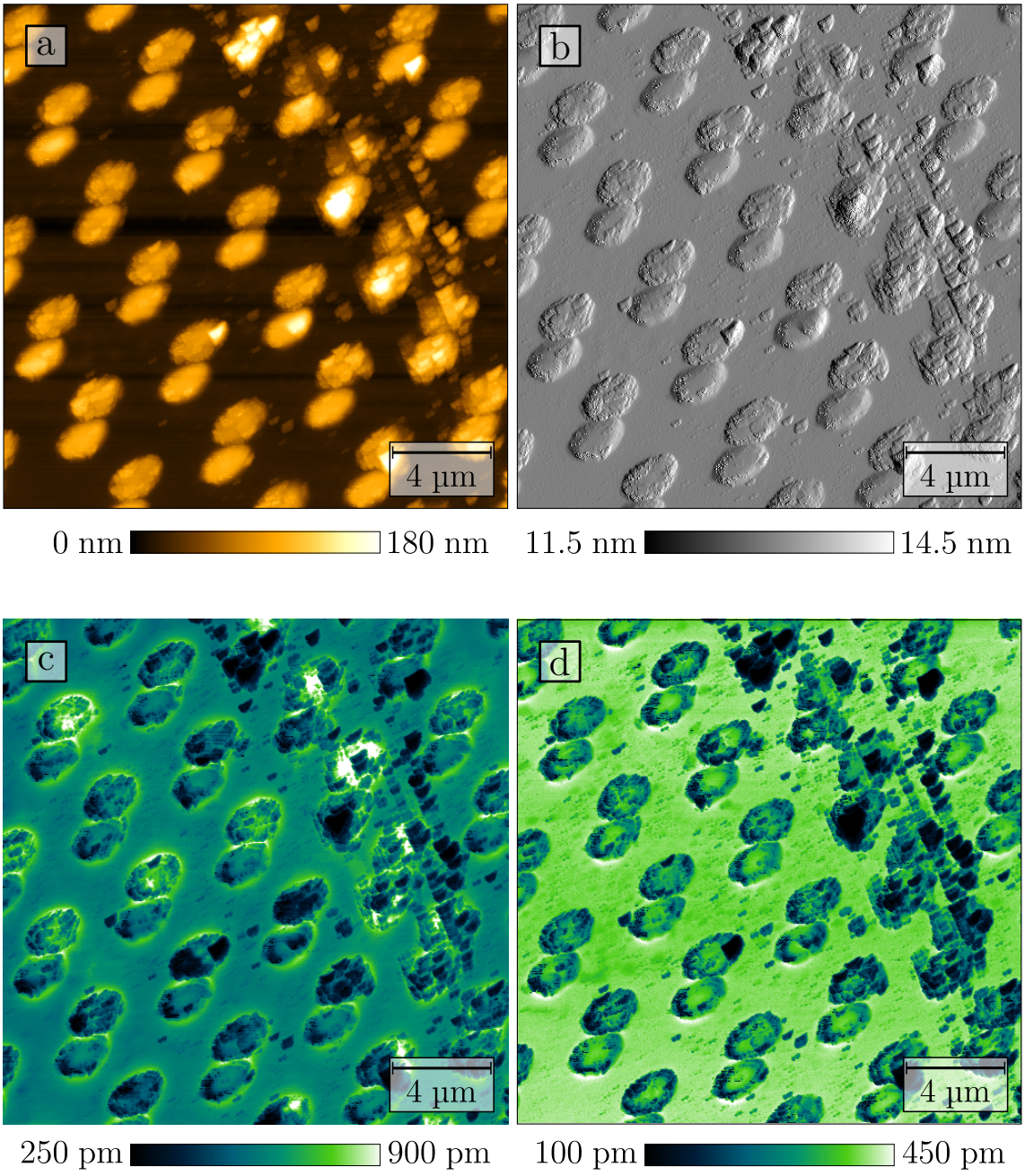

Figure B.20.: *Full data set of the measurement on the "AuIn-sample" in air at an excitation voltage of* $V_{ac} = 700\,\mathrm{mV}$*: a) Topography, b)* CPD_{OL}*, c)* $A_{1\omega_{ac}}$*, d)* $A_{2\omega_{ac}}$*.*
Scan parameters: Cantilever: EFM; $f_{1st} = 76\,\mathrm{kHz}$*;* $A_{1st} = 13\,\mathrm{nm}$*;* $f_{2nd} = 477\,\mathrm{kHz}$*;* $V_{ac} = 700\,\mathrm{mV}$*.*

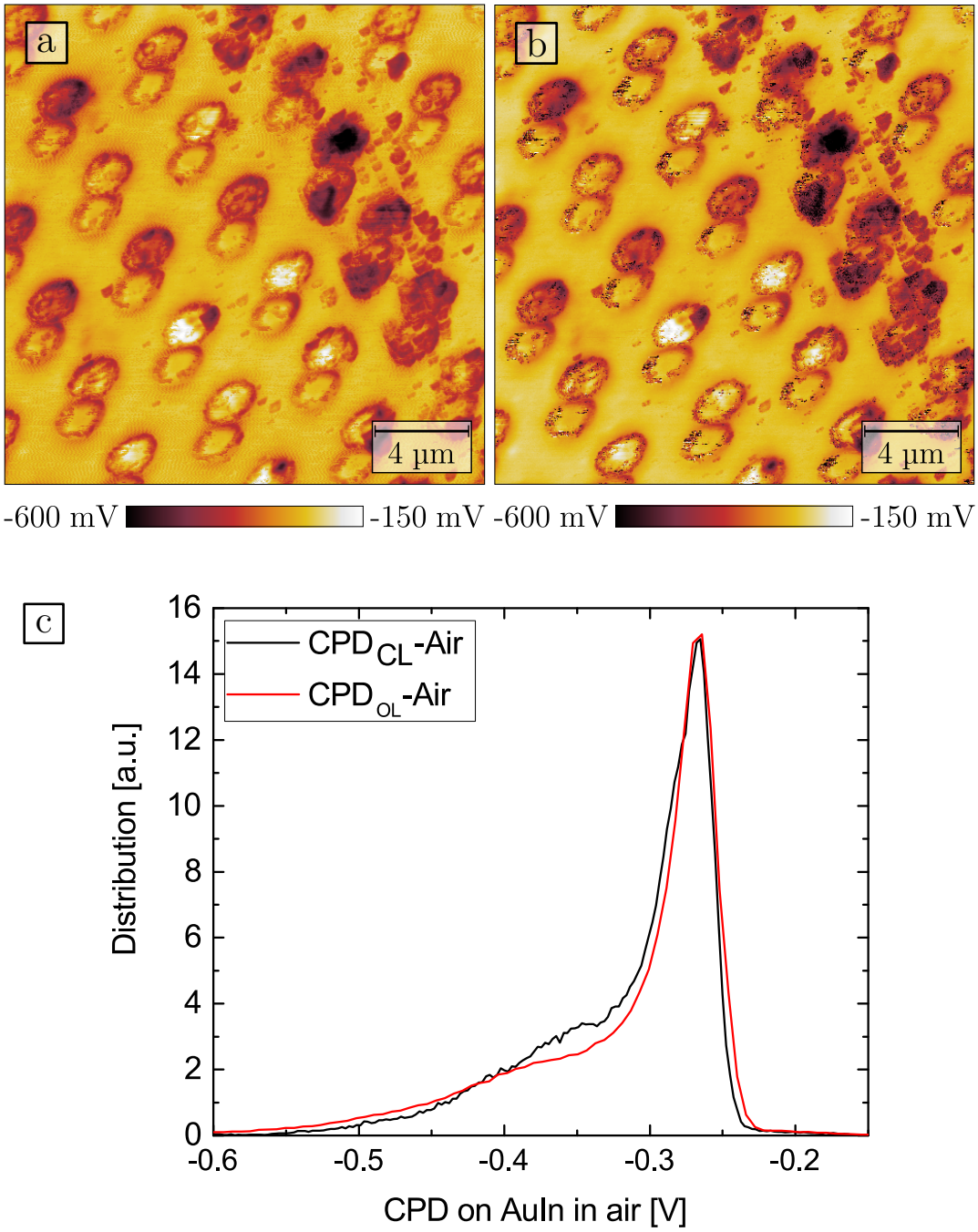

Figure B.21.: *CPD-data of th measurement on the "AuIn-sample" in air. a) CPD_{CL}- and b) CPD_{OL}-signal, with (c) the distribution of the values for these two images. The two distribution curves are very similar, indicating the absence of capacitative cross talk.*
Scan parameters: Cantilever: EFM; $f_{1st} = 76\,\mathrm{kHz}$; $A_{1st} = 13\,\mathrm{nm}$; $f_{2nd} = 477\,\mathrm{kHz}$; $V_{ac} = 700\,\mathrm{mV}$.

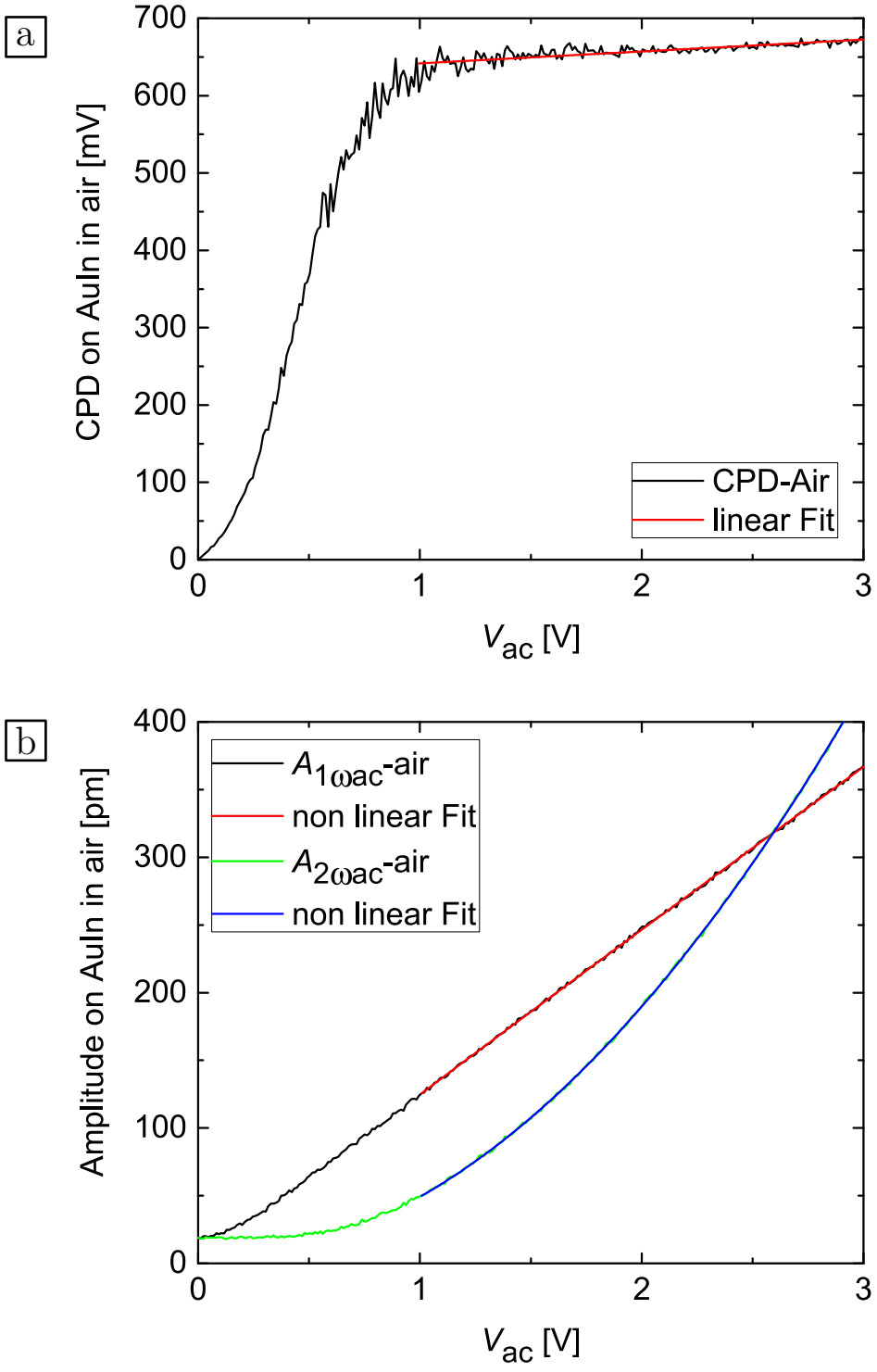

Figure B.22.: *Data of the V_{ac}-spectroscopy-measurements on the "AuIn-sample" in air. a) CPD(V_{ac}) with linear fit at $V_{ac} > 1.5\,\mathrm{V}$, and b) amplitude(V_{ac}) with non linear fits at $V_{ac} > 1\,\mathrm{V}$.*
Scan parameters: Cantilever: NCL-Pt; $f_{1st} = 154\,\mathrm{kHz}$; $A_{1st} = 17.5\,\mathrm{nm}$; $f_{2nd} = 958\,\mathrm{kHz}$; z-control off.

B.2.3. AuIn-sample in NaCl1, $V_{ac} = 1\,\mathrm{V}$

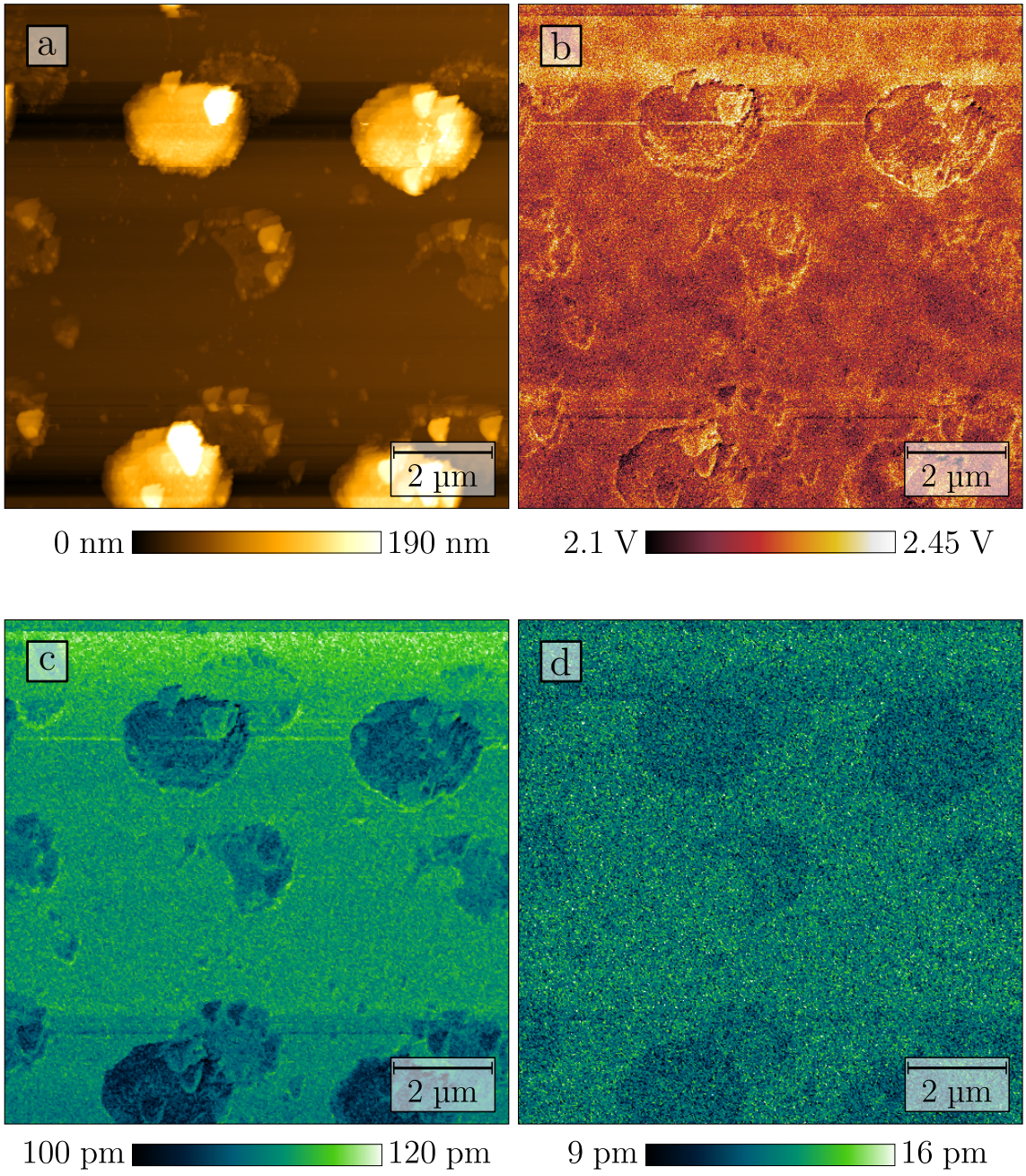

Figure B.23.: *Full data set of the measurement on the "AuIn-sample" in an NaCl solution with a concentration of* 1 mM *at an excitation voltage of* $V_{ac} = 1\,\mathrm{V}$*: a) Topography, b)* CPD_{OL}*, c)* $A_{1\omega_{ac}}$*, d)* $A_{2\omega_{ac}}$*.*
Scan parameters: Cantilever: NCL-Pt; $f_{1st} = 75\,\mathrm{kHz}$*;* $A_{1st} = 14\,\mathrm{nm}$*;* $f_{2nd} = 496\,\mathrm{kHz}$*;* $V_{ac} = 1\,\mathrm{V}$*.*

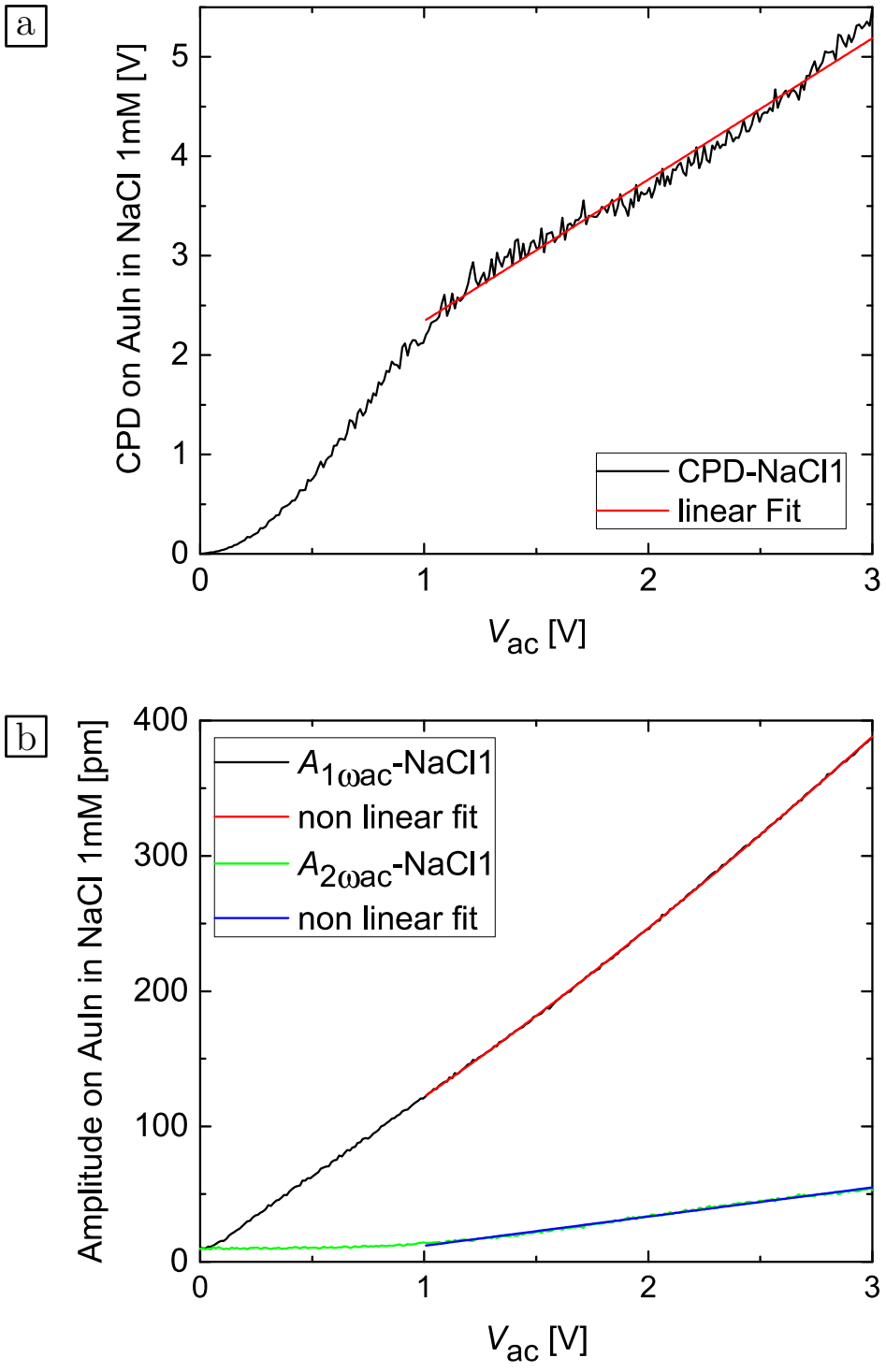

Figure B.24.: *Data of the V_{ac}-spectroscopy-measurements on the "AuIn-sample" in an NaCl solution with a concentration of* 1 mM. *a) CPD(V_{ac}) with a linear fit at $V_{ac} > 1$ V, and b) amplitude(V_{ac}) with non linear fits at $V_{ac} > 1$ V. Scan parameters: Cantilever: NCL-PT; $f_{1st} = 75$ kHz; $A_{1st} = 14$ nm; $f_{2nd} = 496$ kHz; z-control off.*

B.2.4. AuIn-sample in NaCl1, $V_{ac} = 2\,V$

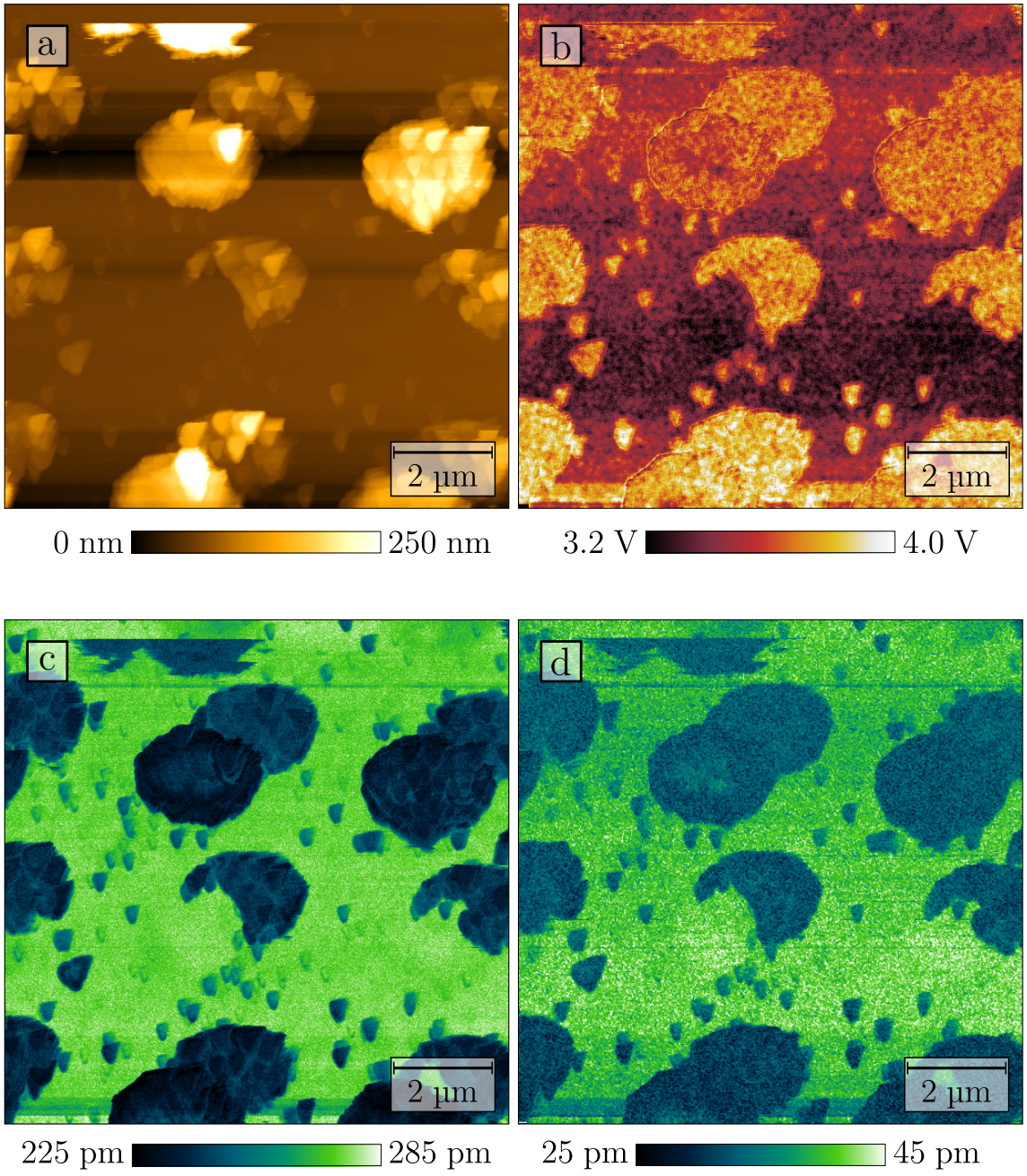

Figure B.25.: *Full data set of the measurement on the "AuIn-sample" in an NaCl solution with a concentration of* 1 mM *at an excitation voltage of* $V_{ac} = 2\,V$*: a) Topography, b)* CPD_{OL}*, c)* $A_{1\omega_{ac}}$*, d)* $A_{2\omega_{ac}}$*. Scan parameters: Cantilever: NCL-Pt;* $f_{1st} = 75\,kHz$*;* $A_{1st} = 14\,nm$*;* $f_{2nd} = 496\,kHz$*;* $V_{ac} = 2\,V$*.*

B.2.5. AuIn-sample in NaCl10, $V_{ac} = 1\,V$

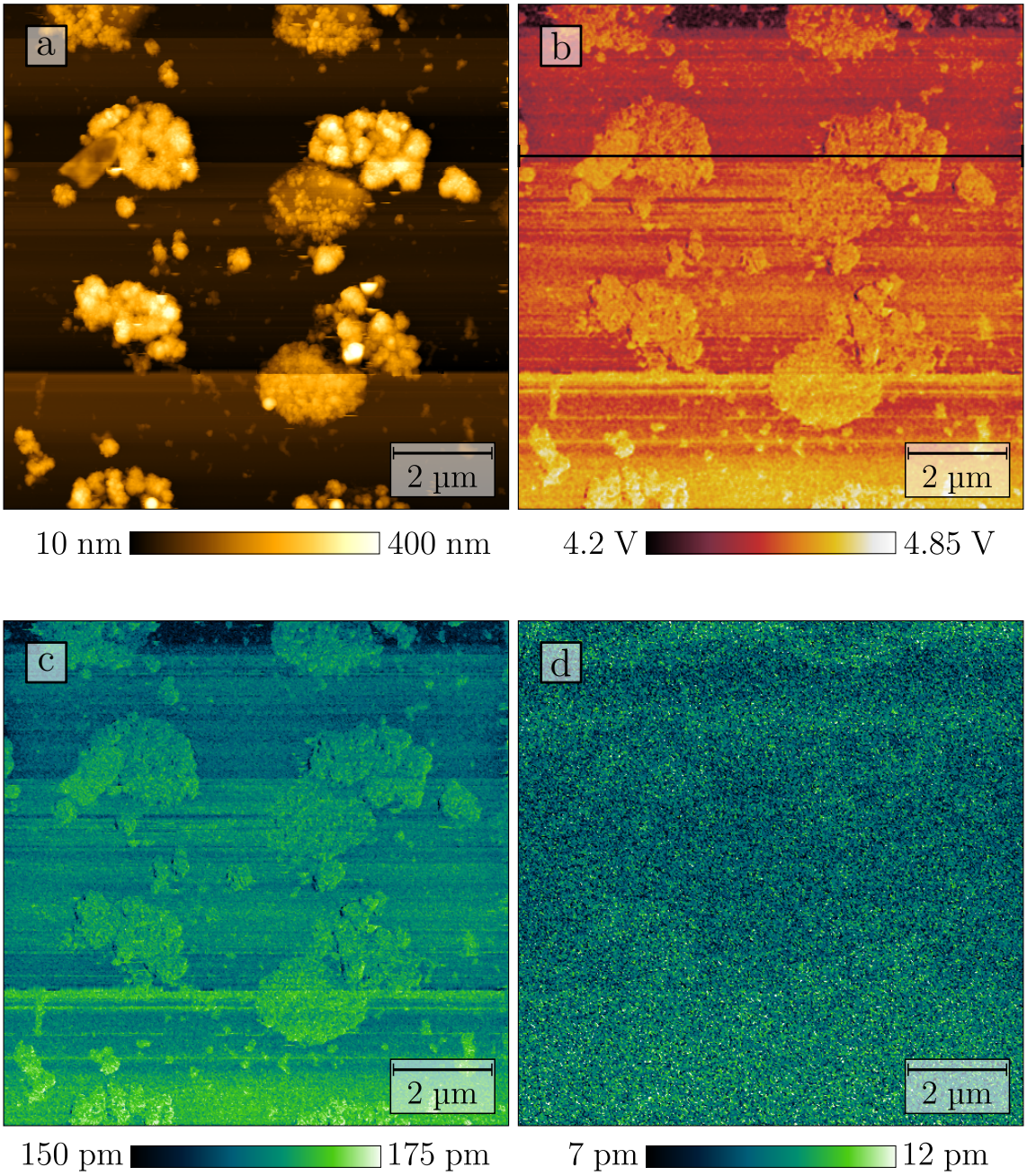

Figure B.26.: *Full data set of the measurement on the "AuIn-sample" in an NaCl solution with a concentration of* 10 mM *at an excitation voltage of* $V_{ac} = 1\,V$*: a) Topography, b)* CPD_{OL}*, c)* $A_{1\omega_{ac}}$*, d)* $A_{2\omega_{ac}}$*. Scan parameters: Cantilever: NCL-Pt;* $f_{1st} = 73\,kHz$*;* $A_{1st} = 5\,nm$*;* $f_{2nd} = 499\,kHz$*;* $V_{ac} = 1\,V$*.*

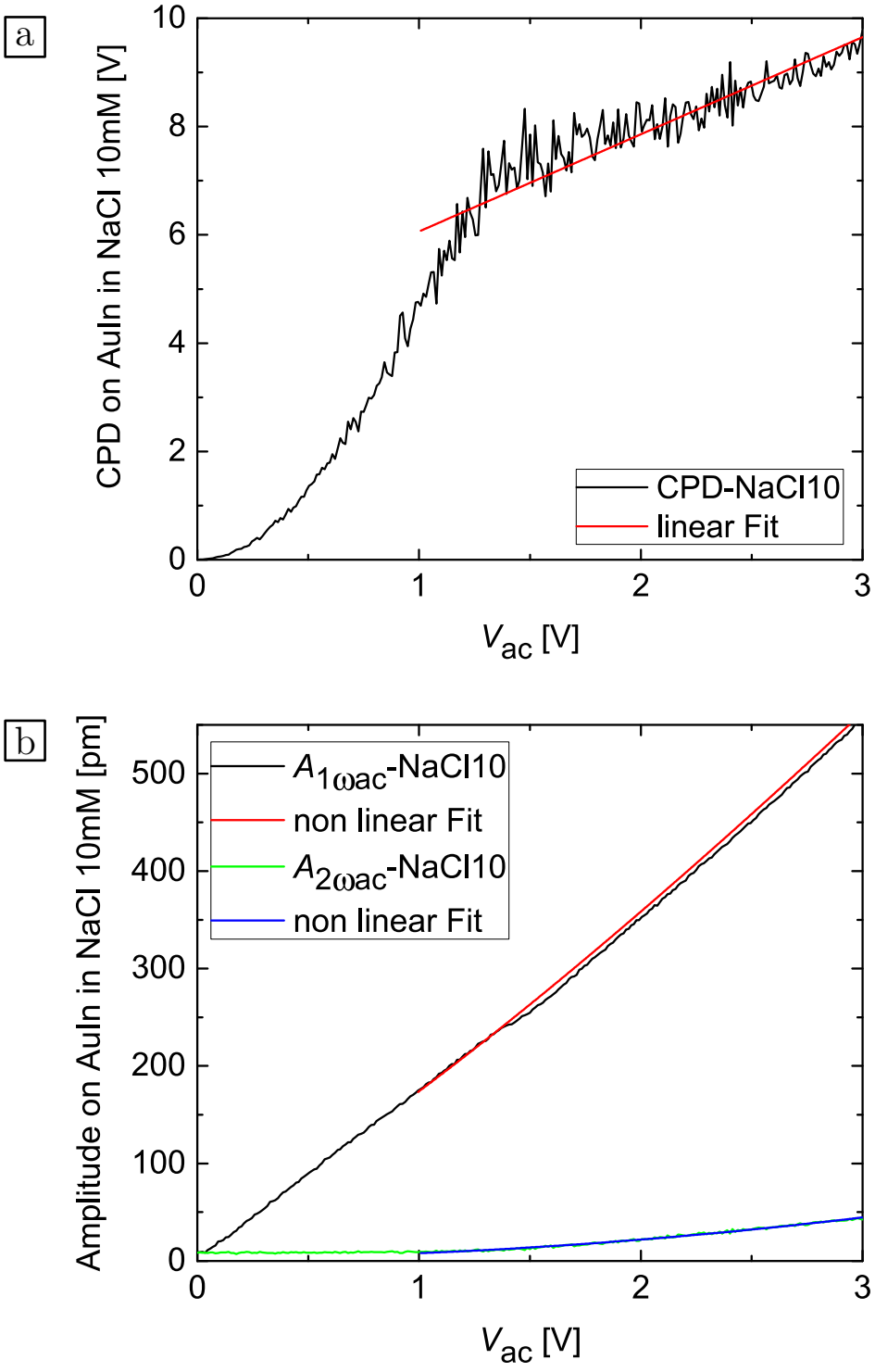

Figure B.27.: *Data of the V_{ac}-spectroscopy-measurements on the "AuIn-sample" in an NaCl solution with a concentration of* 10 mM. *a) CPD(V_{ac}) with a linear fit at $V_{ac} > 1$ V, and b) amplitude(V_{ac}) with non linear fits at $V_{ac} > 1$ V. Scan parameters: Cantilever: NCL-Pt; $f_{1st} = 73$ kHz; $A_{1st} = 5$ nm; $f_{2nd} = 499$ kHz; $V_{ac} = 1$ V.*

B.2.6. AuIn-sample in NaCl10, $V_{ac} = 2\,V$

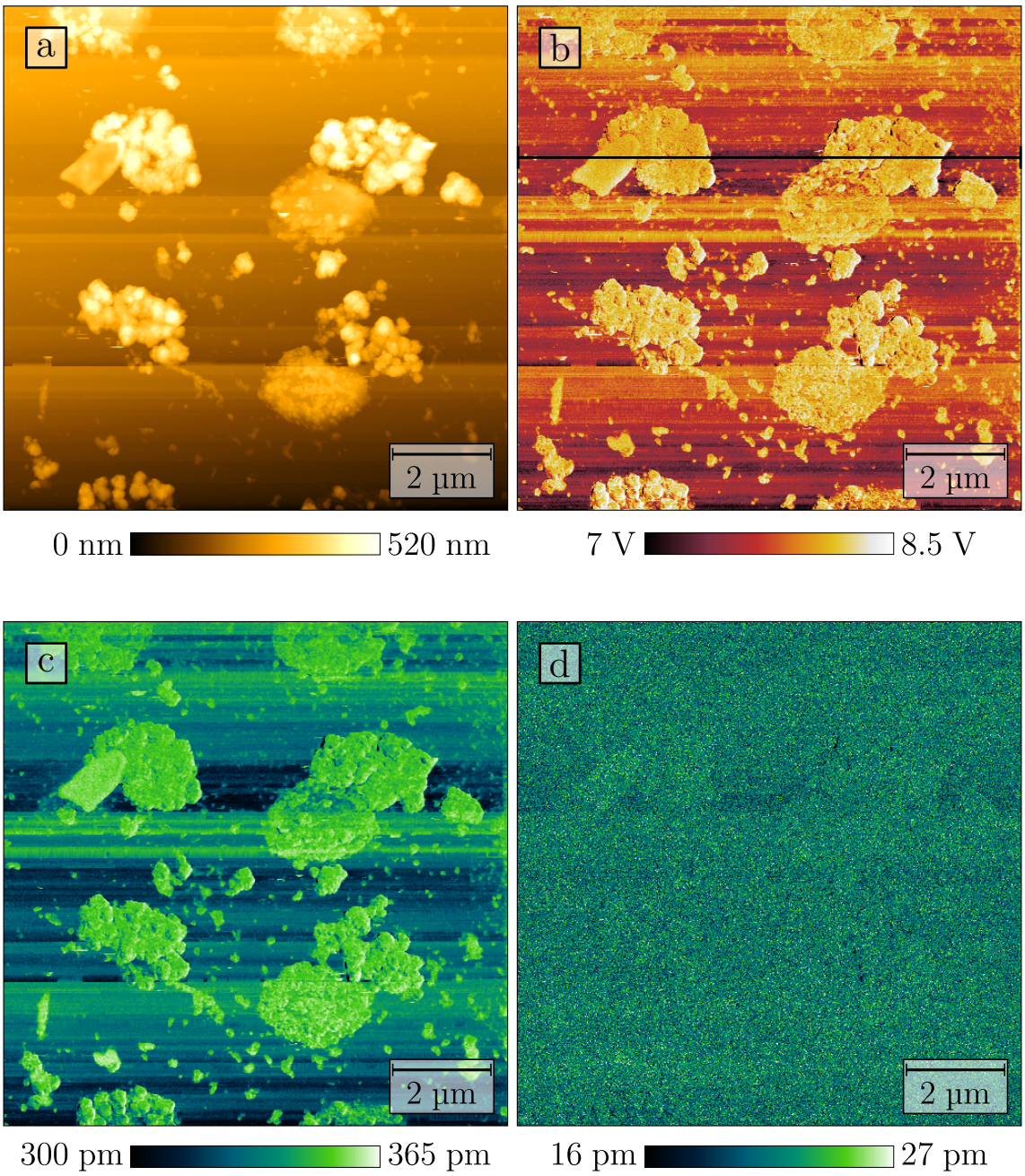

Figure B.28.: *Full data set of the measurement on the "AuIn-sample" in an NaCl solution with a concentration of* 10 mM *at an excitation voltage of* $V_{ac} = 2\,V$*: a) Topography, b)* CPD_{OL}*, c)* $A_{1\omega_{ac}}$*, d)* $A_{2\omega_{ac}}$*. Scan parameters: Cantilever: NCL-Pt;* $f_{1st} = 73\,kHz$*;* $A_{1st} = 5\,nm$*;* $f_{2nd} = 499\,kHz$*;* $V_{ac} = 2\,V$*.*

B.2.7. AuIn-sample in NaCl10, $V_{ac} = 3\,V$

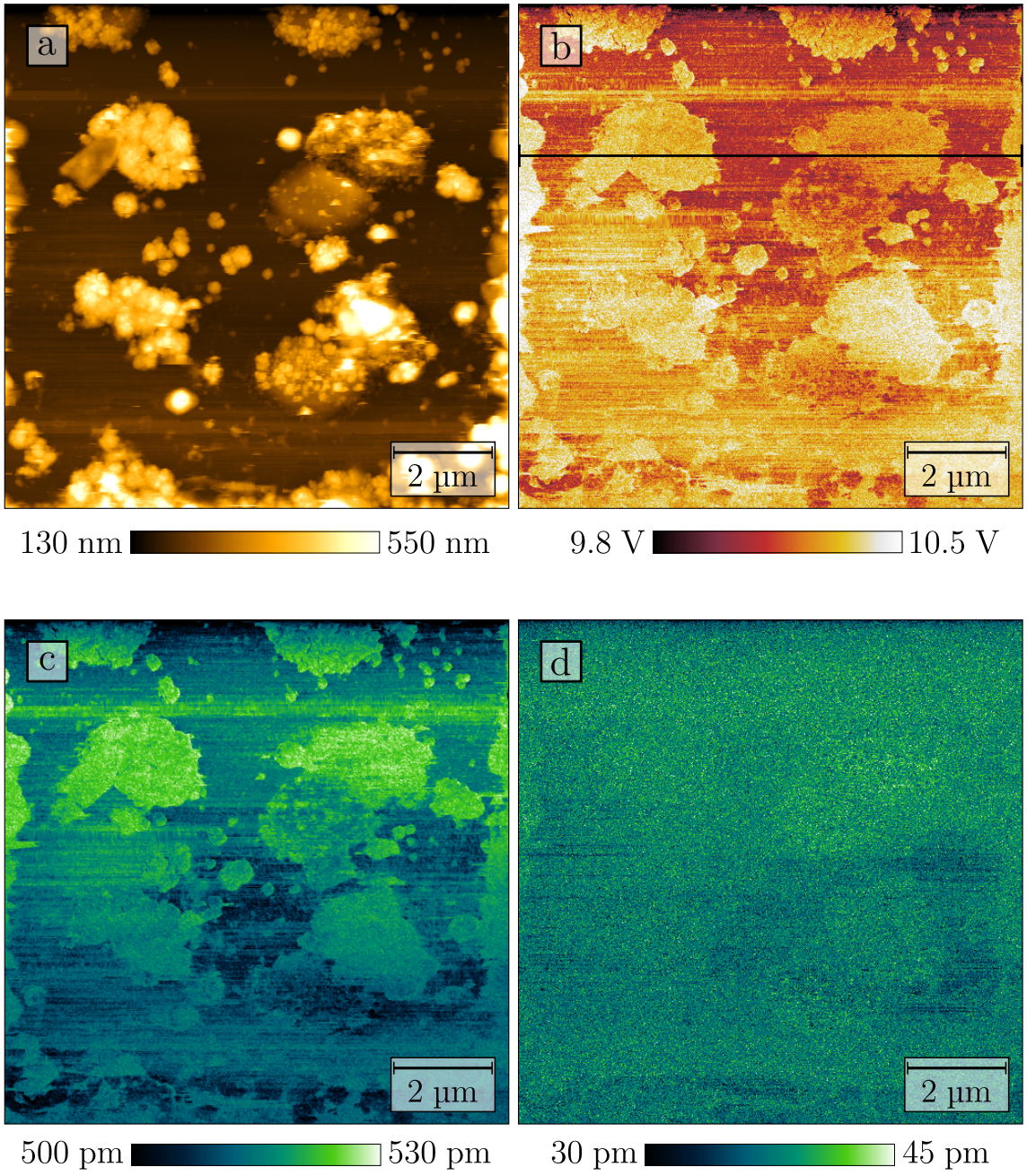

Figure B.29.: *Full data set of the measurement on the "AuIn-sample" in an NaCl solution with a concentration of* 10 mM *at an excitation voltage of* $V_{ac} = 3\,V$*: a) Topography, b)* CPD_{OL}*, c)* $A_{1\omega_{ac}}$*, d)* $A_{2\omega_{ac}}$*. Scan parameters: Cantilever: NCL-Pt;* $f_{1st} = 73\,kHz$*;* $A_{1st} = 5\,nm$*;* $f_{2nd} = 499\,kHz$*;* $V_{ac} = 3\,V$*.*

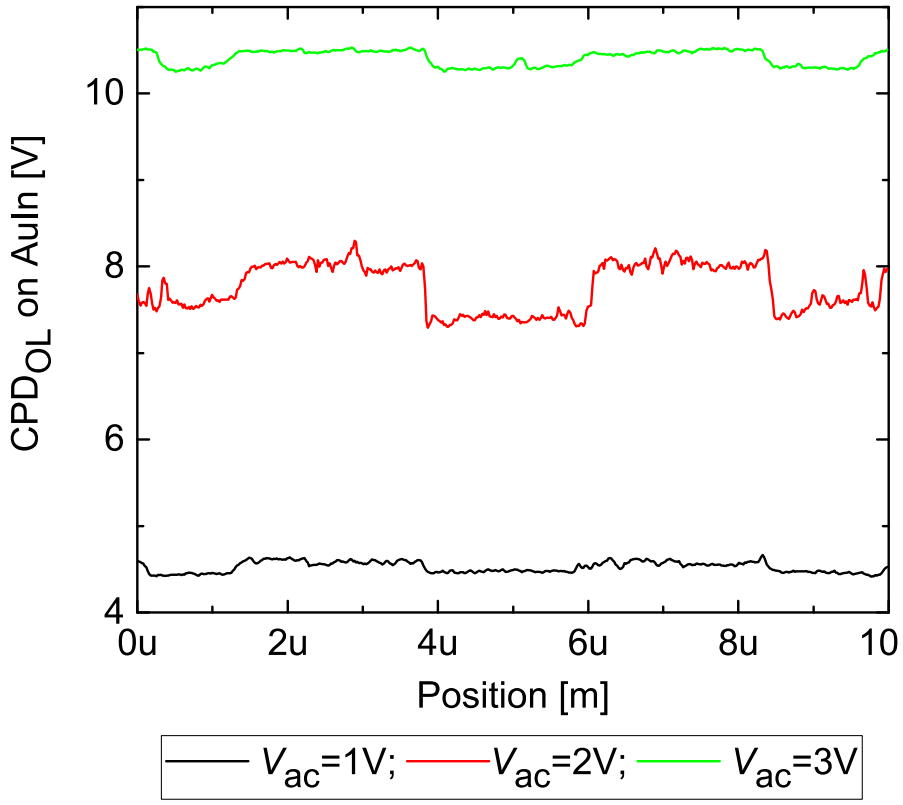

Figure B.30.: *Comparison of the CPD measured on the "AuIn-sample" in an NaCl solution with a concentration of* 10 mM *at different excitation voltages (V_{ac} = 1, 2 and 3 V) by profiles measured at the same position through the three images. The position of the profiles is indicated by black lines in the corresponding images (Figs. B.26b, B.28b and B.29b). An increase of the CPD is obvious, however the difference between the CPD of the gold and the CPD of the background does not follow a trend. Scan parameters: Cantilever: NCL-Pt; f_{1st} = 73 kHz; A_{1st} = 5 nm; f_{2nd} = 499 kHz; V_{ac} = 1, 2 and 3 V.*

C. Labview programs

C.1. IV-measurement setup

The solar-cell characterisation lab set up as part of this thesis consists not only of a commercial sun simulator with a commercial SourceMeter employed for the measurement of IV-curves, but also of a home-built tracer for the same purpose. The home-built system has the advantage of implementing an automatic measurement of the contact resistance of the mounted cells, and the possibility to measure up to 4 DSSCs at one time. Additionally the system features a home-built cell-holder for the IV-measurement, which makes sure the cells are properly fixed, always in the same position relative to the light-output of the solar simulator and which features a temperature control via a peltier element. The entire setup is described in more detail in section 3.2.1.

While the commercial part of the setup included a software, a home-built software for the control of the entire home-built part was necessary. It was written and tailored to our needs in Labview and the important parts will be outlined and described in this section. The software started as a rather simple program enabling only the measurement of IV-curves and repeated measurements thereof over a long time in defined intervals. This enables the examination of the behaviour of the DSSCs upon irradiation with light for multiple hours. Already in that stage the handling of the data was rather complex due to the large number of measured curves. Later on the software evolved, developing new features. The final version allows the measurement of IV-curves in defined intervals over a defined period of time or the measurement of a defined number of IV-curves in defined intervals. In the intervals between the measurements the cells can be illuminated or kept in the dark. It includes the automatic calibration of the light intensity and the tracer at the beginning of a long-time measurement as well as the measurement of the contact resistance of all the mounted cells before starting the IV-curve measurement. The temperature is not only measured during the measurement of each IV-curve, but it is possible to measure IV-curves while running a defined temperature

Figure C.1.: *Overview of the front panel of the IV-measurement software.*

program, thus measuring each IV-curve at a defined temperature. Currently only one dark-curve is measured at the beginning of the long-time measurement, however with only few changes a measurement of a dark curve before each (or before a defined fraction) of the measured IV-curves can be implemented. During a long-time measurement either the data of the current IV-curve or an overview over the development of the most important IV-curve parameters can be displayed. At the end of a measurement a report containing an overview over the development of the important parameters is generated in LaTeX and output as a pdf file.

An overview of the front panel of the software for the long-time measurement is shown in Fig. C.1. It shows the main tabs displaying the general settings for the measurement and the graphs for the data of the current IV-curve, while the settings for the measurement of the light intensity and the contact resistance and the graphs for the data overview (I_{sc} vs time, V_{oc} vs time, efficiency vs time and FF vs time) are in the other tabs.

Fig. C.2 shows an overview of the structure of the block diagram. The long-time measurement is based on a state machine, thus a case structure nested in a while loop. It consists of different cases which manage the initialisation of the long-time measurement, the generation of the files for the handling of the data with their appropriate headers and information written into them, the calibration of the measurement device, the calibration of the light intensity, the measurement of the contact resistance, one case for the measurement of the IV-curves, and a

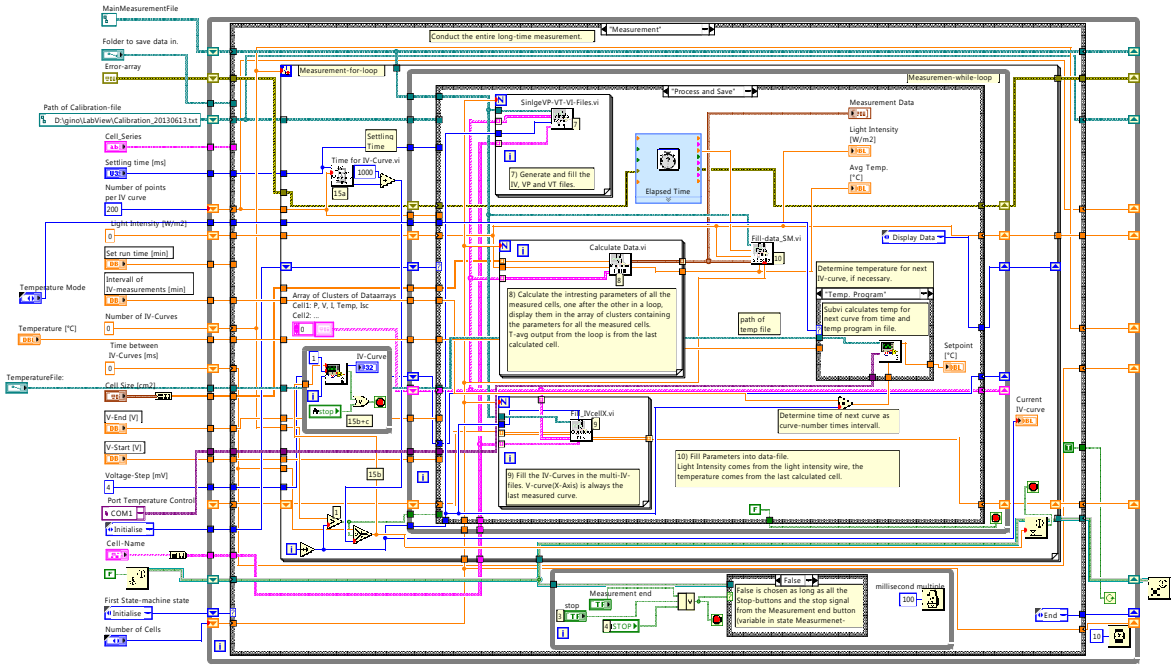

Figure C.2.: *Overview of the block diagram of the IV-measurement software. All the constants and parameters used as inputs are shown on the left. The outer while loop and case structure form the state machine for the entire long-time measurement, and the inner while loop with its case structure the one for the measurement of the IV-curves. The entire inner state machine is repeated by the for loop, thereby repeating the measurement of the IV-curves. This inner state machine shows the case to process and save the data, wherein the IV-curve parameters are calculated (8) and the data is saved in three different kinds of files (7, 9, 10). Inside the for loop but outside the inner state machine on the bottom of its left side is the function generating the wait time before any but the first IV-curve (15), and the small while loop outside the for loop at the bottom is the notifier loop for the abortion of the measurement during the recording of an IV-curve or the waiting interval.*

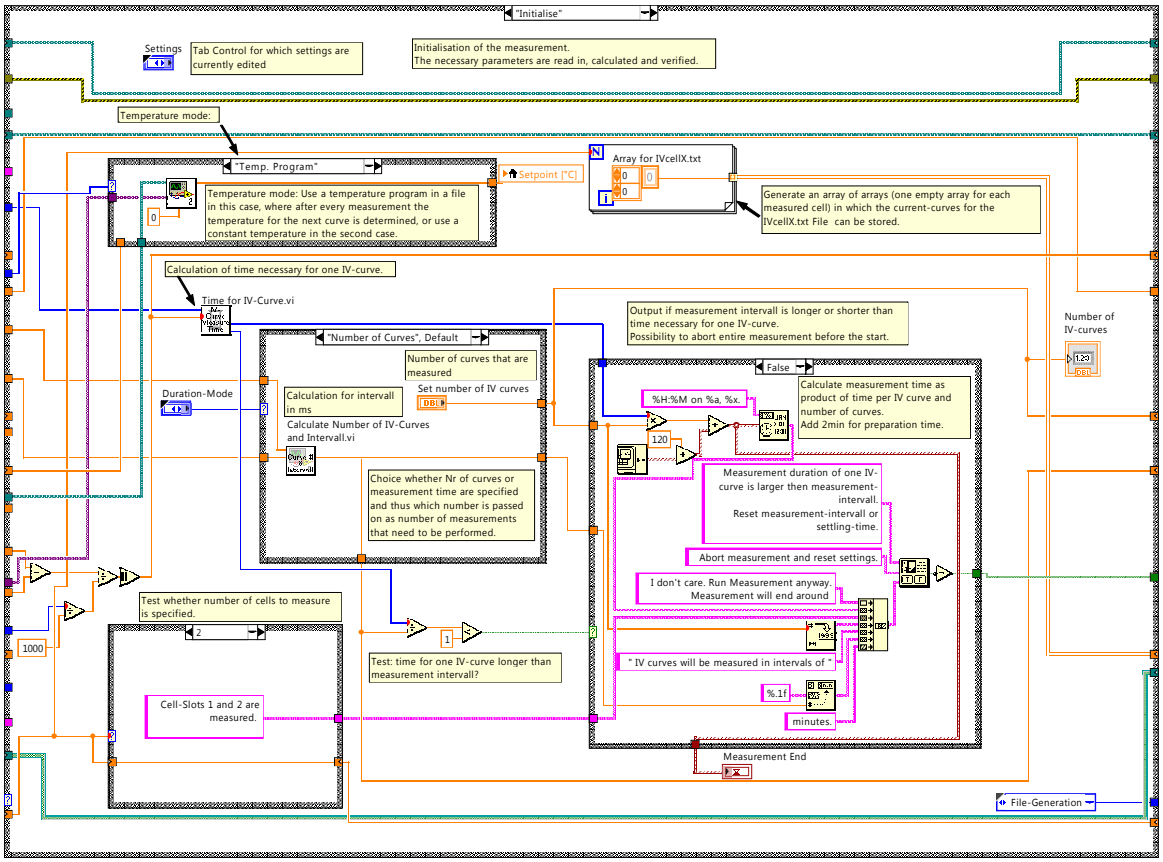

Figure C.3.: *Detail of the IV-measurement software showing the case "Initialise", wherein the initialisation of the setup with the estimation of the entire measurement time and the validation of the interval between the IV-curves and of the number of cells to measure takes place.*

final case to save the used settings, generate the report and close the measurement and the initialised devices.

In the case "Initialise" (Fig. C.3) the input parameters are processed. The program verifies that all the necessary inputs are given and prompts the user for missing information. The chosen measurement interval is checked against an estimated time for the measurement of one IV-curve to make sure measurements do not overlap. The time necessary for the entire measurement is estimated and the measurement mode with the number of total curves, the number and slots of the cells to be measured and the chosen temperature program is defined. In the next step the data files for the storage of the data overview are generated. These are files containing the important parameters for each measurement for each cell as well as all the measurement data for each cell. Files for the storage of the data of every single IV-curve for each cell are generated during the measurement. The next step is the calibration of the

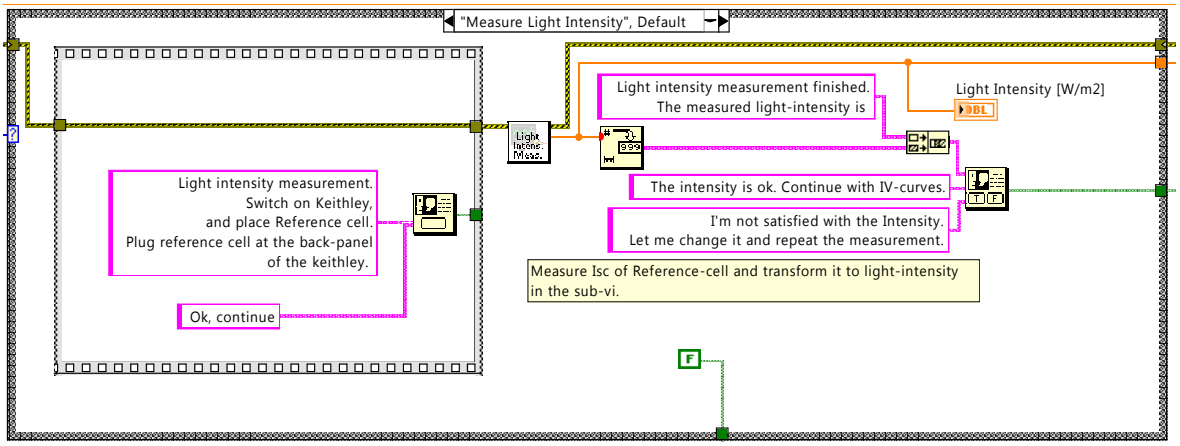

Figure C.4.: *The embedding of the light intensity measurement. The measurement itself is executed in the subvi and consists of the measurement of the I_{sc} of the reference cell and a calibration against the reference value. The software guides the user through the measurement by prompts.*

measurement device. For the calibration a defined resistance is inserted into the circuit and an IV-curve is measured. A linear fit is performed on the resulting straight and the slope and intercept are used for the calculation of the deviation of the measured current from the real current. The calibration parameters are stored for each measurement slot and read from this calibration file when they are needed later. If the calibration was performed recently instead of remeasuring it the calibration file already containing the parameters can be specified.

A detail of the case for the measurement of the light intensity is shown in Fig. C.4. For the measurement of the light intensity the Keithley 2400 SourceMeter and a silicon reference cell are employed. After setting up of the measurement the I_{sc} of the reference cell is measured in the subvi by applying no voltage and measuring the current generated by the cell. This current is compared to the specified current of the reference cell at a light intensity of $1000\,\mathrm{W/m^2}$ and the light intensity is calculated under the assumption of a linear dependence of the I_{sc} thereon. Instead of measuring the light intensity it can be set manually.

The final preparation step is the measurement of the contact resistance, which can be performed either by the Keithley 2400, or by the home-built tracer. The first has the advantage of being built for such measurements and thus allowing the easy measurement of small resistances bellow $1\,\Omega$, however all the contacts have to be measured manually one after the other. The home-built tracer on the other hand is designed for the measurement of IV-curves and its ability to measure resistances (particularly small resistances) is limited since it can not generate more than 20 mA of current. However it has the advantage to be able to measure all 4 cells at once, and to automatically switch between the measurement of the contact

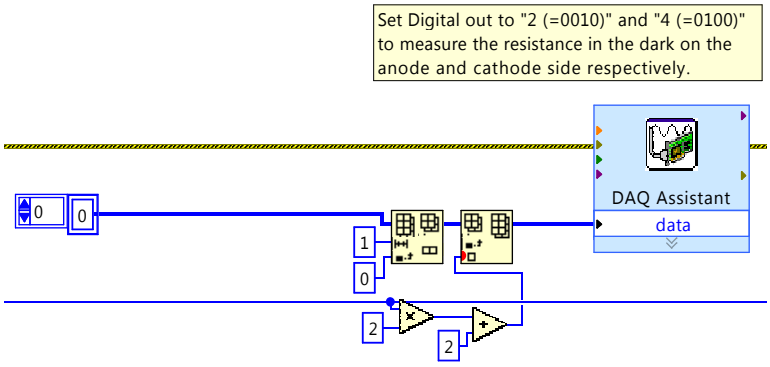

Figure C.5.: *The determination of the channel to be measured. Depending on the number of the run an appropriate setting for the digital output is generated and passed to the device using the DAQ-express subvi.*

resistance of the anode and the one of the cathode. The measured electrode is chosen by the proper setting of a relay in the setup, which changes the connection of the leads used for the measurements. The relays are addressed by a digital output of the device and are switched by changing said output, as is shown in Fig. C.5.

The measurement of the contact resistance is performed by applying a small voltage and measuring the current flowing through the contact as shown in Fig. C.6. The resistance R is calculated from the applied voltage V and the measured current I as $R = \frac{V}{I}$. The measurement does not consist of a single current measurement, but of the measurement of the current over a time span of 3 to 10 s with a frequency of 10 points per second. The entire resistance vs time curve is displayed for each cell, since this enables an easy detection of unstable connections by large variations in the curves.

The data is processed as shown in Fig. C.7. The first and last 10 % of the data is discarded and only the centre part is used for the calculations. The average resistance is determined together with the standard deviation, and the resistance for all the measured cells is collected in one array. The resistance is supposed to be in the range of 0 to 15 Ω. A higher resistance indicates a bad contact, a lower one a bad measurement. Thus the average of the resistance is checked against this interval and values outside the interval are reported by means of LEDs being switched on or off. Also the standard deviation of the data is checked to be below 10 % of the measured resistance and measurements with higher standard deviations are reported as untrustworthy. After the measurement of the resistances the entire resistance vs time curve for all the electrodes are displayed again for clarity, the quality of each measurement is shown by green LEDs and the user is given the choice to repeat the measurement after having replaced cells with bad contacts or to continue the IV-measurement.

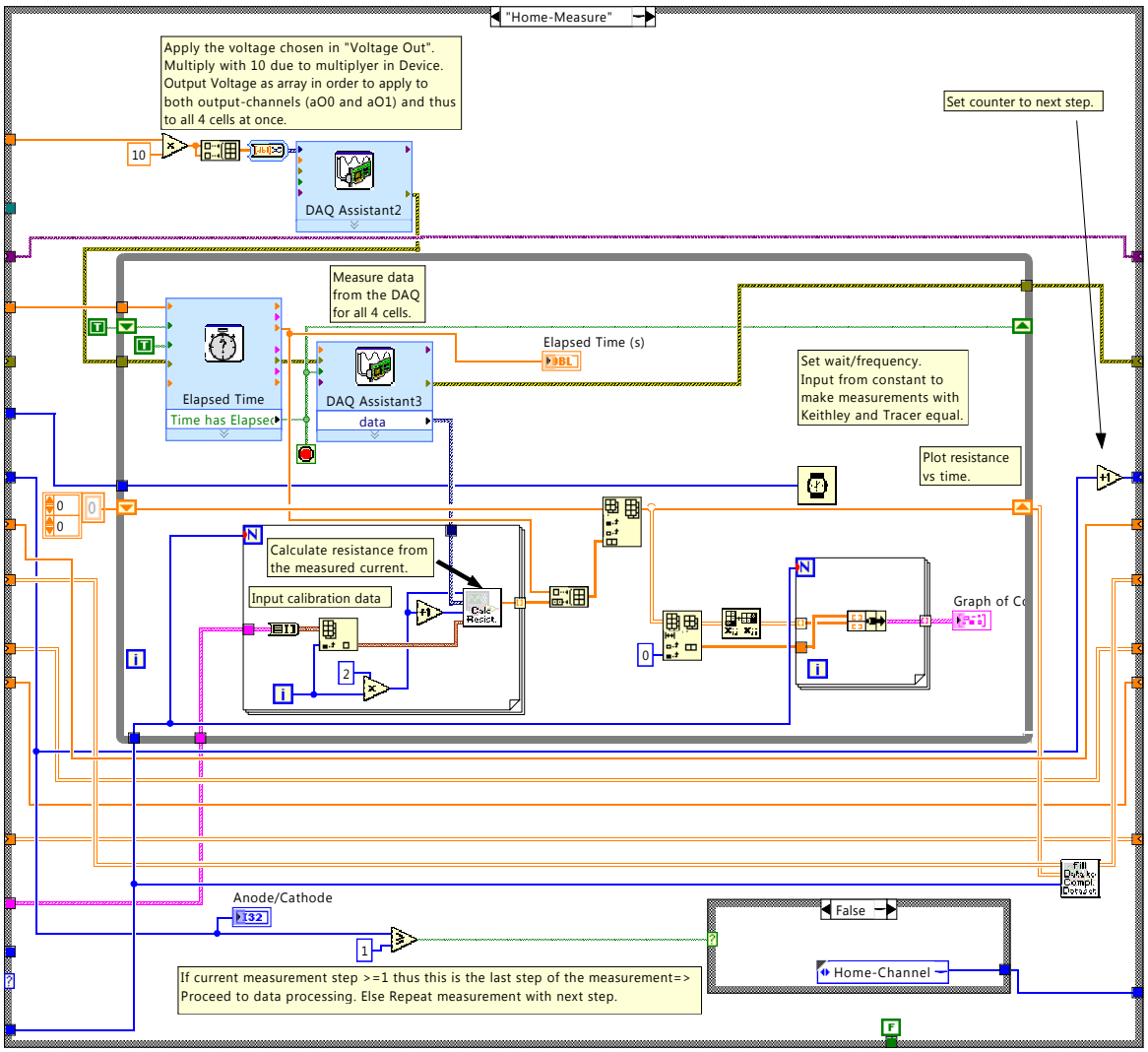

Figure C.6.: *Overview of the measurement of the contact resistance as it is performed with the home-built setup. The first step is the application of the voltage (DAQ Assistant 2), afterwards follows the reading out of the current (DAQ Assistant 3). The application of the calibration and the calculation of the resistance from the current and voltage take place in the subvi.*

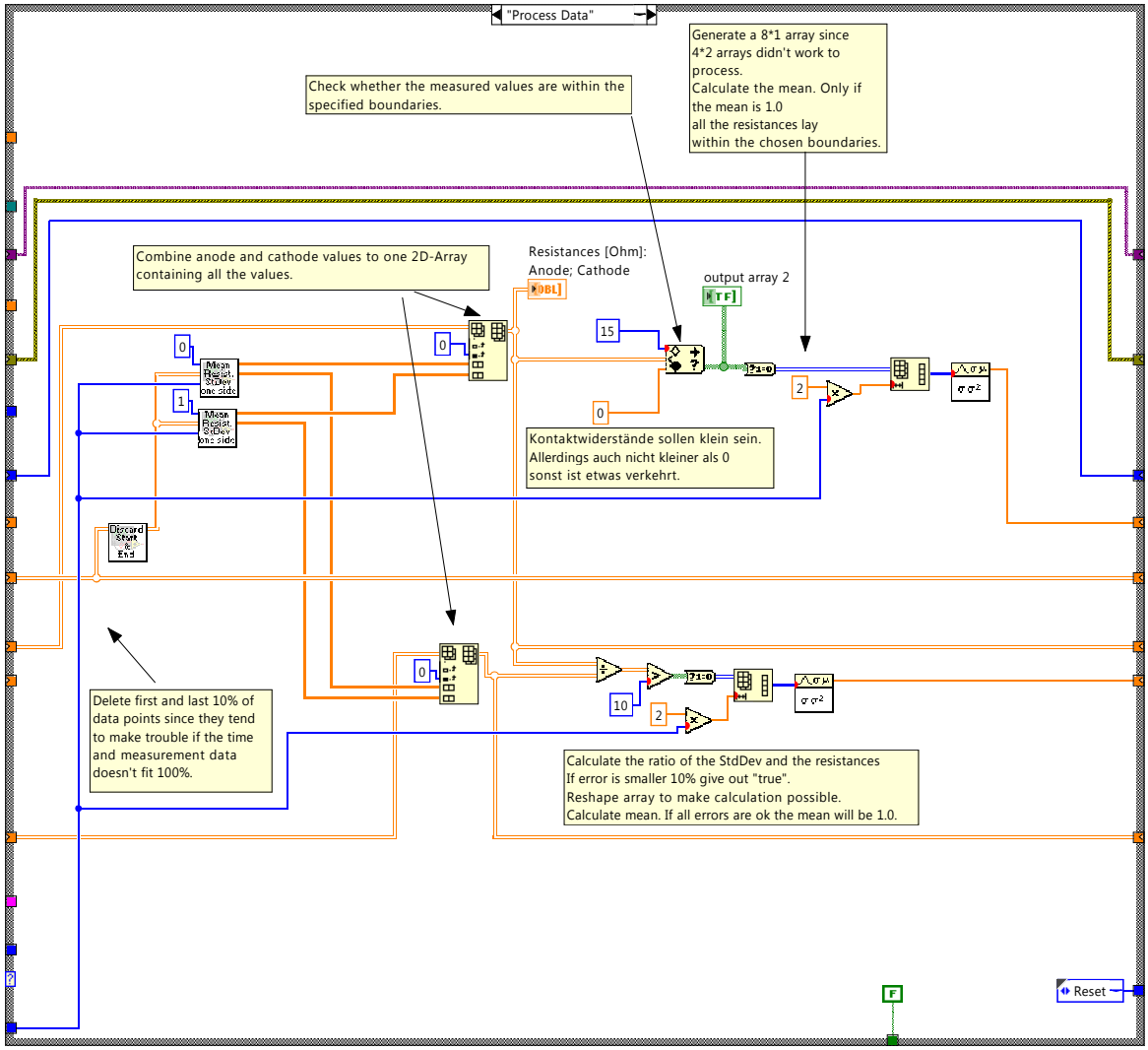

Figure C.7.: *The dataprocessing of the contact resistance measurement. Discarding of the margin-parts of the data, calculation of the mean and the standard deviation and verification of both against ranges of desirable data.*

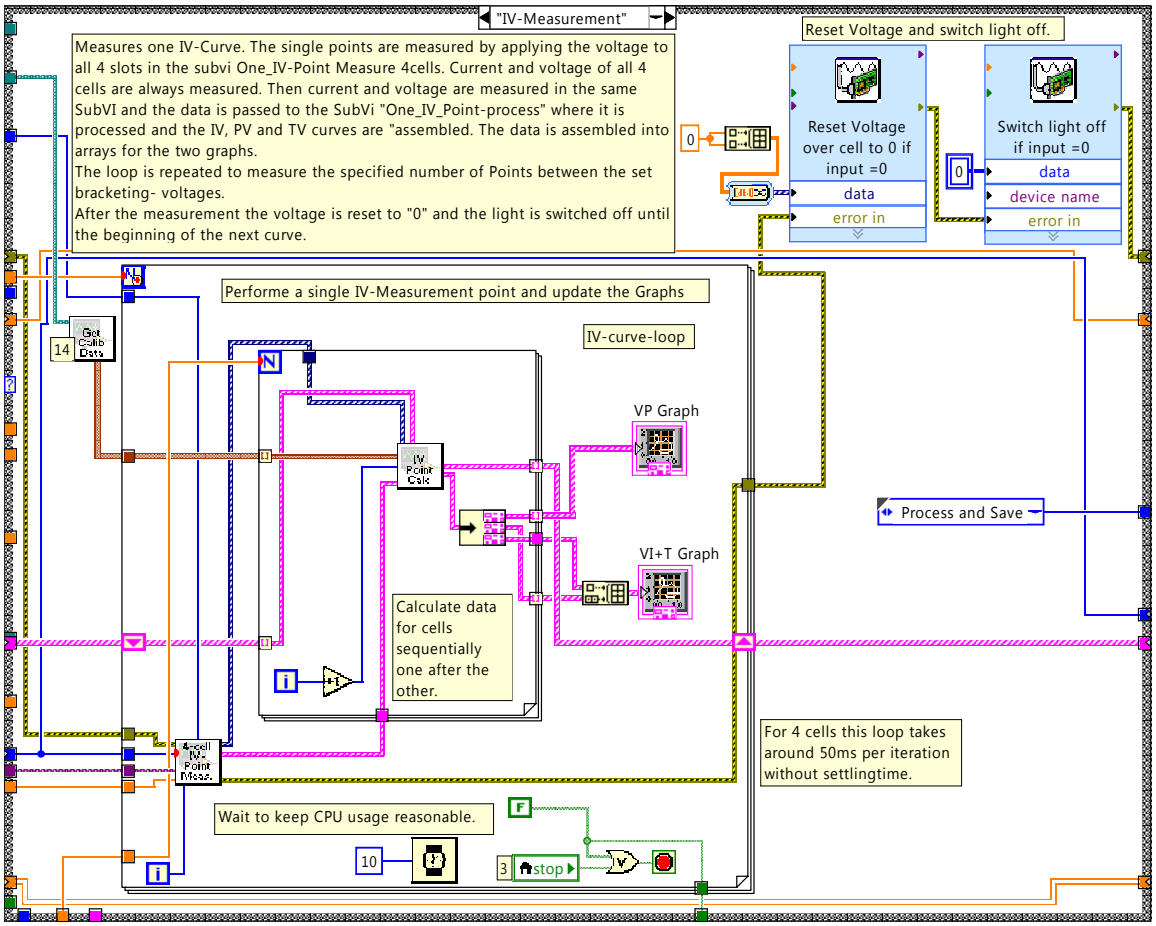

Figure C.8.: *The measurement of a single IV-curve. The application of the voltage, wait and read out of the current and the temperature take place in the first subvi and are shown in detail in Fig. C.9. The calibration of the data takes place in the second subvi.*

After having initialised and calibrated the entire setup, the measurement of the IV-curves is performed. The measurement is managed by a second state machine nested in a case of the first one. In an initialisation step the graphs are adapted to the range of the measurements and the data structure for the handling of the data is prepared. In the first versions of the software the data was handled in clusters. However handling of the data in arrays rather than in clusters simplified the scale-up of the measurement from 1 to 4 cells and thus the entire data structure was adapted. After detecting whether the current IV-curve needs to be measured in the dark or under illumination the I_{sc} is determined. While the V_{oc} is determined from the IV-curve the I_{sc} is measured separately as described before.

The measurement of the IV-curve is shown in Fig. C.8. It is performed in a loop. For each

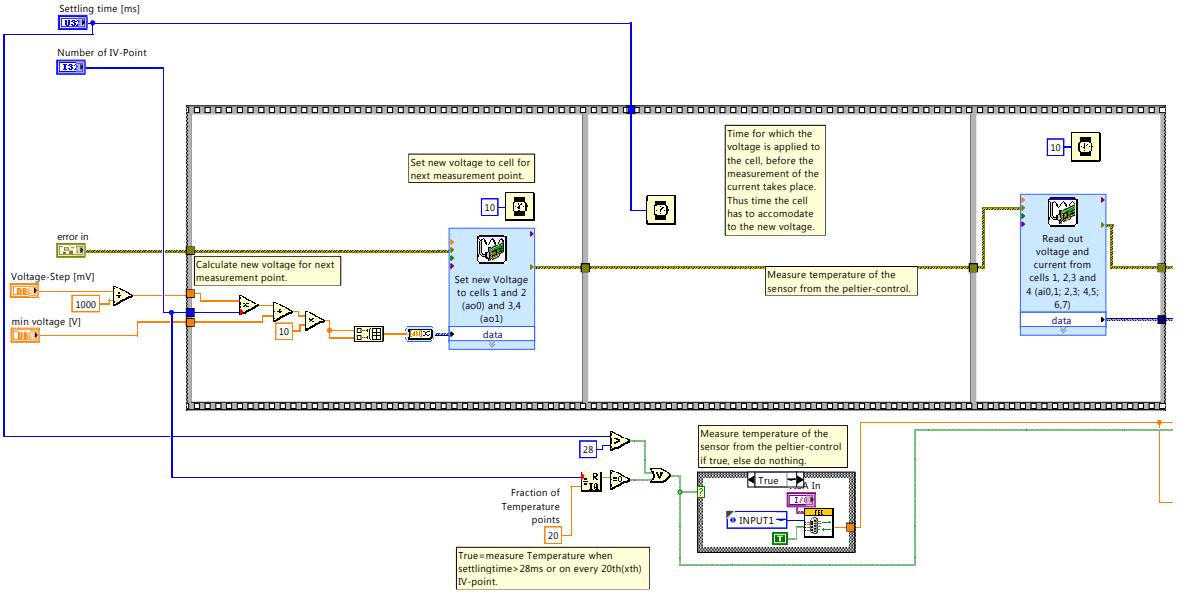

Figure C.9.: *Detail of the procedure to measure a single point of an IV-curve. Calculate and apply the voltage, wait for the settling time and read out the current from left to right in the three frames of the flat sequence. Measure the temperature in parallel depending on the settling time.*

step the necessary voltage is applied to the cells followed by a settling time during which the cells can adapt to the new voltage and a subsequent read out of the current as is shown in detail in Fig. C.9.

Independently of the number of cells the voltage is applied to all 4 cell slots and the current of all 4 slots is read, but the data of the slots not specified for the measurement is discarded. The application of the voltage, waiting for the settling time and reading of the current is performed in one subvi, which also contains the measurement of the temperature, and which is shown in Fig. C.9. The read out of the temperature from the controller of the peltier element is the slowest step in the chain. It is therefore performed in parallel to the measurement of the current. Depending on the settling time the temperature measurement would be rate limiting. Therefore at low settling times (thus fast measurement speed) the temperature is only measured at one of every twenty measurement points to decrease the slowing effect.

After reading out of the current and temperature the measured current is calibrated sequentially for each cell using the calibration parameters determined before in a separate subvi. In the same step the data for the current measurement is displayed in the corresponding graphs, and the calibrated data is passed on.

After the measurement of the IV-curve the data is processed and saved (Fig. C.10). First the

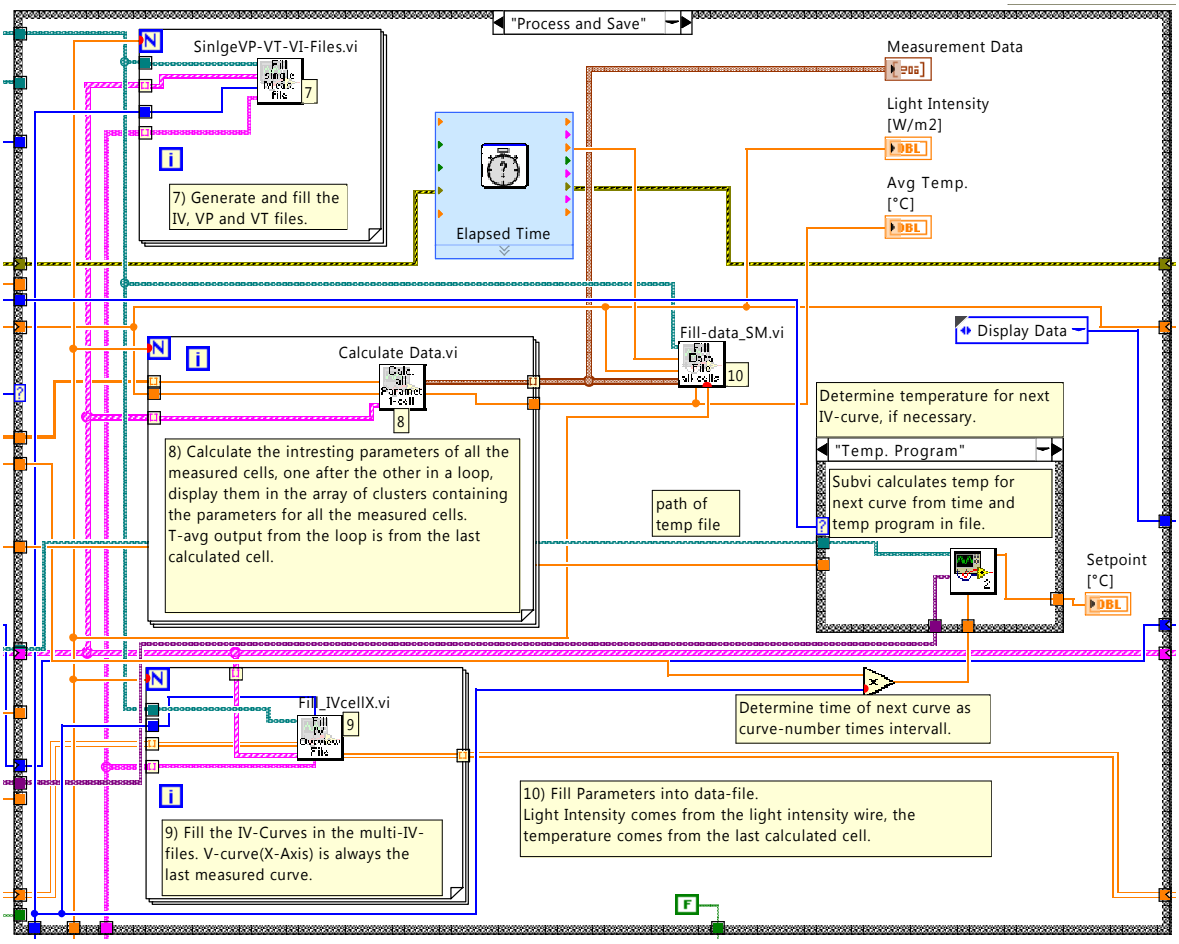

Figure C.10.: *The processing and saving of the data of the IV-measurements: Generate the files for the single traces (7), process the data and store the parameters in the overview file (8, 10), store the IV-curve in the IV-overview file (9) and calculate the temperature for the next IV-curve.*

important parameters (efficiency, V_{oc}, FF, I_{sc}, J_{sc}, J_{MPP}, V_{MPP}, temperature) are calculated in a separate subvi, which is rerun once for each measured cell, since the expense in terms of time was found to be negligible. The data is displayed on the front panel and saved in multiple files. One file for each trace (current-voltage, power-voltage, temperature-voltage) for each cell is generated, one file containing the current trace of each measurement of each cell and one single voltage trace is used as an overview for all the performed measurements. This only works if all the voltage traces are equal, which is true for the present setup. In a third file the important parameters for each cell and each measurement are stored in order to have an overview of the time dependent development thereof. The last part of this case is the determination and setting of the temperature of the next IV-curve according to the temperature program.

In a final step the data overview for the long-time measurement is generated. For this purpose the parameters are reread from the corresponding parameter file and are sorted into the arrays for the appropriate graphs.

The entire software is made more complex by the need to be able to shut down the measurement at any point and to shut it down without the necessity to wait for the end of the measurement state machine, which contains the entire wait period between two IV-curves. This functionality was implemented by a notifier loop, thus a loop which is able to send signals into the running measurement, which is the lower loop shown in Fig. C.2.

C.2. Open Loop Kelvin Probe Force Microscopy

Seeing that the AFM-setup was controlled using the control electronics from Nanonis and the corresponding software, also the OL-KPFM-measurements were performed therewith. The Nanonis software is Labview based. It provides a set of subvis to access and control the microscope and the measurement and thereby to extend its functionality to ones needs. It also provides a multi-pass mode, wherein each line of the SPM-measurement is recorded multiple times and at the beginning of each pass and line a subvi is called. The subvi is supplied with the information which line and which pass are scanned currently. It is inactive during the scan of the lines, and the connector panes of the subvi must not be changed in order to guarantee a correct implementation with the rest of the software. Except for these limitation it can be freely adapted. This multi-pass function in combination with a correspondingly tailored subvi was used for the OL-KPFM-measurements.

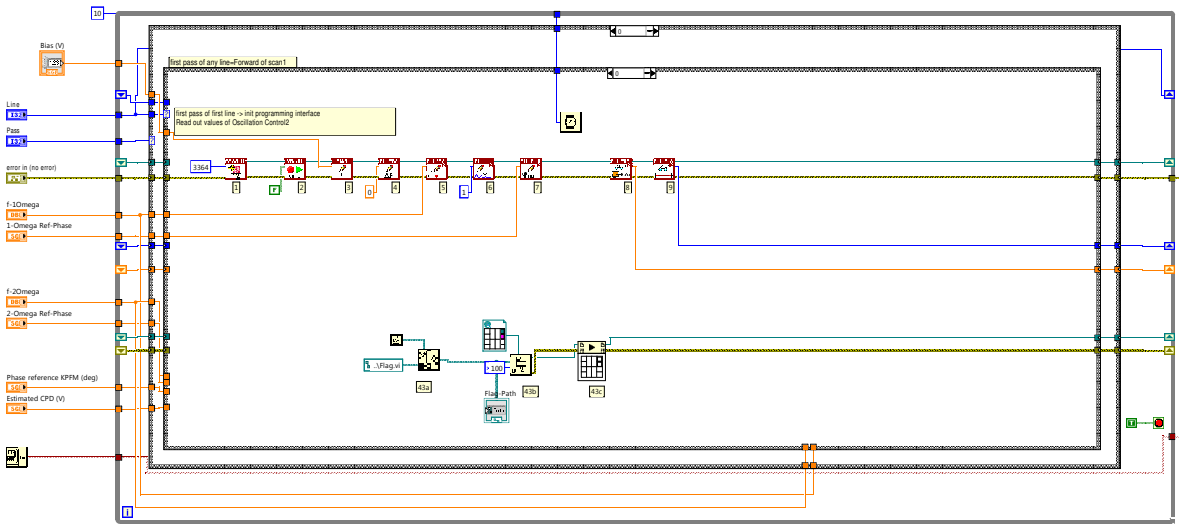

Figure C.11.: *Overview of the multi-pass subvi with the two nested case structures present in the case of the first pass.*

The general function necessary for the OL-KPFM-measurements is to measure every measurement point multiple times with different settings. The most effective way to that purpose is to scan every line multiple times. First the first line is scanned in $F_{1\omega_{ac}}$-setting with a predefined excitation frequency $f_{\text{ex-}1\omega_{ac}}$ and predefined settings for the corresponding lock-in amplifier (harmonic of signal demodulation, reference phase and frequency range). Then the same line is scanned again with $F_{2\omega_{ac}}$-settings. If the measurements are performed in air, a third scan of the first line for the CL-KPFM measurement is necessary, where the settings are the same as in $F_{1\omega_{ac}}$-setting, but instead of measuring the corresponding oscillation amplitude it is nullified by the Kelvin controller, which needs to be switched on. At the end of each recorded image V_{ac}-spectroscopies need to be recorded. Additionally it is desirable to be able to save all the important settings into a single file, since in the measurement files only the settings of the last of the performed scans are saved.

An outline of the block diagram of the Labview-VI for the OL-KPFM-measurement is shown in Fig. C.11. It consists of a while loop with a case structure. The case structure determines the pass of the current scan. Multiple passes occur on each line. The uneven passes are the forward scans and the even passes the backward scans. In the setup used here forward and backward scans were always performed with equal settings, thus corresponding passes (0 and 1, ...) are equal and the settings don't change in the even scans. The settings are adapted in the forward scans and most possibilities occur for the first scan, since there a distinction of the lines is necessary. Therefore the case for the first pass contains a second case structure

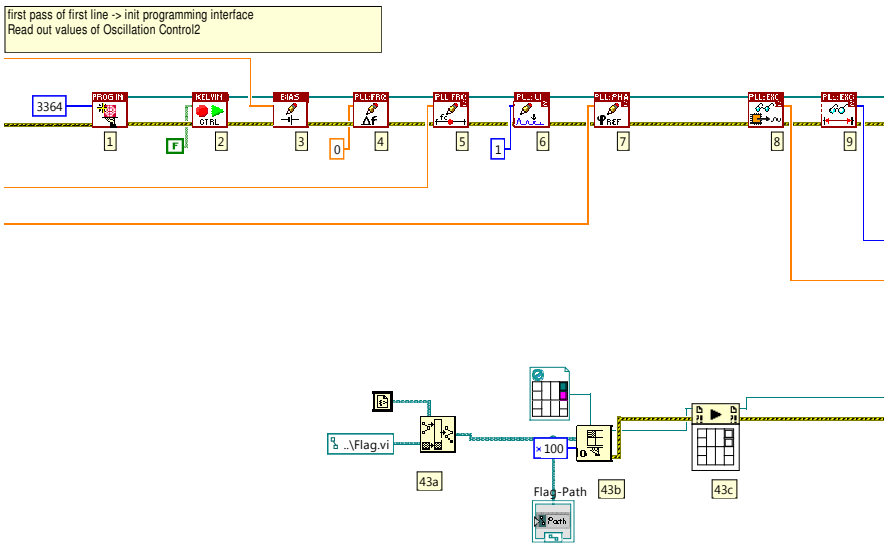

Figure C.12.: *The steps taking place in the first pass of the first line. Top: Initialise device, reset lock-in and set lock-in settings. Bottom: start the subvi to catch the file name from the Nanonis software.*

which distinguishes the different lines. Special cases occur for the first line and the end, which is marked by the Nanonis software by an output of line -10 and pass 1. The case occurring at the first line is shown in the overview image (Fig. C.11) and in more detail in Fig. C.12.

Therein the subvi is first connected to the Nanonis controller (1), the Kelvin controller is switched of (2), the bias is set to a defined value (usually 0 V) (3) and the frequency shift is set to 0 Hz (4). This resetting of the lock-in proved necessary, since alternate settings being present before the start of the measurement can influence the measurement. Afterwards the excitation frequency (5), the harmonic for the demodulation (6) and the reference phase (7) are set for the measurement in $F_{1\omega_{ac}}$-setting. Finally the excitation voltage (8) and the excitation voltage range (9) are read from the controller in order to be able to reset them in the end. The second action (43) calls the subvi "Flag", which is necessary for the storage of the settings in a file with the same name as the main data file of the measurement. The Nanonis software generates the file names by a combination of a base name and a counter. While the first can be read from the software programmatically, the second can not. However at the end of the measurement the Nanonis software provides the file name of the file generated in the current scan. In order to obtain this file name a subvi needs to run continuously and wait for the flag of the Nanonis software which indicates the end of a measurement and discloses the file name. Since the multi-pass subvi is only called at the beginning of each pass and is inactive at all other times it can not perform the waiting for the flag, thus the continuously

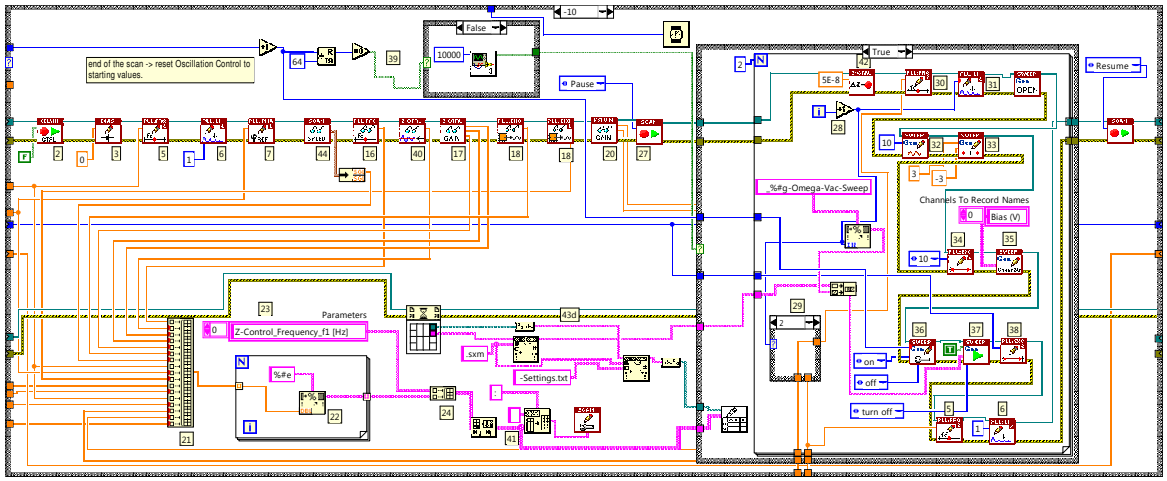

Figure C.13.: *The case for the actions to perform at the end of a recorded image. Storage of all the important parameters and settings in a file with the same name as the recorded image (left part) and recording of the V_{ac}-spectroscopies (right part).*

running subvi "Flag" is necessary and it is started at this point during the first pass of the first line. The case for the first pass of all the measured lines except the first contains the same steps for the switching off of the Kelvin controller, the resetting and the setting of the excitation and demodulation (2-7).

The third possible case is the case called at the end of the measurement, thus either when the entire image was scanned, but also when the measurement is aborted by the user. It is shown in Fig. C.13. It roughly contains 4 actions. The long line of subvis (2, 3, 5, 6,7, 44, 16, 40, 17, 18, 18, 20) reads all the settings which need to be stored after the measurement. These parameters are combined with the parameters specified for the measurement (frequency, reference phase and harmonic for each measurement mode (21)), converted into strings (22) and combined with a corresponding header (23) into one large array (24) and are stored in a file with the same name as the measurement (with the suffix "-settings") (41). The name of the measurement file is provided by the subvi "Flag" which has been running in the background (43d).

The measurement is paused after the reading of the settings (27) in order to enable enough time for the recording of V_{ac}-spectroscopies if necessary. At the same time the number of scanned lines is examined in order to determine whether a measurement was stopped manually or due to the planned end of an image (39). Usually SPM images are recorded with numbers of lines and rows according to powers of 2 (mostly 256, 512 or 1024), which are dividable by 64. Thus a number of rows dividable by 64 indicates a planned ending of the

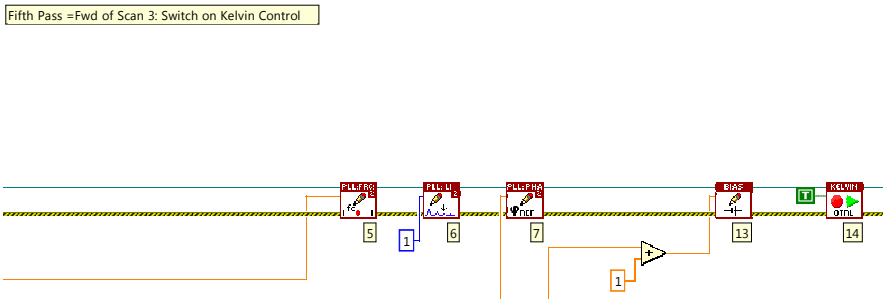

Figure C.14.: *Setting of the CL-KPFM measurement as part of the combine CL-OL-KPFM measurement. Changing lock-in to $F_{1\omega_{ac}}$-settings and switching on of the Kelvin controller.*

measurement and thus the necessity to record V_{ac}-spectroscopies. If the number of rows is not dividable by 64 the user is prompted whether V_{ac}-spectroscopies need to be recorded. In the last part of this case (the case structure on the right) the V_{ac}-spectroscopies are recorded using the generic sweeper functionality of the Nanonis software. Thereto after having defined the tip lift upon switching off of the z-controller (42) the necessary settings ($F_{1\omega_{\mathrm{ac}}}$-setting or $F_{2\omega_{\mathrm{ac}}}$-setting) are set (29-31) and the scan signal is set to the excitation voltage (32). The excitation voltage range is set to 10 V (34), and the scan range to the desired range (33, here ± 3 V). The channels to be recorded are defined and general settings of the generic sweeper are set (35, 36) and the sweep of the excitation voltage is performed (37) before resetting the lock-in (38, 5, 6). The sweep is performed twice, once in $F_{1\omega_{\mathrm{ac}}}$-setting and a second time in $F_{2\omega_{\mathrm{ac}}}$-setting. Finally the paused measurement is resumed.

The settings for the second and the third scan of each line in $F_{2\omega_{\mathrm{ac}}}$-setting and for the CL-KPFM measurement are set in the corresponding cases of the pass case structure. The latter is shown in Fig. C.14. The first contains only the resetting of the Bias and the setting of the frequency, harmonic and reference phase of the lock-in. For the CL-KPFM measurement the Kelvin controller needs to be switched on after setting of the lock-in. To ensure a proper working of the Kelvin controller the bias is set to a value larger than the estimated CPD (13) before the controller is switched on (14).

List of Publications and Presentations

Peer-reviewed journal publications

- A. Henning, G. Günzburger, R. Jöhr, Y. Rosenwaks, B. Bozic-Weber, C. E. Housecroft, E. C. Constable, E. Meyer and Th. Glatzel; "Kelvin probe force microscopy of nanocrystalline TiO_2 photoelectrodes"; *Beilstein Journal of Nanotechnology* 4, 418 (**2013**).

- B. Eren, L. Marot, G. Günzburger, P-O Renault, Th. Glatzel, R. Steiner and E. Meyer; "Hydrogen-induced buckling of gold films"; *Journal of Physics D: Applied Physics* 47(2); 025302 (**2014**).

- R. Jöhr, L. Zajac, G. Günzburger, H. Hug, B. Such, M. Szymonski, E. Meyer, Th. Glatzel; "Impact of photocatalysis on carotenoic acid dye-sensitized solar cells"; *Hybrid Materials* 2(1); (**2015**).

- U. Gysin, E. Meyer, Th. Glatzel, G. Günzburger, H. R. Rossmann, T. A. Jung, S. Reshanov, A. Schöner, H. Bartolf; "Dopant Imaging of Power Semiconductor Device Cross Sections"; Submitted to: *Microelectronic Engineering.*

- G. Günzburger et al; "Kelvin Probe Force Microscopy Analysis of Dye Sensitized Solar Cells in electrolyte", Manuscript in preparation.

Oral Presentations

- G. Günzburger, R. Jöhr, B. Bozic-Weber, C. E. Housecroft, E. C. Constable, H. Hug, P. Hunziker Buchwald, E. Meyer and Th. Glatzel; "Dye Sensitised Solar Cells with Carotenoid Molecules"; *DPG Frühjahrstagung*, **2012**, Berlin, Germany.

Poster Presentations

- A. Henning, G. Günzburger, R. Jöhr, Y. Rosenwaks, P. Kopecky, B. Bozic-Weber, C. E. Housecroft, E. C. Constable, E. Meyer and Th. Glatzel; "Kelvin Probe Force Microscopy of Nanocrystalline TiO_2 Photoelectrodes"; *Swiss Nanoconvention*, **2012**, Lausanne, Switzerland.
- G. Günzburger, R. Jöhr, H. Hug, C. E. Housecroft, E. C. Constable, Th. Glatzel, E. Meyer; "Dye Sensitised Solar Cells with carotenic acid sensitisers"; *Swiss Nanoconvention*, **2013**, Basel, Switzerland.
- G. Günzburger, R. Jöhr, H. Hug, E. Meyer and T. Glatzel; "Kelvin Probe Force Microscopy Analysis of Dye Sensitised Solar Cells"; *Nano in the Snow*, **2014**, Kandersteg, Switzerland.
- G. Günzburger, A. Henning, R. Jöhr, H. Hug, P. Kopecky, E. C. Constable, C. E. Housecroft, B. Bozic-Weber, Th. Glatzel, and Ernst. Meyer; "Kelvin Probe Force Microscopy investigation of Dye Sensitised Solar Cells"; *EMRS Spring Meeting*, **2013**, Strasbourg, France.